Quantum Mechanical Potential Energy Surfaces and State Couplings for Photodissociation and Collision-Induced Dissociation Reactions: New Methods and Applications

A Dissertation
SUBMITTED TO THE FACULTY OF
UNIVERSITY OF MINNESOTA
BY

Ke R. Yang

IN PARTIAL FULFILLMENT OF THE REQUIREMENTS
FOR THE DEGREE OF
DOCTOR OF PHILOSOPHY

Adviser: Donald G. Truhlar

July 2014

Acknowledgments

I sincerely thank my advisor Professor Donald G. Truhlar for his guidance and support throughout my Ph. D. stage. I also want to thank all the Truhlar group members, especially Dr. Xuefei Xu, Dr. Jingjing Zheng, Dr. Yulia Paukku, Dr. Zoltan Varga, and Mr. Jason. D. Bender for discussion and collaboration, and Dr. Bo Wang, Dr. Tao Yu, and Mr. Luke Fiedler for their help and encouragement in my research.

I also want to thank Dr. Shuxia Zhang, Dr. Benjamin Lynch, and other staff members at Minnesota Supercomputing Institute (MSI) for their kind help. The computing resources from MSI and the Environmental Molecular Sciences Laboratory (EMSL) are greatly appreciated.

Finally, I want to thank my parents, Fangsong Yang and Runhua Luo, my brother, Xue Yang, and my wife, Shuang Zhang for their love and support.

Dedication

To my parents, brother, and Shuang

Abstract

Potential energy surfaces (PESs) play essential roles in the study of chemical dynamics. The adiabatic ground-state PES of N_4 was constructed with permutationally invariant polynomials and is suitable for treating high-energy vibrational-rotational energy transfer and collision-induced dissociation in N_2–N_2 collisions. Our adiabatic PES reproduces the ab initio data well but adiabatic surface fitting is not designed to reproduce the cuspidal ridges at state crossings. This motivates working with the diabatic representation for the photodissociation where state crossing seams are key global features. Diabatic representations are also very convenient for fitting state couplings. A new diabatization scheme based on complete-active-space self-consistent-field diabatic molecular orbitals and the fourfold way was proposed to obtain smooth diabatic potentials and couplings at the multi-configurational quasi-degenerate perturbation theory level of electronic structure theory. The new scheme has been used to study the photodissociation of phenol in which three electronic states are involved. A new method for fitting global potential energy surfaces of multi-dimensional reactive systems was developed and is called the anchor points reactive potential (APRP) scheme. The full-dimensional 3×3 matrix of diabatic potential energy surfaces and couplings for the nonadiabatic photodissociation of phenol was constructed with the APRP method. Multidimensional tunneling calculations through the barrier on the shoulder of the conical intersection of the S_1 and S_2 states of phenol suggest the adiabatic nature of the

early dynamics of phenol photodissociation and the importance of tunneling in the photodissociation.

Table of Contents

List of Tables

List of Figures

Chapter 1. Introduction

1.1 General Overview

For a molecular system involving both electrons and nuclei, the electronic and nuclear degrees of freedom can be separated with the widely used Born-Oppenheimer approximation.[1] The electronic degrees of freedom are solved quantum mechanically at fixed nuclear geometry. The sum of the resulting energy eigenvalues of the electronic Hamiltonian and the Coulomb repulsion energies between nuclei are called adiabatic potential energies, and they depend parametrically on the nuclear geometry, which leads to the useful concept of potential energy surfaces (PESs). Minima on PESs correspond to equilibrium structures of molecules, and saddle points on PESs correspond to transition state structures of chemical reactions. Potential energy surfaces are $(3N - 6)$-dimensional hypersurfaces, where N is the number of nuclei.

In the Born-Oppenheimer approximation, the nuclei are assumed to move on a single adiabatic PES, and this motion can be treated either quantum mechanically or classically. PESs are crucial in the study of chemical dynamics. They can be constructed implicitly by solving the electronic structure problem at every step of the nuclear motion, and this is called direct dynamics; in particular, where the potential energy, gradient, and/or Hessian is calculated by electronic structure methods each time the dynamics or sampling algorithm calls for it. An alternative approach is to construct the PES explicitly with analytic functions to represent (fit) a set of individual electronic structure calculations performed prior to the dynamics step.[2-5]

The Born-Oppenheimer approximation works well when PESs are well separated,[6] which is the case for many thermal chemical reactions. However, it breaks down when two or more adiabatic PESs approach closely or intersect. In the latter case, several PESs, rather than one single PES, are needed for the proper description of nuclear motions, and transitions between different adiabatic PESs are governed by nonadiabatic couplings. Nonadiabatic couplings are off-diagonal matrix elements of the nuclear momentum vector and the nuclear kinetic energy, which are often called nonadiabatic derivative couplings and nonadiabatic scalar couplings, respectively. The latter, although they are not necessarily negligible, are often neglected in semiclassical treatments.[7] The nonadiabatic derivative couplings are vectors in the nuclear coordinate space and will be called nonadiabatic couplings for simplicity. Nonadiabatic couplings are responsible for nonadiabatic transitions between different adiabatic states, and they are usually small in region when adiabatic states are well separated. However, they can vary rapidly near avoided crossing and become singular at conical intersections where two adiabatic states are degenerate and two adiabatic PESs touch.[8-10] This makes the adiabatic representation inconvenient for dynamical studies of many nonadiabatic processes such as photodissociation, predissociation, quenching of excited states in collisions, chemiluminescence, etc. The use of diabatic representations[10] has been proposed as an alternative approach to study dynamics.

The notation “diabatic” was first introduced by Lichten[11] in the study of ion-atom collisions. Diabatic states are strictly defined as states have zero nonadiabatic

couplings.[12] However, such diabatic states do not exist in general[13] because the curl condition[14,15] for their existence is generally not fulfilled. Although the strict diabatic states do not exist in general, quasi-diabatic states that are defined to have small nonadiabatic couplings that can be neglected are often very useful, and they are often just called diabatic states.[6] That language will be followed in this thesis.

Diabatic states can be constructed by rotating adiabatic states through an orthogonal transformation called the adiabatic-to-diabatic transformation. Diabatic states are not eigenstates of the electronic Hamiltonian, so the potential energy matrix is not diagonal. The off-diagonal elements are called diabatic couplings, and they promote electronic-state transitions in a diabatic representation. Because it removes the singularity of nonadiabatic couplings at conical intersections, the diabatic representation is suitable for the practical study of dynamics of nonadiabatic processes. However, diabatic states are not merely a mathematical construction to bypass the singularity of nonadiabatic couplings; rather they have solid physical relevance in that they yield smooth molecular properties.[16] Diabatic states can be defined as states whose electronic structures keep their essential characters over the entire range of nuclear coordinates (or at least change slowly over the whole range). It can be shown[17] that by transforming to a diabatic representation, even one that does not remove all of the removable nuclear momentum coupling, one can obtain results where the leading correction to the wave function at energies of interest for photochemistry is of order $M^{-1/2}$, where M is the ratio of an average nuclear mass to the electron mass (thus $M^{-1/2} < 0.024$).

Electronically nonadiabatic processes can be modeled in either the adiabatic representation or a diabatic representation. In the adiabatic representation, adiabatic states are uniquely defined as the eigenstates of the electronic Hamiltonian, and the electronic Hamiltonian is diagonal. The diagonal elements are adiabatic PESs V_i which have ($3N$ – 8)-dimensional cuspidal ridges along conical intersection (CI) seams. The nonadiabatic couplings, which promote nonadiabatic transitions, are vectors in the nuclear space which vary rapidly where two PESs approach and become singular at conical intersections. In a diabatic representation, the nonadiabatic couplings are negligible (or assumed to be negligible), and diabatic electronic states and their associated PESs are coupled through the off-diagonal elements of electronic Hamiltonian.

Potential energy surfaces can be constructed in either the adiabatic or a diabatic representation. However, the cuspidal ridges of adiabatic potentials and the singularity of nonadiabatic couplings in ubiquitous conical intersection regions[18] prevent the analytic fit of adiabatic PESs and nonadiabatic couplings. The wave functions of diabatic states change slowly with respect to nuclear coordinates; thus the diabatic potentials and diabatic couplings are smooth functions of nuclear coordinates that allow for convenient analytic representation. With an analytic representation of diabatic potentials and couplings, one can perform dynamics studies in either the diabatic or adiabatic representation because adiabatic PESs and nonadiabatic couplings can be obtained easily with diabatic potentials and couplings.[19]

1.2 Diabatization schemes

Diabatic states are not uniquely defined so many schemes have be developed to construct diabatic states; they are discussed in two recent reviews. [20,21] These schemes can be classified into two general categories: schemes that try to construct diabatic states without first calculating adiabatic states, and schemes that construct diabatic states as linear combinations of adiabatic states.

Valence bond theory[22] can be used to construct diabatic states,[23,24] and this theory has been used to construct diabatic states in S_N1 reactions[25] and proton-coupled electron transfer.[26] Diabatic states can be constructed by optimizing the wave function subject to a constraint on density, as in frozen density functional method[27,28] and constrained density functional theory (CDFT).[29] The CDFT developed by van Voorhis *et al*.[30-33] computes diabatic states without constructing adiabatic states by minimizing the energy of a system using KS DFT with constraints on either spin or electronic density. Methods like this can be well suited for charge-transfer reactions but may be not as useful in photochemical reactions where no charge transfer is involved.

The second category of methods first constructs a set of adiabatic states; diabatic states are then generated by rotating the adiabatic states by means of an orthogonal adiabatic-to-diabatic transformation matrix. Depending on how the adiabatic-to-diabatic matrix is obtained, these methods can be further classified as coupling-based methods and property-based methods. The coupling-based methods involve the minimization of nonadiabatic couplings.[12-15,34] This type of method was originally proposed by Smith[12]

(for one-dimensional problems where nonadiabatic coupling can be reduced to zero) and Baer,[14,15] and it involves the integration of nonadiabatic couplings along a selected path. Since the curl condition cannot be satisfied in general, the integration of nonadiabatic couplings is path-dependent except for the one-dimensional case. Thus diabatic states constructed with this type of methods depend on the integration path. Requiring the evaluation of nonadiabatic couplings over an extended range of nuclear coordinates along a selected path, the coupling-based methods are quite computationally demanding (because a path that winds through the whole space is long and cumbersome), and their applications are limited to very small systems (with less than three atoms).

The property-based methods focus on the smoothness of properties of diabatic states as functions of nuclear coordinates. The property-based methods have great computational advantages over coupling-based methods since the evaluation of nonadiabatic couplings are not needed to construct diabatic states from adiabatic states. One can enforce the smoothness of a physical property, such as a one-electron property, to construct diabatic states. Mulliken first suggested the use of dipole moments,[35] as was pursued later by Hush,[36] and others.[37,38] The quadruple moment[39] and the transition dipole moment[40,41] have also been employed in the construction of diabatic states. Subotnik and coworkers[42,43] proposed a generalization of the Boys localization algorithm to construct diabatic states with localized electron and spin density. Yarkony[44] showed that any real-valued Hermitian electronic property operator, satisfying only certain limited restrictions, can be used to construct diabatic states near a conical

intersection.

One can also enforce the smoothness of the electronic wave functions themselves (in the language above, the "property" under consideration is wave function smoothness). Hendekovic and coworkers suggested the construction of diabatic states by maximizing of the sum of the squared occupation numbers of natural spin orbitals[45,46] or by an interpolation based on the one-electron reduced density matrices. [47] Spiegelman and Malrieu[48] suggested constructing diabatic states by using effective Hamiltonians based on the CIPSI (Configurational Interaction by Perturbation with multiconfigruational zeroth order wave functions Selected by Iteration) algorithm, and their method has been improved by Cimiraglia *et al*.[49] Köppel and coworkers developed the block diagonalization scheme[50-53] to yield diabatic states in a given block provided that one starts with a reference basis that already behaves diabatically. The block diagonalization scheme can be derived from a least action principle[54] and has been developed within the complete-active-space self-consistent-field (CASSCF)[55-57] framework by Domcke and coworkers.[58,59] The diabatization method proposed by Simah *et al*.[60] is based on condition that both the orbitals and the configuration coefficients of the diabatic wave functions change as little as possible as a function of geometry by maximizing certain functions of the overlap between orbitals at current geometry and those at a neighboring geometry. Average natural orbitals have been shown to quasidiabatic character and may be used to as starting point to construct diabatic states in some cases. García *et al*.[61] suggested the use of state-averaged natural orbitals as starting point to construct diabatic

states since they have nearly diabatic character. Ruedenberg and Atchity proposed a diabatization method based on configurational uniformity.[62-64] The principle of configurational uniformity was used by Nakamura and Truhlar[65-67] in conjunction with their development of the fourfold way diabatization method. The fourfold diabatization method uses a threefold density matrix criterion and reference orbitals to generate diabatic molecular orbitals (DMOs) which change smoothly as the nuclear coordinates follows any continuous path in the region of interest; the fourfold way is more general than the orbital diabatization schemes of García et al. and Atchity and Ruedenberg, which work only for a subset of the commonly occurring cases. In a second stage of the fourfold way, the user recasts the configuration state functions in terms of the DMOs, specifies the diabatic prototypes in term of lists of dominant configuration state functions (CSFs) expressed in terms of the DMOs, and transforms the adiabatic state wave functions to diabatic state wave functions by the principle of configurational uniformity.

As compared to several alternative schemes to construct diabatic states, the fourfold way diabatization method yields diabatic potentials and couplings at a given geometry independent of any path leading to that geometry; in another word, the diabatic states obtained by fourfold way diabatization are path-independent. Another important feature of fourfold-way diabatization is that it yields *N* diabatic electronic states that span the same space as *N* chosen adiabatic states. The fourfold way diabatization method has been applied to the study of photodissociation of ammonia,[68-71] bromoacetyl chloride,[72] hydrogen bromide,[73] and chlorobromomethane.[74]

In this dissertation, we simplified the fourfold diabatization method to include dynamical correlation energy by multi-configuration quasi-degenerate perturbation theory (MC-QDPT) [75,76] while using DMOs based on the CASSCF step (chapter 3). The new algorithm was used to construct MC-QDPT diabatic states with CASSCF DMOs for the photodissociation of phenol to phenoxyl radical and H atom, which has been studied extensively as a prototypical process in photochemistry,[77-98] both experimentally and theoretically (chapter 4).

1.3 Potential energy surfaces construction

Analytic representation of PES is needed for dynamics study except for direct dynamics calculations, which – when accurate electronic structure methods are employed – are only practical for very small systems requiring very little sampling. Molecular mechanics (MM),[99] which denotes an analytical potential expressed in internal coordinates, is perhaps the simplest way to construct a PES, but conventional MM omits cross terms and is valid only near an equilibrium structure. Recently, MM-like force fields for specific molecules based on electronic structure calculations of energies and Hessians at an equilibrium structures have been developed for more accurate simulations.[100,101] Even such molecule-specific force fields, though, are unable to describe bond-breaking processes.

Recently developed methods based on permutation-invariant polynomials (PIP)[102,103] and interpolating moving least squares (IMLS)[104-106] can describe bond dissociation processes and chemical reactions very well; but they are limited to very

small systems, usually five or fewer atoms since they require many electronic structure calculations as input. The number of electronic calculations required for PES fitting grows rapidly with the dimensional of the system. For a system with N atoms, the number of internal degrees of freedom is $F = 3N - 6$, and the number of data points grow as m^F, where m is the number of points needed to span a given degree of freedom. For a molecule with only 13 atoms, such as phenol, using only four points in each dimension for the fit would still require $4^{33} \cong 10^{20}$ data points.

The reactive empirical bond order method,[107,108] ReaXFF,[109,110] and the valence bond order (VBO) method,[111] are aimed to extend MM to bond breaking processes, but such methods have less accuracy for global or semiglobal PESs than conventional MM has near equilibrium structures. It would be desirable to combine analytical potentials in internal coordinates for degrees of freedoms that involve small distortions from equilibrium structures with model potentials based on general functional forms to fit degrees of freedom involved in or closely coupled to bond breaking or bond rearrangements. Such an approach would be analogous to the combined quantum mechanics/molecular mechanics (QM/MM) method where MM is used for degrees of freedom of spectator atoms, and QM is used for degrees of freedom of active ones. Unlike QM/MM, which has been used widely for incorporating MM into electronic structure calculations of PESs of large systems such as enzymes and catalysis,[112-118] very few studies have been performed that incorporate MM-like force fields into the fitting of high-dimensional PESs.[119]

In this dissertation, we constructed a global ground state PES of N_4 using modified permutationally invariant polynomials with the correct asymptotic behavior (chapter 2). A method called anchor points reactive potential (APRP), that combines fitting of quantum mechanical potential energy surfaces for selected degrees of freedom with molecule-specific MM-like force fields for other degrees of freedom, was proposed to obtain a high-dimensional PES to treat bond-breaking processes (chapter 3). The APRP method is used to construct the full dimensional PESs for the photodissociation of phenol (chapter 6).

1.4 Organization of the dissertation

This dissertation is organized to address two issues. The first is the simplification of the fourfold diabatization method to obtain MC-QDPT diabatic states with CASSCF DMOs (chapter 3) and apply the method to study the photodissociation of phenol (chapter 4). The second is the construction of potential energy surfaces. This has two parts: (i) The adiabatic ground-state surface of N_4 was constructed with modified permutation-invariant polynomials with better asymptotic behavior (chapter 2); (ii) a new method to construct high-dimensional PESs for bond dissociation processes was developed (chapter 5) and applied to construct the full-dimensional PESs of the phenol to study the dynamics of photodissociation.

Chapter 2 describes the construction of a global ground-state potential energy surface for N_4 suitable for treating high-energy vibrational-rotational energy transfer and collision-induced dissociation in N_2–N_2 collisions. Modified permutationally invariant

polynomials with the correct asymptotic behavior were used to fit about 17,000 ab initio data point. Our adiabatic PES reproduces the ab initio data well, but fails to reproduce the cuspidal ridges at state crossings, and this motivate us to work with diabatic representation for the photodissociation of phenol. Yuliya Paukku, Zoltan Varga, and Donald G. Truhlar are acknowledged as coworkers for chapter 2.

Chapter 3 describes a new scheme for the direct diabatization of MC-QDPT wave functions. Our new scheme constructs MC-QDPT diabatic states by utilizing CASSCF DMOs. The new diabatization scheme was tested for the dissociation of LiF and the reaction of Li + FH → LiF + H. Xuefei Xu and Donald G. Truhlar are acknowledged as coauthors for chapter 3.

Chapter 4 describes the application of the new fourfold way diabatization method to the photodissociation of phenol. Diabatic potentials of the three low-lying states ($^1\pi\pi$, $^1\pi\pi^*$, and $^1\pi\sigma^*$) and their diabatic (scalar) couplings were calculated at MC-QDPT level along the O–H stretching and C–C–O–H torsion coordinates for the nonadiabatic photodissociation of phenol to phenoxyl radical and hydrogen atom. The work in chapter 4 provides insight into the mode specificity of phenol photodissociation and shows that diabatization at the MC-QDPT level employing CASSCF diabatic MOs can be a good starting point for multi-dimensional dynamics calculations of photochemical reactions. Xuefei Xu and Donald G. Truhlar are acknowledged as coauthors for chapter 4.

Chapter 5 presents a new method for fitting potential energy surfaces in molecular-mechanics-like internal coordinates based on data from electronic structure

calculations. The method is especially suitable to chemical reactions involving bond dissociation but should be extendable to bond-rearrangement reactions as well, and it is used in this chapter to construct the full dimensional PESs for the O-H bond dissociation in methanol and the N–H bond dissociation in dimethylamine. Xuefei Xu and Donald G. Truhlar are acknowledged as coauthors for chapter 5.

Chapter 6 describes the application of our improved APRP method to construct a full-dimensional 3×3 matrix of diabatic potential energy surfaces and couplings for the nonadiabatic photodissociation of phenol. The potential energy surfaces and couplings are used to calculate and characterize the adiabatic surfaces and conical intersections. The surfaces and couplings are used for full-dimensional tunneling calculations of the adiabatic photodissociation rate, and the couplings are used to provide indicators of which vibrational modes are effective in promoting dissociation. Xuefei Xu, Jingjing Zheng, and Donald G. Truhlar are acknowledged as coauthors for chapter 6.

1.5 References

[1] M. Born and R. Oppenheimer, Ann. Phys., **84**, 457 (1927).

[2] G. C. Schatz, Rev. Mod. Phys. **61**, 669 (1989).

[3] T. Hollebeek, T.-S. Ho, and H. Rabitz, Annu. Rev. Phys. Chem. **50**, 537 (1990).

[4] A. Fernández-Ramos, J. A. Miller, S. J. Klippenstein, and D. G. Truhlar, Chem. Rev. **106**, 4518 (2006).

[5] T. V. Albu, J. Espinosa-García, and D. G. Truhlar, Chem. Rev. **107**, 5101 (2007).

[6] B. K. Kendrick, C. A. Mead and D. G. Truhlar, Chem. Phys., **277**, 31 (2002).

[7] M. S. Child, in Atom-Molecule Collision Theory, edited by R. B. Bernstein (Plenum, New York, 1979), p. 427-465.

[8] T. C. Thompson, D. G. Truhlar, and C. A. Mead, J. Chem. Phys. **82**, 2392 (1985).

[9] D. R. Yarkony, J. Phys. Chem. **100**, 18612 (1996).

[10] A. W. Jasper, B. K. Kendrick, C. A. Mead, D. G. Truhlar, in Modern Trends in Chemical Reaction Dynamics, edited by X. Yang, K. Liu (World Scientific, Singapore, 2003), p. 329-391.

[11] W. Lichten, Phys. Rev. **131**, 229 (1963).

[12] F. T. Smith, Phys. Rev. **179**, 111 (1969).

[13] C. A. Mead and D. G. Truhlar, J. Chem. Phys. **77**, 6090 (1982).

[14] M. Baer, Chem. Phys. Lett. **35**, 112 (1975).

[15] M. Baer, Mol. Phys. **40**, 1011 (1980).

[16] E. S. Kryachenko and D. R. Yarkony, Int. J. Quantum Chem. **76**, 235 (2000).

[17] C. A. Mead, J. Chem. Phys. **125**, 204109 (2006).

[18] D. G. Truhlar and C. A. Mead, Phys. Rev. A **68**, 032501 (2003).

[19] A. W. Jasper and D. G. Truhlar, in Conical Intersections: Theory, Computation, and Experiment, edited by W. Domcke, D. Yarkony and H. Köppel (World Scientific, Singapore, 2011), p. 375-414.

[20] H. Köppel, in Conical Intersections: Electronic Structures, Dynamics and Spectroscopy, edited by W. Domcke, D. R. Yarkony, and H. Köppel (World Scientific, Singapore,2004), p. 175-204.

[21] T. Van Voorhis, T. Kowalczak, B. Kaduk, L.-P. Wang, C.-L. Cheng, Q. Wu, Annu. Rev. Phys. Chem. **61**, 149 (2010).

[22] L. Pauling, The Nature of the Chemical Bond, 3rd. ed.; Cornell University Press: Ithaca, NY, 1960.

[23] D. G. Truhlar, J. Comput. Chem. **28**, 73 (2007).

[24] L. Song and J. Gao, J. Phys. Chem. A **112**, 12925 (2008).

[25] H. J. Kim, and J. T. Hynes, J. Am. Chem. Soc. **114**,10508 (1992).
[26] A. Soudackov and S. Hammes-Schiffer, J. Chem. Phys. **113**, 2385 (2000).
[27] T. A. Wesolowski and A. Warshel, J. Phys. Chem. **97**, 8050 (1993)
[28] E. H. M. Olsson, G.-Y. Hong, and A. Warshel, J. Am. Chem. Soc. **125**, 5025 (2003).
[29] P. H. Dederichs, S. Blügel, R. Zeller R, and H. Akai, Phys. Rev. Lett. **53**, 2512 (1984).
[30] Q. Wu and T. van Voorhis, Phys. Rev. A **72**, 024502 (2005).
[31] Q. Wu and T. van Voorhis, J. Phys. Chem. A **110**, 9212 (2006).
[32] Q. Wu and T. van Voorhis, J. Chem. Phys. **125**, 164105 (2006).
[33] Q. Wu and T. van Voorhis, J. Chem. Theory Comput. **2**, 765 (2006).
[34] C. A. Mead, Rev. Mod. Phys. **64**, 51 (1992).
[35] R. S. Mulliken, J. Am. Chem. Soc. **64**, 811 (1952).
[36] N. S. Hush, Progr. Inorg. Chem. **8**, 391 (1967).
[37] H.-J. Werner and W. Meyer, J. Chem. Phys. **74**, 5802 (1981).
[38] R. J. Cave and M. D. Newton, J. Chem. Phys. **106**, 9213 (1997).
[39] G. Hirsch, R. J. Buenker, and C. Petrongolo, Mol. Phys. **70**, 825 (1990).
[40] G. Hirsch, R. J. Buenker, and C. Petrongolo, Mol. Phys. **70**, 835 (1990).
[41] M. Peric, R. J. Buencker, and S. D. Peyerimhoff, Mol. Phys. **71**, 673 (1990).
[42] J. E. Subotnik, S. Yeganeh, R. J. Cave, and M. A. Ratner, J. Chem. Phys. **129**, 244101 (2008).
[43] E. Alguire and J. E. Subotnik, J. Chem. Phys. **135**, 044114 (2011).
[44] D. R. Yarkony, J. Phys. Chem. A **102**, 8073 (1998).
[45] J. Hendekovic, Chem. Phys. Lett. **90**, 193 (1982).
[46] J. Hendekovic, Croat. Chem. Acta **56**, 375 (1983).
[47] J. Kucar, M. Pavlovic, and J. Hendekovic, Int. J. Quantum Chem. **32**, 699 (1987).
[48] F. Spiegelmann and J. P. Malrieu, J. Phys. B: At. Mol. Phys. **17**, 1259 (1984).
[49] R. Cimiraglia, J. P. Malrieu, M. Persico, and F. Spiegelmann, J. Phys. B **18**, 3073 (1985).
[50] L. S. Cederbaum, H. Köppel and W. Domcke, Int. J. Quantum Chem. Symp. **15**, 251 (1981).
[51] T. Pacher, L. S. Cederbaum, and H. Köppel, J. Chem. Phys. **89**, 7367 (1988).
[52] T. Pacher, H. Köppel, and L. S. Cederbaum, J. Chem. Phys. **95**, 6668 (1991).
[53] T. Pacher, L. S. Cederbaum, and H. Köppel, Adv. Chem. Phys. **84**, 293 (1993).
[54] T. Pacher, H. Köppel, and L. S. Cederbaum, J. Chem. Phys. **95**, 6668 (1991).
[55] T. Pacher, L. S. Cederbaum, and H. Köppel, Adv. Chem. Phys. **84**, 293 (1993).
[56] B. O. Roos, P. R. Taylor, and P. E. M. Siegbahn, Chem. Phys. **48**, 157 (1980).
[57] K. Ruedenberg, M. W. Schmidt, G. M. Gilbert, and S. T. Elbert, Chem. Phys. **71**, 41 (1982).

[58] W. Domcke and C. Woywood, Chem. Phys. Lett. **216**, 362 (1993).
[59] W. Domcke, C. Woywood, and M. Stengle, Chem. Phys. Lett. **226**, 257 (1994).
[60] D. Simah, B. Hartke, and H.-J. Werner, J. Chem. Phys. **111**, 4523 (1999).
[61] V. M. García, M. Reguero, R. Caballol, and J. P. Malrieu, Chem. Phys. Lett. **281**, 161 (1997).
[62] G. J. Atchity and K. Ruedenberg, J. Chem. Phys. **99**, 3790 (1993)
[63] K. Ruedenberg and G. J. Atchity, J. Chem. Phys. **99**, 3799 (1993).
[64] G. J. Atchity and K. Ruedenberg, Theor. Chem. Acc. **97**, 47 (1997)
[65] H. Nakamura and D. G. Truhlar, J. Chem. Phys. **115**, 10353 (2001).
[66] H. Nakamura and D. G. Truhlar, J. Chem. Phys. **117**, 5576 (2002).
[67] H. Nakamura and D. G. Truhlar, J. Chem. Phys. **118**, 6816 (2003).
[68] S. Nangia and D. G. Truhlar, J. Chem. Phys. **124**, 124309 (2006).
[69] Z. H. Li, R. Valero, and D. G. Truhlar, Theor. Chem. Acc. **118**, 9 (2007).
[70] D. Bonhommeau and D. G. Truhlar, J. Chem. Phys. **129**, 14302 (2008).
[71] D. Bonhommeau, R. Valero, and D. G. Truhlar, A. Jasper, J. Chem. Phys. **130**, 234303 (2009).
[72] R. Valero and D. G. Truhlar, J. Chem. Phys. **125**, 194305 (2006).
[73] R. Valero, D. G. Truhlar, and A. W. Jasper, J. Phys. Chem. A **112**, 5756 (2008).
[74] R. Valero and D. G. Truhlar, J. Chem. Phys.**137**, 22A539 (2012).
[75] H. Nakano, Chem. Phys. Lett. **207**, 372 (1993).
[76] H. Nakano, J. Chem. Phys. 1993, **99**, 7983 (1993).
[77] X. Xu, K. R. Yang and D. G. Truhlar, J. Chem. Theory Comput., **9**, 3612 (2013).
[78] A. L. Sobolewski and W. Domcke, J. Phys. Chem. A **105**, 9275 (2001).
[79] A. L. Sobolewski, W. Domcke, C. Dedonder-Lardeux and C. Jouvet, Phys. Chem. Chem. Phys. **4**, 1093 (2002).
[80] Z. Lan, W. Domcke, V. Vallet, A. L. Sobolewski and S. Mahapatra, J. Chem. Phys. **122**, 224315 (2005).
[81] M. N. R. Ashfold, B. Cronin, A. L. Devine, R. N. Dixon and M. G. D. Nix, Science **312**, 1637 (2006).
[82] C.-M. Tseng, Y. T. Lee, M.-F. Lin, C.-K. Ni, S.-Y. Liu, Y.-P. Lee, Z. F. Xu and M. C. Lin, J. Phys. Chem. A **111**, 9463 (2007).
[83] A. L. Devine, M. G. D. Nix, B. Cronin and M. N. R. Ashfold, Phys. Chem. Chem. Phys. **9**, 3749 (2007).
[84] G. A. King, A. L. Devine, M. G. D. Nix, D. E. Kelly and M. N. R. Ashfold, Phys. Chem. Chem. Phys. **10**, 6417 (2008).
[85] M. N. R. Ashfold, A. L. Devine, R. N. Dixon, G. A. King, M. G. D. Nix and T. A. A. Oliver, Proc. Natl. Acad. Sci. U. S. A. **105**, 12701 (2008).

[86] M. G. D. Nix, A. L. Devine, R. N. Dixon and M. N. R. Ashfold, Chem. Phys. Lett. **463**, 305 (2008).
[87] O. P. J. Vieuxmaire, Z. Lan, A. L. Sobolewski and W. Domcke, J. Chem. Phys. **129**, 224307 (2008).
[88] G. A. King, T. A. A. Oliver, M. G. D. Nix and M. N. R. Ashfold, J. Phys. Chem. A **113**, 7984 (2009).
[89] A. Iqbal, M. S. Y. Cheung, M. G. D. Nix and V. G. Stavros, J. Phys. Chem. A **113**, 8157 (2009).
[90] M. N. R. Ashfold, G. A. King, D. Murdock, M. G. D. Nix, T. A. A. Oliver and A. G. Sage, Phys. Chem. Chem. Phys. **12**, 1218 (2010).
[91] A. Pino, A. N. Oldani, E. Marceca, M. Fujii, S.-I. Ishiuchi, M. Miyazaki, M. Broquier, C. Dedonder and C. Jouvet, J. Chem. Phys. **133**, 124313 (2010).
[92] H. An and K. K. Baeck, J. Phys. Chem. A **115**, 13309 (2011).
[93] R. N. Dixon, T. A. A. Oliver and M. N. R. Ashfold, J. Chem. Phys. **134**, 194303 (2011).
[94] Y. Zhang, T. A. A. Oliver, M. N. R. Ashfold and S. E. Bradforth, Faraday Discuss. **157**, 141 (2012).
[95] S. G. Ramesh and W. Domcke, Faraday Discuss. **163**, 73 (2013).
[96] X. Zhu and D. R. Yarkony, J. Chem. Phys. **140**, 024112 (2014).
[97] M. C. Capello, M. Broquier, S.-I. Ishiuchi, W. Y. Sohn, M. Fujii, C. Dedonder-Lardeux, C. Jouvet and G. A. Pino, J. Phys. Chem. A **118**, 2056 (2014).
[98] T. N. V. Karsili, A. M. Wenge, B. Marchetti and M. N. R. Ashfold, Phys. Chem. Chem. Phys. **16**, 588 (2014).
[99] C. J. Cramer, Essentials of Computational Chemistry: Theories and Models, 2nd ed., (Wiley & Sons, Chichester, 2004) p. 17-68.
[100] I. Cacelli and G. Prampolini, J. Chem. Theory. Comput. **3**, 1803 (2007).
[101] V. Barone, I. Cacelli, N. De Mitri, D. Licari, S. Monti, and G. Prampolini, Phys. Chem. Chem. Phys. **15**, 3736 (2013).
[102] B. J. Braams and J. M. Bowman, Int. Rev. Phys. Chem. **28**, 577 (2009).
[103] J. M. Bowman, B. J. Braams, S. Carter, C. Chen, G. Czakó, B. Fu, X. Huang, E. Kamarchik, A. R. Sharma, B. C. Shepler, Y. Wang, Z. Xie, J. Phys. Chem. Lett. **1**, 1866 (2010).
[104] R. Dawes, D. L. Thompson, Y. Guo, A. F. Wagner, and M. Minkoff, J. Chem. Phys. **126**, 184108 (2007).
[105] Y. Guo, I. Tokmakov, D. L. Thompson, A. F. Wagner, and M. Minkoff, J. Chem. Phys. **127**, 214106 (2007).
[106] J. D. Bender, S. Doraiswamy, D. G. Truhlar, and G. V. Candler, J. Chem. Phys., **140**, 054302 (2014).

[107] D. W. Brenner, O. A. Shenderova, J. A. Harrison, S. J. Stuart, B. Ni, and S. B. Sinnott, J. Phys. Condens. Matter **14**, 783 (2002).
[108] D. W. Brenner, O. A. Shenderova, J. D. Schall, D. A. Areshkin, S. Adiga, J. A. Harrsion, and S. J. Stuart, in *Handbook of Nanoscience, Engineering, and Technology*, edited by W. A. Goddard III, D. W. Brenner, S. E. Lyshevski, and G. J. Iafrate (CRC Press, Boca Raton, 2003) chapter 24.
[109] A. C. T. van Duin, S. Dasgupta, F. Lorant, and W. A. Goddard III, J. Phys. Chem. A **105**, 9396 (2001).
[110] A. Kulkarni, D. G. Truhlar, S. G. Srinivasan, A. C. T. van Duin, P. Norman, and T. E. Schwartzentruber, J. Phys. Chem. C **117**, 258 (2013).
[111] M. Zhao, M. A. Iron, P. Staszewski, N. E. Schultz, R. Valero, and D. G. Truhlar, J. Chem. Theory Comput. **5**, 594 (2009).
[112] J. Gao, Rev. Comp. Chem. **7**, 119 (1996).
[113] G. Monard and K. M. Merz Jr., Acc. Chem. Res. **32**, 904 (1999).
[114] J. Gao and D. G. Truhlar, Annu. Rev. Phys. Chem. **53**, 467 (2002).
[115] R. A. Friesner and V. Guallar, Annu. Rev. Phys. Chem. **56**, 389 (2005).
[116] H. Lin, and D. G. Truhlar, Theor. Chem. Acc. **117**, 185 (2007).
[117] H. Hu and W. Yang, Annu. Rev. Phys. Chem. **59**, 573 (2008).
[118] H. M. Senn and W. Thiel, Angew. Chem. Int. Ed. **48**, 1198 (2009).
[119] A. Chakraborty, Y. Zhao, H. Lin, and D. G. Truhlar, J. Chem. Phys. **124**, 044315 (2006).

Chapter 2. Global Ab Initio Ground-State Potential Energy Surface of N_4

Adapted with permission from Yuliya Paukku, Ke R. Yang, Zoltan Varga, and Donald G. Truhlar, J. Chem. Phys. **139**, 044309 (2013).

2.1 Introduction

Energy transfer and dissociation in collisions of nitrogen molecules are important for many atmospheric processes. The present motivation for studying such collisions is the role they play within the shocked gases surrounding hypersonic vehicles in establishing non-Boltzmann internal energy distributions that must be understood to model convective heat flow to the vehicles.[1] The shocked gases surrounding hypersonic vehicles are very hot and can have temperature up to 20,000 K. The high-energy collisions of the hot N_2 (molecules with high vibrational–rotational quantum numbers v, j) can involve vibrational-rotational excitation and relaxation,

$$N_2(v_1, j_1) + N_2(v_2, j_2) \rightarrow N_2(v'_1, j'_1) + N_2(v'_2, j'_2)$$

and collision-induced dissociation,

$$N_2(v_1, j_1) + N_2(v_2, j_2) \rightarrow N_2(v'_1, j'_1) + N + N$$

The first step in molecular dynamics studies of such collisions is to obtain a potential energy surface valid up to high energy and large vibrational extensions. Ultimately one must consider coupled potential energy surfaces and electronic as well as vibrational–rotational inelasticity. However, the goal of the research reported here is to obtain a reasonably accurate global potential energy surface (PES) for the ground electronic state.

A potential energy surface for N_4 includes an N_3 surface as a subset. There have been a number of studies for the structures and energetics of N_3 species.[2-4] The dissociation of N_3 has been studied previously[5-7] and several PESs of N_3 have been reported in literature. A London-Eyring-Polanyi-Sato (LEPS) PES for the quartet state of N_3 was developed by Laganà et al.[8] for the classical trajectory study of N (^4S) + N_2 ($^1\Sigma_g^+$) collisions. The LEPS PES yields a collinear transition structure, which does not agree with the bent transition structure suggested by theoretical studies with multi-reference configuration interaction.[2] In order to improve the LEPS PES for the transition structure, the same group developed a series of new PESs[9,10] (denoted as L0 to L4), with the latest L4 PES[10] being fitted to 56 CCSD(T)/aug-cc-pVTZ energies. In 2003, Wang et al.[11] proposed the first full-dimensional ab initio based PES for N_3 $^4A''$ state for the quantum dynamics study of N (^4S) + N_2 ($^1\Sigma_g^+$) collisions. An analytic PES with 68 parameters was fitted by using 3326 points calculated by open-shell CCSD(T) with cc-pVQZ basis set. A very accurate global PES for the ground $^4A''$ state of N_3 was reported in 2007 by Galvão and Varandas[12] based on the double many-body expansion; 1592 points were calculated with CCSD(T) and MRCI+Q and extrapolated to complete basis set (CBS) limit.

Since the ground state of N_3 radical is a doublet,[7] the PESs of doublet N_3 have also attracted much attention. In 2004, an adiabatic PES for the lowest $^2A''$ state of N_3 was constructed by Babikov et al.[13] using tensor product B-cubic spline representation

based on 2286 points calculated by MRCI+Q with aug-cc-pVTZ basis set. Adiabatic PESs for five low-lying doublet states (three $^2A'$ states and two $^2A''$ states) of N_3 have been fitted by Zhang et al.[14] based on 1504 points calculated by MRCI+Q with the aug-cc-pVTZ basis sets. The most recent adiabatic PESs for the two lowest $^2A''$ states of N_3 have also been developed by Galvão and Varandas[15] in 2011 with the double many-body expansion fitting strategy and used for a quasi-classical trajectory study of the N (^2D) + N_2 ($^1\Sigma_g^+$) reaction.

Several studies have been reported for the tetrahedral form of N_4,[16-18] which is considered to be a high energy density material. Theoretical geometries, energies, and physical properties have been reported.

Ab initio studies of van der Waals N_2–N_2 have also been reported. Couronne and Yellinger[19] have reported a study of the structure and stability of the $(N_2)_2$ complex at canted (taken from the crystal structure), T-shaped, X-shaped, parallel, and linear structures. The geometry of each dimer conformation was defined by four parameters, the distance between the centers of mass, two angles, and one dihedral angle, and symmetry-constrained optimization of each conformer was carried out, where only the distance between centers of mass was optimized. T-shaped and canted conformers were found to be the most stable ones. The equilibrium structure, potential energy surface, and van der Waals mode vibration of several $(N_2)_2$ configurations have been studied with coupled

cluster with singles, doubles, and perturbative triples (CCSD(T)) method and quadruple zeta basis set cc-pVQZ by Wada et al.[20]

Unlike N_3, for which there has been considerable work on the full-dimensional ab initio PESs for both doublet and quartet states, very few studies have been carried out for the full-dimensional PESs of N_4. There are, however, many studies on the reduced four-dimensional PESs of N_4 for N_2–N_2 intermolecular interactions with rigid N_2 molecules in literature. [21-31] One of the first ab initio PES of N_2–N_2 was developed by Böhm and Ahlrichs.[21] They fitted a 4-D PES with a site–site ansatz (three sites per molecule) for rigid N_2 to 46 dimer interaction energies that were calculated by the coupled-pair functional (CPF) modification of CISD method with a [6s4p2d] basis set. Van der Avoird et al.[22] proposed a 4-D PES in terms of spherical harmonic expansions to fit 225 ab initio data points. Two empirical parameters were introduced to reproduce the experimental second virial coefficients. By changing five parameters to fit several experimental properties, such as second virial coefficients, scattering crossing sections, etc., the PES was further improved by Cappelletti et al.[24]

Stallcop and Partridge[23] calculated N_2–N_2 interaction energies using CCSD(T) calculations with extensive basis set, the size of at least [6s5p4d]. An analytical PES was constructed with spherical harmonic expansions to fit the ab initio data. Some parameters of the PES were adjusted to experimental data to yield reliable second virial coefficient. Leonhard and Deiters[25] performed CCSD(T) calculations with aug-cc-pVnZ (n = D and T) basis sets and extrapolated the results to CBS limit. They applied a site-site potential

function with five sites per molecule to fit the CCSD(T)/CBS energies; two scaling parameters were introduced to reproduce the experimental second-order virial coefficients.

Aquilanti et al.[26] reported an experimental PES and calculated rovibrational levels of the N_2–N_2 dimer, obtained from multiproperty analysis of scattering data and second virial coefficients. In 2008, Cappelletti et al.[30] developed a PES using bond-bond pairwise additive representation by combining the symmetry adapted perturbation theory (SAPT) results and experimental properties. Karimi-Jafari et al.[27] performed MP2 calculations with basis set up to cc-pVQZ and extrapolated the MP2 results to CBS limit. An analytical PES based on spherical harmonic expansions was then fitted to MP2/CBS results.

Strąk and Krukowski[28] calculated 315 geometries using CCSD(T) with the aug-cc-pVQZ basis set. The CCSD(T) results were used to parameterize an analytic PES with spherical harmonic expansions. Gomez et al.[29] applied the SAPT method with a [5s3p2d1f] basis set to calculate the interaction energies of nearly 460 points on the N_2–N_2 ground state. An analytical PES with spherical harmonic expansions was parameterized to those ab initio data.

The most recent and accurate PES of N_2–N_2 was developed by Hellman in 2012.[31] Hellman performed CCSD(T) calculations with basis sets up to aug-cc-pV5Z supplemented with bond functions; the results were further extrapolated to CBS limit. The corrections for core-core and core-valence correlations, relativistic effects, and

higher order excitations up to CCSDT(Q) were also considered. A 4-D PES was parameterized from 408 high-level ab initio points. Several N_2–N_2 PESs were tested for the *R*-dependence of anisotropy against CCSD(T) with aug-cc-pVTZ and bond functions.[32] It was shown that the potentials with simplified functional forms and parameters based on or extracted from experimental data do not reproduce the correct anisotropy of the PES and ab initio based PES should be the proper way to go.

All the PESs discussed above are reduced 4-D PESs with rigid N_2 molecules. We cannot use them to study high-energy collisions of N_2 with $N_2$where vibrational energy transfer or collision-induced dissociations are involved. The very old PES extracted from experimental data, which was developed by Johnson et al.[33] is one of the very few PESs of N_4 that allows us to study high-energy N_2–N_2 collisions. Morse potentials were used to model the N_2 bond stretches while exponential-six atom–atom potentials were used to model the nonbonding interactions. To the best of our knowledge, no ab-initio-based full-dimensional PES has been reported for N_4. A distinguishing feature of the present study is the attempt to develop a full-dimensional PES valid up to high energy and large vibrational extensions of each N_2 subsystem.

Most of the PESs mentioned above were constructed with spherical harmonics, which can describe the isotropic and anisotropic intermolecular interactions of N_2 very well. Spherical harmonic expansions are a natural choice to represent reduced PESs describing the inter-molecular interactions when the N_2 molecules are well separated and each close to its equilibrium internuclear separation. But this is not the case for global

PESs where the dissociation of N_2 molecules is allowed. The Sorbie-Murrell[34] and Aguado-Paniagua[35] functional forms are widely used in the PESs fitting of triatomic systems. Both of them involve many-body expansions that can treat the short-range and long-range interactions properly and can be constructed to have the proper asymptotic behaviors. Sorbie-Murrell and Aguado-Paniagua many-body expansions have also been used to construct the PES of tetraatomic or pentaatomic systems, such as H_4,[36,37] H_5,[38] H_5^+,[39] but their applications are limited to monovalent atoms. For an adequate treatment of systems with complex spin-couplings of asymptotic fragments, as in current case of N_4, which could involve quartet N_3 + quartet N or doublet N_3 + doublet N, some geometry-dependent switching functions,34 that could be very system-dependent, would have to be used.

Our approach is to use ab initio electronic structure theory to calculate the PES at selected geometries and then to fit this data to a global analytic function. Because we want the PES to be valid even for dissociative collisions and even near state crossings, we use a multireference wave function method that treats both static and dynamic correlation, in particular complete active space second-order perturbation theory (CASPT2).[40,41] The fitting is accomplished using permutation-symmetry-invariant polynomials involving powers of functions of the internuclear distances. This method was pioneered by Brahms and Bowman,[42,43] who developed methods for generating the polynomials by monomial symmetrization. However, there are unphysical terms are in the permutation-invariant polynomials proposed by Brahms and Bowman, which lead to

spurious interactions in asymptotic ranges. A modified strategy was used in our construction of the ground state PES of N_4 by removing all unphysical terms in the Brahms-Bowman's permutationally invariant polynomials.

2.2. Methods

2.2.1. Electronic structure calculations

Multireference second order perturbation theory, in particular, CASPT2,[40,41] is used for the calculations in order to account for dynamical correlation. For the N_2 molecule, the ground state is $^1\Sigma_g^+$, and the excited electronic states are well separated in energy.[44,45] Therefore, single-state CASPT2 calculations are performed with the complete active space self-consistent field (CASSCF)[46] reference wave function optimized for the ground state.

In order to select a reasonable active space for the reference CASSCF wave function and to check the dissociation energies obtained with CASPT2, we performed test calculations for N_2 dissociation placing only 2p orbitals in the active space (active space of six electrons in six orbitals: 6e/6o) and placing both 2s and 2p orbitals in the active space (10e/8o). In the former case, the 2s orbitals were not correlated in either the SCF step or the PT2 step. The (6e/6o) CASPT2 calculation with only 2p orbitals active and correlated yielded a dissociation energy of 228.7 kcal/mol, whereas the CASPT2 dissociation energy with both 2s and 2p orbitals active and correlated is 220.3 kcal/mol. Both calculations lead to reasonably good agreement with experimental data for the

dissociation energy and equilibrium bond length of nitrogen molecule (228.4 kcal/mol and 1.098 A, respectively).[44,47] However, placing 2s orbitals in the active space results in high computational costs because it leads to too many configurations. Fortunately, excluding the 1s and 2s orbitals from both the active space and PT2 correlation calculation gives an almost perfect dissociation energy for N_2. Therefore, we chose a 12e/12o active space for the N_4 system and did not correlate either 1s or 2s electrons. For nonsymmetric geometries, this leads to 40,609,128 contracted configurations. Although the eight lowest-energy orbitals (1s and 2s) are doubly occupied in all configurations, they are fully optimized for each geometry. All electronic structure calculations are performed with the *Molpro* software package.[48,49]

The calculations are carried out at sequences of geometries in which one internal coordinate is scanned while the rest of the coordinates are fixed. The Hartree–Fock wave function is used as an initial guess for the CASSCF reference wave function at the first point of each scan; then, for each of the rest of the points of the scan, the CASSCF reference wave function of the previous point is used as the starting point for the next CASSCF calculation.

For some geometrical arrangements an excited state approaches closely to the ground state. Therefore, a level shift[50] of 0.3 hartree is applied in all CASPT2 calculations in order to eliminate intruder-state problems. The g4 version of the Fock-operator,[49] which is an extension of the g1, g2, and g3 zeroth-order Hamiltonians proposed by Andersson,[51] is selected. This modified Fock-operator makes CASPT2

calculations approximately size extensive in the case of the dissociation of a molecule to high-spin open-shell atoms, which is precisely what is needed here.

The minimally augmented correlation-consistent polarized valence triple zeta basis set, maug-cc-pVTZ[52] is used for all calculations.

For some geometries the 2p orbital from the active space switches place with one of the 2s inactive orbitals (not included in the active space), leading to an inconsistent solution to the CASSCF equations. For N_4 this problem mostly occurs at points with high symmetry and when four nitrogen atoms are close to each other, especially in the case of (N_3 + N)-like geometries. Distorting the geometry by a small amount or using a better initial guess of the wave function helps to avoid this problem.

Occupation restrictions (restriction cards[49]) for the inactive orbitals are used in CASSCF calculations to restrict the occupation patterns in order to avoid so-called primary space (P-space) problems and CASSCF convergence problems. These problems can occur because of the limited active space or if two electronic states in the same symmetry are almost degenerate, for example near avoided crossings. However in our case increasing the active space would make the cost prohibitive, and increasing the primary space threshold or changing configurations did not help to avoid the problem. However, restrictions solved the problem. For example, we restrict 2s inactive orbitals to have a maximum and minimum number of electrons equal to 2. Because restricted orbitals are not in the active space, this restriction does not change the result, but the restriction card changes the algorithm used by the software and eliminates the problem.

The energy of two N_2 molecules infinitely separated and each at its own equilibrium distance, is taken as the zero of energy for the PES. Relative energies with respect to the zero of energy were used for the fitting.

The initial data set consists of energies for a diverse set of geometries. Nine sets of geometries correspond to an N_2 approaching another N_2 geometries, and 3 sets of geometries correspond to a triatomic molecule interacting with an atom (N_3 + N) are used.

Figure 2.1 shows the coordinates used to define the geometries for the N_2 + N_2 sets. In each N_2 + N_2 set, one of the N_2 molecules has a fixed bond length r_A set successively equal to the equilibrium distance of 1.098 Å, to the equilibrium distance decreased by 0.2 Å, and to equilibrium distance increased by 0.2 Å; the other N_2 is dissociating with the bond length r_B varied from 0.8 to 6.0 Å; and the distance d between the centers of mass is varied from 1 to 10 Å to account for long range interaction at large distances. Thus each set corresponds to a set of points on a three-dimensional grid. The sets differ in the internal angles, e.g., collinear, T-shaped, etc. For example, the T-shaped model has two N_2 molecules perpendicular to each other and situated at a distance d between their centers of mass.

In the linear N_2 + N_2 set and in the N_3 + N sets, a different coordinate system was used; see Figure 2.2 where polar coordinates are used to define one of the N_3 + N sets. For the triatomic molecule interacting with an atom, $^2B_1$ and $^4B_1$ bent N_3 structures were

optimized with the CASPT2 (9e/9o)/maug-cc-pVTZ method. Then for each set of N_3 + N calculations, the bond lengths of N_3 were fixed to the optimized values, decreased by 0.2 Å and increased by 0.2 Å. The ground-state linear $^2\Pi_g$ N_3 geometry was taken from experimental results,[53] the N–N bond lengths were set to 1.181 Å, then decreased and increased by 0.2 Å.

The sets just described lead to 16746 points. We then eliminated all points with energies greater than 2000 kcal/mol, leaving 16380 points (15363 points from N_2 + N_2 scanning and 1017 points from N_3 + N scanning). Next we added a point corresponding to a geometry-optimized tetrahedral structure and points corresponding to optimizing cyclic and bent $^2B_1$ and $^4B_1$ structures with one N far from N_3. We also added five randomly generated points and one linear N_3 + N point. And two points with short N–N bond lengths (0.6 and 0.7 Å) and a large distance between centers of mass of nitrogen molecules have been added to the data set to yield a better description of the short-bond-length repulsive region.

We added 30 points along linear synchronous transit[54] (LST) paths connecting points from two different of the 12 arrangements shown in Figure 2.3. For each LST path, the points on the path are generated by

$$q_i = q_i^{(0)} + \lambda\left(q_i^{(1)} - q_i^{(0)}\right)$$

where q_i is an internal coordinate, $q_i^{(0)}$ is a point from one of the systematic sets, $q_i^{(1)}$ is a point from another set, and the LST points are generated by setting the parameter λ to,

for example, -0.2, +0.2, +0.4, etc. Path 1 is from H-shape N_4 to X-shape N_4; path 2 is from linear N_3 + N to N_2 + N_2; path 3 is from T-shape N_4 to X-shape N_4 with one N_2 dissociated; and path 4 is from N + N_3 to H-shape N_4.

Finally, 14 data points with large separation between N_2 and N_2 were added to yield better asymptotic behavior. Putting all these points together yields a total of 16435 points to be used for fitting.[55]

2.2.2. Fitting the potential energy surface

We defined six internuclear distances as follows: $r_1 = r_{12}$, $r_2 = r_{13}$, $r_3 = r_{14}$, $r_4 = r_{23}$, $r_5 = r_{24}$, and $r_6 = r_{34}$, where r_{ij} is the distance between atoms i and j. The variables

$$X_i = \exp(-(r_i - r_e)/a_i),$$

were used to describe the N_4 potential energy surface, where r_e is the equilibrium bond length of 1.098 Å for N_2, and r_i and a_i (i = 1,…, 6) are internuclear distances and non-linear parameters, respectively. Since X_i may be interpreted as a Pauling bond order,[56-60] the X_i are called bond orders. Since a quadratic polynomial in X_i is equivalent to a Morse curve,[61] they may also be called Morse variables.

We chose 0.9 Å for all a_i based on some trial tests. The starting point for an analytic PES is an expansion in a Taylor series of bond orders as

$$V(r_1, r_2, r_3, r_4, r_5, r_6) = \sum_{n_1+n_2+n_3+n_4+n_5+n_6=0}^{k} C_{n_1 n_2 n_3 n_4 n_5 n_6} X_1^{n_1} X_2^{n_2} X_3^{n_3} X_4^{n_4} X_5^{n_5} X_6^{n_6} \qquad (2.1)$$

where n_i is the order of polynomial of X_i, and the coefficients $C_{n_1 n_2 n_3 n_4 n_5 n_6}$ are the linear parameters that need to be determined through least-squares fits. The summation in eq. 2.1 is over all n_1, n_2, n_3, n_4, n_5, and n_6, each starting from 0, such that their sum is less than or equal to *k;* therefore *k* is the highest total degree of the multinomials. Some terms in eq. 2.1, such as $X_1^{n_1} X_6^{n_6}$, are products of functions of unconnected distances, e.g., a function of the 1–2 distance ($r_1 = r_{12}$) times a function of the 3–4 distance ($r_6 = r_{34}$). Those terms, which we call unconnected terms, introduce spurious interactions between two N_2 fragments since they survive even when two N_2 fragments are far from each other. We therefore remove all unconnected terms in eq. 2.1. Also, terms like $X_i^{n_i}$ that only describe pairwise 2-body interactions are replaced with the pre-optimized N_2 potential energy function $V_2(r)$ for better asymptotic behavior. This yields

$$V(r_1, r_2, r_3, r_4, r_5, r_6) = V_0 + \sum_{i=1}^{6} V_2(r_i) + \sum_{\substack{k \\ \text{connected,} \\ n_1+n_2+n_3+n_4+n_5+n_6=2}}' B_{n_1 n_2 n_3 n_4 n_5 n_6} X_1^{n1} X_2^{n_2} X_3^{n_3} X_4^{n_4} X_5^{n_5} X_6^{n_6} \tag{2.2}$$

where V_0 is the relative energy of four separated N atoms ($2D_e$). The reminder "connected" under the sum in eq. 2.2 denotes that unconnected terms are removed from the sum. The prime on the sum in eq. 2.2 denotes that V_0 and two-body terms are also removed from the sum. Due to the permutation symmetry of the four identical N atoms, some of the coefficients are identical by symmetry. One can therefore construct an

explicitly permutationally invariant basis to reduce the number of linear coefficients.[42,43] In the present paper, we follow the monomial symmetrization approach proposed by Xie and Bowman[62] to construct permutationally invariant polynomial basis functions to fit the global potential energy surface of N_4:

$$V(r_1,r_2,r_3,r_4,r_5,r_6) = V_0 + \sum_{i=1}^{6} V_2(r_i) + \sum_{\substack{k \\ \text{connected}, \\ n_1+n_2+n_3+n_4+n_5+n_6=2}}{}' D_{n_1 n_2 n_3 n_4 n_5 n_6} S[X_1^{n1} X_2^{n_2} X_3^{n_3} X_4^{n_4} X_5^{n_5} X_6^{n_6}] \quad (2.3)$$

where $S[X_1^{n_1} X_2^{n_2} X_3^{n_3} X_4^{n_4} X_5^{n_5} X_6^{n_6}]$ are the symmetrized polynomials with correct permutation invariance.

We truncated the Taylor expansion at $k = 9$. This includes 5005 terms if one uses eq. 2.1; however, by removing 2-body and unconnected terms and using symmetrized polynomials $S[X_1^{n_1} X_2^{n_2} X_3^{n_3} X_4^{n_4} X_5^{n_5} X_6^{n_6}]$ as the $k = 9$ basis, the number of independent terms is reduced to 276. The 276 $D_{n_1 n_2 n_3 n_4 n_5 n_6}$ coefficients are determined by least-square fits.

The potential energy function of N_2 was fitted with a generalized Morse potential

$$V_2(r) = D_e[1 - e^{-f(r)(r-r_e)}]^2 - D_e \quad (2.4)$$

where D_e = 228.7 kcal/mol is the equilibrium bond dissociation energy calculated by CASPT2/maug-cc-pVTZ with the CASSCF(6e, 6o) reference wave function. In a standard Morse potential, one has

$$f(r) = \alpha \quad (2.5)$$

where α is a constant. In order to obtain a more accurate fit, we made $f(r)$ depend on r; in particular, we defined intermediate variable $y = \frac{r^4 - r_e^4}{r^4 + r_e^4}$ and expanded $f(r)$ in a Taylor series of y:

$$f(r) = \sum_{i=0}^{6} a_i y^i \tag{2.6}$$

with the optimized coefficients a_0 = 2.70963254293 Å^{-1}, a_1 = 0.132620177271 Å^{-1}, a_2 = 0.296757048793 Å^{-1}, a_3 = 0.197112432229 Å^{-1}, a_4 = -0.502002309588 Å^{-1}, a_5 = 0.380734244606 Å^{-1}, a_6 = 0.121001628750 Å^{-1}.

Since we are interested in high-energy collisions, we need to fit our potential energy surface over a very wide energy range. To avoid putting too much emphasis on the high-energy data points and reducing the fitting quality of data points with relative low energies, we reduced the weight on high-energy points, as has been done before.[63] However in the present work we used a newly devised weighting function; in particular we use the following weighting factor in our weighted-least-square fitting:

$$w(i) = \begin{cases} 1 & \text{for } E_i \le E_c \\ E_c^2 / E_i^2 & \text{for } E_i > E_c \end{cases} \tag{2.6}$$

where $w(i)$ is the weighting factor of data point i with energy E_i, and E_c is a preselected energy threshold to reduce the weights of high-energy data points. In the final fit, we chose E_c to be 100 kcal/mol. Furthermore, we excluded the data points with energies larger than 2000 kcal/mol in our fitting. We think that energies above 2000 kcal/mol would be rarely visited during dynamic studies, and the accuracy in those ranges is not very important.

2.3. Results

Figures 2.4 through 2.7 show comparisons of the global fit to the calculated points on the dissociation curves for N–N interacting with N_2, where the calculations are performed with the CASPT2 method for various dimer arrangements. Results are given as a function of the internuclear distance in one molecule (r_B) with the other molecule (r_A) at its equilibrium distance. Although we do not show plots to illustrate this, the fits also include data like this with the second molecule stretched by 0.2 Å from its equilibrium geometry and with it compressed by 0.2 Å from its equilibrium geometry. Seven more plots similar to Figures 2.4–2.7 but for other geometries are given in supplementary material. A surface cut as a function of two variables is shown in Figure 2.8 for the bent T-shaped dimer. The surface cut is not from the global fit, but rather is based on local interpolation to guide the eye in visualizing the data.

The root-mean-square errors (RMSEs) and mean unsigned errors (MUEs) of the final fit are shown for different energy ranges in Table 2.1.

The results in Table 2.1 are for the final fit to all the data. To further test the quality of our fitted PES, we omitted the data corresponding to the four LST paths to see how our fitting procedure would perform for data quite different from that used in the fit. The energies predicted by this test fit, as well as the CASPT2 energies being predicted, are shown in Figure 2.9.

2.4. Discussion

As a subset of the N_4 surface, the surface of N_3 interacting with an atom has been calculated. Therefore, stationary points of N_3 were used. The geometries of low-lying cyclic $^2B_1$ and bent $^4B_1$ stationary structures were taken from a recent work[7] and optimized with CASPT2. Our optimized nonlinear stationary structures of N_3 agree well with previous theoretical results. For $^2B_1$ calculated bond lengths are 1.45 Å and N–N–N angle is 50.2 degrees. For $^4B_1$ the bond lengths are 1.27 Å and N–N–N angle is 117.4 degrees.

For comparison with previous studies of tetrahedral N_4, we performed an optimization of tetrahedral structure of singlet N_4 with CASPT2(12e/12o)/maug-cc-pVTZ level. The bond lengths and absolute energy obtained with the method we used are consistent with previous computational work:18 the N–N bond length is 1.450 Å, the energy, relative to two nitrogen molecules is 191.7 kcal/mol. At this geometry the fit gives an energy of 173.4 kcal/mol, with an error of 18.3 kcal/mol. Although not very good, the fit is still acceptable. Actually, the large discrepancy of relative energies of the tetrahedral N_4 calculated by CASPT2 and our analytic PES is an example of a more general phenomenon, namely that the fit is less accurate near surface crossings where the fitted PES smoothes out the cusp due to state crossing, as shown clearly in Figure 2.7 for d = 1.0 and 1.4 Å respectively, where d is the distance between the centers of mass of the two N_2 molecules. Our goal here is to fit the lowest adiabatic potential energy surface,

even though that surface has cuspidal ridges due to surface crossings, and the functional form chosen here, with continuous derivatives, must smooth those crossings out. This could be considered a disadvantage or an advantage, with the latter point of view reflecting the fact that Born-Oppenheimer trajectories will be smoother (and hence probably more realistic) if one smoothes the cuspidal ridges. The only truly satisfactory way to fit potential energy surfaces in the presence of surface crossings is to use a diabatic representation and fit more than one surface and their couplings,[64,65] but that is beyond the present scope.

Table 2.1 shows that the average quality of the fitted PES is quite good since the RMSE for $E < 100$ kcal/mol is only 1.7 kcal/mol, and the RMSE for 100 kcal/mol $\leq E <$ 228 kcal/mol is 4.1 kcal/mol. The RMSE is a good criterion for evaluating the fitting accuracy if the errors are normally distributed. However, it could be exaggerated by larger errors, and the MUEs are more robust. That is why Table 2.1 also provides the MUEs for the various energy ranges. The MUEs are quite small, 1.2 kcal/mol for $E < 100$ kcal/mol and 2.3 kcal/mol for 100 kcal/mol $\leq E <$ 228 kcal/mol. Both RMSEs and MUEs show that our fitted PES is quite good (better than the expected accuracy of CASPT2) for energies below the dissociation limit of 228 kcal/mol. For 228 kcal/mol $\leq E <$ 456 kcal/mol, our fitting is still quite good, with RMSE and MUE of 5.8 and 3.1 kcal/mol, respectively. So our PES should be suitable to study high-energy collisions of N_2 with N_2.

The quality of the fitting procedure was further tested by leaving the 30 LST points out of the fitting process, producing a less accurate global surface called the test PES. The test surface reproduces the general trends of the CASPT2 curves for the LST paths. The agreement of energies predicted by test PES and those calculated by CASPT2 is best for energies lower than the dissociation limit (228 kcal/mol), as also implied by RMSEs and MUEs of the final fit. Path 1 calculated by CASPT2 has an energy maximum at $\lambda = 0.8$. The energy maximum has been shifted to $\lambda = 0.6$ with the test PES. But the qualitative shape of path 1 predicted by our test PES agrees with that calculated by CASPT2. Path 2 predicted by our test PES agrees extremely well with the CASPT2 one, especially for the data points with energies below 300 kcal/mol. The test PES reproduces path 3 near the starting T-shaped N_4, but it fails to reproduce the cusp due to a state crossing near $\lambda = 0.6$. Instead, it yields a smooth curve near the cusp. That problem, discussed above for the final fit, is inevitable when one fits adiabatic surfaces to continuous functions, as has been observed before.[66] For path 4, the test fit reproduces the CASPT2 curves very well for energy below 300 kcal/mol, but the agreement degrades for higher energies.

2.5. Summary

A global ground-state potential energy surface for N_4 suitable for treating high-energy vibrational-rotational energy transfer and dissociation in N_2–N_2 collisions has been developed. About 17,000 ab initio data points have been calculated for the N_4 system, distributed along nine series of $N_2 + N_2$ geometries and three series of $N_3 + N$

geometries using CASPT2 with an active space of 12 electrons in 12 orbitals and the maug-cc-pVTZ triple zeta basis set. The six-dimensional ground-state potential energy surface was fitted using least-squares fits to electronic energies based on permutationally invariant polynomials in bond order variables.

2.6 References

[1] I. Nompelis, G. V. Candler, and M. S. Holden, AIAA J. **41**, 2162 (2003).
[2] C. Petrongolo, J. Mol. Struct. **175,** 215 (1988).
[3] J. N. Murrell, O. Novaro, and S. Castillo, Chem. Phys. Lett. **90**, 421 (1982).
[4] I. S. K. Kerkines, Z. Wang, P. Zhang, and K. Morokuma, Mol. Phys. **107**, 1017 (2009).
[5] J. M. L. Martin, J. P. François, and R. Gijbels, J. Chem. Phys. **93**, 4485 (1990).
[6] R. E. Continetti, D. R. Cyr, D. L. Osborn, D. J. Leahy, and D. M. Neumark, J. Chem. Phys. **99**, 2616 (1993).
[7] P. Zhang, K. Morokuma, and A. M. Wodtke, J. Chem. Phys. **122**, 014106 (2005).
[8] A. Laganà, E. Garcià, and L. Ciccarelli, J. Phys. Chem. **91**, 312 (1987).
[9] E. Garcià and A. Laganà, J. Phys. Chem. A **101**, 4734 (1997).
[10] E. Garcià, A. Saracibar, S. Gómez-Carrasco, and A. Laganà, Phys. Chem. Chem. Phys. **10**, 2552 (2008).
[11] D. Wang, J. R. Stallcop, W. M. Huo, C. E. Dateo, D. W. Schwenke, and H. Partridge, J. Chem. Phys. **118**, 2186 (2003).
[12] B. R. L. Galvão and A. J. C. Varandas, J. Phys. Chem. A **113**, 14424 (2009).
[13] D. Babikov, P. Zhang, and K. Morokuma, J. Chem. Phys. **121**, 6743 (2004).
[14] Z. Wang, I. S. K. Kerkines, K. Morokuma, and P. Zhang, J. Chem. Phys. **130**, 044313 (2009).
[15] B. R. L. Galvão and A. J. C. Varandas, J. Phys. Chem. A **115**, 12390 (2011).
[16] M. M. Francl and J. P. Chesick, J. Phys. Chem. **94**, 526 (1990).
[17] T. J. Lee and J. E. Rice, J. Chem. Phys. **94**, 1215 (1991).
[18] M. L. Leininger, T. J. Van Huis, and H. F. Schaefer III, J. Phys. Chem. A **101**, 4460 (1997).
[19] O. Couronne and Y. Ellinger, Chem. Phys. Lett. **306**, 71 (1999).
[20] A. Wada, H. Kanamori, and S. Iwata, J. Chem. Phys. **109**, 9434 (1998).
[21] H.-J. Böhm and R. Ahlrichs, Mol. Phys. **55**, 1159 (1985).
[22] A. van der Avoird, P. E. S. Wormer, and A. P. J. Jansen, J. Chem. Phys. **84**, 1629 (1985).

[23] J. R. Stallcop and H. Partridge, Chem. Phys. Lett. **281**, 212 (1997).
[24] D. Cappelletti, F. Vecchiocattivi, F. Pirani, E. L. Heck, and A. S. Dickinson, Mol. Phys. **93**, 485 (1998).
[25] K. Leonhard and U. K. Deiters, Mol. Phys. **100**, 2571 (2002).
[26] V. Aquilanti, M. Bartolomei, D. Cappelletti, E. Carmona-Novillo, and F. Pirani, J. Chem. Phys. **117**, 615 (2002).
[27] M. H. Karimi-Jafari, A. Maghari, and S. Shahbazian, Chem. Phys. **314**, 249 (2005).
[28] P. Strąk and S. Krukowski, J. Chem. Phys. **126**, 194501 (2007).
[29] L. Gomez, B. Bussery-Honvault, T. Cauchy, M. Bartolomei, D. Cappelletti, and F. Pirani, Chem. Phys. Lett. **445**, 99 (2007).
[30] D. Cappelletti, F. Pirani, B. Bussery-Honvault, L. Gomez, and M. Bartolomei, Phys. Chem. Chem. Phys. **10**, 4281 (2008).
[31] R. Hellmann, Mol. Phys. **111**, 387 (2012).
[32] M. H. Karimi-Jafari and M. Ashouri, Phys. Chem. Chem. Phys. **13**, 9887 (2011).
[33] J. D. Johnson, M. S. Shaw, and B. L. Holian, J. Chem. Phys. **80**, 1279 (1983).
[34] K. S. Sorbie and J. N. Murrell, Mol. Phys. **29**, 1387 (1975).
[35] A. Aguado and M. Paniagua, J. Chem. Phys. **96**, 1265 (1992).
[36] A. J. C. Varandas and J. N. Murrell, Farad. Discuss. **62**, 92 (1977).
[37] A. Aguado, C. Suárez, and M. Paniagua, J. Chem. Phys. **101**, 4004 (1994).
[38] C. Tablero, A. Aguado, and M. Paniagua, J. Chem. Phys. **110**, 7796 (1999).
[39] A. Aguado, P. Barragán, R. Prosmiti, G. Delgado-Barrio, P. Villarreal, and O. Roncero, J. Chem. Phys. **133**, 024306 (2010).
[40] K. Andersson, P.-Å. Malmqvist, and B. O. Roos, J. Chem. Phys. **96**, 1218 (1992).
[41] H.-J. Werner, Mol. Phys. **89**, 645 (1996).
[42] B. J. Braams and J. M. Bowman, Int. Rev. Phys. Chem. **28**, 577 (2009).
[43] J. M. Bowman, B. J. Braams, S. Carter, C. Chen, G. Czakó, B. Fu, X. Huang, E. Kamarchik, A. R. Sharma, B. C. Shepler, Y. Wang, and Z. Xie, J. Phys. Chem. Lett. **1**, 1866 (2010).
[44] F. R. Gilmore, J. Quant. Spectrosc. Radiat. Transfer **5**, 369 (1965).
[45] J. W. McGowan and H. H. Michels, Adv. Chem. Phys. **45**, 224 (1981).
[46] P. J. Knowles and H.-J. Werner, Chem. Phys. Lett. **115,** 259 (1985).
[47] K. P. Huber and G. Herzberg, *Molecular Spectra and Molecular Structure. IV. Constants of Diatomic Molecules* (Van Nostrand Reinhold Co., 1979) p. 412.
[48] H.-J. Werner, P. J. Knowles, G. Knizia, F. R. Manby, and M. Schütz, WIREs Comput. Mol. Sci. **2**, 242 (2012).
[49] H.-J. Werner, P. J. Knowles, G. Knizia, F. R. Manby, M. Schütz, et al., *Molpro*, version 2010, University College Cardiff Consultants, Cardiff, Wales, 2010.

[50] B. O. Roos and K. Andersson, Chem. Phys. Lett. **245**, 215 (1995).
[51] K. Andersson, Theor. Chim. Acta **91**, 31 (1995).
[52] E. Papajak, H. R. Leverentz, J. Zheng, and D. G. Truhlar, J. Chem. Theory Comput. **5**, 1197 (2009).
[53] C. R. Brazier, P. F. Bernath, J. B. Burkholder, and C. J. Howard, J. Chem. Phys. **89**, 1762 (1988).
[54] T. A. Halgren and W.N. Lipscomb, Chem. Phys. Lett. **49**, 225 (1977).
[55] See supplementary material at http://dx.doi.org/10.1063/[to be filled in] for the full data of geometries and energies used for the fit.
[56] L. Pauling, *The Nature of the Chemical Bond*, 3rd. ed.; Cornell University Press: Ithaca, NY, 1960, p. 98.
[57] H. S. Johnston, Adv. Chem. Phys. **3**, 131 (1961).
[58] A. Laganà, G. O. D. Aspuru, E. Garcia, J. Chem. Phys. **108**, 3886 (1998).
[59] G. Lendvay, J. Mol. Strucrt. THEOCHEM **501-502**, 389 (2000).
[60] M. Zhao, M. A. Iron, P. Staszewski, N. E. Schultz, R. Valero, and D. G. Truhlar, J. Chem. Theory Comput. **5**, 594 (2009).
[61] P. M. Morse, Phys. Rev. **34**, 57 (1929).
[62] Z. Xie and J. M. Bowman, J. Chem. Theory Comput. **6**, 26 (2010).
[63] A. W. Jasper, N. E. Schultz, and D. G. Truhlar, J. Phys. Chem. B **109**, 3915 (2005).
[64] S. Nangia and D. G. Truhlar, J. Chem. Phys. **124**, 124309 (2006).
[65] Z. H. Li, R. Valero, and D. G. Truhlar, Theoretical Chemistry Accounts **118**, 9 (2007).
[66] B. Fu, E. Kamarchik, and J. M. Bowman, J. Chem. Phys. **133**, 164306 (2010).

Table 2.1 The mean unsigned errors (MUEs) and root-mean-square errors (RMSEs) of the fitted potential energy surface with respect to CASPT2/maug-cc-pVTZ results for different energy ranges (in kcal/mol).

	NO. of points	MUE	RMSE
$E < 100.0$	693	1.2	1.7
$100.0 \leq E < 228.0$	1941	2.3	4.1
$228.0 \leq E < 456.0$	11858	3.1	5.8
$456 \leq E < 1000.0$	1610	10.9	14.6
$E > 1000.0$	333	21.7	30.9
All data	16435	4.1	8.2

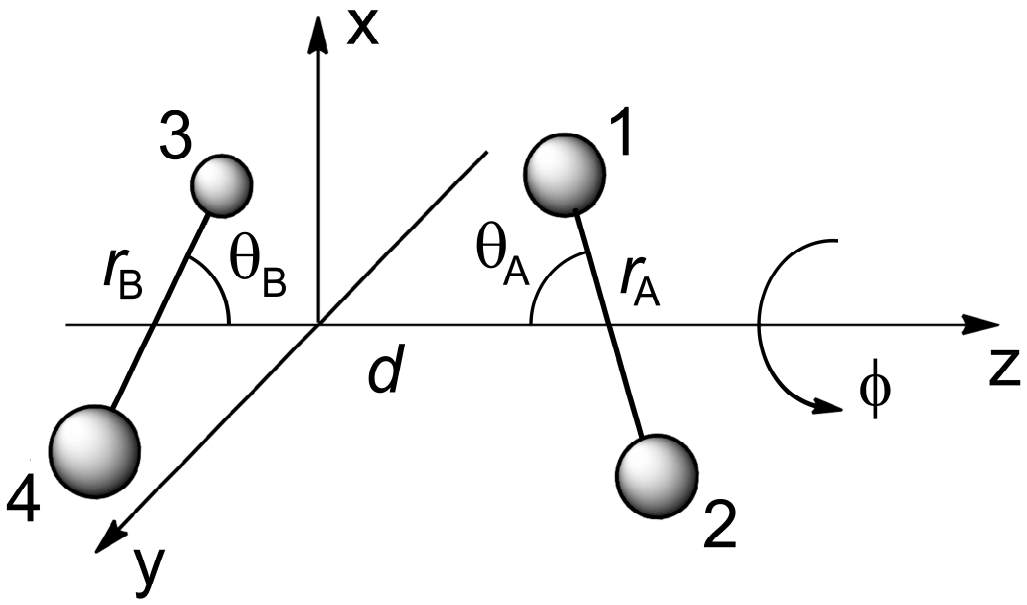

Figure 2.1. Coordinates for $N_2 + N_2$. $r_{A:}$ $r_e - 0.2$ Å, r_e, $r_e + 0.2$ Å, r_B: 1.0 – 5.0 Å, d: 1.0 – 10.0 Å, θ_A, θ_B : 0, π/3, π/2, φ: 0, π/2, π/3.

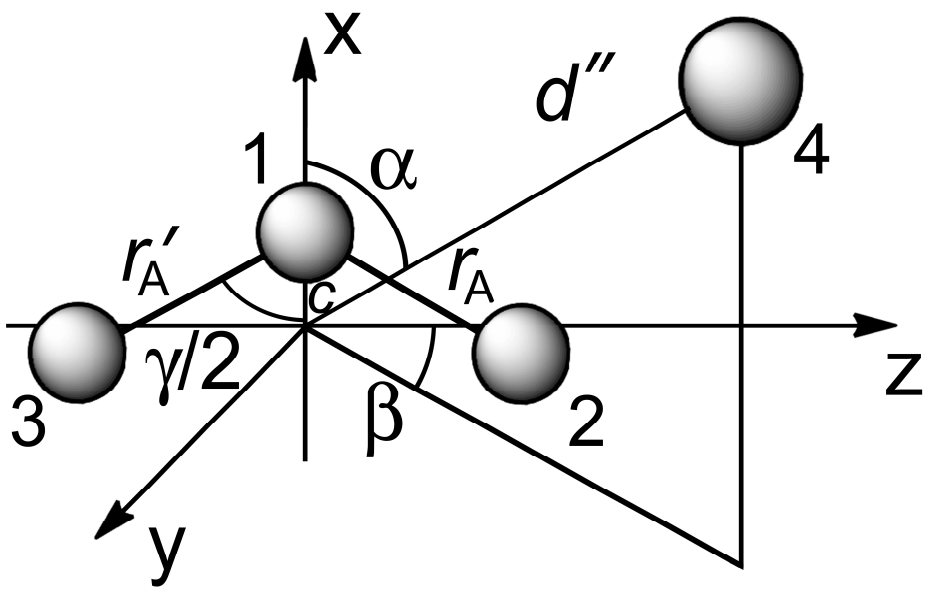

Figure 2.2. Polar coordinates for the bent $^4N_3$ + ^4N interaction.

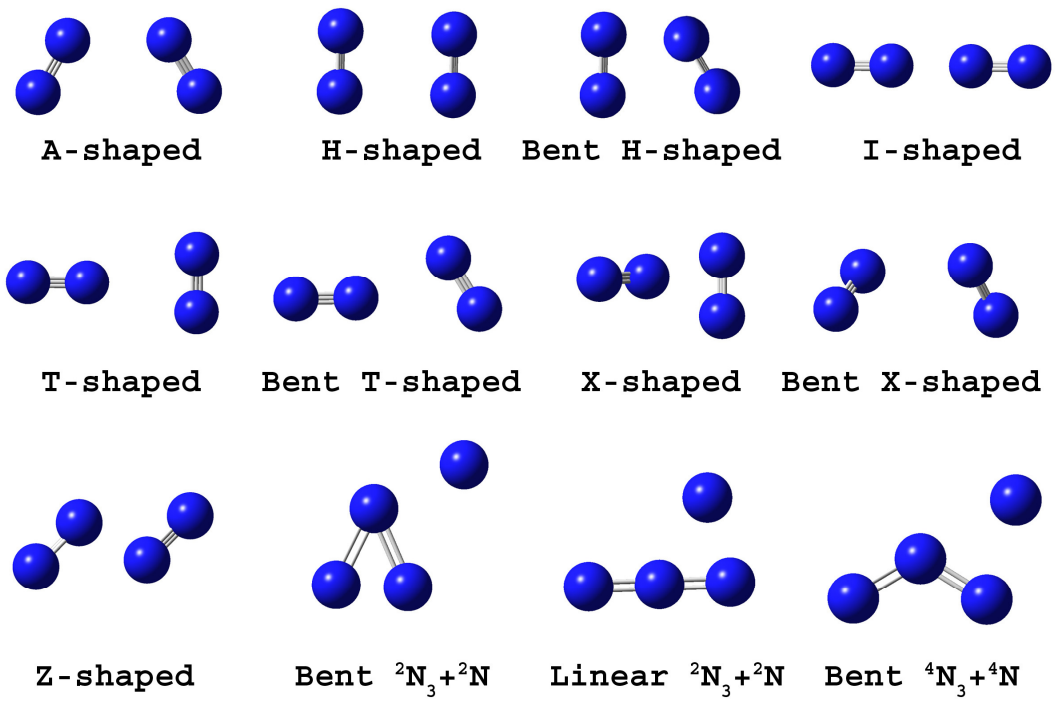

Figure 2.3. Molecular arrangements for N_4.

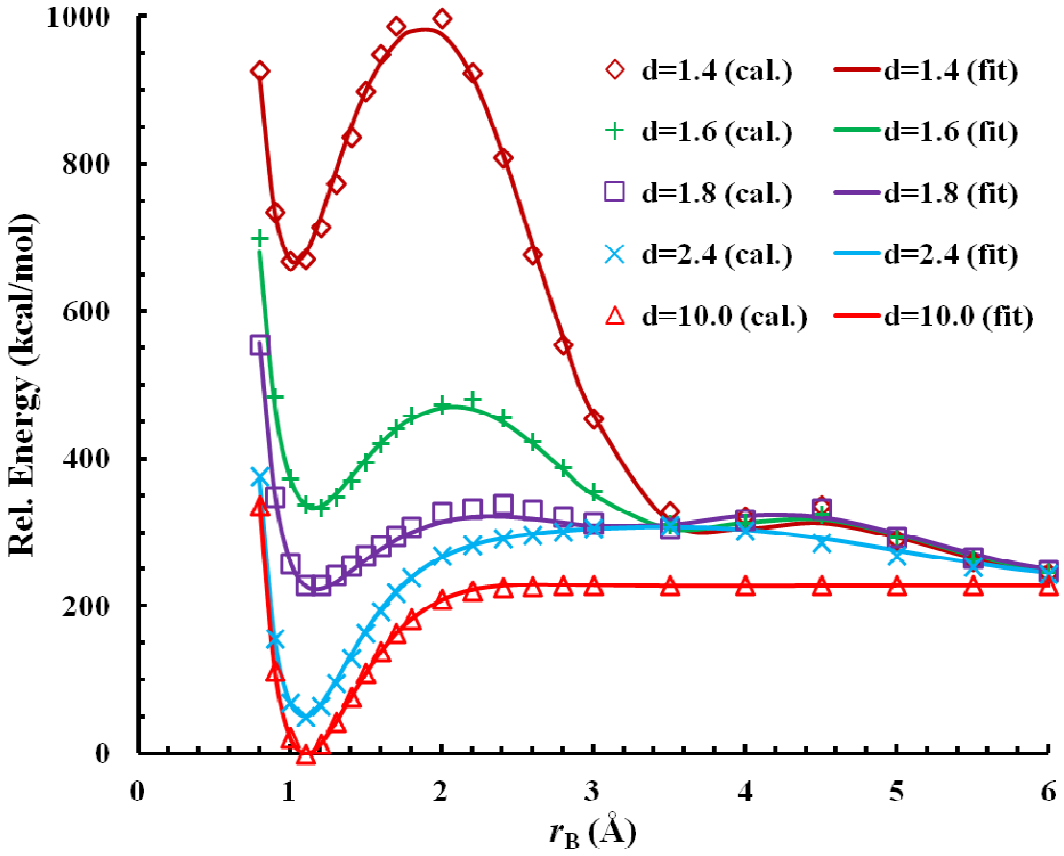

Figure 2.4. Dissociation curves for $N_2 + N_2$: comparison of the global fit to the values obtained with the CASPT2 method for the A-shaped set with one N_2 fixed to its equilibrium distance. Both r_B and d are in Å. In Figure 2.4-2.7, d is the distance between the centers of mass of the two nitrogen molecules.

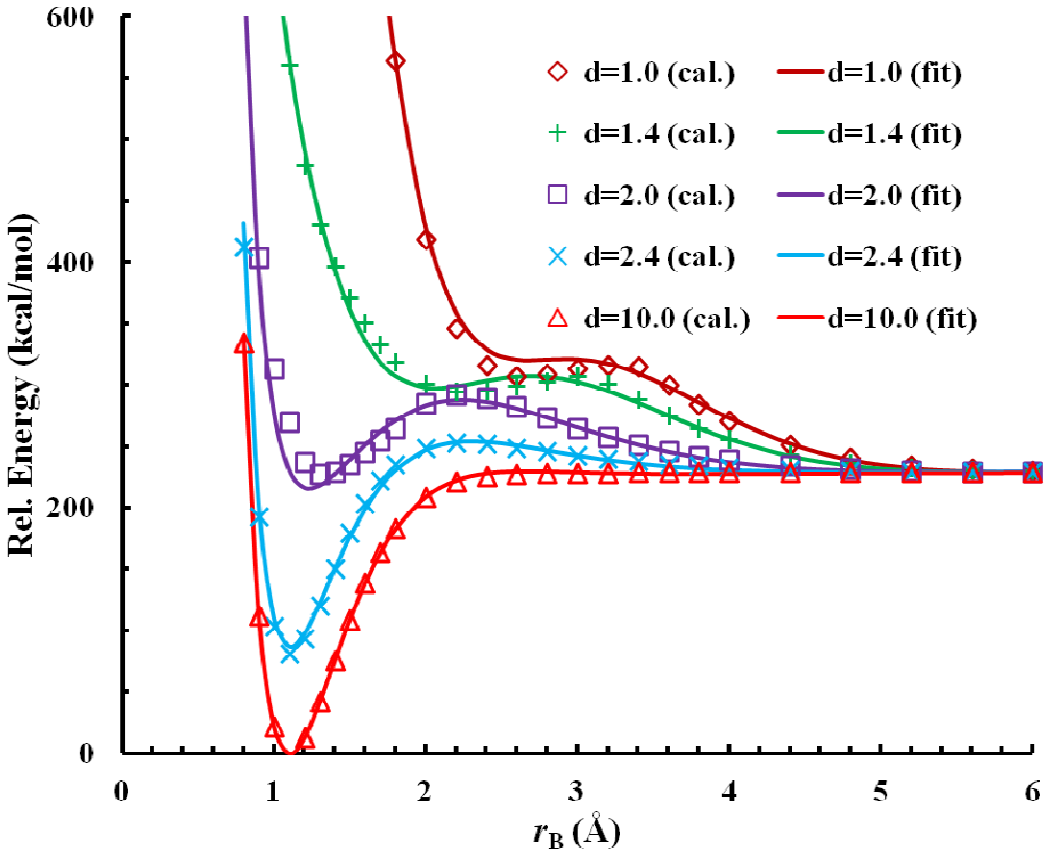

Figure 2.5. Dissociation curves for $N_2 + N_2$: comparison of the global fit to the values obtained with the CASPT2 method for the T-shaped set with one N_2 fixed to its equilibrium distance.

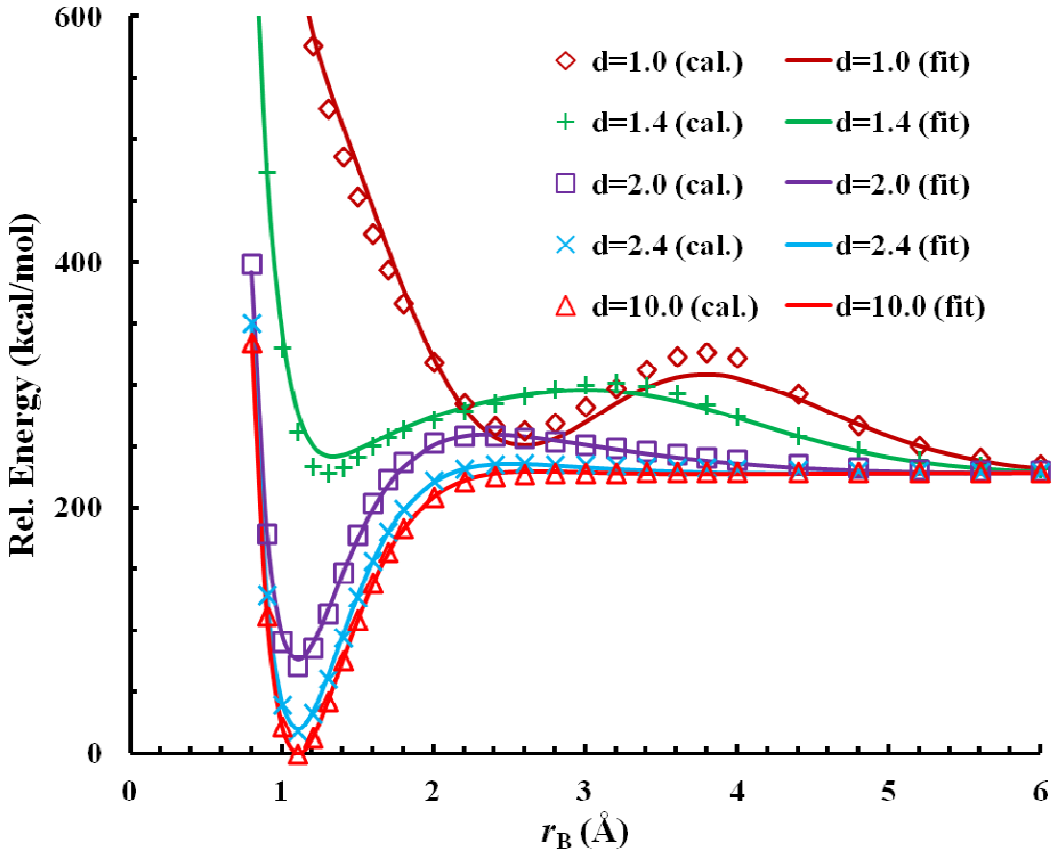

Figure 2.6. Dissociation curves for $N_2 + N_2$: comparison of the global fit to the values obtained with the CASPT2 method for the H-shaped set with one N_2 fixed to its equilibrium distance.

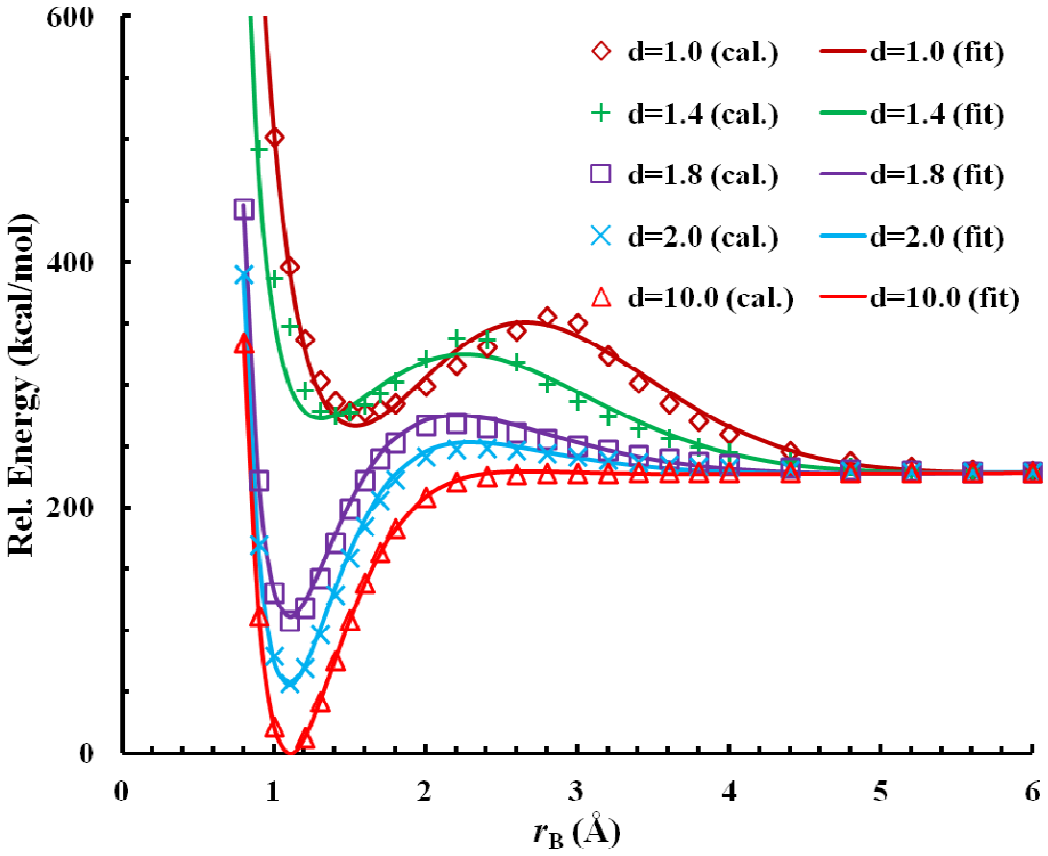

Figure 2.7. Dissociation curves for $N_2 + N_2$: comparison of the global fit to the values obtained with the CASPT2 method for the X-shaped set with one N_2 fixed to its equilibrium distance.

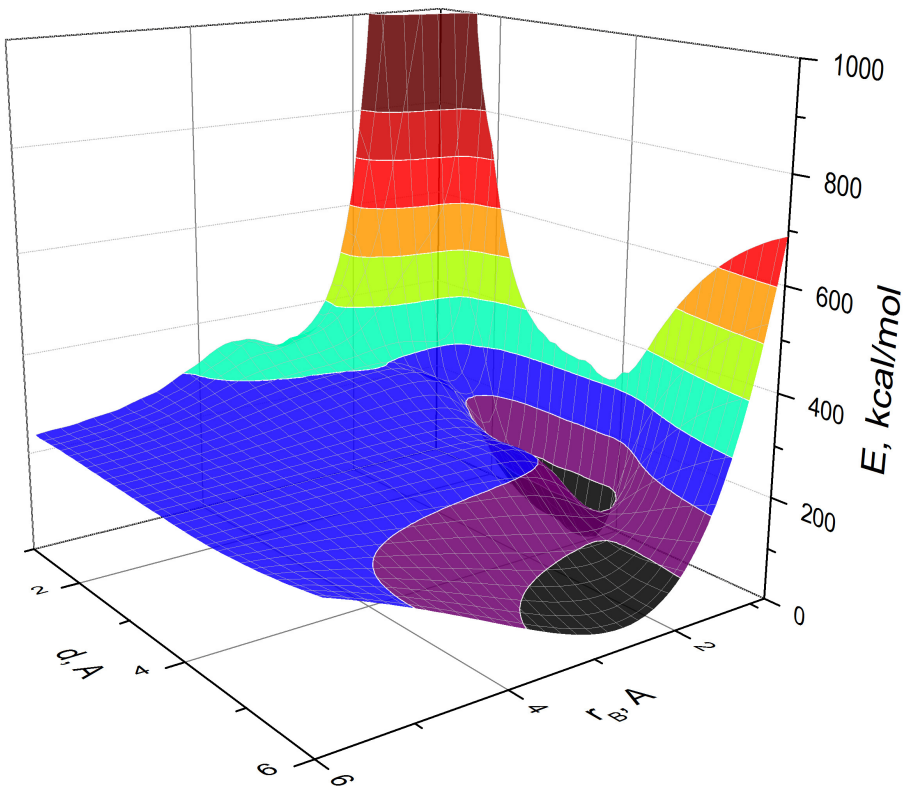

Figure 2.8. Three-dimensional surface for N_2 + N_2, obtained with the CASPT2 method for bent T–shaped arrangement.

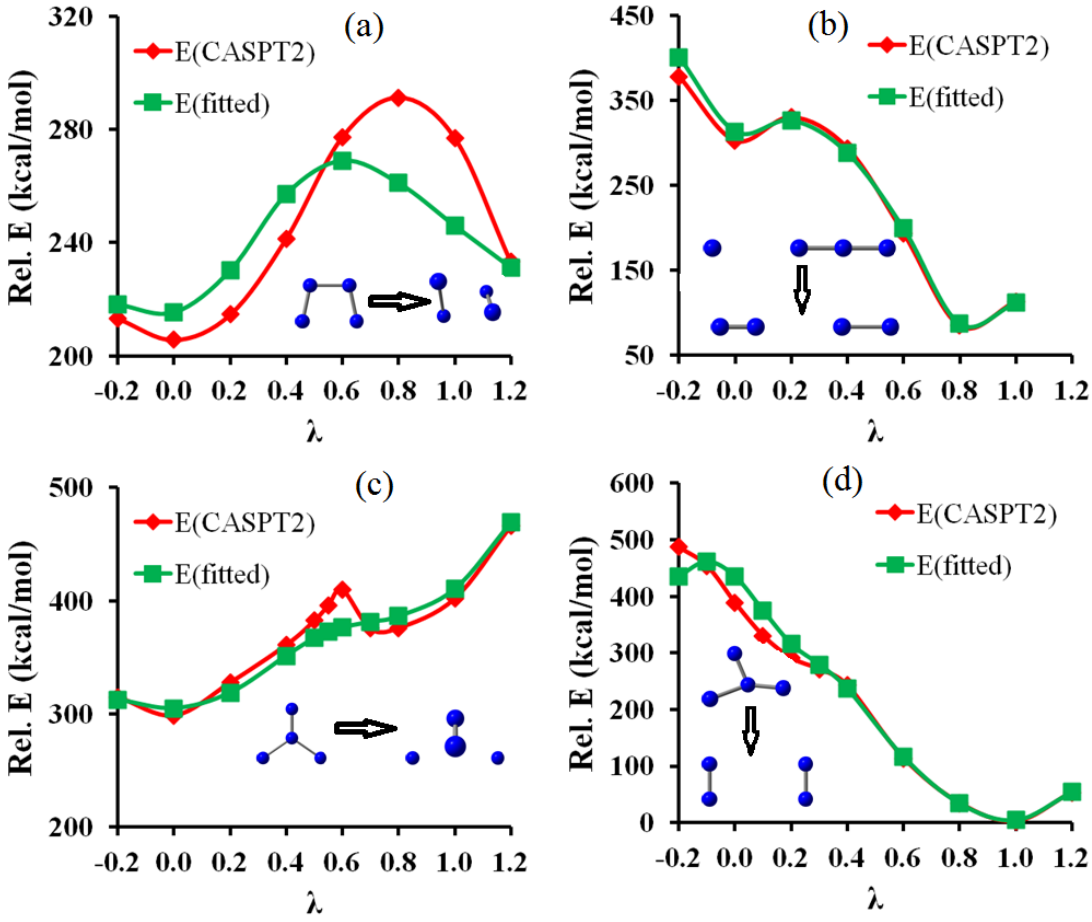

Figure 2.9. Comparison of the test fit (green) to the CASPT2/maug-cc-pVTZ data (red) for the four LST paths. (The data points along the 4 paths are not included in the test fit to see the ability of the fitting strategy to predict the relative energies of N_4.)

Chapter 3. Direct Diabatization of electronic states by the fourfold way: Including dynamical correlation by multi-configuration quasidegenerate perturbation theory with complete active space self-consistent-field diabatic molecular orbitals

Adapted with permission from Ke R. Yang, Xuefei Xu, and Donald G. Truhlar, Chem. Phys. Lett. **573**, 84 (2013).

3.1 Introduction

The widely used Born-Oppenheimer (BO) approximation separates the electronic and nuclear motions, which leads to the concepts of adiabatic states and potential energy surfaces (PESs). Adiabatic PESs are associated with adiabatic electronic states, which are the eigenstates of the electronic Hamiltonian at each nuclear configuration. The couplings between nuclear motions and electronic motions are usually called nonadiabatic coupling. In the adiabatic representation, nonadiabatic couplings are off-diagonal matrix elements of the nuclear momentum vector and the nuclear kinetic energy, although the latter is often neglected in semiclassical treatments.[1] The former are $(3N_A - 6)$-dimensional vectors, where N_A is the number of atoms in the molecule. The couplings can be rapidly varying in avoided crossing regions where two or more adiabatic PESs approach closely, and they are singular along $(3N_A - 8)$-dimensional conical intersection seams; this makes them inconvenient for dynamical studies of photodissociation, predissociation, quenching of excited states in collisions, chemiluminescence, etc. The use of diabatic representations[2] has been proposed as an alternative approach to study dynamics. In nonadiabatic representations (any representation except the adiabatic one), the states are

coupled not only by the nuclear momentum and kinetic energy but also by the electronic Hamiltonian; diabatic states are nonadiabatic states whose momentum and kinetic energy couplings are negligible compared to the electronic Hamiltonian couplings, which are off-diagonal elements of the electronic Hamiltonian matrix. The electronic Hamiltonian couplings are slowly varying, nonsingular scalars and hence are much more convenient for dynamical calculations. Strictly diabatic states would be states whose nuclear momentum and kinetic energy couplings (nonadiabatic couplings) vanish completely and globally; they do not exist in general,[3] so one has to develop methods to obtain diabatic states whose nonadiabatic couplings are negligible but not strictly vanishing.

Many methods, based on a variety of criteria, have been proposed to calculate diabatic states, which are not unique, and they are briefly discussed in Refs. 4 and 5 (with more than 50 references to previous treatments). Among these methods, the fourfold way diabatization scheme[4-6] proposed by Nakamura and one of the authors is very promising and has been applied to study of the photodissociation of ammonia,[7-10] bromoacetyl chloride,[11] hydrogen bromide,[12] and chlorobromomethane.[13] One important advantage of the fourfold way over alternative schemes is that it is "direct," which in this context means that the diabatic potentials and couplings calculated at a given geometry are independent of any path leading to that geometry. Another important feature of fourfold-way diabatization is that one obtains N diabatic electronic states that span the same space as N chosen adiabatic states (for example, the N lowest).

The fourfold-way algorithm is based on the density matrix, and it was originally proposed[4] for the diabatization of complete-active-space (CAS) self-consistent-field (CASSCF)[14-16] wave functions. However, CASSCF is not quantitatively accurate because it includes only a small fraction of the dynamical correlation. To include dynamical correlation, the method was further developed for the diabatization of multi-configuration quasi-degenerate perturbation theory (MC-QDPT),[17,18] which (like multi-state CASPT2 (Ref. 19) is a "perturb, then diagonalize" effective Hamiltonian variant of the multi-reference perturbation theory (MRPT).[20-23] In this letter, we present a simpler scheme to perform diabatization of MC-QDPT wave functions, and we test its performance for two test cases, namely, the dissociation of LiF and the reaction Li + FH → LiF + H.

In order to obtain diabatic states, the multi-electron wave functions are expressed in terms of diabatic molecular orbitals (DMOs) rather than the usual canonical molecular orbitals (CMOs) because the DMOs vary smoothly with geometry, whereas the CMOs need not be smooth along continuous nuclear-coordinate paths. In the original algorithms, the CASSCF diabatic states were expressed in terms of DMOs obtained from the CASSCF wave function, and the MC-QDPT diabatic states were expressed in terms of DMOs obtained using a density matrix based on the eigenvectors of the MC-QDPT effective Hamiltonian. In the algorithm presented here, the MC-QDPT diabatic states are expressed in terms of the CASSCF DMOs; this simplifies the treatment and, more importantly, it was motivated by our observation that the CASSCF DMOs are sometimes

smoother than the DMOs that result from the more complicated MC-QDPT procedure. The quality of the diabatic states is not compromised by using the CASSCF DMOs because the new diabatic states still span the same space as the *N* MC-QDPT adiabatic states that they replace.

We stress that the goal of the diabatization scheme considered here is to obtain a set of diabatic states that span the same space as a chosen set of adiabatic states, but for which the coupling by the nuclear momentum operator is negligible compared to the effect of coupling by the electronic Hamiltonian. This will allow convenient treatments of electronically nonadiabatic states. (Since nonadiabatic states are not unique, some other workers have defined them with other objectives in mind, for example[24] to account for electron–nuclear correlation.) Because the diabatic states span the same space as the adiabatic ones, the method is not designed to overcome any limitations in the method used to obtain adiabatic states. For example, if or when the MC-QDPT method makes significant errors due to an incomplete treatment of electron correlation or gives nonsmooth adiabatic potential curves near places where the CASSCF states cross, the diabatization scheme does not correct these problems. But it does provide a convenient way to carry out dynamics at the MC-QDPT level, and this level (which is essentially the same as multistate CASPT2) has been demonstrated to provide useful accuracy for studying many photochemical processes. Nevertheless, it would be useful in future work to apply this diabatization scheme to other methods for calculating sets of ground and excited state potential energy surfaces, such as extended multi-configuration quasi-

degenerate perturbation theory (XMC-QDPT)[25] or extended multi-state complete active space second-order perturbation theory (XMS-CASPT2)[26] which would be expected to produce smoother adiabatic curves near surfaces crossings, or even to more significantly different methods such as multireference configuration interaction.[27-29] The present simplification of the method such that the DMOs are determined at the CASSCF level will facilitate such extensions.

3.2 Theory

The fourfold-way diabatization scheme is limited (at the present time) to complete active space methods (e.g., CASSCF, CASPT2, and MC-QDPT based on a CASSCF reference). In CAS methods, the molecular orbitals are divided into three classes: inactive orbitals that are doubly occupied in all reference configurations, external orbitals that are unoccupied in all reference configurations, and active orbitals that have variable occupation (0, 1, or 2) in reference configuration state functions (CSFs). The limitation to CAS methods is because we take advantage of the invariance of CASSCF wave functions to orbital rotations that do not mix orbitals from the different classes, in particular transformations that mix the active orbitals among themselves.

We will briefly discuss the fourfold-way diabatization method and then present our new scheme for diabatization of MC-QDPT wave functions with CASSCF DMOs. For more details of the original scheme, please refer to the original fourfold-way diabatization papers.[4,5]

3.2.1 The original fourfold way algorithms for diabatization

We obtain *N* diabatic states ϕ_k, with $k = 1 \cdots N$, by orthogonal transformation (assuming all wave functions are real) of the *N* adiabatic states ψ_n, with $n = 1 \cdots N$, as follows

$$\phi_k = \sum_{n=1}^{N} \psi_n T_{nk} , \tag{3.1}$$

where T_{nk} is an element of the orthogonal adiabatic-to-diabatic transformation matrix **T**. The adiabatic states are linear combinations of *L* orthonormal CSFs, χ_α,

$$\psi_n = \sum_{\alpha=1}^{L} c_{\alpha n} \chi_\alpha , \tag{3.2}$$

where the coefficients $c_{\alpha n}$ are obtained variationally or by perturbation methods. We consider systems for which each adiabatic state is dominated by a small set of CSFs at potential reference geometries, which are geometries where adiabatic states are almost equal to diabatic states. At potential reference geometries, one can identify "dominant" CSFs, χ_δ (called diabatic prototypes), that make large contributions to one and only one of the *N* adiabatic states of interest, and one can divide them into *N* groups as follows:

Group G_1: { χ_δ }, $\delta = 1 \cdots a_1$, which are mainly important for ψ_1;

Group G_k: { χ_δ }, $\delta = (a_{k-1} + 1) \cdots a_k$, which are mainly important for ψ_k;

Group G_N: { χ_δ }, $\delta = (a_{N-1} + 1) \cdots (a_N = M)$, which are mainly important for ψ_N.

where M is the total number of diabatic prototypes in all of the groups. The dominant CSF group lists G_k (with $k = 1 \cdots N$) may be used to form templates of the diabatic states $\phi_k, k = 1 \cdots N$, provided that we exclude any CSF that would be prominent in more than one diabatic state as we vary the geometry. One may need to consider more than one potential reference geometry and make dominant CSF lists by taking the union of the dominant CSF lists at each of them. Furthermore, sometimes one needs to add diabatic prototypes to the lists even when they are not identified at potential reference geometries.

At any geometry, we can obtain approximate wave functions for the N adiabatic states ψ_n, with $n = 1 \cdots N$, by using either CASSCF or MC-QDPT. With the predefined dominant CSF lists G_k and the calculated coefficients $c_{\alpha n}$ of the N adiabatic states ψ_n expressed in terms of these CSFs, the adiabatic/diabatic transformation matrix $\mathbf{T}$ is determined by the configuration uniformity procedure introduced by Atchity and Ruedenberg.[30] The details of the step to determine $\mathbf{T}$ are given in Refs. 4 and 5, and we will not change or discuss them here.

The CSFs in the group lists must be smooth functions along nuclear-coordinate paths, as required for them to fulfill their mandate as diabatic prototypes; thus the molecular orbitals (MOs) that are used to construct these dominant CSFs have to change smoothly along paths in nuclear coordinate space. These MOs that change smoothly are the DMOs we mentioned above.

The fourfold algorithm for constructing DMOs consists of the threefold density matrix criterion and the maximum overlap reference MOs (MORMO) criterion. The threefold density matrix criterion is the maximization of the functional defined as:

$$D_3 = \alpha_N D^{\mathrm{NO}} + \alpha_R D^{\mathrm{ON}} + \alpha_T D^{\mathrm{TD}}, \tag{3.3}$$

where α_N, α_R, and α_T are predefined parameters. Here we use the standard values of 2, 1, and 0.5. The functional D^{NO} is called the natural orbital term and is defined as

$$D^{\mathrm{NO}} = N \sum_{\mu=1}^{\eta} (\bar{p}_{\mu\mu})^2, \tag{3.4}$$

where η is the number of active MOs used to construct CSFs, and $\bar{\mathbf{p}}$ is the state-averaged density matrix (averaged over the *N* states of interest). The functional D^{ON} is called the occupation number term and is defined as

$$D^{\mathrm{ON}} = \sum_{\mu=1}^{\eta} \sum_{n=1}^{N} (p^n_{\mu\mu})^2, \tag{3.5}$$

where $p^n_{\mu\mu}$ is the one-particle density matrix element of the adiabatic wave function ψ_n. The third term D^{TD} is called the transition density term and is defined as

$$D^{\mathrm{TD}} = \frac{2}{N-1} \sum_{\mu=1}^{\eta} \sum_{m<n}^{N} (p^{mn}_{\mu\mu})^2, \tag{3.6}$$

where $\mathbf{p}^{mn}$ is the transition density matrix between adiabatic states ψ_m and ψ_n.

The MORMO criterion involves introducing λ reference MOs u^{ref}_τ, $\tau = 1 \cdots \lambda$, and a reference orbital functional D^{RO}. For a specific geometry *Q*, D^{RO} is defined as[4-6]

$$D^{\mathrm{RO}} = \sum_{\tau=1}^{\lambda} \left(\sum_{i=1}^{I} \sum_{j=1}^{I} a_{\tau i}^{\mathrm{ref}} a_{\tau j} \left\langle \xi_i(Q) \middle| \xi_j(Q) \right\rangle \right)^2 , \tag{3.7}$$

where I is the number of atomic basis functions, $\xi_i(Q)$, $i = 1 \cdots I$ are the normalized atomic orbitals, and $a_{\tau i}^{\mathrm{ref}}$ and $a_{\tau j}$ are the coefficients of MO u_{τ}^{ref} at geometry Q_{ref} and Q, respectively.

To apply the fourfold way to determine DMOs, one first maximizes D^{RO} by rotating all η active orbitals, and the λ rotated MOs that maximize D^{RO} are taken as the first λ DMOs. Then D_3 is maximized by orbital rotations within the remaining set of $\eta - \lambda$ active MOs to determine the remaining DMOs. After determining DMOs with the fourfold way, those DMOs need to be ordered according to the DMOs at nearby geometries to construct consistent CSFs to obtain the adiabatic/diabatic transformation matrix $\mathbf{T}$ based on configuration uniformity. The determination of the transformation matrix $\mathbf{T}$ is explained in previous work.[4,5]

The fourfold-way diabatization algorithm has been implemented for adiabatic states described by both CASSCF and MC-QDPT wave functions. For CASSCF wave functions, it is very clear that only DMOs spanning the same space of η active orbitals need to be determined with fourfold way, since the occupancies of inactive and external orbitals are the same in all CSFs, either doubly occupied or unoccupied. But this requires further justification for MC-QDPT wave functions. In general the adiabatic state, ψ_n^{MQ}, obtained with MC-QDPT can be written as

$$\psi_n^{\mathrm{MQ}} = \sum_{\alpha=1}^{L_{\mathrm{CAS}}} c_{\alpha n}\chi_\alpha \quad + \sum_{\alpha=L_{\mathrm{CAS}}+1}^{L} c_{\alpha n}\chi_\alpha \quad , \tag{3.8}$$

where L_{CAS} is the number of CSFs in the CAS configuration space, and L is the total number of CSFs. In CSFs χ_α with $\alpha = 1 \cdots L_{\mathrm{CAS}}$, all inactive and external orbitals are doubly occupied and unoccupied, respectively, as for CASSCF wave functions. But this is not the case for CSFs χ_α with $\alpha = L_{\mathrm{CAS}}+1 \cdots L$, in which the occupancies of inactive and external orbitals can differ from 2 and 0. However, if the active space is chosen large enough for a good description of all *N* states, one can expect that

$$\sum_{\alpha=1}^{L_{\mathrm{CAS}}} c_{\alpha n}^2 \quad >> \sum_{\alpha=L_{\mathrm{CAS}}+1}^{L} c_{\alpha n}^2 \quad . \tag{3.9}$$

So we make the assumption that, even when dynamical correlation is included, only the DMOs spanning the active orbital space need to be determined, while the remaining orbitals can be taken as CMOs.

3.2.2 Including dynamical correlation by MC-QDPT with CASSCF DMOs

The original implementation of the fourfold-way diabatization of MC-QDPT wave functions is conceptually complicated by the use of MC-QDPT DMOs, and the smooth variation of the DMOs is dependent on smooth variation of the MC-QDPT effective Hamiltonian eigenvectors. Here we propose a simplified scheme to include dynamical correlation in diabatic states. The first steps are the same as before: we use the fourfold way to obtain the CASSCF DMOs, and then the CASSCF wave functions are

expressed in terms of CSFs constructed with CASSCF DMOs. In the previous MC-QCPT algorithm, the CASSCF DMOs are only used as initial MOs in the MC-QDPT adiabatic calculations, and we determine the final DMOs by applying the fourfold way at the MC-QDPT level (these new DMOs are the MC-QDPT DMOs); then we express the wave function by eq. 3.8 where χ_α is a CSF expressed in terms of MC-QDPT DMOs for the active space and CMOs for the inactive and virtual spaces. Finally the coefficients of eq. 3.) are used with the predefined dominant CSF lists in the configurational uniformity scheme to obtain the diabatic states.

In contrast, in the new method we skip the step to obtain MC-QDPT DMOs, and we replace eq. 3.8 by

$$\psi_n^{\mathrm{MQ}} = \sum_{\alpha=1}^{L_{\mathrm{CAS}}} c_{\alpha n}^0 \chi_\alpha^0 \quad + \quad \sum_{\alpha=L_{\mathrm{CAS}}+1}^{L} c_{\alpha n}^0 \chi_\alpha^0 \tag{3.10}$$

where χ_α^0 is a CSF expressed in terms of CASSCF DMOs for the active space and CMOs for the inactive and virtual spaces. With the predefined dominant CSF lists and the coefficients in Eq. 3.10, we calculate the adiabatic/diabatic transformation matrix and do the diabatization of MC-QDPT adiabatic states without the complication of MC-QDPT DMOs.

3.3 Applications

This section will illustrate the new diabatization scheme presented in Sec. 3.2 by applying it to two test systems, the dissociation of LiF and the reaction Li + FH → LiF +

H. The two test cases are quite different, and they provide critical tests of the new method. The first case was chosen because it is a classic case[31] of a curve crossing whose location is very sensitive to dynamical correlation. In particular the curve crossing of the ionic and covalent interactions occurs at a much larger distance when dynamical correlation is fully included. This provides a severe test of the applicability of using CASSCF DMOs in a calculation with post-CASSCF dynamical correlation. The second test case was chosen because it is a multi-arrangement reaction system where the DMOs derived by the fourfold way must change their character smoothly along a reaction pathway,[4,5] which required an extension of the original configurational uniformity concept of Atchity and Ruedenberg.[30]

All calculations were carried out with a locally modified version of the HONDOPLUS v5.2 program.[32,33] Computational details and results are given in the following two subsections.

3.3.1 First test case: LiF dissociation (1 $^1\Sigma^+$, 2 $^1\Sigma^+$)

The two lowest $^1\Sigma^+$ states of LiF exhibit an ionic–covalent diabatic curve crossing at large bond length. LiF is a good example to test a diabatization scheme since the location of its weakly avoided crossing of the adiabats is very sensitive to dynamical correlation; the location of the avoided crossing point is quite different for CASSCF and MC-QDPT wave functions. It is therefore a good check to demonstrate that our new scheme is able to give the proper location of the avoided crossing in LiF.

The basis set we used is 6-311G(3df,3pd)[34,35] augmented by diffuse s and p functions with exponents 0.0052 (s) and 0.0097 (p) for Li and 0.089 (s) and 0.083 (p) for F. The active space contains the 2s and 2p orbitals of Li and the 2p orbitals of F; this choice gives an active space with 6 electrons in 7 orbitals. The 1s orbitals of the Li and F atoms and the 2s orbitals of F were kept doubly occupied in the CASSCF calculations, but only the two sets of 1s orbitals are kept doubly occupied in the MC-QDPT calculations.

The geometry with an Li–F bond length of 3.0 a_0 was taken as the reference geometry to obtain the dominant CSF lists, which are $G_1 = \{\chi_1\}$ and $G_2 = \{\chi_2\}$, where χ_1 is $(4\sigma)^2(5\sigma)^0(1\pi)^4$ and χ_2 is $(4\sigma)^1(5\sigma)^1(1\pi)^4$. No reference orbital is needed, so we used $(\alpha_N, \alpha_R, \alpha_T; \gamma) = (2,1,0.5;0)$ to determine the CASSCF and MC-QDPT DMOs for the original CASSCF and MC-QDPT diabatization schemes and for the new diabatization scheme in which MC-QDPT wave functions are expressed in terms of CASSCF DMOs.

The adiabatic potential energy curves V_1 and V_2, the diabatic potential energy curves U_{11} and U_{22}, and the diabatic coupling U_{12} obtained by diabatization of CASSCF wave functions with CASSCF DMOs are shown in Figure 3.1a. The adiabatic potential energy curves have an avoided crossing at large bond length, and the two diabatic potential energy curves (the ionic U_{11} and the covalent U_{22}) cross each other near $r_{\mathrm{LiF}} =$ 10.5 a_0, which is a much smaller than the experimental[36] distance of 13.7 a_0. The calculated adiabatic potential energy curves and diabatic coupling by diabatization of MC-QDPT wave functions with MC-QDPT DMOs, are shown in Figure 3.1b. By

including dynamical correlation, the diabatic states obtained by MC-QDPT cross at r_{LiF} = 12.5 a_0, which is a significant improvement over CASSCF. The physical reason for the improved performance of the MC-QDPT method is that the electron affinity of fluorine is greatly improved by including dynamical correlation, as is well known from previous work.[37]

With our new scheme, we first obtained CASSCF DMOs. Then the adiabatic MC-QDPT wave functions were expressed in terms of the CASSCF DMOs and were used for direct diabatization to obtain the energies of diabatic states and diabatic couplings. The calculated adiabatic and diabatic potential energy curves and diabatic couplings are shown in Figure 3.1c. The diabatic states U_{11} and U_{22} calculated by our new scheme with CASSCF DMOs cross at r_{LiF} = 12.5 a_0, which is the same distance as found with the more complicated scheme with MC-QDPT DMOs. Not only do we get a similar crossing distance, we also find that the diabatic potential energy curves calculated with our new scheme are very similar to those calculated by diabatization of MC-QDPT wave function with MC-QDPT DMOs.

3.3.2 Second test case: Li + HF chemical reaction ($1\,^2A'$, $2\,^2A'$)

Along the reaction path of Li(^2S) + HF($^1\Sigma^+$) → LiF($^1\Sigma^+$) + H(^2S) and near to the transition state, the two lowest adiabatic states of LiFH have a strongly avoided crossing.[38] This avoided crossing may be interpreted as the crossing of the valence bond curves corresponding to the reactant bonding configuration and the product bonding

configuration. The excited state of the two states involved correlates with Li(^2P) + HF($^1\Sigma^+$) in the reactant asymptotic and with LiF($^3\Sigma^+$) + H (^2S) at the product.

We studied this system with the 6-311G(3df,3pd) basis set[34,35] augmented by diffuse s and p functions with exponents 0.0052 (s) and 0.0097 (p) for Li, 0.089 (s), 0.00001 (s), and 0.083 (p) for F, and 0.037 (s), 0.012 (s), and 0.055 (p) for H. The active space contains the 2s and 2p orbitals of Li, the 2p orbitals of F, and the 1s orbital of H, yielding 7 electrons in 8 orbitals. The 1s orbitals of Li and F atoms and the 2s orbitals of F were kept doubly occupied in the CASSCF calculations, but only the two sets of 1s orbitals are kept doubly occupied in the MC-QDPT calculations.

The potential reference geometries in our calculations were: r_{LiF} = 15.0 a_0 and r_{FH} = 1.73 a_0 in the reactant region and r_{LiF} = 2.96 a_0 and r_{FH} = 15.0 a_0 in the product region with three different Li-F-H angles γ: 45°, 90°, and 135°.

A reference orbital is needed to disentangle the orbital pair 6a' and 7a', where 6a' is the 2s orbital of Li, and 7a' is a 2p orbital of Li near reactant asymptotic. Since the 6a' orbital remains 2s-like along the whole reaction path, but 7a' becomes the 1s orbital of H in the product, we chose 6a' as the reference orbital, and the MORMO reference geometry was chosen to have the coordinates: r_{LiF} = 15.0 a_0, r_{FH} = 1.73 a_0, and Li-F-H angle equal to 135°.

Next, the dominant CSF lists need to be determined for all reference geometries. For the reactant region we have $G_1 = \{\chi_1\}$ and $G_2 = \{\chi_2\}$, where:

χ_1: ...$(4a')^2(5a')^2(6a')^1(7a')^0(1a'')^2$

χ_2: ...$(4a')^2(5a')^2(6a')^0(7a')^1(1a'')^2$

where $5a'$ is the $2p_y$ orbital of F (the Li–F axis is the z axis). In the product region we again have $G_2 = \{\chi_2\}$, but—based on the dominant CSFs at all potential reference geometries—we have to add two more CSFs to G_1 to provide a good representation in the product region. In particular we add $\{\chi_3^{(1)}, \chi_3^{(2)}\}$ where the spatial parts of the electronic configurations of $\chi_3^{(1)}$ and $\chi_3^{(2)}$ are the same,

$\chi_3^{(1)}, \chi_3^{(2)}$: ...$(4a')^2(5a')^1(6a')^1(7a')^1(1a'')^2$

but they differ in the spin functions.

For the reaction path with $\gamma = 120°$, we performed diabatization with the original CASSCF and MC-QDPT methods as well as with our new scheme. The resulting potential energy curves and diabatic coupling are shown in Figure 3.2. As the Li atom approach HF molecule, the energy of the ground state decreases slightly along the reaction path, which can be rationalized as noncovalent attraction between Li atom and HF molecule. Then, as the reaction coordinate s approaches -0.6 amu$^{1/2}a_0$, the Li atom gets close to the F atom ($r_{\mathrm{LiF}} = 3.68\ a_0$), and the strong HF bond begins to break, so the energy of the ground state increases rapidly. The energy of the ground state further increases as the Li atom continues toward the HF molecule, and finally it decreases after passing the saddle point as the LiF bond is formed. The energy of the ground state near the product asymptotic is higher than that near the reactant asymptote because the HF bond is stronger than the LiF bond.

In Figure 3.2a, the diabatization is done with CASSCF wave functions, so no dynamical correction is included. The two adiabatic states have a strongly avoided crossing near the transition state, and the two diabatic states cross near $s = 0.03\ a_0$, where s is the distance along the minimum energy path in an isoinertial coordinate system scaled to 1 amu. The barrier height for reaction on the ground-state potential energy surface is about 1.1 eV. With MC-QDPT wave functions, which include dynamical correlation, the adiabatic and diabatic potential energy curves and the diabatic coupling change significantly as compared to Figure 3.2a, and the barrier height is reduced to about 0.5 eV, as shown in Figure 3.2b. With our new method, in which we include the dynamical correlation by MC-QDPT with CASSCF DMOs, the resulting adiabatic and diabatic energies and diabatic coupling agree well with the more complicated diabatization scheme with MC-QDPT DMOs, as shown in Figure 3.2c.

3.4 Concluding remarks

The fourfold way is a direct diabatization method for converting adiabatic electronic wave functions to diabatic ones and computing the diabatic potential energy surfaces and couplings. The key steps are to compute DMOs, to re-express the adiabatic states in terms of DMOs, and to use the re-expressed states to compute the adiabatic-to-diabatic transformation by configurational uniformity. We previously presented algorithms for applying this method to compute both CASSCF diabatic states and MC-QDPT diabatic states. The latter algorithm was based on DMOs determined using the eigenvectors of the effective Hamiltonian that underlies the MC-QDPT calculation. Here

we present an algorithm in which the MC-QDPT diabatic states are expressed in terms of the CASSCF DMOs; this simplifies the treatment and, more importantly, it was motivated by our observation that the CASSCF DMOs tend to be smoother than the DMOs that result from the more complicated MC-QDPT procedure. The quality of the diabatic states is not compromised by using the CASSCF DMOs because the new diabatic states still span the same space as the *N* MC-QDPT adiabatic states that they replace. We illustrate the method on two test cases, the dissociation of LiF and the reaction of Li with HF to yield LiF + H. With the inclusion of dynamical correlation, the results obtained by both the original MC-QDPT diabatization scheme and our new scheme improve over those obtained by the CASSCF diabatization, giving more realistic ionic-covalent crossing distances for LiF and smaller reaction barriers for Li + FH. The results with our new scheme are quite similar to those obtained with the original MC-QDPT diabatization scheme, which is more complicated, validating the new scheme and suggesting that it would be a good choice for nonadiabatic dynamics studies in the future.

3.5 References

1 M. S. Child, in *Atom-Molecule Collision Theory*, edited by R. B. Bernstein (Plenum, New York, 1979), p. 427-465.

2 A. W. Jasper, B. K. Kendrick, C. A. Mead, D. G. Truhlar, in *Modern Trends in Chemical Reaction Dynamics*, edited by X. Yang, K. Liu (World Scientific, Singapore, 2003), p. 329-391.

3 C. A. Mead and D. G. Truhlar, J. Chem. Phys. **77**, 6090 (1982).

4 H. Nakamura and D. G. Truhlar, J. Chem. Phys. **115**, 10353 (2001).

5 H. Nakamura and D. G. Truhlar, J. Chem. Phys. **117**, 5576 (2002).

6 H. Nakamura and D. G. Truhlar, J. Chem. Phys. **118**, 6816 (2003).

[7] S. Nangia and D. G. Truhlar, J. Chem. Phys. **124**, 124309 (2006).
[8] Z. H. Li, R. Valero, and D. G. Truhlar, Theor. Chem. Acc. **118**, 9 (2007).
[9] D. Bonhommeau and D. G. Truhlar, J. Chem. Phys. **129**, 14302 (2008).
[10] D. Bonhommeau, R. Valero, D. G. Truhlar, A. Jasper, J. Chem. Phys. **130**, 234303 (2009).
[11] R. Valero and D. G. Truhlar, J. Chem. Phys. **125**, 194305 (2006).
[12] R. Valero, D. G. Truhlar, and A. W. Jasper, J. Phys. Chem. A **112**, 5756 (2008).
[13] R. Valero and D. G. Truhlar, J. Chem. Phys.**137**, 22A539 (2012).
[14] P. Siegbahn, A. Heiberg, B. O. Roos, and B. A. Levy, Phys. Scripta **21**, 323 (1980).
[15] B. O. Roos, P. R. Taylor, and P. E. M. Siegbahn, Chem. Phys. **48**, 157 (1980).
[16] K. Ruedenberg, M. W. Schmidt, G. M. Gilbert, and S. T. Elbert, Chem. Phys. **71**, 41 (1982).
[17] H. Nakano, J. Chem. Phys. **99**, 7983 (1993).
[18] H. Nakano, Chem. Phys. Lett. **207**, 372 (1993).
[19] J. Finley, P.-Å. Malmqvist, B. O. Roos, and L. Serrano-Andrés, Chem. Phys. Lett. **288**, 299 (1998).
[20] K. Andersson, P.-Å. Malmqvist, B. O. Roos, A. J. Sadlej, and K. Wolinski, J. Phys. Chem. **94**, 5488 (1990).
[21] K. Andersson, P.-Å. Malmqvist, and B. O. Roos, J. Chem. Phys. **96**, 1218 (1992).
[22] K. Hirao, Chem. Phys. Lett. **190**, 374 (1992).
[23] P. M. Kozlowski and E. R. Davidson, Chem. Phys. Lett. **222**, 615 (1994).
[24] N. I. Gidopoulos and E. K. U. Gross, arXiv:cond-mat/0502433.
[25] A. Granovsky, J. Chem. Phys. **134**, 214113 (2011).
[26] T. Shiozaki, W. Győrffy, P. Celani, and H.-J. Werner, J. Chem. Phys. **135**, 81106 (2011).
[27] C. Woywod, W. Domcke, A. L. Sobolewski, and H.-J. Werner, J. Chem. Phys. **100**, 1400 (1994).
[28] M. S. Topaler, D. G.Truhlar, X. Y. Chang, P. Piecuch, and J. C. Polanyi, J. Chem. Phys. **108**, 5349 (1998).
[29] H. Lischka, M. Dallos, P. G. Szalay, D. R. Yarkony, and R. Shepard, J. Chem. Phys. **120**, 7322 (2004).
[30] G. J. Atchity and K. Ruedenberg, Theor. Chem. Acc. **97**, 47 (1997).
[31] L. R. Kahn, P. J. Hay, and I. Shavitt, J. Chem. Phys. **61**, 3530 (1974).
[32] H. Nakamura, J. D. Xidos, et al., HONDOPLUS-v5.2, based on HONDO–v99.6, University of Minnesota, Minneapolis, MN, 2013.

[33] HONDO 99.6, by M. Dupuis, A. Marquez, E. R. Davidson, 1999, based on HONDO 95.3, by M. Dupuis, A. Marquez, E. R. Davidson, Quantum Chemistry Program Exchange (QCPE), Indiana University, Bloomington, IN.
[34] R. Krishnan, J. S. Binkley, R. Seeger, and J. A. Pople, J. Chem. Phys. **72**, 650 (1980).
[35] M. J. Frisch, J. A. Pople, and J. S. Binkley, J. Chem. Phys. **80**, 3265 (1983).
[36] R. Grice and D. R. Herschbach, Mol. Phys. **27**, 159 (1974).
[37] F. Sasaki and M. Yoshimine, Phys. Rev. A **9**, 26 (1974).
[38] A. W. Jasper, M. D. Hack, D. G. Truhlar, and P. Piecuch, J. Chem. Phys. **116**, 8353 (2002).

Figure captions:

Figure 3.1. Potential energy curves of the two lowest $^1\Sigma^+$ states of LiF. V_1 and V_2 are adiabatic energies; U_{11} and U_{22} are diabatic energies; and U_{12} is the diabatic coupling. We take the zero of energy as the ground-state energy of the dissociation limit. (a) diabatization with CASSCF DMOs and CASSCF wave functions; (b) diabatization with MC-QDPT DMOs and MC-QDPT wave functions; (c) diabatization with CASSCF DMOs and MC-QDPT wave functions.

Figure 3.2.Potential energy curves of the two lowest doublet states of LiFH along the reaction path at a Li-F-H angle γ of 120.0°. We chose the ground state energy of the reactant asymptote, Li(^2S) + HF($^1\Sigma^+$), as the zero reference energy. V_1 and V_2 are adiabatic energies; U_{11} and U_{22} are diabatic energies; and U_{12} is the diabatic coupling. (a) diabatization with CASSCF DMOs and CASSCF wave functions; (b) diabatization with MC-QDPT DMOs and MC-QDPT wave functions; (c) diabatization with CASSCF DMOs and MC-QDPT wave functions**.**

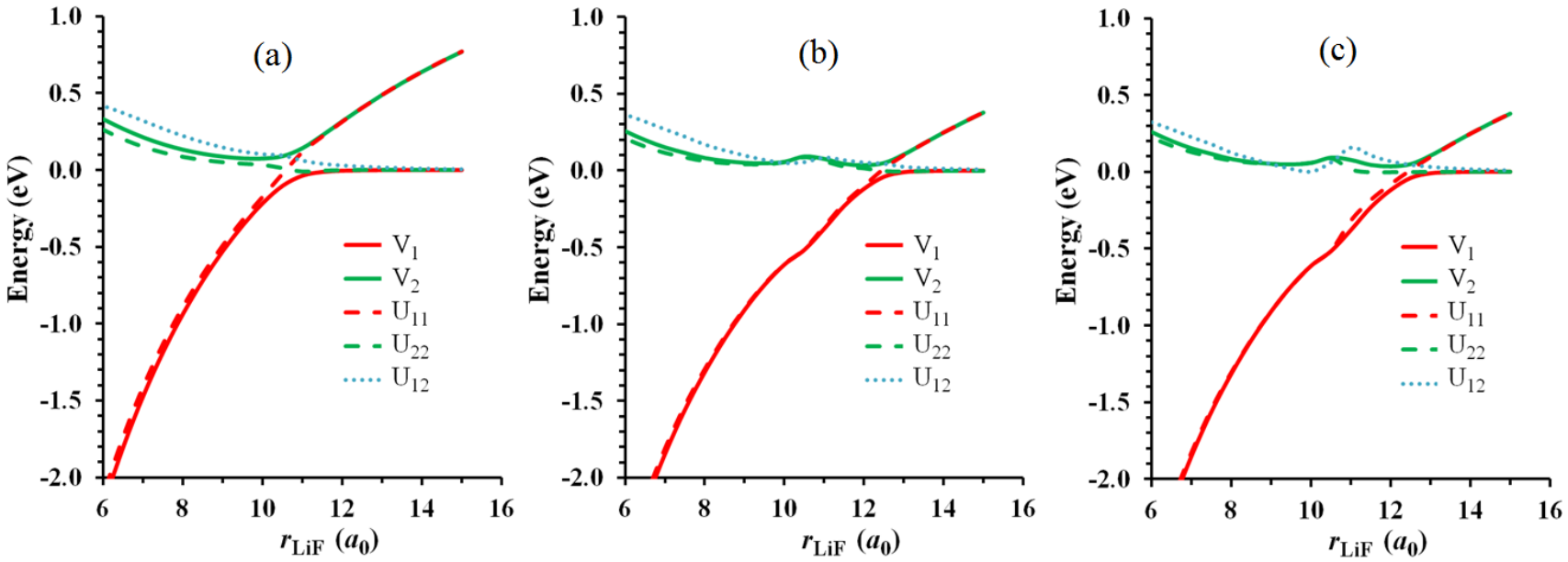

Figure 3.1. Potential energy curves of the two lowest $^1\Sigma^+$ states of LiF. V_1 and V_2 are adiabatic energies; U_{11} and U_{22} are diabatic energies; and U_{12} is the diabatic coupling. We take the zero of energy as the ground-state energy of the dissociation limit. (a) diabatization with CASSCF DMOs and CASSCF wave functions; (b) diabatization with MC-QDPT DMOs and MC-QDPT wave functions; (c) diabatization with CASSCF DMOs and MC-QDPT wave functions.

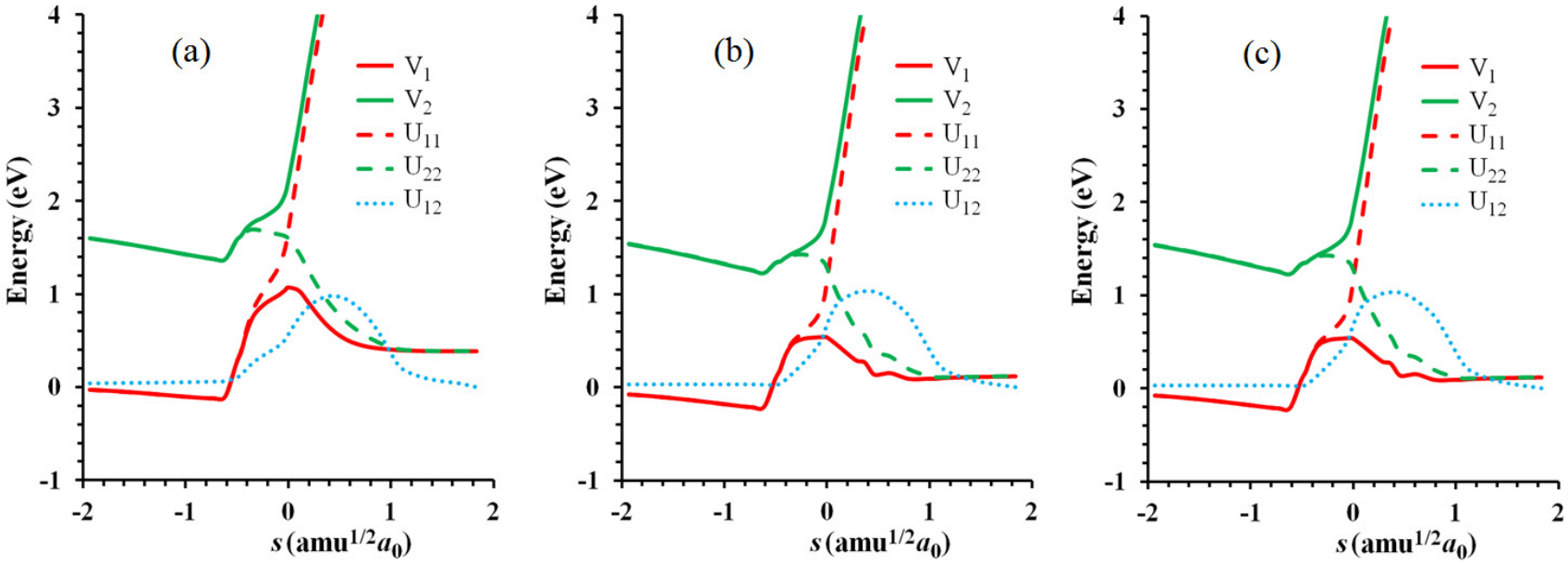

Figure 3.2.Potential energy curves of the two lowest doublet states of LiFH along the reaction path at a Li-F-H angle γ of 120.0°. We chose the ground state energy of the reactant asymptote, Li(^2S) + HF($^1\Sigma^+$), as the zero reference energy. V_1 and V_2 are adiabatic energies; U_{11} and U_{22} are diabatic energies; and U_{12} is the diabatic coupling. (a) diabatization with CASSCF DMOs and CASSCF wave functions; (b) diabatization with MC-QDPT DMOs and MC-QDPT wave functions; (c) diabatization with CASSCF DMOs and MC-QDPT wave functions.

Chapter 4. Diabatic Molecular Orbitals, Potential Energies, and Potential Energy Surface Couplings by the Fourfold Way for Photodissociation of Phenol

Adapted with permission from Xuefei Xu, Ke R. Yang, and Donald G. Truhlar, J. Chem. Theory Comput. **9**, 3612 (2013).

4.1 Introduction

Photodissociation of phenol to phenoxyl radical and hydrogen atom is a well-studied photochemical reaction in which nonadiabatic transitions and conical intersections (CIs) of potential energy surfaces (PESs) play important roles. In 2002, Sobolewski and Domcke[1] first revealed the importance of the dark $^1\pi\sigma^*$ state in the photoinduced O–H fission process. The PES of the higher-energy $^1\pi\sigma^*$ state (1A´´ in C_s symmetry) undergoes two symmetry-allowed crossings along the hydrogen detachment reaction coordinate of phenol, first with the bright $^1\pi\pi^*$ state (2A´ in C_s symmetry), then with the electronic ground state $^1\pi\pi$ (1A´ in C_s symmetry). The two symmetry-allowed crossings of PESs for planar geometries are potions of conical intersection seams that also extend to nonplanar geometries,[2] and they are expected to play prominent roles in photodissociation.

In the past ten years, both theoretical and experimental methods have been used for in-depth investigation of the roles of these two CIs in the phenol photodissociation

dynamics and determining the vibrational modes most strongly coupled to the $^1\pi\sigma^*$ state, which is the only state connecting diabatically upon dissociation to ground-state phenoxyl plus a hydrogen atom. Although the $^1\pi\sigma^*$ state of phenol is not be populated directly, at high enough photoexcitation energy it can be accessed through the CI with the bright $^1\pi\pi^*$ state. There is, however, controversy over the early time dynamics after phenol is excited to $v = 0$ level of the first $^1\pi\pi^*$ state. Considering the high energy barrier separating the originally excited system from the first CI ($^1\pi\pi^*/^1\pi\sigma^*$), one mechanism suggested is $^1\pi\pi^* \dashrightarrow (^1\pi\pi)^\#$ internal conversion (IC) from the first excited state $^1\pi\pi^*$ to the vibrationally excited ($^\#$) ground state ($^1\pi\pi$), with O-H vibrations as efficient acceptor modes, followed by predissociation along the ground-state PES as the dominant non-radiative decay process.[3] An alternative mechanism is H atom tunneling to the $^1\pi\sigma^*$ state through the barrier on the shoulder of the $^1\pi\pi^*/^1\pi\sigma^*$ CI.[1,4] Recent experimental studies of the dependence of the $^1\pi\pi^*$ state lifetimes of bare phenol and several substituted phenols on the energy gaps between $^1\pi\pi^*$ and $^1\pi\sigma^*$ state by Pino[4c] are the strongest supports for the H tunneling mechanism via a $^1\pi\pi^*/^1\pi\sigma^*$ CI, because the $^1\pi\pi^*$ state lifetime should be independent on the properties of $^1\pi\sigma^*$ state based on the $^1\pi\pi^* \dashrightarrow (^1\pi\pi)^\#$ IC mechanism. The recent Faraday Discussion[4e] offers further evidence against the $^1\pi\pi^* \dashrightarrow (^1\pi\pi)^\#$ ground-state predissociation mechanism: the similar reaction dynamics of the isolated phenol molecule to that in liquid cyclohexane, i.e., long lifetime of the first excited state and slow appearance of phenoxyl radical (on a nanosecond timescale).

Because the solvent will cause fast (sub-nanosecond) vibrational energy relaxation, the late (nanosecond) appearance of phenoxyl radical cannot be explained by the ground-state predissociation mechanism, and this indirectly supports the H tunneling dissociation mechanism.

The mechanism of the early time dynamics through nonadiabatic $^1\pi\pi^*/^1\pi\sigma^*$ coupling or $^1\pi\pi^* \dashrightarrow (^1\pi\pi)^{\#}$ internal conversion will have a large effect on the later dynamics, including the final branching ratio of the products. The second CI ($^1\pi\sigma^*/^1\pi\pi$) in the later stage of the dynamics will also exert some influence on the branching ratios of the products.

The coupling modes of CIs are another focus of dynamics studies of phenol dissociation.[3-6] The two CIs ($^1\pi\pi^*/^1\pi\sigma^*$, $^1\pi\sigma^*/^1\pi\pi$) of the three states of interest along the H detachment coordinates under C_s symmetry are both symmetry-allowed intersections because the $^1\pi\sigma^*$ state is A´´ symmetry whereas the $^1\pi\pi^*$ and $^1\pi\pi$ states are of A´ symmetry for planar phenol. Nonadiabatic transitions between the two states at the two CIs are therefore mediated in planar geometries by a´´ vibrational modes. Ashfold et al.[3c,3d] assigned the out-of-plane ring vibrations ν_{16b} (a´´) and ν_{16a} (a´´) as the dominant coupling modes for the $^1\pi\pi^*/^1\pi\sigma^*$ CI and the $^1\pi\sigma^*/^1\pi\pi$ CI, respectively, by identification of product (phenoxyl radical) vibrational states. Vieuxmaire and Lan et al.[4a,5] suggested the C–C–O–H torsion as the strongest coupling mode for both the two CIs based on their ab initio calculations of PESs along each of all ten normal modes coordinates of a´´ symmetry of phenol at the CIs. They argued[4a] that C–C–O–H torsion is

a disappearing mode for product phenoxyl radical that Ashfold et al. had ignored it in the analysis of the total kinetic energy release (TKER) spectrum. In a recent study Dixon et al.[4d] took into account the two-fold torsional degeneracy of phenol and reconsidered the coupling modes of these states at the CIs in light of the non-rigid molecular symmetry group G_4 (which is isomorphous with C_{2v}). The electronic symmetries of the three states ($^1\pi\pi$, $^1\pi\pi^*$, and $^1\pi\sigma^*$) of interest are A_1, B_2 and B_1 in the group G_4. This symmetry argument led to the conclusion that only vibrational modes with a_2 symmetry can enable coupling of the states at the $^1\pi\pi^*/^1\pi\sigma^*$ CI, and b_1 modes can enable coupling at the $^1\pi\sigma^*/^1\pi\pi$ CI. Based on the measured TKER spectrum and 2D dynamics calculations, they assigned ν_{16a} (a_2 in G_4) as the dominant coupling mode for the $^1\pi\pi^*/^1\pi\sigma^*$ CI. Such symmetry considerations also invalidated the hypothesis of ν_{16a} as the coupling mode of CI ($^1\pi\sigma^*/^1\pi\pi$) and C–C–O–H torsion (b_1 in G_4) as coupling mode of CI ($^1\pi\pi^*/^1\pi\sigma^*$). Dixon et al. said that "Within G_4, the b_1 torsional mode has two components separated by an angle of 180° and a high potential barrier. In calculating the $\left\langle {}^1\pi\pi^* \middle| H' \middle| {}^1\pi\sigma^* \right\rangle$ matrix element for torsional coupling, the phases of these two components are such that they exactly cancel."[4d] At the same time they emphasized that the two components reinforce each other at the lower CI ($^1\pi\sigma^*/^1\pi\pi$).

Wave packet studies of the phenol photodissociation process have been carried out,[3f,4a,4d,5,6] usually using two-dimensional PESs that are functions of the R_{O-H} reaction coordinate and a selected coupling coordinate. The conclusions of theoretical

dynamics studies of the nonadiabatic process are strongly dependent on the assumptions made about the global PESs. Therefore it is desirable to use full-dimensional PESs obtained from electronic structure calculations with less simplifications.

In modeling an electronically nonadiabatic process where two or more electronic states are coupled via BO breakdown terms, one can choose either an adiabatic or a diabatic representation for the potential energy surfaces and their couplings.[7] The well-defined adiabatic representation can be obtained directly from variational or other conventional electronic structure calculations, which is convenient; however, adiabatic PESs have high-dimensional cuspidal ridges in ubiquitous[8] conical intersection regions. Furthermore, in the adiabatic basis, the nonadiabatic couplings are off-diagonal matrix elements of the nuclear momentum vector (and its square) and are often rapidly varying and have singularities on conical intersection seams.[9,10] The cuspidal ridges and singularities have high dimensionality and are not symmetry determined, and this makes analytical representations (fits) essentially impossible. The nonadiabatic couplings in the adiabatic representation also require special attention to the choice of coordinate system origin and to avoiding spurious long-range effects,[11] and they require consistent treatment of momentum and momentum-squared couplings in regions where the couplings are large. The inconveniences (even failure for some process[12]) in using adiabatic bases make diabatic representations preferable for dynamics studies, and interest in diabatic states is increasing.[13-29] A diabatic representation can be obtained by rotating the adiabatic electronic states to diabatic states in electronic state space via a

unitary transformation to make the nonadiabatic coupling negligibly small compared to the off-diagonal elements of the electronic Hamiltonian matrix (the diabatic couplings). Strictly speaking, the diabatic states based on this definition should be called quasidiabatic states because the strict diabatic states are electronic states with vanishing nonadiabatic vector coupling; however such strict diabatic states do not exist in general[30] because the curl condition[31] for their existence cannot be satisfied. We are following the common convention of labeling quasidiabatic states as diabatic states; in particular a diabatic representation "is any electronic representation where the nuclear momentum matrix elements are less significant than the off-diagonal matrix elements of the electronic Hamiltonian or, preferably, insignificant compared to these."[34a] A diabatic representation provides smooth PESs, and smooth, nonsingular, scalar couplings with the acceptable disadvantage of neglecting some portion of the coupling.[10] It can be shown[32] that by transforming to a diabatic representation, even one that does not remove all of the removable nuclear momentum coupling,[33] one can obtain results where the leading correction to the wave function at energies of interest for photochemistry is of order $M^{-1/2}$, where M is the ratio of an average nuclear mass to the electron mass (thus $M^{-1/2} < 0.024$).

Diabatic representations are not unique, and there are many methods to calculate diabatic states.[7,12-35] In the present work we will chose the fourfold-way approach[34,35] which is based on the principle of configurational uniformity,[36] to perform direct calculations of diabatic states for the three states ($^1\pi\pi$, $^1\pi\pi^*$, and $^1\pi\sigma^*$) of interest for the

photolysis PESs of phenol and their couplings. The fourfold way is a general diabatization scheme based on configurational smoothness (configurational uniformity), and it is designed to require only information obtained from adiabatic wave functions without estimation of any other physical property; it takes advantage of the variational principle or perturbation theory for electronically adiabatic states to optimize the space spanned by the set of electronic wave functions under consideration, and it yields a unique (within a phase factor) diabatization for each nuclear geometry independent of any path in configuration space. The fourfold-way algorithm now is available both for diabatization of complete-active-space (CAS) self-consistent-field (CASSCF)[37] wave functions and for more accurate diabatization of multi-configuration quasi-degenerate perturbation theory (MC-QDPT)[38] wave functions, which include dynamical correlation. Including dynamical correlation is essential for quantitative or semiquantitative accuracy, and the original diabatization scheme for MC-QDPT diabatic states employed diabatic molecular orbitals (DMOs) based on the dynamically correlated wave function. Recently[35] it was shown that MC-QDPT diabatization can be achieved with CASSCF DMOs, and in the present article we show that one can obtain MC-QDPT diabatic states with CASSCF DMOs even for phenol photodissociation, which is complex for the reasons discussed above and also because the extent of delocalization of various orbitals depends on geometry.

4.2 Computational details

The ground state minimum of phenol has been optimized by the complete active space self-consistent-field (CASSCF) method using the aug-cc-pVTZ basis set.[39] The active space includes 12 active electrons and 11 active orbitals consisting of three π, three π*, σ_{CO}, σ_{OH}, σ^*_{CO}, and σ^*_{OH} orbitals, and one lone pair orbital (p_z) on oxygen as shown in Fig. 4.1 (phenol is placed in the *xy* plane); we label this calculation CAS(12,11). The optimized equilibrium geometry of phenol is a planar structure with C_s symmetry. The adiabatic PESs of the three states of interest (which are $^1\pi\pi$, $^1\pi\pi^*$, and $^1\pi\sigma^*$ in the vicinity of the equilibrium structure of phenol), have been calculated along the H detachment reaction coordinate, $R_{O-H,}$ and the C–C–O–H torsion coordinate by using the state-averaged CASSCF method with the same weights for each state, denoted as SA(3)-CAS(12,11) with the jul-cc-pVDZ[40] basis set. The other geometric parameters in the calculations of cuts of PESs are fixed at their values at the equilibrium geometry.

Taking the resulting SA(3)-CAS(12,11) wave functions as the reference, the MC-QDPT method was used to include the dynamical correlations effects, denoted as SA(3)-MCQDPT(12,11). A reasonable value 0.02 E_h^2 of the intruder-state-avoidance (ISA)[41] energy denominator shift has been used in all MC-QDPT calculations. The corresponding diabatic states and couplings were obtained by the fourfold way at the MC-QDPT level with CASSCF DMOs. The procedure of diabatization will be reviewed and details will be presented in the subsection 4.2.1.

Ground-state geometry optimizations of phenol and phenoxyl were performed using the *GAMESS*[42] program package, and all other adiabatic and diabatic calculations were done using the *HONDOPLUS-v*5.2[43] program package.

4.2.1 Fourfold-way diabatization procedure

The diabatization scheme and theory of the fourfold way have been presented in detail in previous papers.[34,35] Here, we only review the key concepts and present the application of the fourfold way to phenol photodissociation.

4.2.1.1 Diabatic molecular orbitals (DMOs)

To apply the configurational uniformity approach to obtain suitable diabatic states, the configuration state functions (CSFs) should be expressed in terms of smoothly varying molecular orbitals (MOs), which are called diabatic MOs (DMOs). The DMOs for the inactive and virtual spaces are taken to be the same as the canonical MOs (CMOs) of the CASSCF calculation, and those for the active space, denoted $\{ u_j, j = 1, 2, \cdots, N_{\text{active}} \}$ where N_{active} is the number of active orbitals, are obtained by transforming the active CMOs by orbital rotations determined in a systematic way by a scheme called the ***fourfold way***.

The orbitals generated by the fourfold way satisfy the threefold density criterion and, when needed, the maximum overlap reference MOs (MORMO) criterion. The threefold density criterion is often insufficient to ensure that the DMOs change smoothly in the strong-interaction regions, especially when multiple nonbonding p orbitals are

involved. In such cases, which include phenol photodissociation, the MORMO criterion also has to be applied. In general the MORMO criterion involves λ reference MOs $\{ u_\tau^{\mathrm{ref}}, \tau = 1, 2, \cdots, \lambda \}$, which are a subset of DMOs at a reference geometry, called the MORMO reference geometry (Q^{ref}). For phenol, we use $\lambda = 1$ (so we now drop the subscript τ), and in the present work the single reference MO is taken to be the oxygen p_y orbital of a phenoxyl radical that is essentially infinitely separated from H (in practice, the O–H distance is equal to 5 Å with the phenyl ring in the *xy* plane with the *x* axis along the C–O bond). The reference orbital $u^{\mathrm{ref}}(Q)$ at any other geometry (Q) is defined as

$$u^{\mathrm{ref}}(Q) = \sum_i a_i(Q)\xi_i(Q) \tag{4.1}$$

where $\xi_i(Q)$ is an atomic (contracted) basis function at the geometry Q, and $a_i(Q)$ is a coefficient that depends on Q. Because the DMOs are numbered to have maximum likeness to the active canonical MOs at the reference geometry, and the oxygen p_y orbital is most similar to the first active canonical orbital at the equilibrium structure of phenol (where the first active canonical orbital of phenol, by which we mean the lowest-energy active orbital, is a bonding combination of O p_y and the H 1s orbital), we use the reference oxygen p_y orbital as to determine the DMO with $j = 1$, that is, to determine $u_1(Q)$. This is accomplished by determining the $a_j(Q)$ to maximize

$$D^{\mathrm{RO}} = \left| \sum_i \sum_j a_i(Q^{\mathrm{ref}}) a_j(Q) \left\langle \xi_i(Q) \middle| \xi_j(Q) \right\rangle \right|^2, \tag{4.2}$$

which is called the reference overlap (RO) term. The remaining DMOs, u_j, $j = 2, 3, \cdots, 11$, are then determined by maximizing (in the remaining space) the threefold density functional

$$D_3 = \alpha_N D^{\mathrm{NO}} + \alpha_R D^{\mathrm{ON}} + \alpha_T D^{\mathrm{TD}}, \tag{4.3}$$

which involves a weighted sum of three functionals with weights α_N, α_R, and α_T. The functionals are a state-averaged natural orbital term (D^{NO}), the sum of the squares of the orbital occupation numbers for all the states (D^{ON}), and a transition density term (D^{TD}). The meaning of the terms in the D_3 functional and the importance of the RO term with respect to the D_3 functional are explained in the original papers[34] and are reviewed in the next paragraph.

Equation 4.3 is called the threefold density criterion, and the use of eq 4.2 with eq 4.3 is called the fourfold way. The physical meaning of the terms in eqs 2 and 3 are as follows. Maximizing D^{NO} by itself would yield the state-averaged natural orbitals (SANOs), maximizing D^{ON} by itself would maximize the sum of the squares of the occupation numbers of the molecular orbitals in the adiabatic states, maximizing D^{TD} corresponds to minimizing the sum of the squares of the off-diagonal elements of the transition density matrix, and maximizing D^{RO} with a valence bond reference orbital would correspond to introducing some valence bond character into the diabatic states. The use of the first three of these functionals was motivated in part by the work of García et al.,[44] who showed the quasidiabatic character of state-averaged natural orbitals

(SANOs) in selected cases, by the work of Atchity and Ruedenberg[36a] who used the fact diabatic orbitals can sometimes be obtained by maximizing the occupation number, and by our own work[34a] that showed that maximizing D^{TD} corresponds to recognizing that the diabatic MOs should provide a more economical expansion of the adiabatic states. Furthermore, the use of D^{RO} is based on the recognition that neglecting the nuclear momentum and kinetic energy coupling due the gradient and Laplacian acting on electronic basis functions that simply translate with nuclei provides a consistent scheme for obtaining physically reasonable nonadiabatic couplings at chemical energies.[30,45-48] However we found[34] that maximization of any of these four terms by itself did not yield useful diabatic molecular orbitals in the general case, whereas using the linear combination of eq 4.3 (with parameters α_N, α_R, and α_T of the order of magnitude unity) combined with the pre-determination of one or a few DMOs by eq 4.2 does very generally yield reasonable DMOs.

We consider that the occupation number term (D^{ON}) is a refinement of the natural orbital term (D^{NO}), so it is recommended that α_R be smaller than α_N. The transition density term (D^{TD}) is generally less important than the other two terms, and for some cases, α_T should be set as 0 to avoid unphysical contributions. Although the parameters α_N, α_R, and α_T in eq 4.3, were introduced for flexibility, it was recommended that values of 2, 1, and 0.5 respectively provide a reasonable starting point for trials on new systems, and in practical applications we have found that these values

are usually adequate and need not be changed. (In particular, the three parameters have been set to the standard values[34] of 2, 1, and 0.5 in the application to phenol.)

Some additional comments on the D^{RO} term may be worthwhile at this point. Use of the threefold density criterion may be called[49] an intrinsic procedure in that it finds the DMOs by analyzing the adiabatic wave functions (by way of the adiabatic density matrices that may be computed from the adiabatic wave functions) with a self-contained procedure, whereas the D^{RO} term may be called extrinsic[49] because (like the block diagonalization method of Pacher, Cederbaum. and Köppel,[48] in which one begins with an "initial basis" that is known to behave diabatically) it presupposes that one has identified one or more valence-bond-like orbitals as DMOs having significant overlap with the occupied orbitals in the dominant configurations. Extrinsic methods are in our opinion less desirable because, rather than simply requiring application of a system-independent automatic algorithm, they require system-dependent judgments about nearly diabatic orbitals that are appropriate for describing the diabatic configurations of interest; and therefore we always attempt to employ the minimum number of reference MOs. However, all three terms of D_3 are functionals of the state-dependent one-electron density matrices and the one-electron transition density matrices, and we have shown that it is impossible to design a functional of these matrices alone that will yield acceptable DMOs in the general case,[34a] so it is not possible to completely exclude the need for D^{RO} in some cases. Fortunately we have found that one can usually obtain acceptable results with a very small number of reference orbitals, often just one or two. The most common

case encountered so far where one has to introduce reference orbitals is when one has two or more nonbonding orbitals on the same non-spectator center, such as found in photodissociations producing halogen atoms, OH radicals, or NH_2 radicals. In such cases the reference orbital prevents non-smooth mixing of these nonbonding orbitals. (This problem arises because such a pair of orbitals, for some geometries, is special case of a pair of orbitals with nearly degenerate state-averaged occupation numbers.[34a]) The need for an extrinsic algorithm is perhaps not surprising since the treatment of intrinsically multiconfigurational systems or excited states usually requires some judgment, such as, for example, the choice of active space and the choice of states to be averaged over in CASSCF calculations.

After the DMOs are determined by the fourfold way, we express all CSFs in terms of DMOs rather than canonical MOs, and then we define the diabatic prototype CSFs.

4.2.1.2 Diabatic prototype CSFs

In the fourfold way diabatization scheme we need to define one or more potential reference geometries to construct dominant CSF lists for the diabatic states of interest by calculating adiabatic states at these geometries. These geometries may be called prototype-selection geometries. The CSFs in the group G_k are prototypes of the diabatic state ϕ_k. The group list G_k should remain the same for all nuclear geometries, however, the dominant CSFs in G_k are not necessarily always dominant for ϕ_k, but at least one

CSF of G_k is dominant for ϕ_k in any nuclear geometry. A dominant CSF χ_δ belonging to the group G_k must not be dominant for any other diabatic state $\phi_{k'}(k' \neq k)$ at any geometry. The potential reference geometries are usually chosen in weak-interaction regions where adiabatic states are, to a good approximation, the same as diabatic states. For planar phenol, due to the symmetries of the states, there is no interaction between the PESs of $^1\pi\pi^*$ and $^1\pi\sigma^*$ or between the $^1\pi\sigma^*$ and $^1\pi\pi$ PESs, even in their crossing regions. Therefore, in the present work, we choose the ground-state equilibrium geometry of phenol in C_s symmetry and two geometries respectively in middle and asymptotic regions of H detachment of phenol with only different OH distances ($R_{O–H}$ = 1.3, 5.0 Å) compared to the equilibrium geometry ($R_{O–H}$ = 0.964 Å at CASSCF level) as prototype geometries to construct the consistent diabatic prototype CSF lists by combining the dominant CSFs of adiabatic states at all three prototype-selection geometries. The resulting diabatic prototype CSF lists are shown in Table 4.1.

The U_2 state obtained in the adiabatic-to-diabatic transformation requires some discussion. To understand this state, recall that a key desirable feature of our diabatization is that our diabatic states span in the same space as the selected adiabatic states. The third adiabatic state at large $R_{O–H}$ has an intersection with the fourth one at an energy above 6 eV. But this high-energy region is not important for understanding the mechanistic issues reviewed in the introduction. Thus rather than add a fourth state to the manifold studied, we simply let the U_2 diabatic state be the union of the second diabatic

state at small R_{O-H} with the new diabatic state appearing at high energy at large R_{O-H}. This should have a negligible effect on the dynamics under consideration, but it does mean that the U_2 diabatic state has a long diabatic prototype list consisting of the union of the state lists for two configurationally uniform states. It also means that the diabatic couplings involving U_2 are not smooth at geometries corresponding to this intersection of the third and fourth adiabatic states, but again this is not important because at those geometries U_2 is not important to the dynamics under consideration. This kind of behavior can be expected to be a rather universal phenomenon when one calculates global potential energy surfaces. In a typical case, the first adiabatic state would somewhere intersect the second, the second would somewhere intersect the third, and so forth up to the Nth adiabatic state that would somewhere intersect the $(N + 1)$st. Thus we would need (at least) $N + 1$ diabatic states to represent the first N adiabatic states. If the intersection of states N and $N + 1$ occurs in an energetically accessible and important dynamical region, we should add one more state to the manifold, pushing the problem higher up until it occurs at such a high energy that it is not important to have accurate surfaces at the last intersection. In the present case, the surfaces above 6 eV are not expected to be important for the mechanistic issues discussed in the introduction, so three states are enough.

4.2.1.3 Configurational uniformity

We obtain N diabatic states $\{\phi_k\}_{k=1\cdots N}$ by orthogonal transformation of the N adiabatic states $\{\psi_n\}_{n=1\cdots N}$ as follows:

$$\phi_k = \sum_{n=1}^{N} \psi_n T_{nk} \,, \tag{4.4}$$

where T_{nk} is an element of the orthogonal adiabatic/diabatic transformation matrix that is obtained by configurational uniformity. This involves projecting the adiabatic CSFs onto the prototype lists and transforming to states that maximize the dominance of the diabatic prototypes. This configurational uniformity criterion can be applied at any geometry, yielding diabatic states that span same function space as the adiabatic states and also yielding a nondiagonal scalar diabatic potential matrix **U** replacing the adiabatic potentials **V** and the vectors that couple them.

In the present case for phenol, $N = 3$. The adiabatic states are expressed by CI expansions in terms of L orthonormal configuration state functions (CSFs) χ_α as

$$\psi_n = \sum_{\alpha=1}^{L} c_{\alpha n} \chi_\alpha \,. \tag{4.5}$$

4.2.2 MC-QDPT diabatization with CASSCF DMOs

Recently, a simplified scheme[35] for MC-QDPT fourfold-way diabatization was proposed: first, use the fourfold way at the CASSCF level to obtain CASSCF DMOs, then use these CASSCF DMOs to express the MC-QDPT adiabatic states:

$$\psi_n^{\mathrm{MQ}} = \sum_{\alpha=1}^{L_{\mathrm{CAS}}} c_{\alpha n}^0 \chi_\alpha^0 + \sum_{\alpha=L_{\mathrm{CAS}}+1}^{L} c_{\alpha n}^0 \chi_\alpha^0 \qquad (4.6)$$

where χ_α^0 is a CSF expressed in terms of CASSCF DMOs for the active space and CMOs for the inactive and virtual spaces, L_{CAS} is the number of CSFs in the CAS configuration space, and L is the total number of CSFs. For the present application, the value of L_{CAS} in eq 4.6 is 60984 for all geometries of phenol. With the predefined dominant CSF lists and the coefficients in eq 4.6, we calculate the adiabatic/diabatic transformation matrix and do the diabatization of MC-QDPT adiabatic states. Compared to the original scheme of MC-QDPT diabatization, which only uses CASSCF DMOs as initial MOs in the MC-QDPT calculations and needs to determine the final DMOs at the MC-QDPT level, this new scheme simplifies the treatment without compromising the quality of the diabatic states.

4.3 Results and discussion

The calculated vertical excitation energies of the $^1\pi\pi^*$ and $^1\pi\sigma^*$ states are shown and compared to previous theoretical[4d,5] and experimental results[50,51] in Table 4.2. This table shows that SA(3)-CAS(12/11) calculations overestimate the vertical excitation energy of the $^1\pi\pi^*$ state. The vertical excitation energy (4.70 eV) of the $^1\pi\pi^*$ state obtained by SA(3)-MCQDPT(12,11)/jul-cc-pVDZ in the present study is comparable to the other high-level theoretical results that include both dynamical and static correlations, and it is only 0.12 eV higher than the experimental highest peak value (4.58 eV) of the

spectrum of the $^1\pi\pi^*$ state in hexane.[50] The present MC-QDPT calculations significantly overestimate the vertical excitation energy (5.86 eV) of the $^1\pi\sigma^*$ state compared to the experimental data[51] (5.12 eV), but the result is comparable to the other high-level theoretical results (5.64–5.76 eV) with larger basis sets. One advantage of working in the diabatic representation is that it would be much easier to make an empirical correction for such systematic errors when fitting analytical potentials for dynamics when one is working in a diabatic representation than when one is working in the adiabatic one.

Table 4.2 also shows the equilibrium bond dissociation energy of the O–H bond of phenol and the vertical excitation energies of the D_1 and D_2 doublet excited states of phenoxyl radical relative to its ground state D_0, which is also a doublet. The ground state D_0 has a singly occupied π orbital delocalized on both the phenyl ring and the p_z π orbital of O. The first excited state D_1 is an excitation of that orbital to a p_y σ orbital on O; and the second excited state D_2 is a single-electron excitation of a π orbital of the ring (the highest doubly occupied orbital in the ground state) to the singly occupied orbital of the ground state. The MC-QDPT values of the bond dissociation energy of phenol and excitation energies of phenoxyl are comparable to the experimental values.[52-57] A larger basis set would be expected to improve the present SA(3)-MCQDPT(12,11) results; however, for the purpose of demonstrating the ability to make a successful diabatic transformation, semiquantitative accuracy is sufficient, and we will continue to use the jul-cc-pVDZ basis set in the calculations of PESs.

4.3.1 Smooth diabatic MOs (DMOs)

For any geometry, we number the active canonical MOs (CMOs) in order of increasing energy. We find that orbitals 5, 6, 8, 9, 10, and 11 are smooth, but orbitals 1, 2, 3, 4, and 7 are not suitable for diabatization based on configurational smoothness, because they can completely change their character as functions of geometry. As shown in Fig. 4.2, the canonical MOs 1 and 2 have mixed oxygen p_x and p_y character at $R_{O–H}$ = 1.04 Å, and when $R_{O–H} \geq 1.32$ Å, the orders of orbitals 1–4 change. Figure 4.3 shows the interconversion of oxygen p_y and p_z CMOs at $R_{O–H}$ = 1.32 Å along the C-C-O-H torsion angle. These mixings of p_x and p_y, or p_z and p_y orbitals of oxygen as nuclear coordinates are changed are also observed for DMOs obtained by applying only the threefold density criterion. This is why we used the full fourfold way with the p_y orbital of oxygen as a MORMO reference orbital. The DMOs at various geometries obtained by the fourfold way are shown in Figs. 4.4 and 4.5. The DMOs are originally numbered to approximately match the ordering of the CMOs at the equilibrium geometry of phenol. Then, at any other geometry, they are numbered so that they are smooth continuations of the orbitals at the equilibrium geometry; this would not be possible for the CMOs because they do not change smoothly, but the DMOs remain smooth with little deformation along continuous nuclear-coordinate paths.

4.3.2 Potentials and couplings along the O–H stretching and C–C–O–H torsion

We find, for the geometries considered along O-H stretching and C-C-O-H torsion coordinates in this paper, that the energy gap between U_1 and U_2 is always at

least 1.55 eV, and $|U_{12}|^2/|U_1 - U_2|$ is always less than 0.03 eV. Therefore, except for the reaction path from the equilibrium geometry of phenol to its prefulvenic structure to be discussed in section 4.3.5, the U_{12} diabatic coupling is not dynamically important, and in the rest of this section we do not discuss it, but rather we focus on the more important U_{13} and U_{23} diabatic couplings and the diagonal diabatic potentials. A diabatic coupling is a signed quantity, but the sign is not unique. It depends on the arbitrary phase factors of diabatic states, and it is not permutationally invariant. Although the signed diabatic coupling is not permutationally invariant, the absolute square of the diabatic coupling is permutationally invariant. Hence, we calculate the squared magnitude of diabatic couplings ($(U_{n'n})^2$) in the present work, and we can assign consistent signs to the couplings in future semiclassical dynamics studies by a calculation of the signs at one geometry (to establish a consistent set of phase relations) plus continuity along a trajectory.

4.3.2.1 Potentials and couplings along the O–H stretching coordinate

The MC-QDPT adiabatic potentials (V_1, V_2, and V_3) of the three lowest states along the O–H stretching coordinate, $R_{\mathrm{O–H}}$, are shown in Fig. 4.6a. The adiabatic potentials V_1, V_2, and V_3 are numbered in order of increasing energy at any geometry. In the vicinity of the equilibrium structure of the ground state, these states have the characters $^1\pi\pi$, $^1\pi\pi^*$, and $^1\pi\sigma^*$, respectively. The other geometric parameters in the calculations of cuts of PESs are fixed at their ground-state values as obtained at the

CASSCF level. The zero of energy is the ground-state MC-QDPT energy at $R_{O–H}$ = 0.964 Å. The corresponding MC-QDPT diabatic potentials (U_1, U_2, and U_3) and the squares of diabatic couplings ((U_{13})^2 and (U_{23})^2) as obtained with the smooth CASSCF DMOs based on the fourfold way scheme are shown in Figs. 4.6b and 4.6c.

We observe two intersections of the adiabatic potentials along the O–H stretching coordinate in Fig. 4.6a and the corresponding two crossings of diabatic potentials in Fig. 4.6b. Analyzing the coefficients of 11 diabatic prototypes (dominant CSFs) in the three states along the O–H stretching coordinate shown in Fig. 4.7 shows that the first crossing (CI1) at $R_{O–H} \approx 1.32$ Å is the crossing of the second diabatic state U_2 ($^1\pi\pi^*$ with dominant configurations $\chi_2^1 — \chi_2^4$) and the third diabatic state U_3 ($^1\pi\sigma^*$ with dominant configuration χ_3^1). The second crossing (CI2) occurs at $R_{O–H} \approx 2.26$ Å; this is the crossing of the third diabatic state U_3 ($^1\pi\sigma^*$, which corresponds at long $R_{O–H}$ distance to the doublet state of phenoxyl with a singly occupied π orbital and an H atom, with the most dominant configuration χ_3^1) and the first diabatic state U_1 ($^1\pi\pi$ corresponds at long $R_{O–H}$ distance to the doublet state of phenoxyl with a singly occupied σ orbital and an H atom, with the most dominant configuration being χ_1^2).

Because only the $R_{O–H}$ distance is changed from the planar equilibrium geometry, the system retains C_s symmetry along the O–H stretching coordinate. The $^1\pi\pi$ and $^1\pi\pi^*$ states have A´ symmetry, which differs from the A´´ symmetry of the $^1\pi\sigma^*$ state;

therefore the diabatic couplings U_{13} along the OH stretching coordinate and the diabatic couplings U_{23} for $R_{O–H} < 1.48$ Å are zero as shown in Fig. 4.6c. However, as shown in Fig. 4.7b and as has been discussed in the final paragraph of section 4.2.1.2, when $R_{O–H} \geq 1.48$ Å, the dominant configurations of diabatic state U_2 change to $\chi_2^5 — \chi_2^7$ due to a higher-energy crossing of potentials (this higher energy crossing is not particularly interesting for the photodissociation considered here, but we note that the success of the diabatization even in the presence of this higher-energy crossing is encouraging), so that in this long $R_{O–H}$ region the U_2 state is a high-energy $^1\pi\sigma^*$ state (denoted as $2\pi\sigma^*$ in Fig. 4.6b) instead of the $^1\pi\pi^*$ state. Thus, nonzero coupling of U_{23} is observed for $R_{O–H} \geq$ 1.48 Å as a result of U_2 ($2\pi\sigma^*$) and U_3 ($1\pi\sigma^*$ state in Fig. 6b) both being of the same A´´ symmetry. This non-zero coupling U_{23} is small as compared to the energy gap between the two states, so that along O–H stretching coordinate the adiabatic and diabatic potentials of the three states always agree well with each other.

4.3.2.2 Potentials and couplings along the O–H stretching coordinate at various C–C–O–H torsion angles

The MC-QDPT adiabatic (V_1, V_2 and V_3) and diabatic (U_1, U_2 and U_3) potentials and the squares of diabatic couplings ((U_{13})^2 and (U_{23})^2) of the three low-energy states along the O–H stretching coordinates $R_{O–H}$ at various C–C–O–H torsion angles (C–C–O–H = 30, 50, 70, 90°) are shown in Fig. 4.8. At these geometries, except for those with C–C–O–H = 90°, the phenol is asymmetric, and all states have the same A symmetry.

The crossings of adiabatic potential curves (V_3 and V_2 at short $R_{O–H}$ distances, and V_1 and V_2 at long $R_{O–H}$ distances) at planar structures (Fig. 4.6a) become avoided crossings at these C–C–O–H torsion angles. At C–C–O–H = 90°, the phenol has C_s symmetry again, but the symmetry plane is different from that of planar phenol. Now the $^1\pi\pi^*$ is A´´ symmetry, and the $^1\pi\sigma^*$ is A´ symmetry; thus they again have different symmetries, just as they do for planar geometries. Consequently, a symmetry-allowed crossing (CI1) of V_3 and V_2 is observed in Fig. 4.8d for C–C–O–H = 90°. However, the second crossing at long $R_{O–H}$ distance becomes an avoided crossing even for C–C–O–H = 90° because the $^1\pi\sigma^*$ state has the same A´ symmetry as one of the dominant configurations (χ_1^1) of the $^1\pi\pi$ state.

In contrast to the sudden changes of adiabatic potentials in the two avoided-crossing (or crossing) regions, the diabatic potentials always change smoothly, and they cross each other without complications. For C–C–O–H = 30–70°, the crossing of U_2 and U_3 occurs before the avoided crossing of V_2 and V_3 as shown in Figs. 4.8a-4.8c. In the regions where diabatic potentials cross, large diabatic couplings are observed, except for the first crossing at C–C–O–H = 90° because of the symmetry.

4.3.2.3 Potentials and couplings along the C–C–O–H torsion angles at two conical intersections

The two crossings of interest for planar geometries, CI1 ($^1\pi\pi^*/^1\pi\sigma^*$) and CI2 ($^1\pi\pi/^1\pi\sigma^*$), occur at $R_{O–H} \approx 1.32$ and 2.26 Å respectively (Fig. 4.6) based on the present MC-QDPT calculations. At $R_{O–H} = 1.32$ and 2.26 Å, the MC-QDPT adiabatic (V_1, V_2, and V_3) and diabatic (U_1, U_2, and U_3) potentials and the squares of most relevant diabatic couplings for each case [$(U_{23})^2$ for CI1 and $(U_{13})^2$ for CI2] are shown as functions of C–C–O–H torsion coordinates (C–C–O–H angles) in Fig. 4.9. The C–C–O–H torsion lifts both the degeneracy of the $^1\pi\pi^*$ and $^1\pi\sigma^*$ states and the degeneracy of the $^1\pi\pi$ and $^1\pi\sigma^*$ states. The figure shows that the strongest repulsion of adiabatic potentials V_2 and V_3 at $R_{O–H} = 1.32$ Å happens at C–C–O–H = 20–30° where U_{23} has its largest absolute value, which is 0.17 eV. When the C–C–O–H torsion reaches 90°, V_2 and V_3 become nearly degenerate again, but at a higher energy. The repulsion of adiabatic potentials V_1 and V_2 at $R_{O–H} = 2.26$ Å increases continuously along the C–C–O–H torsion coordinate, and the diabatic coupling U_{13} has its largest absolute value, 0.12 eV, at C–C–O–H = 60°, but the absolute value of U_{13} is reduced to 0.005 eV at C–C–O–H = 90°. This small U_{13} coupling at C–C–O–H = 90° can be explained by symmetry, i.e., the most dominant configuration χ_1^2 of U_1 at $R_{O–H} = 2.26$ Å has different symmetry (A´´) than the U_3 state (A´).

4.3.3 $^1\pi\pi^*/^1\pi\sigma^*(U_2 = U_3)$ and $^1\pi\pi/^1\pi\sigma^*(U_1 = U_3)$ seams as functions of $R_{O–H}$ distance and the C–C–O–H angle

The $^1\pi\pi^*/^1\pi\sigma^*$ diabatic crossing seam is where $U_2 = U_3$, and the $^1\pi\pi/^1\pi\sigma^*$ diabatic crossing seam is where $U_1 = U_3$. The MC-QDPT diabatic crossing seams are plotted in Fig. 4.10 as functions of $R_{O\text{-}H}$ distance and C–C–O–H angle, along with the corresponding adiabatic potentials and their projections in the coordinate plane defined by the O-H distance and the C–C–O–H angle. The diabatic potentials of the $^1\pi\pi^*$ (U_2) and $^1\pi\sigma^*$ (U_3) states intersect at short O–H distances of $R_{O–H}$ = 1.21−1.33 Å for various C–C–O–H angles, and the diabatic potentials of $^1\pi\pi$ (U_1) and $^1\pi\sigma^*$ (U_3) intersect at long O–H distances of 1.65–2.26 Å. The shortening of this distance as the torsion angle increases could also be seen in Fig. 4.8. Based on the present MC-QDPT calculations, the diabatic $^1\pi\pi^*/^1\pi\sigma^*$ seam is in the energy range of 5.7–6.5 eV relative to the ground-state minimum energy, and an energy of ~ 1 eV has to be overcome for the H tunneling mechanism of the photolysis of phenol.

4.3.4 Potentials and couplings along the vibrational modes ν_{16a} and ν_{16b} at two conical intersections

MC-QDPT adiabatic (V_1, V_2, and V_3) and diabatic (U_1, U_2, and U_3) potentials at the two conical intersections (CI1 and CI2) and the squares of the most relevant diabatic couplings [$(U_{23})^2$ for CI1 and $(U_{13})^2$ for CI2] are shown in Figs. 4.11 and 4.12 along Cartesian normal-mode displacements of the ν_{16a} and ν_{16b} modes. As discussed in the

introduction, these two modes – along with the C–C–O–H torsion that we have already discussed – have been considered to be the most likely candidates for dominant coupling modes for the two crossings. Modes 16a and 16b are out-of-plane ring distortions, and their normalized Cartesian displacements were calculated using the M06-L density functional**Error! Bookmark not defined.** with the aug-cc-pVTZ basis set and are shown respectively in Figs. 4.11a and 4.12a.

The smooth diabatic potentials and couplings that we obtained along the two out-of-plane phenyl ring vibrational modes further demonstrate the suitability of the fourfold way for generating global potential energy surfaces and couplings for a complex reaction. Both of the two modes lift the degeneracy of V_2 and V_3 at the first CI1 ($^1\pi\pi^*/^1\pi\sigma^*$), and the U_{23} couplings along the atomic displacement coordinates of the two out-of-plane distortion modes are significantly different from those along the C-C-O-H torsion angles. For example, at CI1, the calculated values of $|U_{23}|^2/|U_2 - U_3|$ along the ν_{16a} mode can be around three times larger than the $|U_{23}|^2/|U_2 - U_3|$ values along the ν_{16b} mode, and over 300 times larger than those along C–C–O–H torsion. Along the ring distortion modes, we see both larger $|U_{23}|$ and smaller diabatic energy gaps. Although ν_{16a} and ν_{16b} have comparable U_{23} couplings, the G_4 symmetry analysis of Dixon et al.[4d] shows that only a_2 modes can couple $^1\pi\pi^*$ and $^1\pi\sigma^*$ states; thus we assign the ν_{16a} mode (which is a_2 in G_4) rather than ν_{16b} (which is b_1 in G_4) as the dominant coupling mode for CI1 ($^1\pi\pi^*/^1\pi\sigma^*$).

As shown in Figs. 4.9, 4.11, and 4.12, neither ν_{16a} nor ν_{16b} shows U_{13} couplings that are larger than those along the C–C–O–H torsion at the CI2 ($^1\pi\sigma^*/^1\pi\pi$) intersection. (Figure 4.8 shows larger U_{13} couplings at some other geometries, but it is most relevant for the photochemical mechanism to focus on the regions of strong interaction of the potential energy surfaces, as we do in Figs. 4.9, 4.11, and 4.12). The ν_{16b} mode only barely lifts the degeneracy of V_1 and V_2, and the magnitudes of the U_{13} couplings along the ν_{16b} mode are smaller than 0.03 eV. The calculated U_{13} couplings along ν_{16a} mode are larger than those for ν_{16b} but comparable with those obtained along C–C–O–H torsion. Again, considering the implications of the G_4 symmetry (see the introduction), we assign the C-C-O-H torsion (b_1 in G_4) as the dominant coupling mode for CI2 ($^1\pi\sigma^*/^1\pi\pi$).

We have seen in Figs. 4.9, 4.11, and 4.12 that the relevant 1–3 couplings for CI2 are far less than the 2–3 couplings for CI1 along each of the three vibrational modes that we investigated. A smaller diabatic coupling implies more diabatic behavior (whereas a larger diabatic coupling implies more widely separated adiabats and hence more adiabatic behavior). The smallness of the calculated diabatic coupling at CI2 therefore provides a possible explanation of the experimental observation that ground-state phenoxyl radical is the dominant product in the UV photolysis of phenol at all photolysis wavelengths.[4e] That is, the system approaches CI2 on U_3 (or equivalently on V_2) and traverses this

region mainly diabatically, which leads to dissociation on U_3, which corresponds at large O-H distance to V_1.

4.3.5 Potentials and Couplings along reaction path from equilibrium geometry of phenol to prefulvenic form of phenol

A nonadiabatic process leading to a prefulvenic form of phenol though a prefulvenic conical intersection (of character $^1\pi\pi/^1\pi\pi^*$, which is the U_1/U_2 in the notational convention of the present paper) may contribute to the photolysis of phenol.[5] Here we show that our diabatization method remains valid even for the significant nonplanarity of the ring along a high-energy reaction path leading to the prefulvenic structure. To examine this reaction pathway, we first optimized the prefulvenic structure on the $^1\pi\pi^*$ surface of phenol using the same method as in the Ref. 5 but a different basis set (jul-cc-pVDZ) and a larger active space, in particular a CAS(12,9) active space that includes 12 active electrons and nine active orbitals as follows: three σ bonding orbitals of C–C bonds in the ring, one σ bonding orbital and one σ^* antibonding orbital of the newly formed C–C bond, one π bonding orbital and one π^* antibonding orbital, one lone pair orbital of the three sp^2 hybridized carbon atoms, and one lone pair orbital of the carbon atom bonded to the oxygen atom. MC-QDPT adiabatic (V_1, V_2, and V_3) and diabatic (U_1, U_2, and U_3) potentials along the reaction path connecting equilibrium geometry of phenol with its prefulvenic structure and the squares of the most relevant diabatic couplings [$(U_{12})^2$ and $(U_{13})^2$] are calculated and shown in Fig. 4.13, for which

eight intermediate geometries between the equilibrium and prefulvenic structures of phenol are obtained by linear interpolation (in other words, it is a linear synchronous transit path[58]). The active space used in the potential calculations along this reaction path is same as that used for the other reaction paths, i.e., it includes 12 active electrons and 11 active orbitals. A crossing of U_1 and U_2 states is observed in Fig. 4.13, and it is associated with an avoided crossing on the shoulder of a prefulvenic conical intersection of the two lower-energy states.

The actual paths followed in experiments at typical photolysis energies would be lower-energy paths than the one shown in Fig. 4.13. Since Fig. 4.13 shows that the present diabatization scheme remains valid even for out-of-plane ring distortions large enough to raise the energy more than 6 eV, we expect that it is more than adequate to represent such lower-energy paths.

The reader should keep in mind that if a diabatization scheme is used to create a full potential energy surface, one must re-examine the adequacy of the methods for each new region of space encountered; this is not an issue specific to present method, but rather it affects all methods. For example, one might find regions of space where the active space is not adequate to yield accurate adiabatic surfaces for the states of interest, and the active space would need to be increased even for an adiabatic calculation. In addition, if a diabatization is to be performed, it is possible that some regions of space will require one to expand or delimit the diabatic prototype list. It is very encouraging that in the study reported here we were able to use a single practical choice of active

space and single manageable list of diabatic prototypes to map out adiabatic potentials, diabatic potentials, and diabatic couplings over the whole combined ranges of the O–H dissociation coordinate and the C–C–O–H torsion and over significant ranges (> 6 eV) of out-of-plane ring distortions that we examined.

4.4 Concluding remarks

This article reports the application of our recently simplified algorithm for diabatization to a very demanding case, namely the photodissociation of phenol. This case is demanding because the extent of conjugation of the oxygen atom p orbitals to the ring is a sensitive function of the O–H bond dissociation coordinate, the C–C–O–H torsion coordinate, and the ν_{16a} and ν_{16b} out-of-plane vibrations of the phenyl group, all of which are studied and successfully treated.

The MC-QDPT adiabatic potentials of the three low-energy states (which are $^1\pi\pi$, $^1\pi\pi^*$, and $^1\pi\sigma^*$ for the most relevant geometries) of phenol are calculated along the O–H stretching coordinate, the C–C–O–H torsion coordinate, and the ν_{16a} and ν_{16b} distortion modes with three state-averaged CASSCF wave functions as reference states. Smooth CASSCF diabatic MOs are obtained by the fourfold way and are successfully used to perform direct MC-QDPT diabatization calculations for the three states and their diabatic couplings based on configurational uniformity along the various nuclear-motion coordinates for the nonadiabatic photodissociation reaction of phenol to phenoxyl radical and hydrogen atom. In the present context, "direct MC-QDPT diabatization" means that the diabatic potentials can be computed from MC-QDPT calculations at any geometry

independently of other geometries (i.e., without having to follow a path to that geometry, as is required in most diabatization algorithms). The seams of $^1\pi\pi^*/^1\pi\sigma^*$ and $^1\pi\pi/^1\pi\sigma^*$ diabatic intersections are plotted as functions of O–H distance and C–C–O–H torsion angles.

In order to assign the dominant coupling modes at the two conical intersections ($^1\pi\pi^*/^1\pi\sigma^*$ and $^1\pi\pi/^1\pi\sigma^*$), except for along C–C–O–H torsion, the adiabatic, and diabatic potentials and the diabatic couplings of the three low-energy states have been calculated along Cartesian normal-mode displacements of the two vibrational modes ν_{16a} and ν_{16b} at the two conical intersections. Based on the calculated couplings and the G_4 symmetry analysis, we assign ν_{16a} and C–C–O–H torsion as the dominant coupling modes for the $^1\pi\pi^*/^1\pi\sigma^*$ and for $^1\pi\pi/^1\pi\sigma^*$ intersections, respectively.

The fourfold way diabatization method is confirmed to be valid even along a significantly distorted reaction path from the planar equilibrium geometry of phenol to its prefulvenic form.

The present work, using the photolysis of phenol as a test case, shows that MC-QDPT diabatization based on CASSCF DMOs can provide a good starting point for multi-dimensional dynamics studies of complex processes. We anticipate that the promising results in this paper will be the beginning of a new line of research for studying photochemical dynamics.

4.5 References

[1] A. L. Sobolewski, W. Domcke, C. Dedonder-Lardeux, and C. Jourvet, Phys. Chem. Chem. Phys. **4**, 1093 (2002).

[2] A. L. Sobolewski and W. Domcke, J. Phys. Chem. A. **105**, 9275 (2001).

[3] (a) A. Sur and P. M. Johnson, J. Chem. Phys. **84**, 1206 (1986); (b) R. J. Lipert and S. D. Colson, J. Phys. Chem. 93, 135 (1989); (c) M. N. R. Ashfold, B. C. Cronin, A. L. Devine, R. N. Dixon, and M. G. D. Nix, Science, **312**, 1637 (2006); (d) M. G. D. Nix, A. L. Devine, B. C. Cronin, R. N. Dixon, and M. N. R. Ashfold, J. Chem. Phys. **125**, 133318 (2006); (e) M. N. R. Ashfold, A. L. Devine, R. N. Dixon, G. A. King, M. G. D. Nix, and T. A. A. Oliver, PNAS, **105**, 12701 (2008); (f) M. G. D. Nix, A. L. Devine, R. N. Dixon, and M. N. R. Ashfold, Chem. Phys. Lett. **463**, 305 (2008).

[4] (a) Z. Lan, W. Domcke, V. Vallet, A. L. Sobolewski, and S. Mahapatra, J. Chem. Phys. **122**, 224315 (2005); (b) A. Iqbal, M. S. Y. Cheung, M. G. D. Nix, and V. G. Stavros, J. Phys. Chem. A. **113**, 8157 (2009); (c) A. Pino, A. N. Oldani, E. Marceca, M. Fujii, S.-I. Ishiuchi, M. Miyazaki, M. Broquier, C. Dedonder, C. Jouvet, J. Chem. Phys. **133**, 124313 (2010); (d) R. N. Dixon, R. N.; T. A. A. Oliver, and M. N. R. Ashfold, J. Chem. Phys. **134**, 194303 (2011); (e) Y. Zhang, T. A. A. Oliver, M. N. R. Ashfold, and S. E. Bardforth, Faraday, Discuss. **157**, 141 (2012).

[5] O. P. J.Vieuxmaire, Z. Lan, A. L. Sobolewski, and W. Domcke, J. Chem. Phys. **129**, 224307 (2008).

[6] H. An and K. K. Baeck, J. Phys. Chem. A **115**, 13309 (2011).

[7] A. W. Jasper, C. Zhu, S. Nangia, and D. G. Truhlar, Faraday Discuss. **127**, 1 (2004), and references cited therein.

[8] D. G. Truhlar and C. A. Mead, Phys. Rev. A **68**, 32501 (2003).

[9] T. C. Thompson, D. G. Truhlar, and C. A. Mead, J. Chem. Phys. **82**, 2392 (1985).

[10] A. W. Jasper, B. K. Kendrick, C. A. Mead, and D. G. Truhlar, Adv. Ser. Phys. Chem. **14**, 329 (2004).

[11] B. C. Garrett, D. G. Truhlar, and C. F. Melius, in *Energy Storage and Redistribution in Molecules*, edited by J. Hinze, (Plenum: New York, 1983), p. 375–395.

[12] W. Lichten, Phys. Rev. **131**, 229 (1963).

[13] P. H.-L. Sit, M. Cococcioni, and N. Marzari, Phys. Rev. Lett. **97**, 28303 (2006).

[14] O. Godsi, C. R. Evenhuis and M. A. Collins, J. Chem. Phys. **125**, 104105 (2006).

[15] G. A. Arteca and O. Tapia, Int. J. Quantum Chem. **107**, 382 (2007).

[16] F. D. X. George and S. Kumar, J. Chem. Phys. **119**, 409 (2007).

[17] Z. H. Li, R. Valero, and D. G. Truhlar, Theor. Chem. Acc. **118**, 9 (2007).

[18] B. N. Papas, M. S. Schuuman, and D. R. Yarkony, J. Chem. Phys. **129**, 124104 (2008).

[19] J. E. Subotnik, S Yeganeh, R. J. Cave, and M. A. Ratner, J. Chem. Phys. **129**, 244101 (2008).
[20] T. Ichino, J. Gauss, and J. F. Stanton, J. Chem. Phys. **130***,* 174105 (2009).
[21] R. Valero, D. G. Truhlar, and A. W. Jasper, J. Phys. Chem. A **112**, 5756 (2008).
[22] S. Olsen and R. H. McKenzie, J. Chem. Phys. **131**, 234306 (2009).
[23] T. van Voorhis, T. Kowalczak, B. Kaduk, L.-P. Wang, C.-L. Cheng, Q. Wu, *Annu. Rev. Phys. Chem.* **61**, 149 (2010).
[24] A. Sirjoosingh, and S. Hammes-Schifffer, S. J. Phys. Chem. A **115**, 2367 (2011).
[25] E. Alguire and J. E. Subotnik, J. Chem. Phys. **135**, 044114 (2011).
[26] M. Pavanello, and J. Neugebauer, J. Chem. Phys. **135**, 134113 (2011).
[27] Y. C. Park, H. An, H. Choi, Y. S. Lee, and K. K. Baeck, Theor. Chem. Acc. **131**, 1212 (2012).
[28] X. Zhu, X. and D. R. Yarkony, J. Chem. Phys. **137**, 22A511 (2012).
[29] R. Valero and D. G. Truhlar, D. G. J. Chem. Phys. **137**, 22A539 (2012).
[30] C. A. Mead and D. G. Truhlar, J. Chem. Phys. **77**, 6090 (1982).
[31] (a) M. Baer, Chem. Phys. Lett. **35**, 112 (1975); (b) M. Baer, Mol. Phys. **40**, 1011 (1980).
[32] C. A. Mead, J. Chem. Phys. **125**, 204109 (2006).
[33] B. K. Kendrick, C. A. Mead, and D. G. Truhlar, Chem. Phys. **277**, 31 (2002).
[34] (a) H. Nakamura and D. G. Truhlar, J. Chem. Phys. **115**, 10353 (2001), and references cited therein; (b) H. Nakamura and D. G. Truhlar, J. Chem. Phys. **117**, 5576 (2002); (c) H. Nakamura and D. G. Truhlar, J. Chem. Phys. **118**, 6816 (2003).
[35] K. R. Yang, X. Xu, and D. G. Truhlar, Chem. Phys. Lett. **573**, 84 (2013).
[36] (a) G. J. Atchity and K. Ruedenberg, Theor. Chem. Acc. **97**, 47 (1997); (b) G. J. Atchity and K. Ruedenberg, J. Chem. Phys. **99**, 3790 (1993); (c) K. Ruedenberg and G. J. Atchity, J. Chem. Phys. **99**, 3799 (1993).
[37] (a) P. Siegbahn, A. Heiberg, B. O. Roos, and B. A. Levy, Phys. Scripta, **21**, 323 (1980); (b) B. O. Roos, P. R. Taylor, and P. E. M. Siegbahn, Chem. Phys. **48**, 157 (1980); (c) K. Ruedenberg, M. W. Schmidt, G. M. Gilbert, and S. T. Elbert, Chem. Phys. **71**, 41 (1982).
[38] (a) H. Nakano, J. Chem. Phys. **99**, 7983 (1993); (b) H. Nakano, Chem. Phys. Lett. **207**, 372 (1993).
[39] (a) T. H. Dunning Jr., J. Chem. Phys. **90**, 1007 (1989); (b) R. A. Kendall, T. H. Dunning Jr., and R. J. Harrison, J. Chem. Phys. **96**, 6796 (1992).
[40] (a) E. Papajak, H. R. Leverentz, J. Zheng, and D. G. Truhlar, J. Chem. Theory Comput. **5**, 1197 (2009); erratum: **5**, 3330 (2009); (b) E. Papajak and D. G. Truhlar, J. Chem. Theory Comput. **7**, 10 (2011).
[41] H. A. Witek, Y.-K. Choe, J. P. Finley, and K. Hirao, J. Comput. Chem. **23**, 957 (2002).

[42] M. S. Gordon and M. W. Schmidt, in *Theory and Applications of Computational Chemistry: The First Forty Years*, edited by C. E. Dykstra, G. Frenking, K. S. Kim, and G. E. Scuseria (Elsevier, Amsterdam, 2005) p. 1167−1189.

[43] (a) H. Nakamura, J. D. Xidos, A. C. Chamberlin, C. P. Kelly, R. Valero, K. R. Yang, J. D. Thompson, J. Li, G. D. Hawkins, T. Zhu, B. J. Lynch, Y. Volobuev, D. Rinaldi, D. A. Liotard, C. J. Cramer, and D. G. Truhlar, HONDOPLUS-v5.2, University of Minnesota, Minneapolis, MN, 2013; (b) M. Dupuis, A. Marquez, and E. R. Davidson, *HONDO 99.6*, Quantum Chemistry Program Exchange (QCPE), Indiana University, Bloomington, IN, 1999; (c) M. Dupuis, A. Marquez, and E. R. Davidson, *HONDO95.3*, Quantum Chemistry Program Exchange (QCPE), Indiana University, Bloomington, IN, 1995.

[44] V. M. García, M. Reguero, R. Caballol, and J. P. Malrieu, Chem. Phys. Lett. **281**, 161 (1997).

[45] R. W. Numrich and D. G. Truhlar, J. Phys. Chem. **79**, 2745 (1975).

[46] J. R. Delos and W. R. Thorson, J. Chem. Phys. **70**, 1774 (1979).

[47] B. C. Garrett and D. G. Truhlar, in *Theoretical Chemistry – Theory of Scattering: Papers in Honor of Henry Eyring*, edited by D. Henderson (Academic Press, New York, 1981), p. 216-289.

[48] T. Pacher, L. S. Cederbaum, and H. Köppel, J. Chem. Phys. **89**, 7367 (1988).

[49] J. P. Malrieu and F. Spiegelmann, in *Photophysics and Photochemistry Above 6 eV*, edited by F. Lahmani (Elsevier, Amsterdam, 1985), p. 305-317.

[50] R.-C. Fuh, Oregon Medical Laser Center, Portland, OR, 1995, http://omlc.ogi.edu/spectra/PhotochemCAD/html/072.html . (accessed April 11, 2013).

[51] (a) H. D. Bist, J. C. D. Brand, and D. R. Williams, J. Mol. Spectrosc. **21**, 76 (1966); (b) H. D. Bist, J. C. D. Brand, and D. R. Williams, J. Mol. Spectrosc. **24**, 402 (1967); (c) H. D. Bist, J. C. D. Brand, and D. R. Williams, J. Mol. Spectrosc. **24**, 413 (1967).

[52] Y.-R Luo, *Handbook of Bond Dissociation Energies in Organic Compounds*, University of Science and Technology of China: Hefei, 2006, p. 182.

[53] G. A. King, T. A. A. Oliver, M. G. D. Nix, and M. N. R. Ashfold, J. Phys. Chem. A. **113**, 7984 (2009).

[54] B. Ward, *Spectrochim. Acta Part A* **24**, 813 (1968).

[55] I. M. Alecu, J. Zheng, Y. Zhao, and D. G. Truhlar, J. Chem. Theory Comput. **6**, 2872 (2010).

[56] Y. Zhao and D. G. Truhlar, J. Chem. Phys. **125**, 194101 (2006).

[57] M. J. Frisch, G. W. Trucks, H. B. Schlegel, G. E. Scuseria, M. A. Robb, J. R. Cheeseman, G. Scalmani, V. Barone, B. Mennucci, G. A. Petersson, H. Nakatsuji, M. Caricato, X. Li, H. P. Hratchian, A. F. Izmaylov, J. Bloino, G. Zheng, J. L. Sonnenberg, M. Hada, M. Ehara, K. Toyota, R. Fukuda, J. Hasegawa, M. Ishida, T.

Nakajima, Y. Honda, O. Kitao, H. Nakai, T. Vreven, J. A. Montgomery, Jr. J. E. Peralta, F. Ogliaro, M. Bearpark, J. J. Heyd, E. Brothers, K. N. Kudin, V. N. Staroverov, R. Kobayashi, J. Normand, K. Raghavachari, A. Rendell, J. C. Burant, S. S. Iyengar, J. Tomasi, M. Cossi, N. Rega, J. M. Millam, M. Klene, J. E. Knox, J. B. Cross, V. Bakken, C. Adamo, J. Jaramillo, R. Gomperts, R. E. Stratmann, O. Yazyev, A. J. Austin, R. Cammi, C. Pomelli, J. W. Ochterski, R. L. Martin, K. Morokuma, V. G. Zakrzewski, G. A. Voth, P. Salvador, J. J. Dannenberg, S. Dapprich, A. D. Daniels, Ö. Farkas, J. B. Foresman, J. V. Ortiz, J. Cioslowski, and D. J. Fox, Gaussian 09, *Revision C*.01, Gaussian, Inc. Wallingford CT, 2009.

[58] T. A. Halgren and W. N. Lipscomb, Chem. Phys. Lett. **49**, 225 (1977).

Table 4.1. Definitions of the configuration state functions occurring in each of the three prototype lists, where each configuration state function is defined by the occupancies of the eleven DMOs, each of which is a linear combination of the eleven active canonical MOs.

Group G_1, prototype CSFs for diabatic state ϕ_1
χ_1^1 : 222222 00000
χ_1^2 : 122222 10000
Group G_2, prototype CSFs for diabatic state ϕ_2
χ_2^1 : 222221 01000
χ_2^2 : 222212 00100
χ_2^3 : 222121 01100
χ_2^4 : 222122 01000
χ_2^5 : 222212 10000
χ_2^6 : 222220 11000
χ_2^7 : 222211 10100
Group G_3, prototype CSFs for diabatic state ϕ_3
χ_3^1 : 222221 10000
χ_3^2 : 122221 20000

Table 4.2. The vertical excitation energies (eV) of the $^1\pi\pi^*$ and $^1\pi\sigma^*$ states of phenol and of the D_1 and D_2 states for phenoxyl radical and equilibrium bond dissociation energy (eV) of ground-state phenol.

	phenol			phenoxyl radical	
Method	$^1\pi\pi^*$-$^1\pi\pi$	$^1\pi\sigma^*$-$^1\pi\pi$	D_e	D_1	D_2
SA(3)-CAS(12,11)/jul-cc-pVDZ[a]	5.04	5.56	2.54	1.79	2.63
SA(3)-MCQDPT(12,11)/jul-cc-pVDZ[a]	4.70	5.86	4.37	0.94	2.28
MRCI/aug-cc-pVDZ[b]	4.75	5.76			
CASPT2(10/10)/aug(O)-AVTZ[c]	4.52	5.64	4.31	0.65	2.43
EOM-CCSD/aug(O)-AVTZ[c]	4.97	5.67			
Exp.	4.58[d]	5.12[d]	4.18[e]/4.08[e]	0.7[f]/0.99[g]	2.08[f]/2.03[g]

[a] The equilibrium geometry of phenol is optimized at CAS(12,11)/aug-cc-pVTZ level for the present study. The phenoxyl geometry is optimized at the CAS(11,10)/aug-cc-pVTZ level.

[b] Ref. 5

[c] Ref. 4d

[d] Ref. 50 and 51

[e] The experimental D_e is obtained from the experimental D_0 of Ref. 52 (first value given) or the experimental D_0 of Ref. 51 (second value given), in each case converted to D_e by using the calculated zero point energies for phenol and phenoxyl as obtained from M06-L/aug-cc-pVTZ vibrational frequencies from the present work scaled with a scaling factor of 0.980 from ref. 55. The M06-L exchange-correlation functional is from ref. 56, and the density functional calculations were carried out with ref. 57.

[f] Ref. 53

[g] Ref. 54

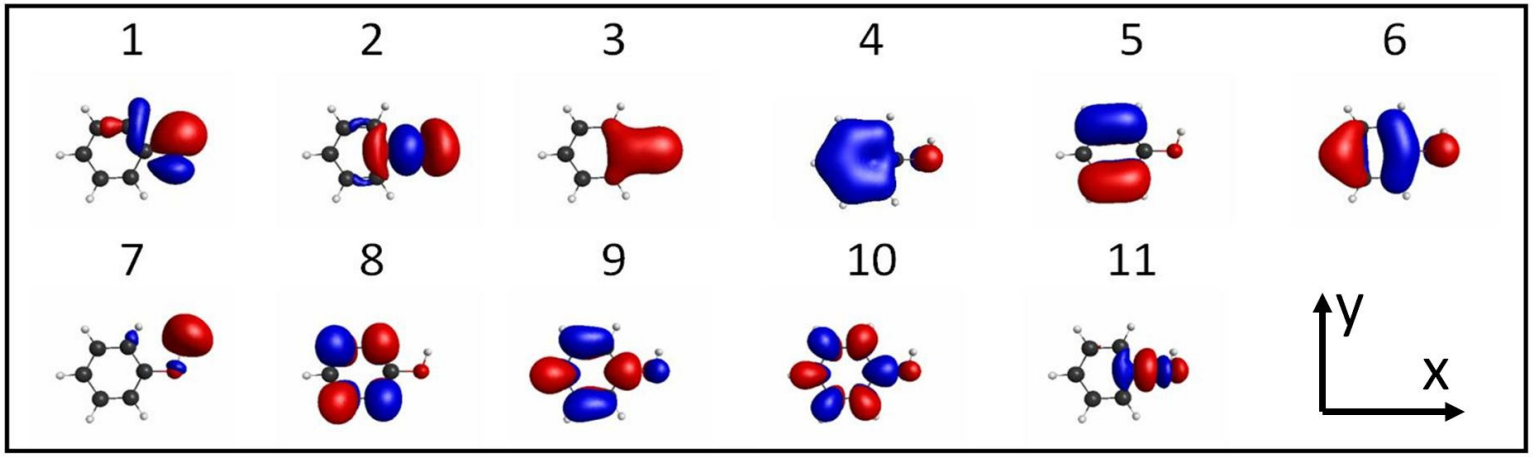

Figure 4.1. The eleven canonical active orbitals for $R_{O-H} = R_e = 0.964$ Å and C–C–O–H = 0°.

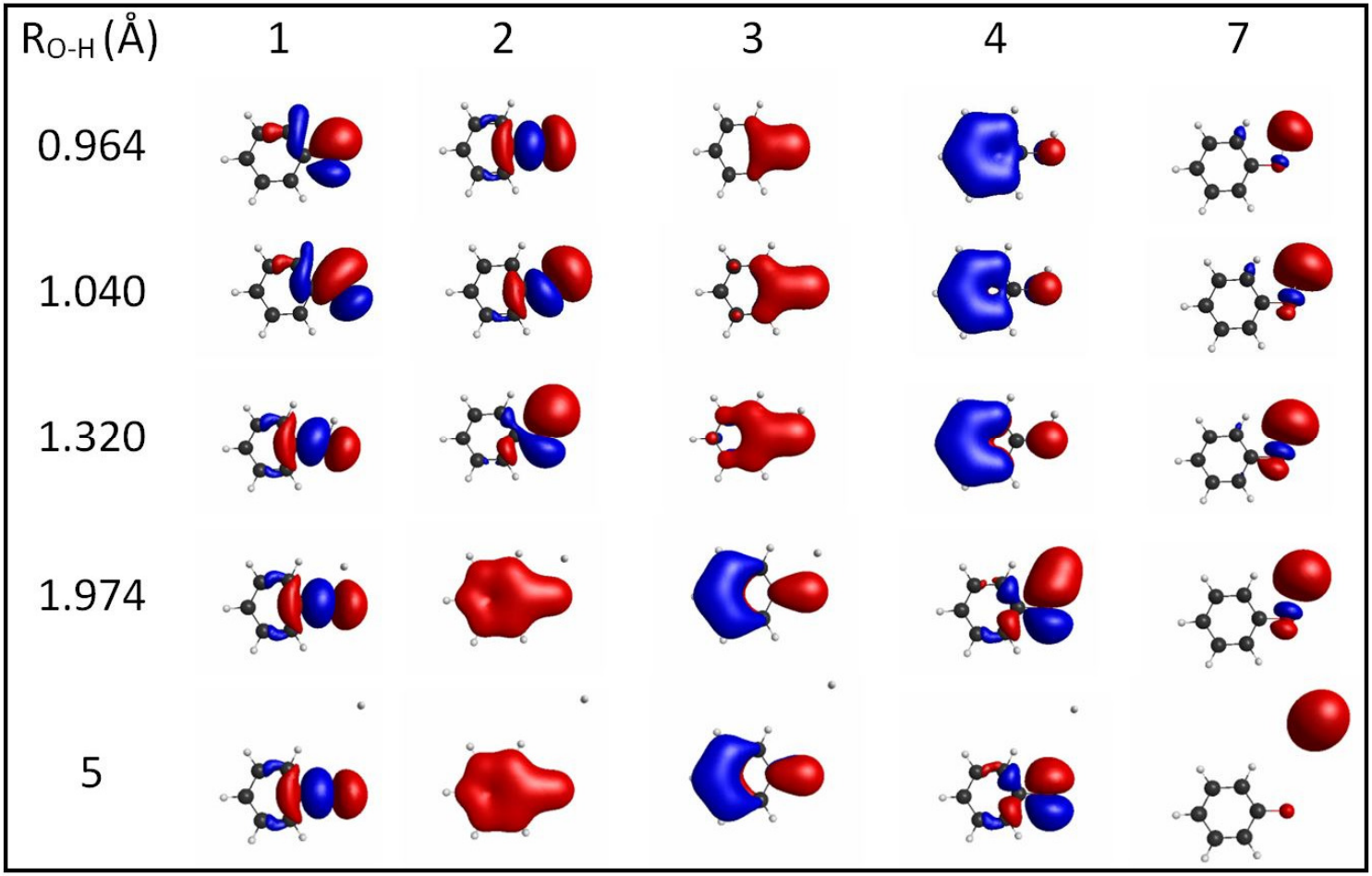

Figure 4.2. Canonical MOs (1, 2, 3, 4, and 7) in active space at C–C–O–H = 0°.

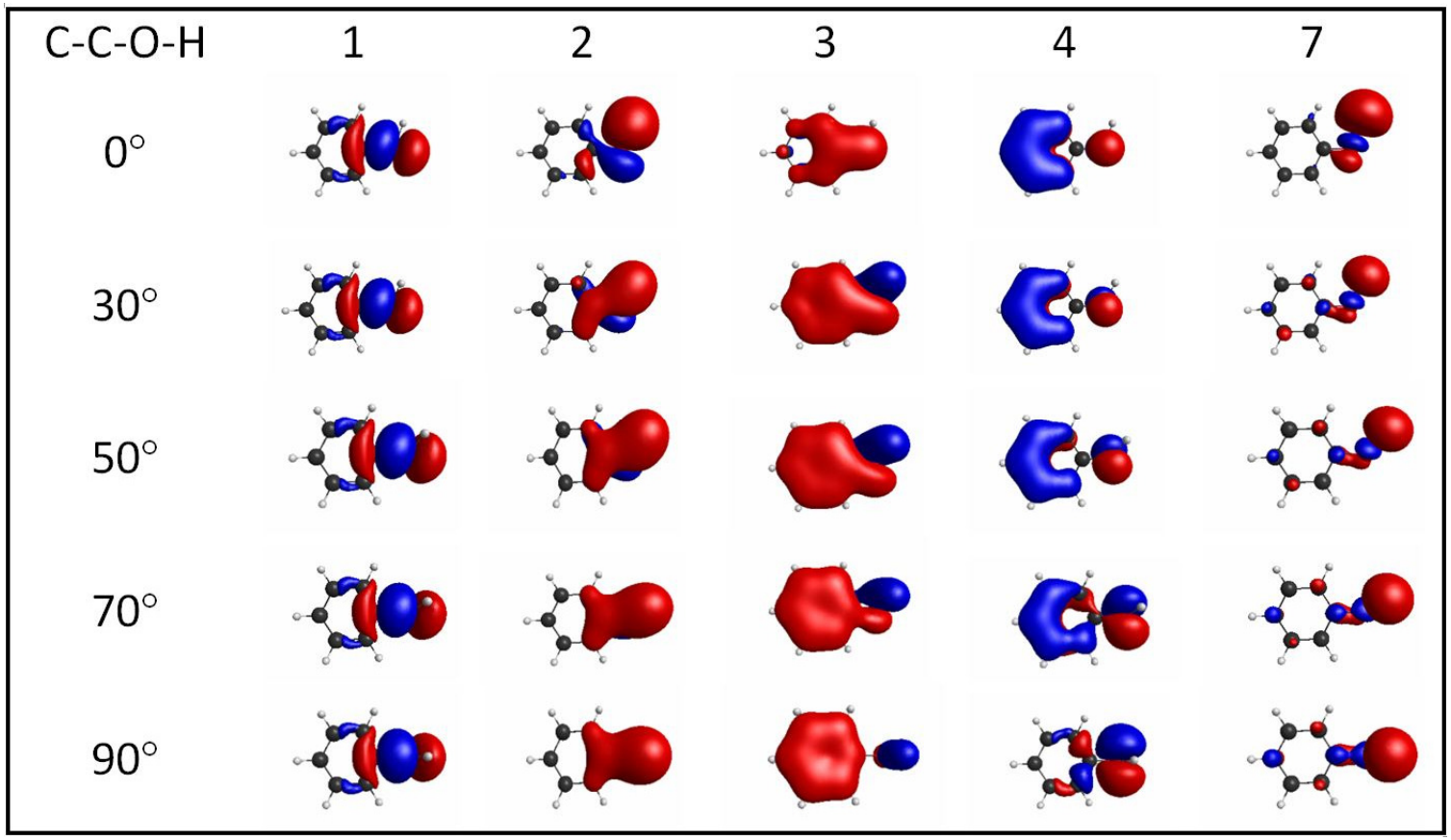

Figure 4.3. Canonical MOs (1, 2, 3, 4, and 7) in active space at $R_{O–H}$ = 1.32 Å.

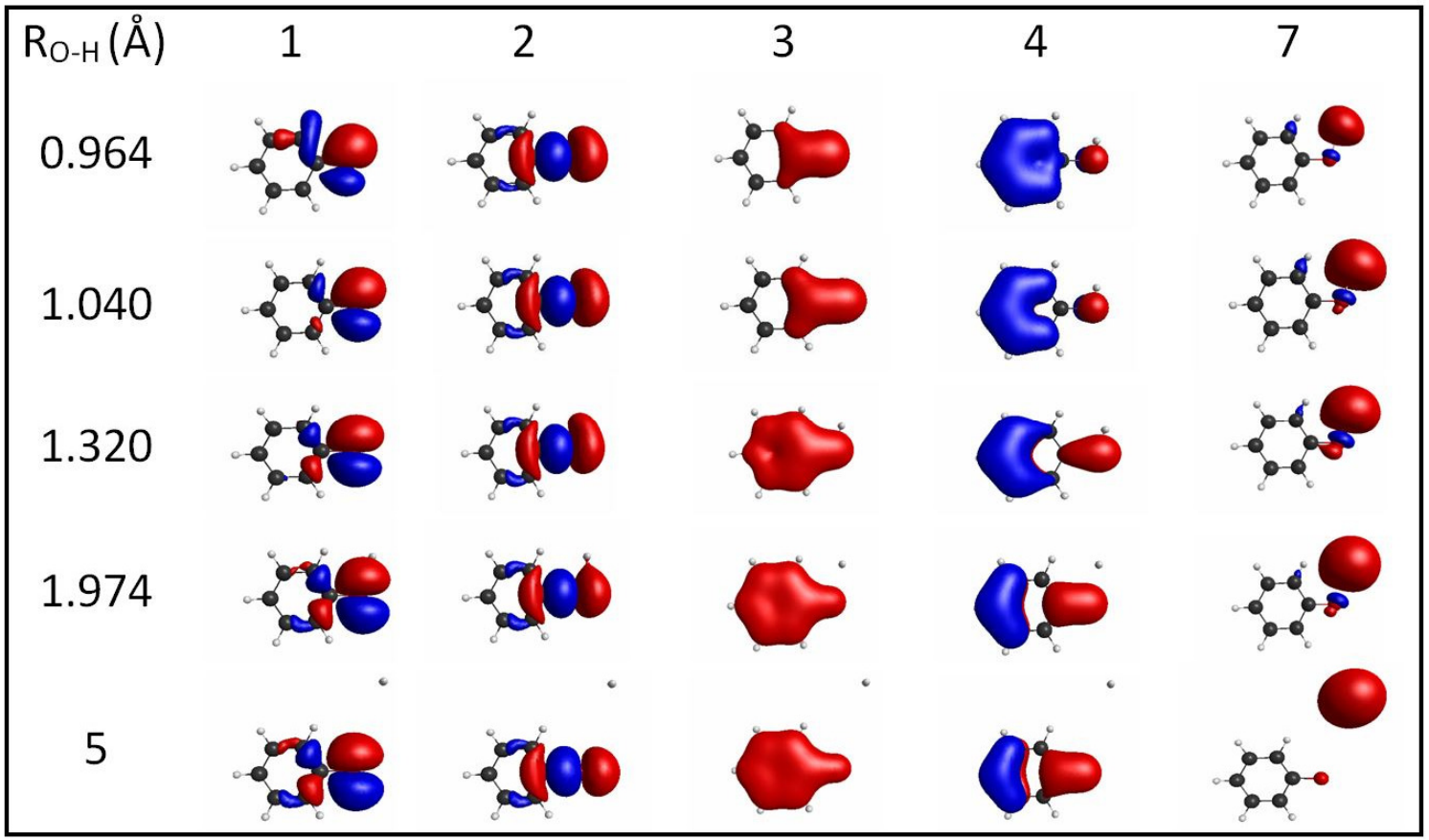

Figure 4.4. Diabatic MOs (1, 2, 3, 4, and 7) in active space at C–C–O–H = 0°.

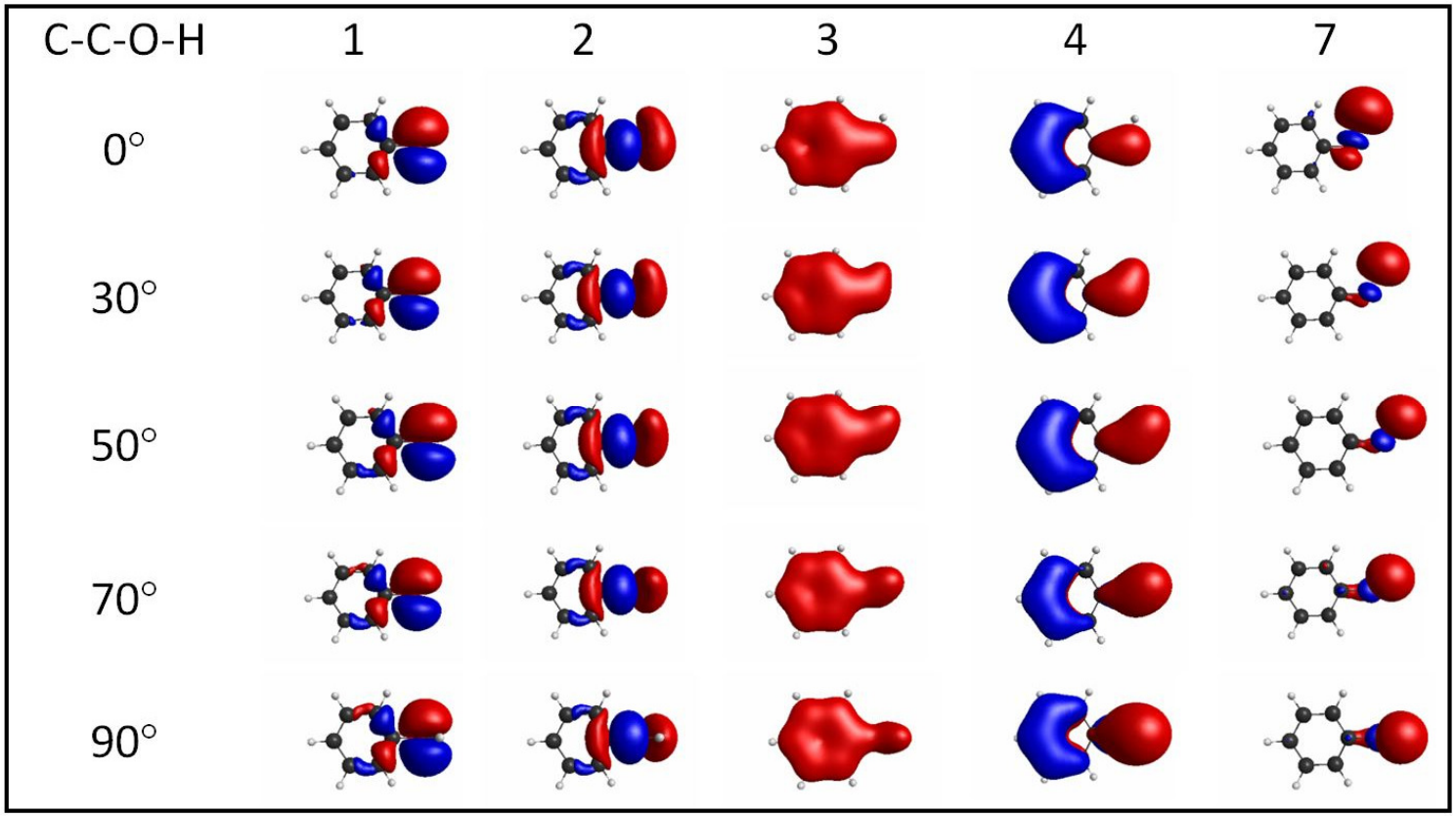

Figure 4.5. Diabatic MOs (1, 2, 3, 4, and 7) in active space at R_{O-H} = 1.32 Å.

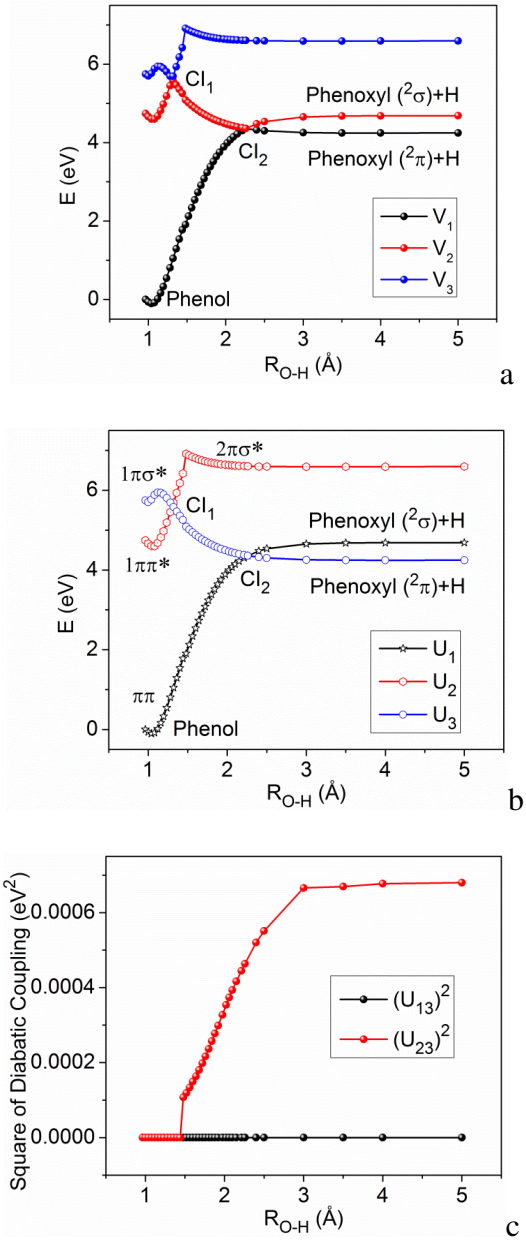

Figure 4.6. Adiabatic (V_1, V_2, and V_3) and diabatic (U_1, U_2, and U_3) potentials and square of diabatic couplings ((U_{13})^2 and (U_{23})^2) along $R_{O–H}$ distance, the other geometric parameters are fixed at their values at the ground-state equilibrium geometry.

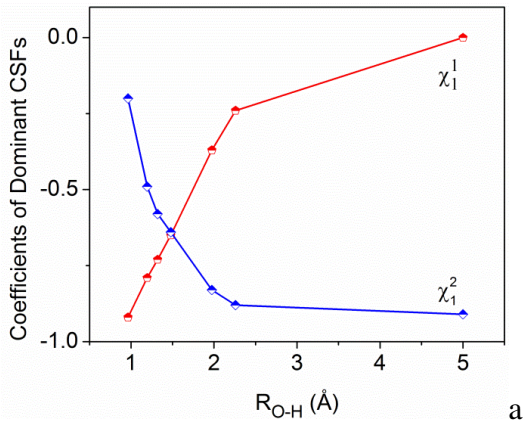

a

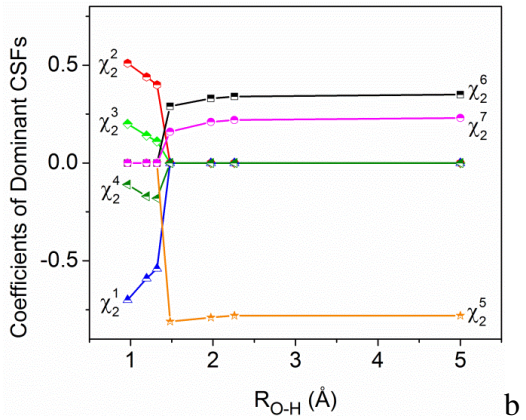

b

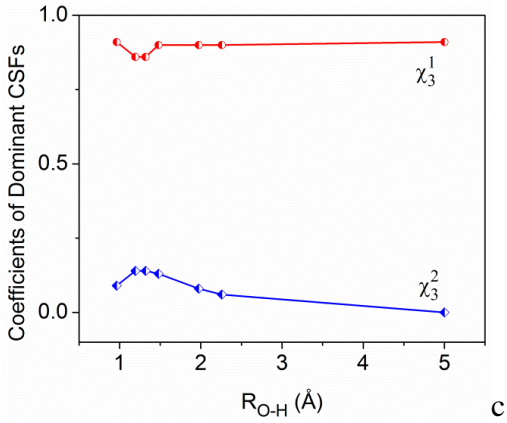

c

Figure 4.7. Plots of coefficients of 11 diabatic prototypes along R_{O-H} distance, the other geometric parameters are fixed at their values at the ground-state equilibrium geometry.

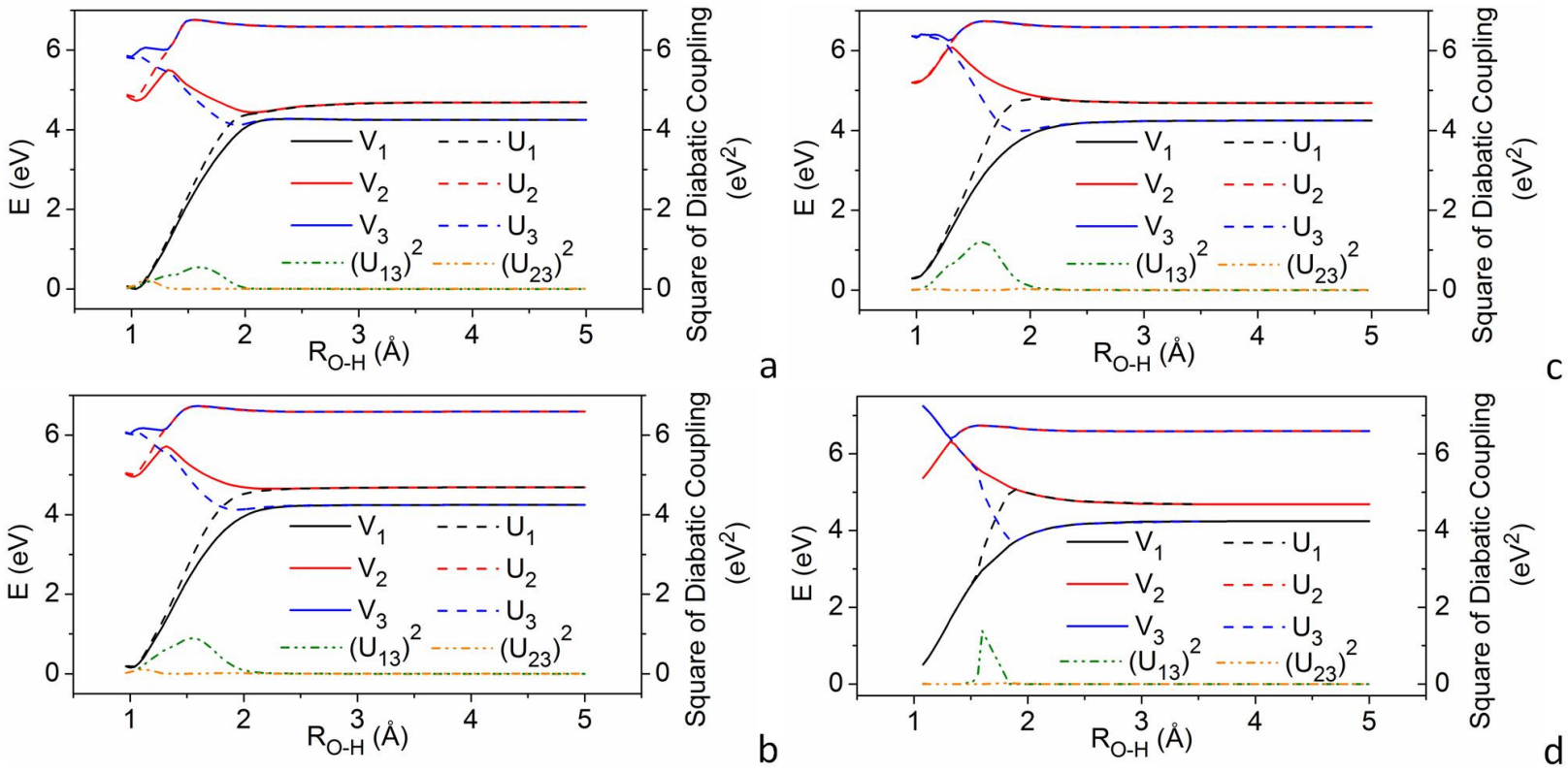

Figure 4.8. Adiabatic (V_1, V_2, and V_3) and diabatic (U_1, U_2, and U_3) potentials and squares of the diabatic couplings ((U_{13})^2 and (U_{23})^2) along the R_{O-H} coordinate at various C–C–O–H angles (a: 30°, b: 50°, c: 70°, d: 90°), with the other geometric parameters fixed at their values at the ground-state equilibrium geometry.

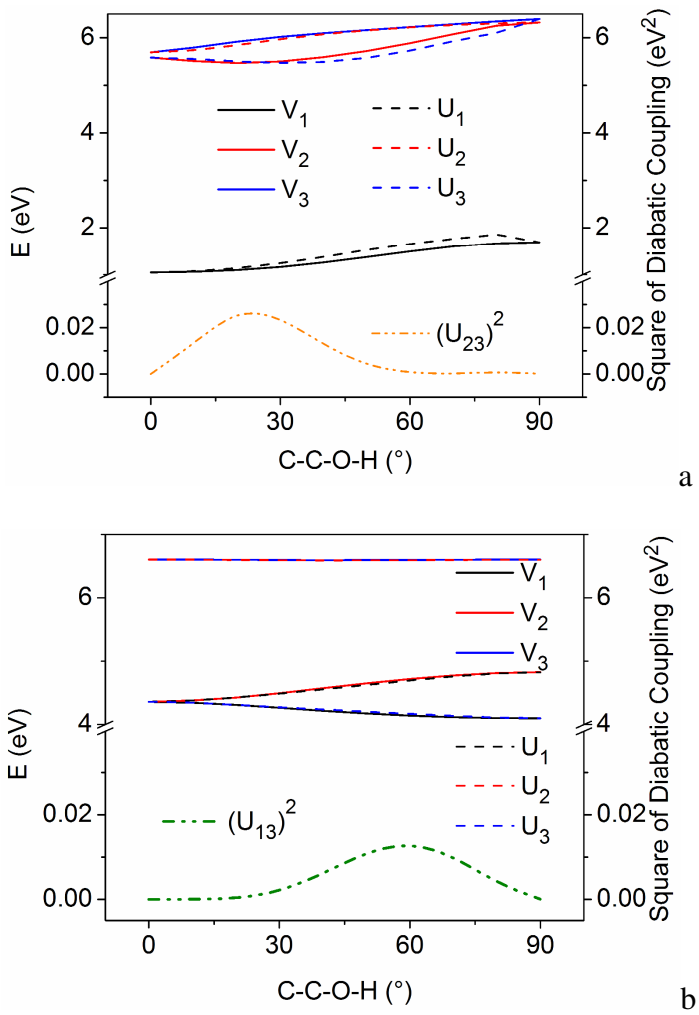

Figure 4.9. Adiabatic (V_1, V_2, and V_3) and diabatic (U_1, U_2, and U_3) potentials along the C–C–O–H angle at two conical intersections [the CI at $R_{O–H}$ = 1.32 Å (a) and the CI at $R_{O–H}$ = 2.26 Å (b)] and the corresponding squares of the most relevant diabatic couplings in each case [$(U_{23})^2$ at the first CI (a) and $(U_{13})^2$ at the second CI (b)]; the other geometric parameters are fixed at their values for the ground-state equilibrium geometry.

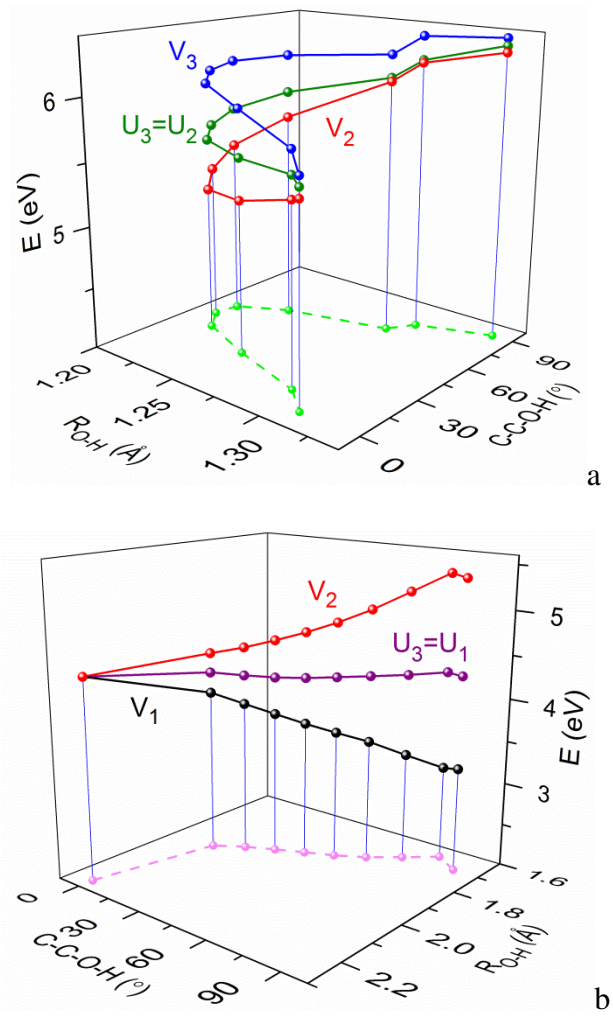

Figure 4.10. Diabatic crossing seams: the $^1\pi\pi^*/^1\pi\sigma^*$ (where $U_2 = U_3$) and $^1\pi\pi/^1\pi\sigma^*$ (where $U_1 = U_3$) seams as functions of $R_{O–H}$ distance and C–C–O–H angle.

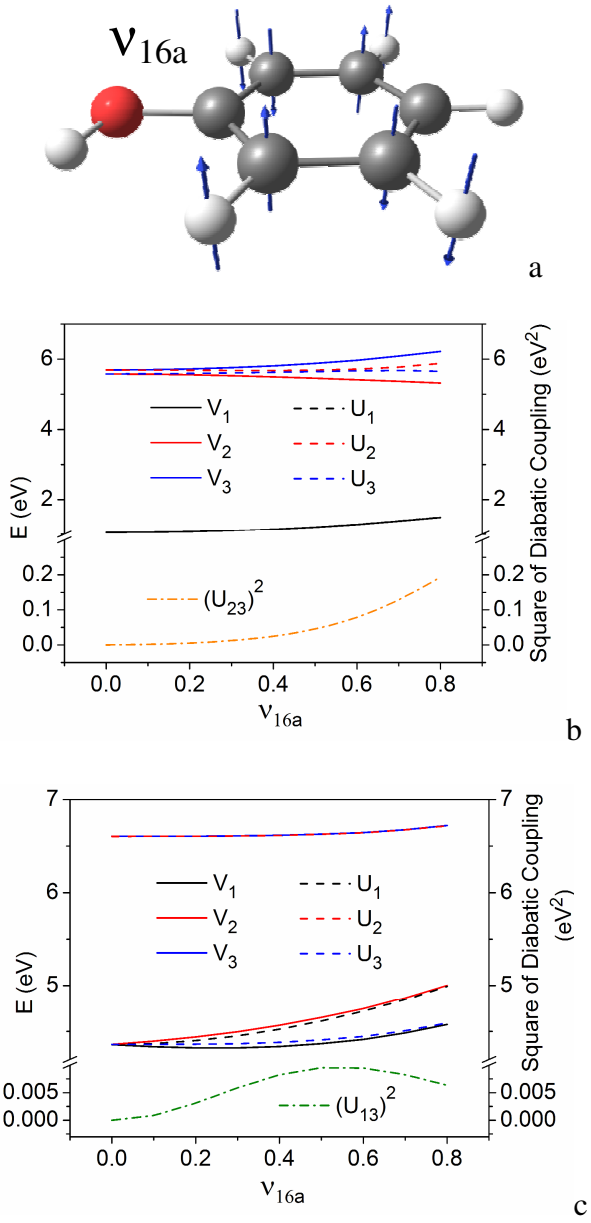

Figure 4.11. The atomic displacements of vibrational mode ν_{16a} (a), and adiabatic (V_1, V_2, and V_3) and diabatic (U_1, U_2, and U_3) potentials along scaled Cartesian normal-mode displacements (Å) of ν_{16a} at two CIs [R_{O-H} = 1.32 Å (b) and 2.26 Å (c)] and the corresponding squares of the most relevant diabatic couplings in each case [$(U_{23})^2$ at the first CI (b) and $(U_{13})^2$ at the second CI (c)].

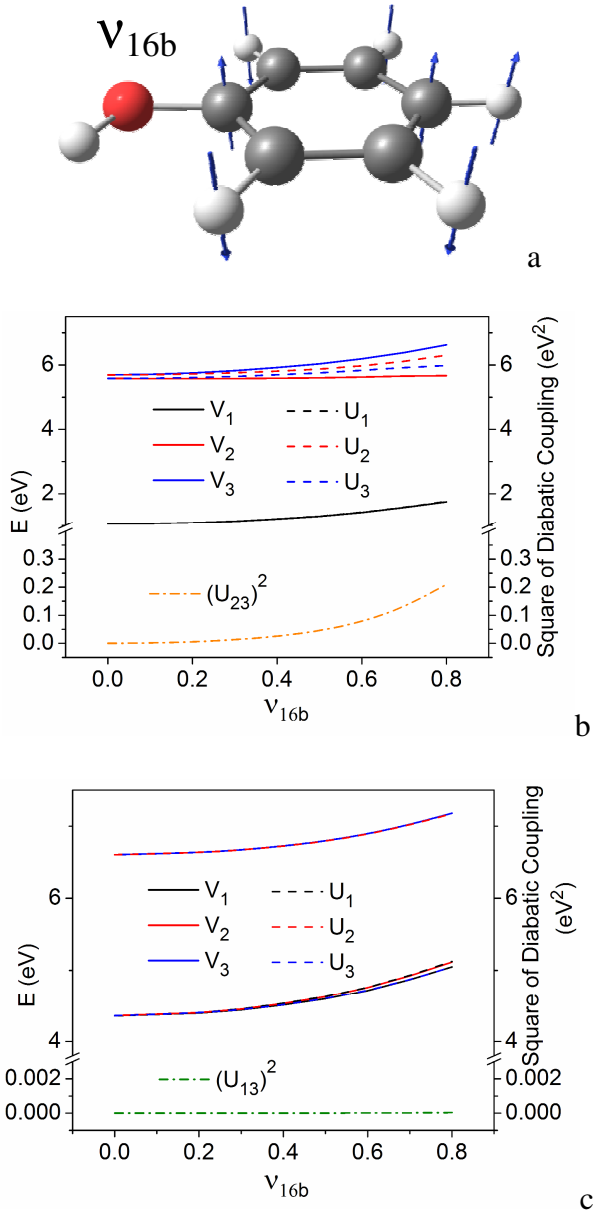

Figure 4.12. The atomic displacements of vibrational mode ν_{16b} (a), and adiabatic (V_1, V_2, and V_3) and diabatic (U_1, U_2, and U_3) potentials along scaled Cartesian normal-mode displacements (Å) of ν_{16b} at two CIs (R_{O-H}=1.32 Å (b) and 2.26 Å (c)) and the corresponding squares of the most relevant diabatic couplings in each case [$(U_{23})^2$ at the first CI (b) and $(U_{13})^2$ at the second CI (c)].

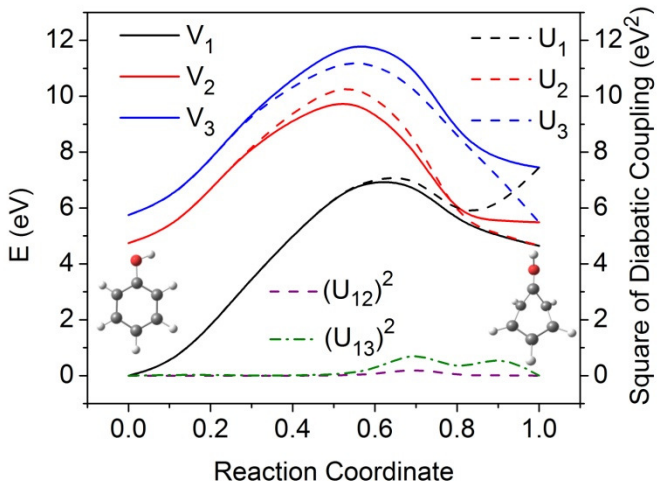

Figure 4.13. Adiabatic (V_1, V_2, and V_3) and diabatic (U_1, U_2, and U_3) potentials and squares of diabatic couplings $(U_{12})^2$ and $(U_{13})^2$ along a linearly interpolated reaction coordinate from the equilibrium geometry of phenol (reaction coordinate = 0) to its prefulvenic form (reaction coordinate = 1). The curves are B-spline fits to ten points along the linear synchronous reaction path.

Chapter 5. Anchor Points Reactive Potential for Bond-Breaking Reactions

Adapted with permission from Ke R. Yang, Xuefei Xu, and Donald G. Truhlar, J. Chem. Theory Comput. **10**, 924 (2014).

5.1 Introduction

Potential energy surfaces (PESs) and their associated force fields play critical roles in chemical reactions and molecular interactions; the construction of a PES is the first step in computing the dynamics[1-4] or optimizing a geometry. The PES may be implicit, as in direct dynamics, or explicit, when an analytical PES is available. Molecular mechanics (MM), which denotes an analytical potential expressed in internal coordinates, is perhaps the simplest way to construct a PES, but conventional MM omits cross terms and is valid only near an equilibrium structure. Nevertheless MM finds a myriad of uses and is widely used in the study of protein folding, drug docking, and materials simulations. Many MM force fields, for instance CHARMM,[5-8] AMBER,[9-13] GROMOS,[14] MM3,[15-17] OPLS,[18-20] UFF,[21] MMFF94,[22-25] GAFF,[26] and TraPPE[27,28] have been developed for the study of biopolymers, other polymers, and small organic molecules. The key advantage of popular MM force fields is that they involve transferable parameters that need not be redetermined for each new molecule studied. Recently, MM-like force fields for specific molecules based on quantum mechanical electronic structure calculations of energies and Hessians at an equilibrium structure have

been developed for more accurate simulations.[29,30] However, one of the limitations of even such molecule-specific internal-coordinate force fields is their inability to describe bond-breaking processes.

Recent development in potential energy surfaces fitting such as using global permutationally-invariant polynomials[31,32] and the interpolated moving least square (IMSL) method,[33-35] can describe bond breaking processes and have been used successfully to generate global potential energy surfaces based on electronic structure calculations, but they require many such calculations. In particular, the number of electronic calculations required for PES fitting grows rapidly with the dimensional of the system, and therefore most fitted PESs are limited to systems with five or less atoms. For a system with N atoms, the number of internal degrees of freedom is $F = 3N - 6$, and the number of data points grow as m^F, where m is the number of points needed to span a given degree of freedom. For a molecule with only ten atoms, using only four points in each dimension for the fit still requires $4^{24} \cong 10^{14}$ data points.

Conventional MM can be extended to include bond breaking by substituting a Morse curve or similar one-dimensional potential energy curve for the usual bond stretching term, but this does not allow for the change in geometrical parameters and force constants in other modes as the breaking bond is extended, and so it can be very inaccurate. Some work has been carried out to extend MM to bond breaking processes without assuming such separability of the bond breaking coordinate, but still allowing for the possibility of using general or specific-range parameters, as in the reactive empirical

bond order method,[36,37] ReaXFF,[38,39] or the valence bond order (VBO) method,[40] but such methods have less accuracy for global or semiglobal PESs than conventional MM has near equilibrium structures. It would be desirable to combine analytical potentials in internal coordinates for degrees of freedoms that involve small distortions from equilibrium structures with model potentials based on general functional forms to fit degrees of freedom involved in or closely coupled to bond breaking. Such an approach would be analogous to the combined quantum mechanics/molecular mechanics (QM/MM) method where MM is used for degrees of freedom of spectator atoms, and QM is used for degrees of freedom of active ones. Unlike QM/MM, which has been used widely for incorporating MM into electronic structure calculations of PESs of large systems such as enzymes and catalysis,[41-47] very few studies have been performed that incorporate MM-like force fields into the fitting of high-dimensional PESs.[48] In this article, we present a method called anchor points reactive potential (APRP) that combines fitting of quantum mechanical potential energy surfaces for selected degrees of freedom with molecule-specific MM-like force fields for other degrees of freedom to obtain a high-dimensional PES to treat bond-breaking processes.

5.2 Methodology

5.2.1 Anchor Points Reactive Potential (APRP) Method

Conventional molecular mechanics force field cannot describe chemical reactions in which bond breaking processes are involved. In our proposed anchor points reactive

potential method, the contributions to a potential energy surfaces (PES) are divided according to their dependence on three pre-defined groups of internal coordinates:

1. Reaction coordinates: **q**
2. Secondary coordinates: **s**
3. Tertiary coordinates: **Q**

The potential energy is written as

$$V = V^{[1]}(\mathbf{q}) + V^{[2]}(\mathbf{s} \mid \mathbf{q}) + V^{[3]}(\mathbf{Q} \mid \mathbf{q}), \tag{5.1}$$

where $f(x|y)$ denotes a function with a dependence on x and a parametric dependence on y. The three terms in eq 5.1 will be called the primary, secondary, and tertiary potentials; the primary and secondary terms can be completely general. In the present application, the reaction coordinate group consists of a single bond length r, and we will present the equations in the present subsection for this single-reaction-coordinate case to make the ideas more clear. To fit $V^{[2]}(\mathbf{s} \mid r)$ and $V^{[1]}(r)$, we need to calculate many data points in the space of **s** and r for a set of fixed values of the tertiary coordinates corresponding to a reference structure, and for the calculation of the torsional term in the secondary potential, we also calculate a grid of energies in a two-dimensional subspace with the other coordinates relaxed (see further details below).

The tertiary potential is described by analytic potentials in internal displacement coordinates $\mathbf{Q}^{[a]}$ relative to a set of anchor structures a with the anchor structures spaced along the reaction coordinates at a set of anchor values $\{r_a = r_i, i = 1, 2, ..., N_A\}$:

$$V^{[3]}\left(\mathbf{Q}\,|\,r\right)=\sum_{a=1}^{N_{\mathrm{A}}}V_a\left(\mathbf{Q}^{[a]}\right)T_a\left(r\right). \tag{5.2}$$

In eq 5.2, N_{A} is the number of anchor structures, $V_a\left(\mathbf{Q}^{[a]}\right)$ is a molecular mechanics-like potential with molecule-specific and anchor-point-specific parameters at anchor structure a, and $T_a\left(r\right)$ is called a tent function. The tent function is defined by

$$T_1\left(r\right)\rightarrow\begin{cases}1 & r<r_1\\ \dfrac{\left(r-r_2\right)^4}{\left(r-r_2\right)^4+\left(r-r_1\right)^4} & r_1\le r<r_2\end{cases}, \tag{5.3a}$$

$$T_a\left(r\right)\rightarrow\begin{cases}\dfrac{\left(r-r_{a-1}\right)^4}{\left(r-r_a\right)^4+\left(r-r_{a-1}\right)^4} & r_{a-1}\le r<r_a\\ \dfrac{\left(r-r_{a+1}\right)^4}{\left(r-r_{a+1}\right)^4+\left(r-r_a\right)^4} & r_a\le r<r_{a+1}\end{cases}\quad\text{for } a=2,\ldots,N_{\mathrm{A}}-1, \tag{5.3b}$$

$$T_{N_{\mathrm{A}}}\left(r\right)\rightarrow\begin{cases}\dfrac{\left(r-r_{N_{\mathrm{A}}-1}\right)^4}{\left(r-r_{N_{\mathrm{A}}}\right)^4+\left(r-r_{N_{\mathrm{A}}-1}\right)^4} & r_{N_{\mathrm{A}}-1}\le r<r_{N_{\mathrm{A}}}\\ 1 & r_{N_{\mathrm{A}}}\le r\end{cases}, \tag{5.3c}$$

Tertiary coordinates $\mathbf{Q}$ are further divided into two subgroups: stiff coordinates $\mathbf{Q}_{\mathrm{stiff}}$ such as stretches, bends, and rigid torsions, and soft torsion coordinates $\mathbf{Q}_{\mathrm{ST}}$, which involve wide-amplitude motion. The tertiary potential at anchor structure a is written as

$$V_a\left(\mathbf{Q}^{[a]}\right)=V_a^{\mathrm{stiff}}\left(\mathbf{Q}_{\mathrm{stiff}}^{[a]}\right)+V_a^{\mathrm{ST}}\left(\mathbf{Q}_{\mathrm{ST}}^{[a]}\right), \tag{5.4}$$

where $V_a^{\text{stiff}}\left(\mathbf{Q}_{\text{stiff}}^{[a]}\right)$ is the potential energy contribution from stiff coordinates, and $V_a^{\text{ST}}\left(\mathbf{Q}_{\text{ST}}^{[a]}\right)$ is the potential energy contribution from soft torsions.

Partial optimization is performed for each anchor structure *a*, with the only constraint being $r = r_a$, and the force constant matrix $\mathbf{F}^{[a]}$ in internal displacement coordinates is calculated for the optimized structure. Element *i* of the stiff internal displacement coordinate vector $\mathbf{Q}_{\text{stiff}}^{[a]}$ is defined as

$$Q_{\text{stiff},\,i}^{[a]} = S_i - S_{i,e}^{[a]}, \tag{5.5}$$

where S_i is an internal coordinate , and $S_{i,e}^{[a]}$ is the optimized value of S_i in the constrained optimized geometry of anchor point *a*.

Since $V^{[2]}(\mathbf{s}\,|\,\mathbf{q})$ and $V^{[1]}(\mathbf{q})$ are fitted to data corresponding to a rigid tertiary subspace corresponding to a reference structure, while the tertiary potential is expanded at partially optimized anchor structure *a*, a relaxation energy $V^{[a]}$ needs to be considered; this is defined as the energy difference between partially optimized anchor structure *a* and the rigid geometry with the same r_a. Then $V_a^{\text{stiff}}\left(\mathbf{Q}_{\text{stiff}}^{[a]}\right)$ is expanded near anchor structure *a* as

$$V_a^{\text{stiff}}\left(\mathbf{Q}_{\text{stiff}}^{[a]}\right) = V^{[a]} + \frac{1}{2}\mathbf{Q}_{\text{stiff}}^{[a]\,\mathsf{T}}\,\mathbf{F}_{\text{stiff}}^{[a]}\,\mathbf{Q}_{\text{stiff}}^{[a]}, \tag{5.6}$$

where $\mathbf{F}_{\text{stiff}}^{[a]}$ is the partial force constant matrix in the stiff subspace. The other tertiary potential term is parameterized as:

$$V_a^{\text{ST}}\left(\mathbf{Q}_{\text{ST}}^{[a]}\right) = \sum_{\tau=1}^{N_{\text{ST}}} V_\tau^{[a]}\left[1-\cos n_\tau\left(\varphi_\tau - \varphi_{\tau,e}^{[a]}\right)\right], \tag{5.7}$$

where N_{ST} is the number of soft torsions, n_τ is the local periodicity of the torsion, and $V_\tau^{[a]}$ and $\varphi_{\tau,e}^{[a]}$ are respectively the torsion barrier and equilibrium torsion angle for torsion τ at anchor structure a.

5.2.2 Analytical Cartesian gradient

In order to perform efficient dynamic studies, we require analytic Cartesian gradients of the PES. Denoting a column vector containing 3N Cartesian coordinates ($\xi_{3i-2} = x_i$, $\xi_{3i-1} = y_i$, $\xi_{3i} = z_i$, $i = 1, \ldots, N$, where N is the number of atoms) as $\boldsymbol{\xi}$, eq 5.1 yields

$$\frac{dV}{d\boldsymbol{\xi}} = \frac{dV^{[1]}(\mathbf{q})}{d\boldsymbol{\xi}} + \frac{dV^{[2]}(\mathbf{s}\,|\,\mathbf{q})}{d\boldsymbol{\xi}} + \frac{dV^{[3]}(\mathbf{Q}\,|\,\mathbf{q})}{d\boldsymbol{\xi}}. \tag{5.8}$$

Each term in eq 5.8 is constructed with internal coordinates, so the chain rule must be applied to obtain the analytic Cartesian gradient. This yields

$$\frac{dV}{d\boldsymbol{\xi}} = \left(\frac{\partial V^{[1]}(\mathbf{q})}{\partial \mathbf{q}} + \frac{\partial V^{[2]}(\mathbf{s}\,|\,\mathbf{q})}{\partial \mathbf{q}} + \frac{\partial V^{[3]}(\mathbf{Q}\,|\,\mathbf{q})}{\partial \mathbf{q}}\right)\frac{\partial \mathbf{q}}{\partial \boldsymbol{\xi}} + \frac{\partial V^{[2]}(\mathbf{s}\,|\,\mathbf{q})}{\partial \mathbf{s}}\frac{\partial \mathbf{s}}{\partial \boldsymbol{\xi}} + \frac{\partial V^{[3]}(\mathbf{Q}\,|\,\mathbf{q})}{\partial \mathbf{Q}}\frac{\partial \mathbf{Q}}{\partial \boldsymbol{\xi}}. \tag{5.9}$$

For the APRP PES of eq 5.1, $\frac{\partial V^{[1]}(\mathbf{q})}{\partial \mathbf{q}}$, $\frac{\partial V^{[2]}(\mathbf{s}\,|\,\mathbf{q})}{\partial \mathbf{q}}$, $\frac{\partial V^{[3]}(\mathbf{Q}\,|\,\mathbf{q})}{\partial \mathbf{q}}$, $\frac{\partial V^{[2]}(\mathbf{s}\,|\,\mathbf{q})}{\partial \mathbf{s}}$, and $\frac{\partial V^{[3]}(\mathbf{Q}\,|\,\mathbf{q})}{\partial \mathbf{Q}}$ can be evaluated straightforwardly. The other derivatives, $\frac{\partial \mathbf{q}}{\partial \xi}$, $\frac{\partial \mathbf{s}}{\partial \xi}$, and $\frac{\partial \mathbf{Q}}{\partial \xi}$, are Wilson's rectangular B matrices[49] for reaction coordinates and secondary and tertiary coordinates, with dimensions of $N_{\mathbf{q}} \times 3N$, $N_{\mathbf{s}} \times 3N$, and $N_{\mathbf{Q}} \times 3N$, where $N_{\mathbf{q}}$, $N_{\mathbf{s}}$, and $N_{\mathbf{Q}}$ are the number of reaction, secondary, and tertiary coordinates, and they can be evaluated analytically.[50,51]

5.3 Results and Discussion

We provide two examples to illustrate the APRP method, namely the O–H dissociation in CH_3OH and the N–H dissociation in $(H_3C)_2NH$. The electronic structure calculations for geometry optimization and energy and force constant calculations were performed with the unrestricted Kohn-Sham formalism with *Gaussian 09*.[52] The M06 exchange–correlation functional[53] and the 6-31+G(d) basis set[54] were used. For integrations to compute the exchange-correlation energy, we used a pruned (99, 590) grid [called the ultrafine grid] for all single-point energy calculations and a (150,974) grid [called the superfinegrid] for optimizations and force constant calculations.

5.3.1Dissociation of Methanol

The reference structure for the parametrization of the primary and secondary potentials is taken to be the equilibrium geometry of CH_3OH. The CH_3OH molecule

possesses C_s symmetry. When the H atom is removed, the CH_3O radical undergoes Jahn-Teller distortion from C_{3v} symmetry to C_s symmetry.[55] The optimized geometries and atomic labeling are shown in Figure 5.1. To treat the O–H bond dissociation, the O–H distance ($r_{OH} = r_{56}$) was chosen as the reaction coordinate; the bending and torsional coordinates that involve the separating H atom ($\theta_{HOC} = \theta_{651}$ and $\varphi_{HOCH} = \varphi_{6512}$), were chosen as secondary coordinates; and the other coordinates are tertiary ($r_{CH} = r_{12}$, r_{13}, r_{14}, $r_{CO} = r_{15}$, $\theta_{HCH} = \theta_{213}$, θ_{214}, θ_{314}, and $\theta_{HCO} = \theta_{215}$, θ_{315}, and θ_{415}) were chosen as tertiary coordinates.

The Varshni model potential, given by

$$V^{[1]}(r_{OH}) = D_1\{1-(r_1/r_{OH})\exp[-\beta_1((r_1/r_{OH})^2-1)]\}^2, \qquad (5.10)$$

was used to fit the O–H dissociation curve in CH_3OH since it has been shown to provide better approximations than the widely used Morse model in diatomics[56,57] and in the C–H dissociation of CH_4.[58] The optimized parameters are given in the supporting information and the calculated and fitted O–H dissociation curves are shown in Figure 5.2. The H–O–C bending and H–O–C–H torsion in secondary coordinates both involve the dissociated H atom, so they were parameterized with flexible functional forms that depend parametrically on the O–H bond length.

A scan was performed for r = 0.65-4.0 Å and θ = 60-180° with other internal coordinates of the equilibrium structure held rigid; the scan showed that at least a cubic term is needed to account for anharmonicity, so we used:

$$V_{\text{bend}}^{[2]}(\theta \mid r) = k_2(r)[\cos\theta - \cos\theta_0(r)]^2 + k_3(r)[\cos\theta - \cos\theta_0(r)]^3 . \qquad (6.11)$$

Notice that eq 6.11 has physically correct behavior in the vicinity of $\theta = 180°$, whereas a polynomial in θ rather than $\cos\theta$ would have unphysical behavior. The quadratic and cubic force constants, $k_2(r)$ and $k_3(r)$, as well as the equilibrium bond angles $\theta_0(r)$ depend parametrically on the O–H bond length. The parametric dependence of the equilibrium bond angle on the O–H bond length is fitted with a switching function:

$$\cos\theta_0(r) = \cos\theta_1 + \frac{1+\tan a(r-r_0)}{2}(\cos\theta_2 - \cos\theta_1), \qquad (6.12)$$

where $\cos\theta_1$, $\cos\theta_2$, a, and r_0 are adjustable parameters. The force constants were fitted with linear combinations of Gaussian functions:

$$k_i(r) = \sum_{j=1}^{N_{G,i}} A_{i,j} \exp[-\alpha_{i,j}(r - r_{i,j})^2], \qquad (6.13)$$

where $N_{G,i}$ is the number of Gaussian functions used to fit $k_i(r)$. Contour plots of the calculated and fitted bending potentials are compared in Fig. 6.3; they are in good agreement.

The H–O–C–H torsion potential was calculated for φ_{HOCH} = 0-180° with a step size of 10° for r = 0.65-4.0 Å. Contour plots of the torsion energy profiles along the O–H dissociation are shown in Figure 5.4a. The H–O–C–H torsion energy reaches its minimum for φ_{HOCH} = 180°, 60°, and by symmetry, -60°. It is interesting that the torsion barrier increases first as the O–H bond length increases, reaching its maximum around

1.7 Å, and decreases as the O–H bond length increases further; this nonmonotonic trend is understandable since in the two limits of r_{OH} equal to 0 and to infinity, the barrier should be zero. A cosine function was used to fit the torsion energy

$$V_{tor}^{[2]}(\varphi \mid r) = V_3(r)\left[1 - \cos 3(\varphi - \varphi_0)\right] \tag{5.14}$$

The parametric dependence of torsion barrier $V_3(r)$ on O–H bond length is fitted with linear combination of Gaussian functions:

$$V_3(r) = \sum_{i=1}^{N_G} A_i \exp[-\alpha_i (r - r_i)^2] \tag{5.15}$$

A contour plot of the fitted torsion energy is shown in Figure 5.4b. It reproduces the calculated result in Fig. 5.4a very well. Unlike the other terms in the primary and secondary potentials, the parameters in the secondary torsion were explained with relaxed structures, that is, all internal coordinates except r_{OH} and φ_{HOCH} are relaxed in the calculation.

Now we turn to $V^{[3]}$ which depends on tertiary coordinates and depends parametrically on r_{OH}. We optimized CH_3OH and CH_3O to obtain their equilibrium geometric parameters and force constant matrices (hessians) needed for the molecular mechanics force fields in the tertiary subspace. In addition to CH_3OH and CH_3O, three more structures were partially optimized with fixed O–H bond lengths (r_{OH} = 1.5, 2.0, and 3.0 Å) to obtain the equilibrium geometric parameters and force constants matrices along the dissociation path. Five anchor structures were used to describe the distortion of

tertiary coordinates along the O–H bond dissociation path. Four of these structures were the optimized structure with r_{OH} = 0.966 Å and the partially optimized structures with r_{OH} = 1.5, 2.0, and 3.0 Å; the fifth was an anchor structure at r_{OH} = 5.0 Å, taken to have the energy and force constant matrix of CH_3O. Since there are no soft torsions in the tertiary coordinates for this system, eq 5.6 was used to describe distortions of tertiary coordinates in the vicinity of each anchor structure, and eq 5.2 was be used to describe the tertiary potential all along the dissociation path.

As specified above, redundant internal coordinates are used as the tertiary coordinates for the construction of APRP PES. However, to test the performance of APRP, one needs to work with nonredundant coordinates that uniquely define a structure. A set of nonredundant internal coordinates are chosen as the following: S_1-S_4: r_{12}, r_{13}, r_{14}, r_{15}

S_5: r_{56}

S_6: $(\theta_{314} + \theta_{213} + \theta_{214} - \theta_{215} - \theta_{315} - \theta_{415})/\sqrt{6}$

S_7: $(2\theta_{314} - \theta_{213} - \theta_{214})/\sqrt{6}$

S_8: $(\theta_{213} - \theta_{214})/\sqrt{2}$

S_9: $(2\theta_{215} - \theta_{315} - \theta_{415})/\sqrt{6}$

S_{10}: $(\theta_{315} - \theta_{415})/\sqrt{2}$

S_{11}: θ_{651}

S_{12}: φ_{6512}

In this choice of non-reduandant internal coordinates, S_5 is the reaction coordinate equal to the O–H bond length, S_{11}, and S_{12} are the H–O–C bending and H–O–C–H torsion included in the secondary coordinates. S_1-S_4 are bond lengths in tertiary coordinates, and S_6-S_{10} are linear combinations of bond angles to constructed non-redundant internal coordinates as suggested by Pulay and coworkers.[59] Three slices of the potential energy curves along the non-reduandant internal coordinates, S_4, S_6, and S_8, are shown in Figure 5.5 for three different O–H bond lengths ($r_{OH} = r_e$, 2.0, and 4.0 Å).

Figure 5.5a, 5.5d, and 5.5g show the comparison of DFT calculated potential energy curves and APRP potential energy curves along the C–O bond stretching. They agree with each other near the equilibrium bond distance, but the APRP curves are too replusive for stretched bonds and not repulsive enough for compressed bonds, which is a typical result of bond stretrch anharmonicity. Model potentials such as Morse potential or Varshni potential can be used for bond stretching if more accurate descriptions is needed. However, in the photodissociation reaction under consideration, the dispecements along these coordiantes are expected to be small at the energies of interest, so the harmonic approximation should be adequate.

The comparison of DFT and APRP potential energy curves along S_6 and S_8 are shown in Figure 5.5b) and 5.5c, Figure 5.5e and 5.5f, and Figure 5.5h and 5.5i, for $r_{OH} = r_e$, 2.0, and 4.0 Å, respectively. They agree well with each other in all cases. We note that no information (neither equilibrium geometric parameters nor Hessians) were input to the

fit at r_{OH} = 4.0 Å , but APRP nevertheless describes the potential energy curves quite well for this O–H distance.

5.3.2 Dissociation of Dimethyl Ammonia

The reference structure for the parametrization of the primary and secondary potentials is taken to be the equilibrium geometry of $(H_3C)_2NH$. The $(H_3C)_2NH$ molecule has C_s symmetry. When the H atom is dissociated, the $(H_3C)_2N$ radical has C_{2v} symmetry. The optimized geometries and atomic labeling are shown in Figure 5.6. To treat the N–H bond dissociation, the N-H distance (which may be called either r_{NH} or r_{9-10}) was chosen as the reaction coordinate; and the bends and torsion that involve the dissociating H are chosen as secondary coordinates; in particular the secondary coordinates are two H–N–C bond angles θ_{HNC} (θ_{10-9-1} and θ_{10-9-5}) and the H–N–C–C out-of-plane torsion θ_{HNCC} ($\theta_{10-9-1-5}$). These three coordinates cannot all change independent, so we used θ_{HNCC} and a linear combination, $\phi = \frac{1}{\sqrt{2}}(\theta_{10-9-1} - \theta_{10-9-5})$, of the other two coordinates as nonredundant coordinates for fitting $V^{[2]}$. The other 8 bond lengths, 13 bond angles, and 6 torsions, in which the dissociated H atom (H10) is not involved, were chosen as tertiary coordinates.

The Varshni model potential, eq 5.10, was used to fit the N–H dissociation curve in $(H_3C)_2NH$. The calculated and fitted N–H dissociation curves are shown in Figure 5.7; they agree well.

A scan was performed for r = 0.7 Å to 4.0 Å and ϕ = -43° to 43° with other coordinates constrained to their values at the $(H_3C)_2NH$ equilibrium geometry. The calculated H–N–C bending potential energies along the N–H dissociation are shown in Figure 5.8a. The following functional form was chosen to fit the H–N–C bending potential energies

$$V_{\text{bend}}^{[2]}(\phi \mid r) = k_2(r)\phi^2 + k_4(r)\phi^4 \tag{5.16}$$

The cubic force constant, $k_3(r)$, is zero as a result of our definition of ϕ. The quadratic and quartic force constants, $k_2(r)$ and $k_4(r)$, depend parametrically on the N–H bond length, and they were fitted with linear combinations of Gaussian functions as shown in eq 5.13. A contour plot of the fitted H–N–C bending potential energies along the N–H dissociation is shown in Figure 5.8b, and it reproduces the main features of the calculated one in Figure 5.8a, where they are seen to agree well.

The H–N–C–C out-of-plane bend potentials are calculated for θ_{HNCC} = 0-90° and r = 0.7-4.0 Å. Figure 5.9a shows 2D contour plots of the out-of-plane bending potential energy profiles along the N–H dissociation. Equation 5.11 was used to fit this potential, and a 2D contour plot of the fitted potential is shown in Figure 5.9b.

The tertiary potential for $(H_3C)_2NH$ was obtained by performing optimization and frequency analysis of $(H_3C)_2NH$ and $(H_3C)_2N$, and partial optimization and frequency analysis of three other anchor structures with r_{NH} = 1.5, 2.0, and 3.0 Å. The bond stretches and bond angle bends were treated with eq 5.6 as in the case of CH_3OH. Since

$(H_3C)_2NH$ has soft torsions, in particular HCNC torsions, in the tertiary subspace, eq 5.7 was used for this molecule although it was not needed for methanol. The HCNC torsion potentials of $(H_3C)_2NH$ at the five anchor structures were fitted with the following functional form

$$V_a^{\mathrm{MM}}(\varphi) = V_i^{[a]}\left[1 - \cos 3(\varphi - \varphi_0)\right] \tag{5.17}$$

where a is the index of anchor structures. The calculated and fitted torsion potentials in $(H_3C)_2NH$ and $(H_3C)_2N$ are shown in Figure 5.10.

Again, to test the performance of APRP for tertiary coordinates, a set of non-redundant internal coordinates was chosen for $(H_3C)_2NH$. Potential energy curves along three selected coordinates (S_1, S_{10}, and S_{20}) at $r_{NH} = r_e$, 2.0, and 4.0 Å were calculated with both DFT and APRP and are shown in Figure 5.11. The definition of nonredundant internal coordinates is described in detail in the supporting information and the potential dependence on the coordinates is shown for only three selected coordinates:

S_1: r_{1-2}

S_{10}: $(\theta_{3-1-4} + \theta_{2-1-3} + \theta_{2-1-4} - \theta_{2-1-9} - \theta_{3-1-9} - \theta_{4-1-9}/\sqrt{6})$

S_{20}: θ_{1-9-5}

As in the case of CH_3OH, the APRP potential energy curves agree well with the DFT ones near the equilibrium bond lengths but fail to describe the anhormonicity for large bond stretches. The APRP potential energy curves along bond angle coordinates reproduce the DFT ones well, both for anchor structures and for non-anchor structures.

These plots show that APRP is able to describe the potential well for small distortions along the bond dissociation coordinate by interpolating between anchor structures.

5.4 Concluding remarks

By combining model potentials and internal coordinate force fields, we have developed a new scheme called anchor points reactive potential (APRP) to fit high-dimensional PESs. Analytic gradients of APRP PESs can be easily implemented for dynamic studies by using Wilson's B matrix. We illustrated the APRP method by applying it to construct the full dimensional PESs of CH_3OH and $(H_3C)_2NH$ to describe the X−H (X = O or N) bond breaking processes. It would be impractical to fit these potential energy surfaces with conventional PES fitting methods, but the present method is straightforwardly applicable and indeed would be applicable to much larger systems as well. The new method may be considered to be an extension of some previous methods[29,30,60,61] for fitting analytical potentials based in whole or in part on quantum mechanical Hessians, but those methods were developed for representing the potential in the vicinity of a single equilibrium structure, and the present method is designed for reactive potentials. It may also be compared to Shepard interpolation,[62,63] but it is more systematic in its design.

Although these examples involve only bond breaking, the method could be extended in a straightforward way to isomerization processes in which bonds are both broken and formed. Another generalization is that, although the APRP is applied here to Born-Oppenheimer processes occurring on the ground electronic state, it could also be

applied to electronically nonadiabatic processes of large molecules, such as light-induced DNA damage or photodissociation. The method would be especially well suited to fitting diabatic PESs for photodissociation, such as those recently reported for phenol.[64]

5.5 References

1 G. C. Schatz, Rev. Mod. Phys. **61**, 669 (1989).
2 T. Hollebeek, T.-S. Ho, and H. Rabitz, Annu. Rev. Phys. Chem. **1990**, *50*, 537-570.
3 A. Fernández-Ramos, J. A. Miller, S. J. Klippenstein, and D. G. Truhlar, Chem. Rev. **106**, 4518 (2006).
4 T. V. Albu, J. Espinosa-García, and D. G. Truhlar, Chem. Rev. **107**, 5101 (2007).
5 B. R. Brooks, R. E. Bruccoleri, B. D. Olafson, D. J. States, S. Swaminathan, and M. Karplus, J. Comput. Chem. **4**, 187 (1983).
6 A. D. MacKerell Jr., D.; Bashford, M. Bellott, R. L. Dunbrack Jr., J. D. Evanseck, M. J. Field, S. Fischer, J. Gao, H. Guo, S. Ha, D. Joseph-McCarthy, L. Kuchnir, K. Kuczera, F. T. K. Lau, C. Mattos, S. Michnick, T. Ngo, D. T. Nguyen, B. Prodhom, W. E. Reiher III, B. Roux, M. Schlenkrich, J. C. Smith, R. Stote, J. Straub, M. Watanabe, J. Wiorkiewicz-Kuczera, D. Yin, and M. Karplus, J. Phys. Chem. B **102**, 3586 (1998).
7 A. D. Mackerell Jr., M. Feig, and C. L. Brooks, J. Comput. Chem. **25**, 1400 (2004).
8 K. Vanommeslaeghe, E. Hatcher, C. Acharya, S. Kundu, S. Zhong, J. Shim, E. Darian, O. Gubench, P. Lopes, I. Vorobyov, and A. D. Mackerell Jr., J. Comput. Chem. **31**, 671 (2010).
9 S. J. Weiner, P. A. Kollman, D.T. Nguyen, and D. A. Case, J. Comput. Chem. **7**, 230 (1986).
10 W. D. Cornell, P. Cieplak, C. I. Bayly, I. R. Gould, K. M. Merz Jr., D. M. Ferguson, D. C. Spellmeyer, T. Fox, J. W. Caldwell, and P. A. Kollman, J. Am. Chem. Soc. **117**, 5179 (1995).
11 V. Hornak, R. Abel, A. Okur, B. Strockbine, A. Roitberg, and C. Simmerling, Protein **65**, 712 (2006).
12 A. Pérez, I. Marchán, D. Svozil, J. Sponer, T. E. Cheatham, C. A. Laughton, and M. Orozco, Biophys. J. **92**, 3817 (2007).
13 K. Lindorff-Larsen, S. Piana, K. Palmo, P. Maragakis, J. L. Klepeis, R. O. Dror, and D. E. Shaw, Proteins **78**, 1950 (2010).
14 W. R. P. Scott, P. H. Hunenberger, I. G. Tironi, A. E. Mark, S. R. Billeter, J. Fennen, A. E. Torda, T. Huber, P. Kruger, and W. F. van Gunsteren, J. Phys. Chem. A **103**, 3596 (1999).
15 N. L. Allinger, Y. H. Yuh, J.-H. Lii, J. Am. Chem. Soc. **111**, 8551 (1989).

16 J.-H. Lii and N. L. Allinger, J. Am. Chem. Soc. **111**, 8566 (1989).
17 J.-H. Lii and N. L. Allinger, J. Am. Chem. Soc. **111**, 8576 (1989).
18 G. Kaminski, E. M. Duffy, T. Matsui, and W. L. Jorgensen, J. Phys. Chem. **98**, 13077 (1994).
19 W. Damm, A. Frontera, J. Tirado-Rives, and W. L. Jorgensen, J. Comput. Chem. **18**, 1955 (1997).
20 W. L. Jorgensen and J. Tirado-Rives, J. Comput. Chem. **26**, 1689 (2005).
21 A. K. Rappe, C. J. Casewit, K. S. Colwell, W. A. Goddard III, and W. M. Skiff, J. Am. Chem. Soc. **114**, 10024 (1992).
22 T. A. Halgren, J. Comput. Chem. **17**, 490 (1996).
23 T. A. Halgren, J. Comput. Chem. **17**, 520 (1996).
24 T. A. Halgren, J. Comput. Chem. **17**, 553 (1996).
25 T. A. Halgren and R. B. Nachbar, J. Comput. Chem. **17**, 587 (1996).
26 J. Wang, R. M. Wolf, J. W. Caldwell, P. A. Kollman, and D. A. Case, J. Comput. Chem. **25**, 1157 (2004).
27 B. Chen and J. I. Siepmann, J. Phys. Chem. B **103**, 5370 (1999).
28 N. Rai and J. I. Siepmann, J. Phys. Chem. B **117**, 273 (2013).
29 I. Cacelli and G. Prampolini, J. Chem. Theory. Comput. **3**, 1803 (2007).
30 V. Barone, I. Cacelli, N. De Mitri, D. Licari, S. Monti, and G. Prampolini, Phys. Chem. Chem. Phys. **15**, 3736 (2013).
31 B. J. Braams and J. M. Bowman, Int. Rev. Phys. Chem. **28**, 577 (2009).
32 J. M. Bowman, B. J. Braams, S. Carter, C. Chen, G. Czakó, B. Fu, X. Huang, E. Kamarchik, A. R. Sharma, B. C. Shepler, Y. Wang, Z. Xie, J. Phys. Chem. Lett. **1**, 1866 (2010).
33 R. Dawes, D. L. Thompson, Y. Guo, A. F. Wagner, and M. Minkoff, J. Chem. Phys. **126**, 184108 (2007).
34 Y. Guo, I. Tokmakov, D. L. Thompson, A. F. Wagner, and M. Minkoff, J. Chem. Phys. **127**, 214106 (2007).
35 R. Dawes, D. L. Thompson, A. F. Wagner, and M. Minkoff, J. Chem. Phys. **128**, 084107 (2008).
36 D. W. Brenner, O. A. Shenderova, J. A. Harrison, S. J. Stuart, B. Ni, and S. B. Sinnott, J. Phys. Condens. Matter **14**, 783 (2002).
37 D. W. Brenner, O. A. Shenderova, J. D. Schall, D. A. Areshkin, S. Adiga, J. A. Harrsion, and S. J. Stuart, in *Handbook of Nanoscience, Engineering, and Technology*, edited by W. A. Goddard III, D. W. Brenner, S. E. Lyshevski, and G. J. Iafrate (CRC Press, Boca Raton, 2003) chapter 24.
38 A. C. T. van Duin, S. Dasgupta, F. Lorant, and W. A. Goddard III, J. Phys. Chem. A **105**, 9396 (2001).

[39] A. Kulkarni, D. G. Truhlar, S. G. Srinivasan, A. C. T. van Duin, P. Norman, and T. E. Schwartzentruber, J. Phys. Chem. C **117**, 258 (2013).
[40] M. Zhao, M. A. Iron, P. Staszewski, N. E. Schultz, R. Valero, and D. G. Truhlar, J. Chem. Theory Comput. **5**, 594 (2009).
[41] J. Gao, Rev. Comp. Chem. **7**, 119 (1996).
[42] G. Monard and K. M. Merz Jr., Acc. Chem. Res. **32**, 904 (1999).
[43] J. Gao and D. G. Truhlar, Annu. Rev. Phys. Chem. **53**, 467 (2002).
[44] R. A. Friesner and V. Guallar, Annu. Rev. Phys. Chem. **56**, 389 (2005).
[45] H. Lin, and D. G. Truhlar, Theor. Chem. Acc. **117**, 185 (2007).
[46] H. Hu and W. Yang, Annu. Rev. Phys. Chem. **59**, 573 (2008).
[47] H. M. Senn and W. Thiel, Angew. Chem. Int. Ed. **48**, 1198 (2009).
[48] A. Chakraborty, Y. Zhao, H. Lin, and D. G. Truhlar, J. Chem. Phys. **124**, 044315 (2006).
[49] E. B. Wilson Jr., J. C. Decius, and P. C. Cross, *Molecular vibrations: The theory of infrared and raman vibrational spectra*. McGraw-Hill: London, 1955, p. 54-63.
[50] I. H. Williams, J. Mol. Spectrosc. **66**, 288 (1977).
[51] D. F. McIntosh and K. H. Michaelian, Can. J. Spectrosc. **24**, 65 (1979).
[52] M. J. Frisch, G. W. Trucks, H. B. Schlegel, G. E. Scuseria, M. A. Robb, J. R. Cheeseman, G. Scalmani, V. Barone, B. Mennucci, G. A. Petersson, H. Nakatsuji, M. Caricato, X. Li, H. P. Hratchian, A. F. Izmaylov, J. Bloino, G. Zheng, J. L. Sonnenberg, M. Hada, M. Ehara, K. Toyota, R. Fukuda, J. Hasegawa, M. Ishida, T. Nakajima, Y. Honda, O. Kitao, H. Nakai, T. Vreven, J. A. Montgomery, Jr. J. E. Peralta, F. Ogliaro, M. Bearpark, J. J. Heyd, E. Brothers, K. N. Kudin, V. N. Staroverov, R. Kobayashi, J. Normand, K. Raghavachari, A. Rendell, J. C. Burant, S. S. Iyengar, J. Tomasi, M. Cossi, N. Rega, J. M. Millam, M. Klene, J. E. Knox, J. B. Cross, V. Bakken, C. Adamo, J. Jaramillo, R. Gomperts, R. E. Stratmann, O. Yazyev, A. J. Austin, R. Cammi, C. Pomelli, J. W. Ochterski, R. L. Martin, K. Morokuma, V. G. Zakrzewski, G. A. Voth, P. Salvador, J. J. Dannenberg, S. Dapprich, A. D. Daniels, Ö. Farkas, J. B. Foresman, J. V. Ortiz, J. Cioslowski, and D. J. Fox, Gaussian 09, *Revision D*.01, Gaussian, Inc. Wallingford CT, 2009.
[53] Y. Zhao and D. G. Truhlar, Theor. Chem. Acc. **120**, 215 (2008).
[54] (a) W. J. Hehre, R. Ditchfield, and J. A. Pople, J. Chem. Phys. **56**, 2257 (1972); (b) P. C. Hariharan and J. A. Pople, Theoretica. Chimica. Acta. **3**, 213 (1973); (c) T. Clark, J. Chandrasekhar, G. W. Spitznagel, and P. v. R. Schleyer, J. Comput. Chem. **4**, 294 (1983).
[55] I. B. Bersuker, Chem. Rev. **101**, 1067 (2001).
[56] Y. P. Varshni, Rev. Mod. Phys. **29**, 664 (1957); erratum: **31**, 839 (1959).
[57] D. Steele, E. R. Lippincott, and J. T. Vanderslice, Rev. Mod. Phys. **34**, 239 (1962).

[58] F. B. Brown and D. G. Truhlar, Chem. Phys. Lett. **113**, 441 (1985).
[59] P. Pulay, G. Fogarasi, F. Pang, and J. E. Boggs, J. Am. Chem. Soc. **101**, 2550 (1979).
[60] G. Pongor, G. Fogarezi, J. E. Boggs, and P. Pulay, J. Mol. Spectrosc. **114**, 445 (1985).
[61] S. Dasgupta, K. A. Brameld, C.-F. Fan, and W. A. Goddard III, Spectrochim. Acta. **53**, 1347 (1997).
[62] K. C. Thompson, M. J. T. Jordan, and M. A. Collins, J. Chem. Phys. **108**, 8302 (1998).
[63] O. Tishchenko and D. G. Truhlar, J. Chem. Phys. **132**, 084109 (2010).
[64] X. Xu, K. R. Yang, and D. G. Truhlar, J. Chem. Theory Comput. **9**, 3612 (2013).

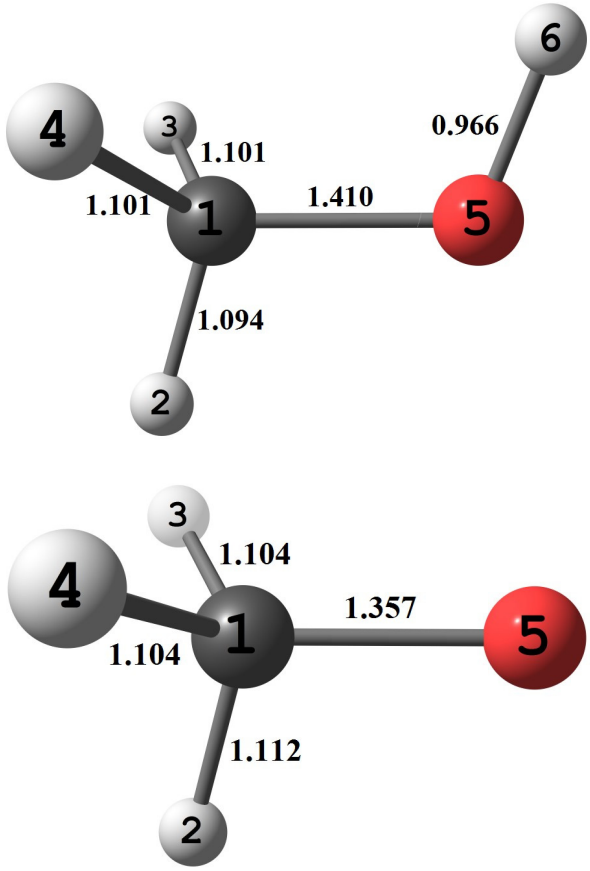

Figure 5.1. Geometries of CH_3OH (top) and CH_3O (bottom) (both in C_s symmetry).

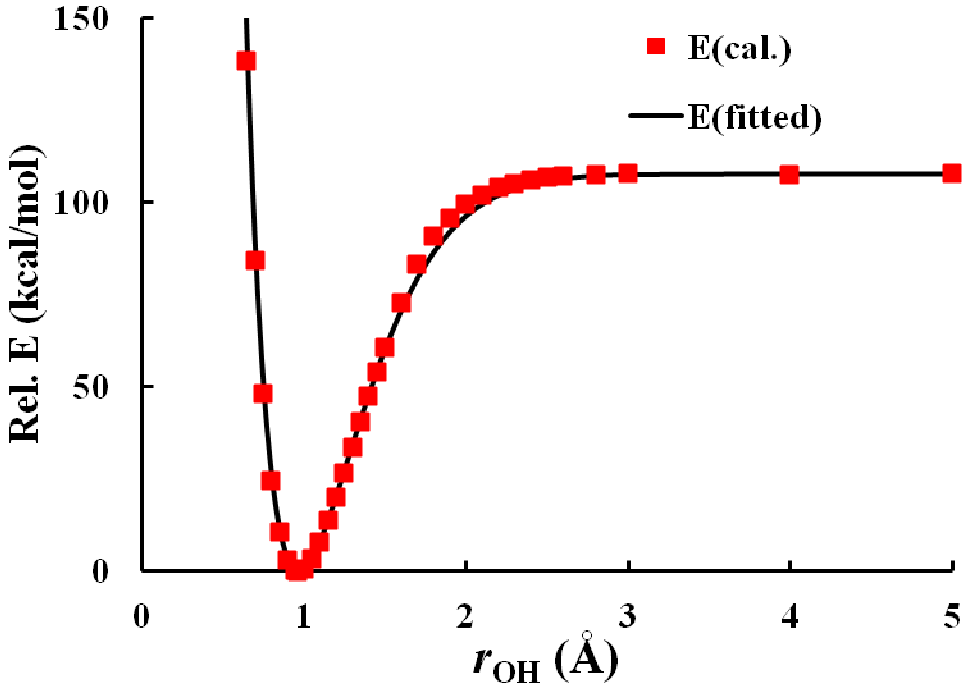

Figure 5.2. Varshini potential to describe the O–H bond dissociation in CH_3OH. All internal coordinates except the O-H bond distance are held constant along the path used for this figure.

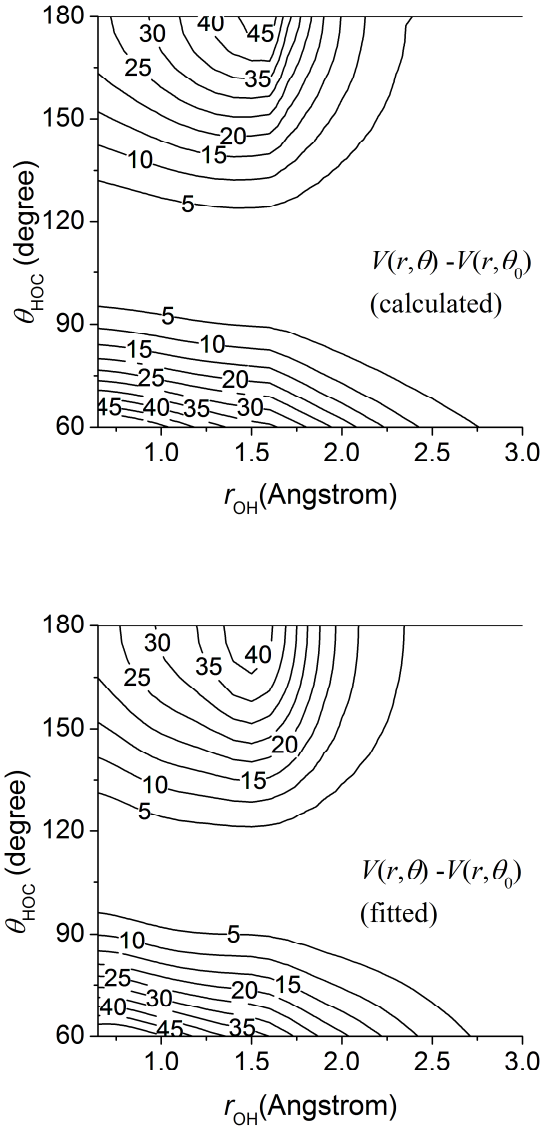

Figure 5.3. Contour plots of calculated and fitted H–O–C bending potential energies (in kcal/mol) along the O–H dissociation path (Note that θ_0 is a function of r_{OH}). All internal coordinates except r_{OH} and θ_{HOC} are held constant at their reference values for this figure.

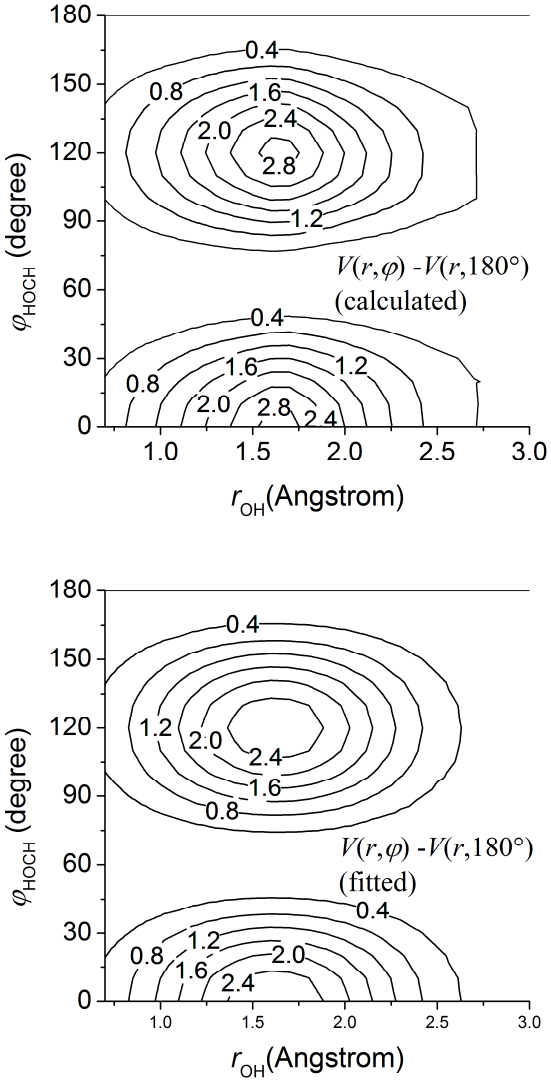

Figure 5.4. Contour plots of calculated and fitted H–O–C–H torsional potential energies (in kcal/mol) along the O-H dissociation path. All internal coordinates except r_{OH} and φ_{HOCH} are relaxed in the calculation of this secondary torsion.

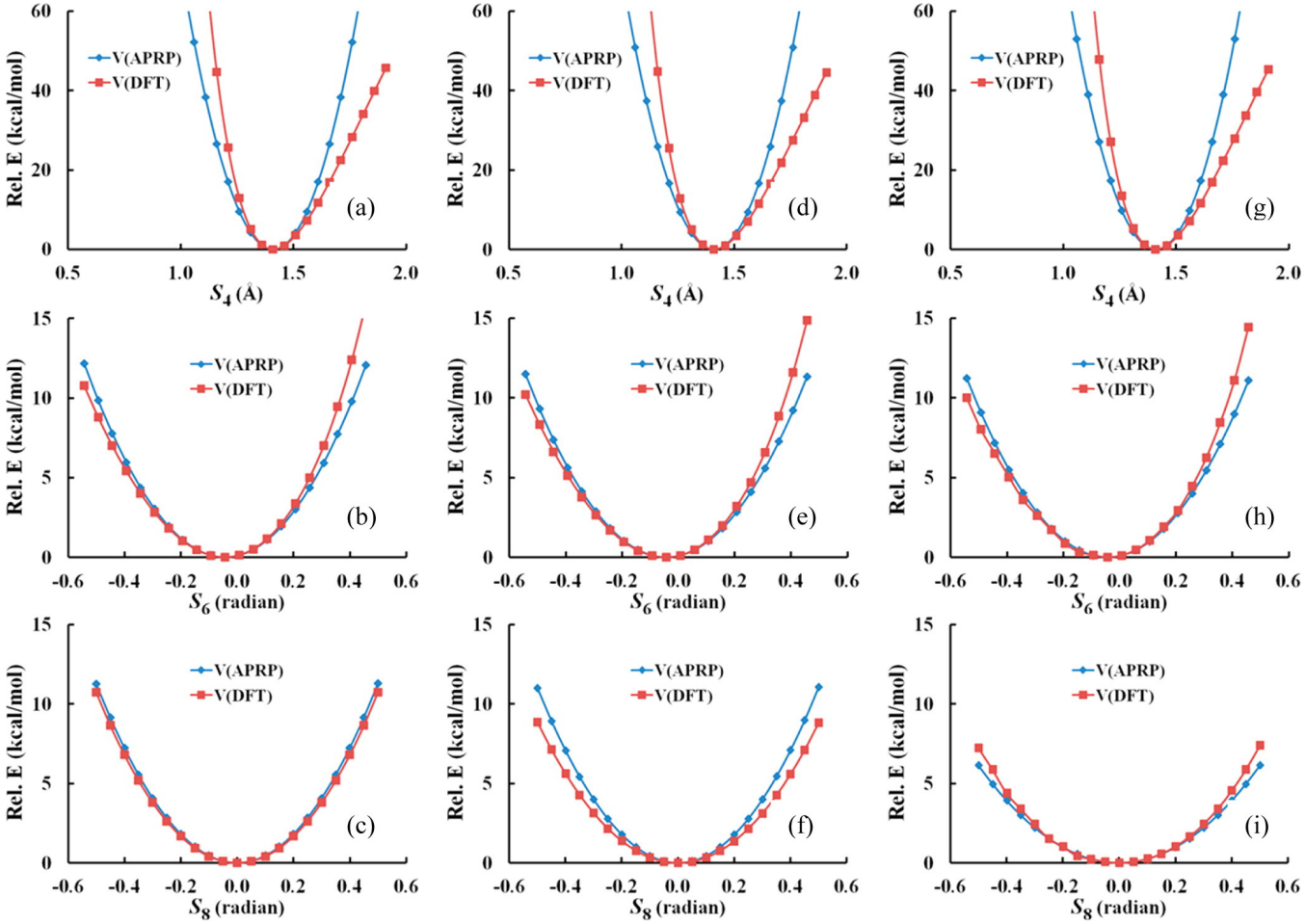

Figure 5.5. Slected slices along the degrees of freedom S_4, S_6, and S_8 (From left to right $r_{OH} = r_e$, 2.0, and 4.0 Å).

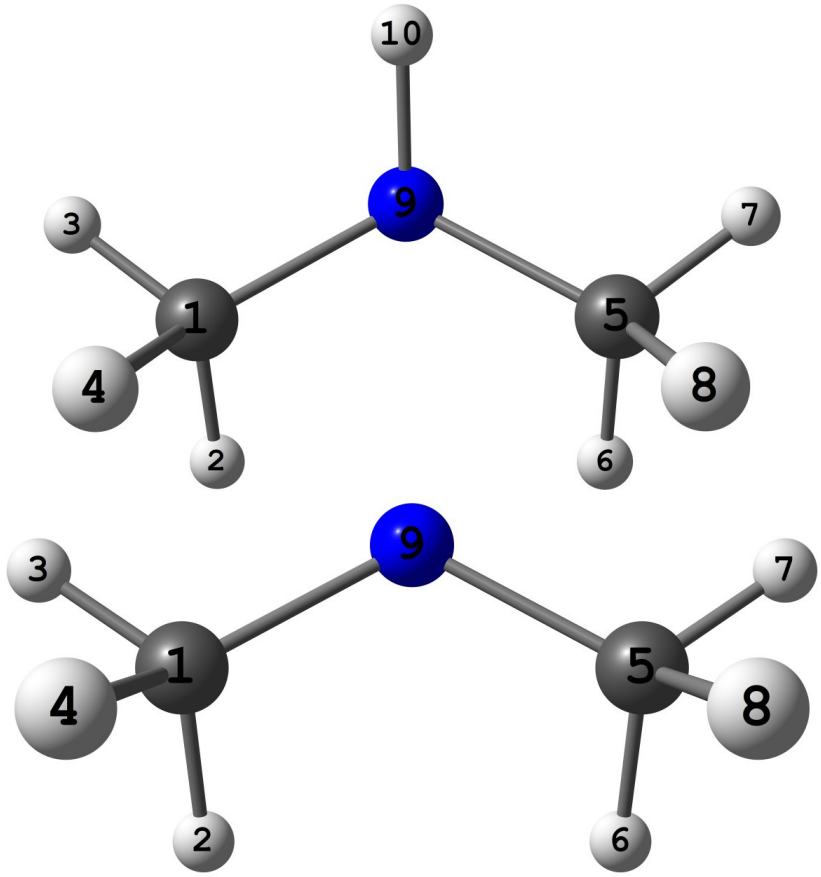

Figure 5.6 Geometries of $HN(CH_3)_2$ (top, C_s) and $N(CH_3)_2$ (bottom, C_{2v}).

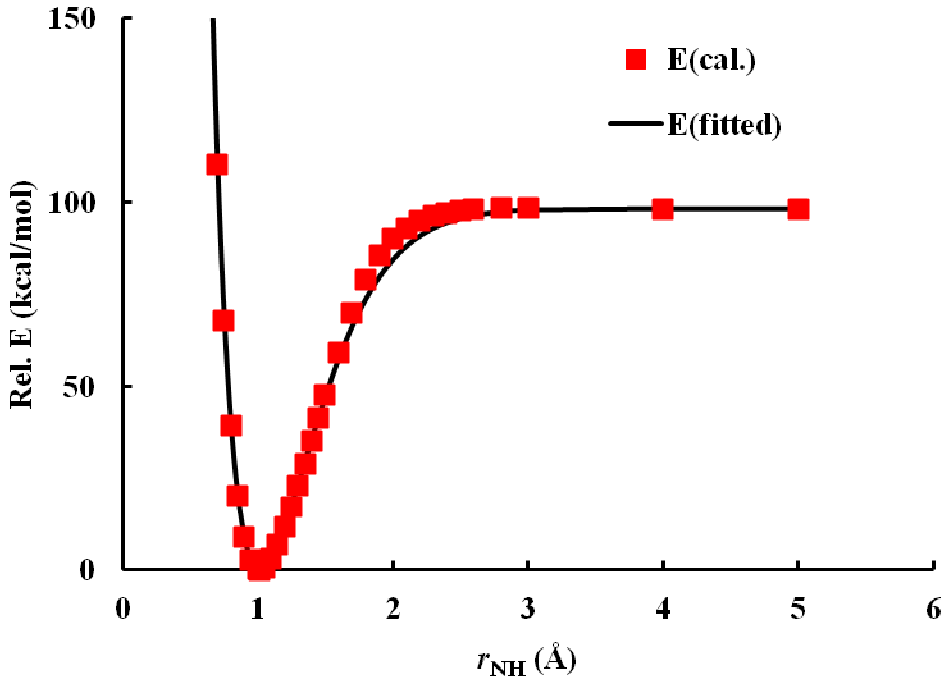

Figure 5.7. Varshini potential to describe the N−H bond dissociation in $HN(CH_3)_2$.

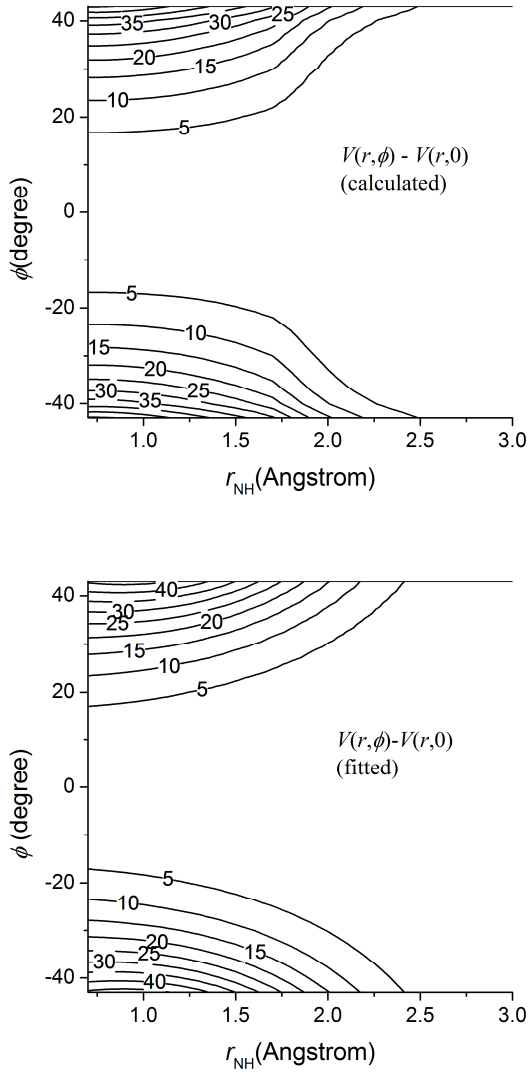

Figure 5.8. Contour plots of calculated and fitted H–N–C bending potential energies (in kcal/mol) along the N–H dissociation path.

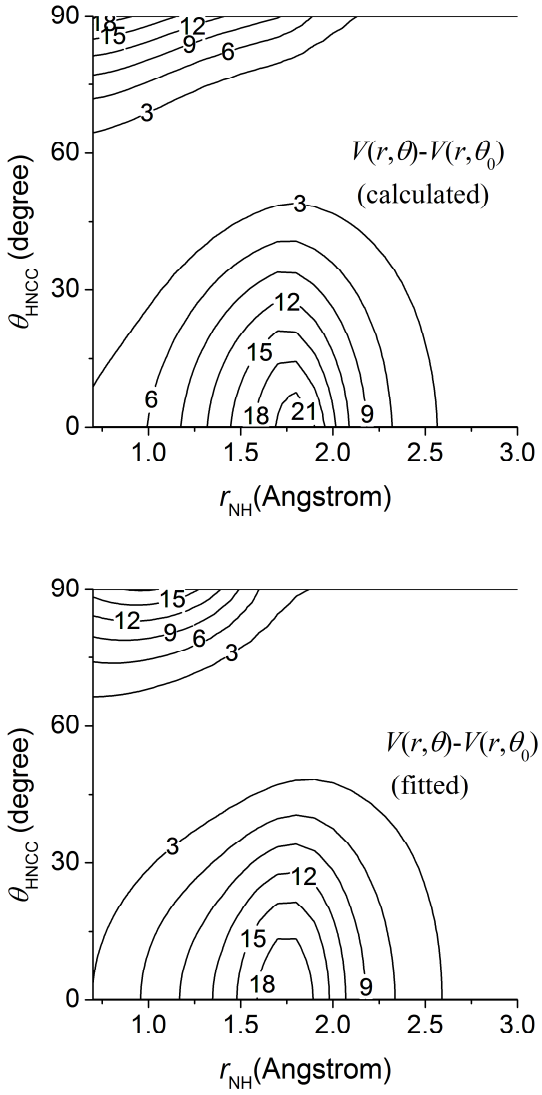

Figure 5.9. Contour plots of calculated and fitted H–N–C–C out-of-plane potential energies (in kcal/mol) along the N-H dissociation (Note that θ_0 is a function of r_{NH}).

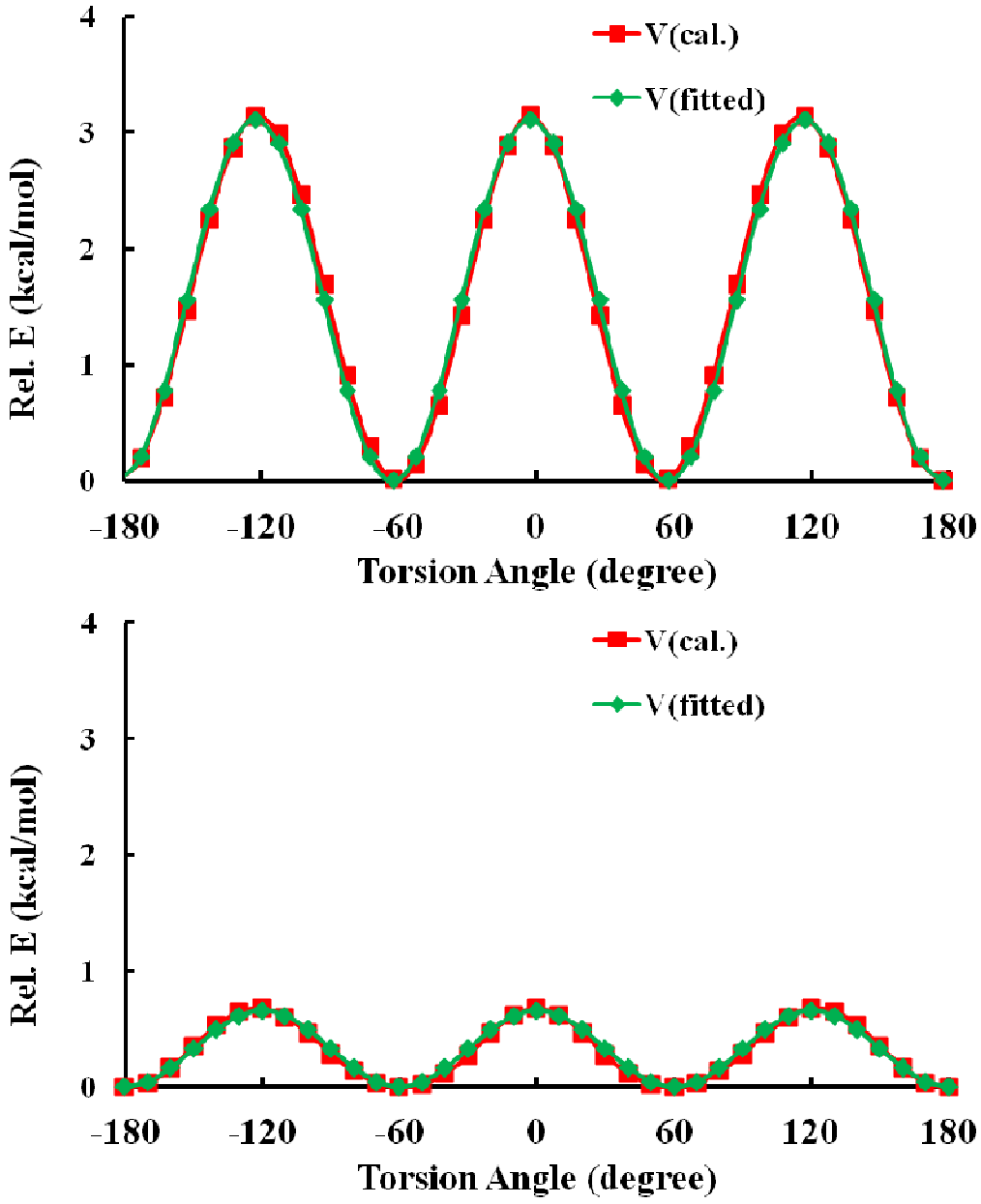

Figure 5.10. The calculated and fitted H-C-N-C torsion profiles of $HN(CH_3)_2$ (top) and $N(CH_3)_2$ (bottom).

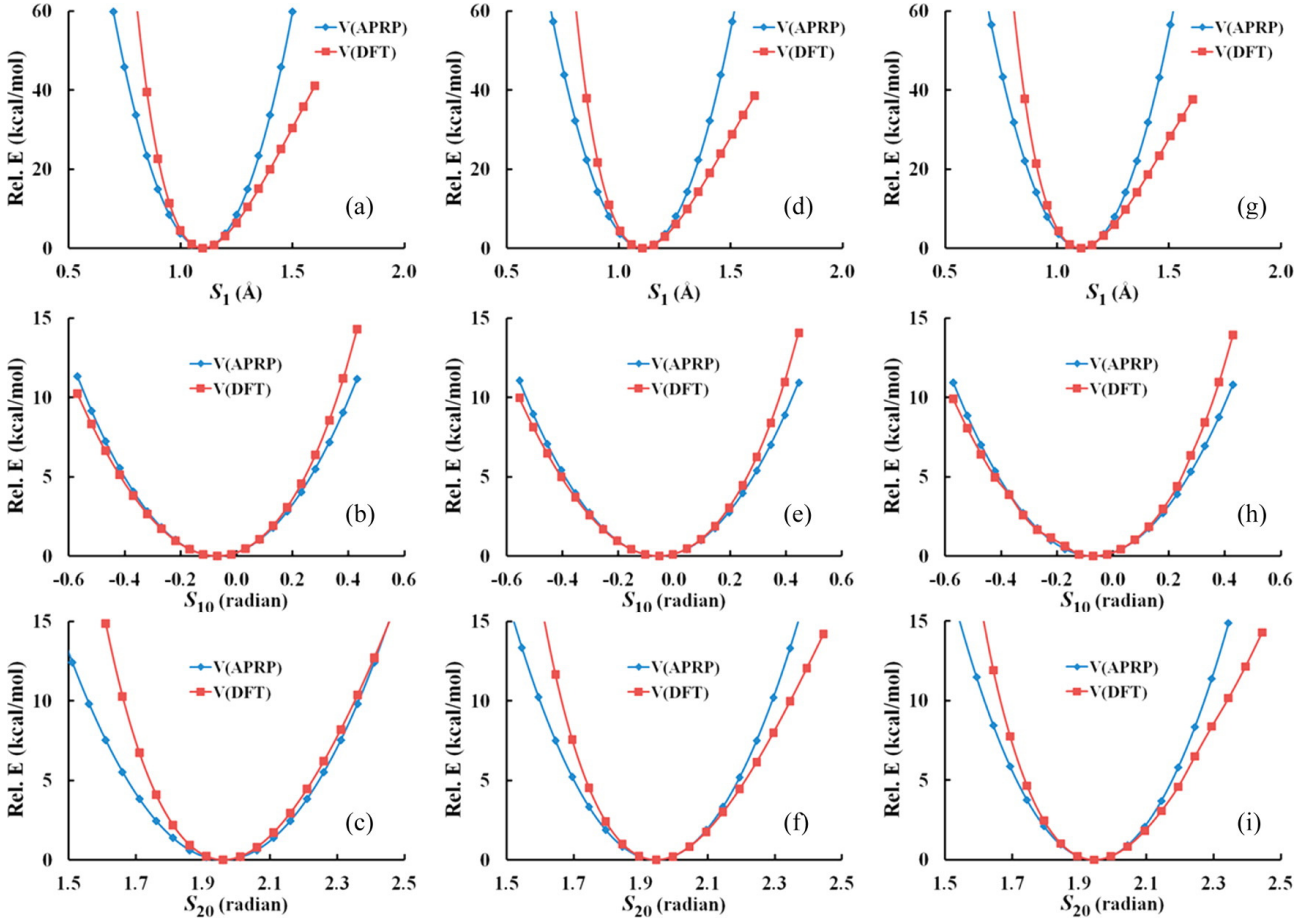

Figure. 5.11. Slices of the potential surface along the degrees of freedom S_1, S_{10}, and S_{20}. (From left to right, $r_{NH} = r_e$, 2.0, and 4.0 Å.)

Chapter 6. Full-dimensional potentials and state couplings and multidimensional tunneling calculations for the photodissociation of phenol

6.1 Introduction

By separating the electronic and nuclear degrees of freedom, the widely used Born-Oppenheimer (BO) approximation[1] leads the useful concepts of adiabatic states and potential energy surfaces (PESs). Adiabatic PESs are $(3N - 6)$-dimensional hypersurfaces (where N is the number of atoms in a molecule) with $(3N - 8)$-dimensional cuspidal ridges along conical intersection (CI) seams where two or more adiabatic PESs are degenerate. The couplings between nuclear motions and electronic motions are usually called nonadiabatic couplings, and they are responsible for nonadiabatic transitions between different adiabatic states and for the development of coherent superpositions of adiabatic electronic states as the nuclear positions evolve. Nonadiabatic couplings are usually small in regions removed from conical intersection seams and from the regions of near degeneracy surrounding them, and when they are small, nuclear motions can be treated to a good approximation as evolving on a single adiabatic PES.[2]

The BO approximation breaks down when two or more adiabatic PESs approach closely or intersect. The nonadiabatic couplings vary rapidly in such regions and become singular at CIs, thereby promoting nonadiabatic transitions in those regions. To model electronically nonadiabatic processes where two or more electronic states are coupled via nonadiabatic couplings, one can use either the adiabatic representation or a diabatic representation.[3] In the adiabatic representation, which is unique, the electronic

Hamiltonian (always defined here, as usual, to also include nuclear repulsion) is diagonal; the diagonal elements are the adiabatic PESs V_i, and the nonadiabatic couplings are vectors deriving from the action of nuclear momentum operators on the adiabatic electronic wave functions. In a diabatic representation, these vectors couplings are negligible (or assumed negligible), and diabatic electronic states and their associated PESs, U_{ii}, are coupled through scalar off-diagonal elements, U_{ij}, of the electronic Hamiltonian; these off-diagonal elements are called diabatic couplings. Diabatic states are sometimes called quasidiabatic states because strict diabatic states, in which the nuclear-momentum couplings are not just negligible but zero, do not exist in general.[4] Thus diabatic states are not uniquely defined, and many schemes have been proposed to construct diabatic states.[5-31]

Potential energy surfaces can be constructed in either the adiabatic or diabatic representation, but the cuspidal ridges of the adiabatic potentials and the singularity of nonadiabatic couplings in ubiquitous conical intersection regions[32] prevent the analytic representation of adiabatic PESs and nonadiabatic couplings. On the other hand, diabatic potentials and couplings change smoothly with respective to geometrical variations, and they allow for convenient representation. After one has the diabatic PESs available, one can carry out dynamics calculations in either the diabatic or the adiabatic representation, where the latter would be obtained from the diabatic PESs and diabatic couplings by transformations. In the present article, we develop an analytic representation of the multidimensional coupled potential energy surfaces for phenol in the diabatic representation, in particular we use potentials obtained by fourfold-way diabatization,[17,31,33] and the resulting diabatic surfaces and couplings yield the adiabatic surfaces and nonadiabatic couplings by standard equations given elsewhere.[34]

As a prototypical process in photochemistry, the photodissociation of phenol to phenoxyl radical and H atom has been studied extensively both experimentally and theoretically, especially in recent years.[33,35-55] The photodissociation of phenol involves passage through a crossing region of the $^1\pi\pi^*$ excited state and the $^1\pi\sigma^*$ state, which is repulsive along the O–H dissociation coordinate r, and this crossing region surrounds a conical intersection (CI1) of the $^1\pi\pi^*$ and $^1\pi\sigma^*$ states. The repulsive $^1\pi\sigma^*$ state further crosses the $^1\pi\pi$ ground state at another conical intersection (CI2) at larger r. Thus we need to consider three adiabatic PESs called V_i, with i = 1, 2, 3, or three diabatic PESs; the latter are the diagonal elements U_{ii} of a 3×3 matrix potential, but we call them U_i for simplicity. The roles of the two CIs in the photodissociation of phenol and of the vibrational modes that affect the probabilities of transitions at the CIs have been studied extensively, leading to stimulating insights and debates. Wave-packet studies[37,43,49,50] have been carried out to study the dynamics of phenol photodissociation, but they were performed with two-dimensional potential energy surfaces by considering only the O–H stretching coordinate and a selected coupling mode. Due to the complexity of the phenol molecule, which has 13 atoms and whose PESs are therefore 33-dimensional, only recently was there an attempt to get higher-dimensional PESs.[52] Very recently, Zhu and Yarkony constructed full-dimensional coupled PESs of phenol using a diabatic Hamiltonian whose domain of definition was constructed using quasiclassical surface hopping trajectories.[53] In the present article we present full-dimensional coupled PESs of phenol as obtained by a quite different approach. Either set of coupled PESs should be able to lead to more complete studies of the phenol photodissociation process including the key role of the phenoxyl ring vibrations.

The size of phenol prevents the use of many PES fitting approaches, such as permutation-invariant polynomials,[56-58] and the interpolated moving-least squares[59-61] method, that have been widely used for smaller systems. Here we use an improved version of our recently proposed anchor points reactive potential (APRP) method,[62] which combines general analytic forms for large-amplitude modes with molecule-specific and anchor-point-specific molecular mechanics terms for small-amplitude modes, to obtain full-dimensional semiglobal diabatic PESs for photodissociation of phenol. The improvement consists in the use of internal coordinates with better global behavior. The surfaces are based on partitioning the internal coordinates into three groups: the reaction coordinate r (also called the primary coordinate), secondary coordinates **s**, and tertiary coordinates **Q,** and the potentials are semiglobal in that they are defined for all possible values of the primary and secondary coordinates but only for small-amplitude vibrations of the tertiary coordinates away from the planar reference geometry of the phenoxyl fragment.

The geometry and atomic numbering of phenol and phenoxyl radical are shown in Fig. 6.1. (The structures mentioned in the caption of Fig. 1 will be explained more fully below.) In the present work, the O–H fission coordinate was chosen as the reaction coordinate r; the C1–O–H bond angle θ and C2–C1–O–H torsion angle ϕ were chosen as secondary coordinates; and the internal coordinates of phenoxyl were chosen as tertiary coordinates **Q**. We use smooth diabatic potentials and couplings along r and ϕ calculated previously[33] combined with new calculations of the diabatic potentials and couplings along θ and small-amplitude-vibration approximations of the dependence of the potentials on the tertiary coordinates at several anchor points (explained below).

Upon dissociation, the ground $^1\pi\pi$ state of phenol diabatically connects to the excited $\tilde{A}\ ^2B_2$ state of phenoxyl radical and H atom, while the repulsive $^1\pi\sigma^*$ state diabatically connects to the ground $\tilde{X}\ ^2B_1$ state of phenoxyl radical and H atom. These diabatic connections are apparent in Fig. 6.2, which more properly belongs in the results section but is placed here to provide the reader with a picture of the general shapes of the potential surfaces to make the presentation in Section 6.2 clearer.

6.2 Methods and computational details

6.2.1 Anchor points reactive potential (APRP) method for diabatic potentials

Here we summarize the APRP method, specializing the description to the case of phenol photodissociation. The potential of diabatic state *i* is written as

$$U_i = U_i^{[1]}(r) + U_i^{[2]}\left(\mathbf{s} \mid r\right) + U_i^{[3]}\left(\mathbf{Q} \mid r\right), \tag{6.1a}$$

where $f(x|r)$ denotes a function with a dependence on x and a parametric dependence on r, and the three terms on the right side are called the primary, secondary, and tertiary terms. General functional forms were used to fit $U_i^{[1]}$ and $U_i^{[2]}$ with tertiary coordinates fixed at reference geometries, and we take $U_i^{[2]}$ to be separable:

$$U_i^{[2]} = U_i^{[2,\phi]}\left(\phi \mid r\right) + U_i^{[2,\theta]}\left(\theta \mid r\right). \tag{6.1b}$$

The tertiary potentials are described by interpolation between preselected anchor points with tent functions:

$$U_i^{[3]} = \sum_{a=1}^{N_A} U_i^{[a]}\left(\mathbf{Q}^{[a]}\right)\, T_i^{[a]}\left(r\right), \tag{6.2}$$

where $U_i^{[a]}\left(\mathbf{Q}^{[a]}\right)$ is the expansion of the potential energy of diabatic state *i* around anchor point *a,* and $T_i^{[a]}(r)$ is the tent function at anchor point *a*.

The tent functions are defined by

$$T_i^{[1]} = \begin{cases} 1 & r < r_i^{[1]} \\ \dfrac{\left(r - r_i^{[2]}\right)^4}{\left(r - r_i^{[2]}\right)^4 + \left(r - r_i^{[1]}\right)^4} & r_i^{[1]} \le r < r_i^{[2]} \end{cases}, \tag{6.3a}$$

$$T_i^{[a]} = \begin{cases} \dfrac{\left(r - r_i^{[a-1]}\right)^4}{\left(r - r_i^{[a]}\right)^4 + \left(r - r_i^{[a-1]}\right)^4} & r_i^{[a-1]} \le r < r_i^{[a]} \\ \dfrac{\left(r - r_i^{[a+1]}\right)^4}{\left(r - r_i^{[a+1]}\right)^4 + \left(r - r_i^{[a]}\right)^4} & r_i^{[a]} \le r < r_i^{[a+1]} \end{cases} \quad \text{for } a = 2,\ldots,N_\mathrm{A} - 1, \tag{6.3b}$$

$$T_i^{[N_\mathrm{A}]} = \begin{cases} \dfrac{\left(r - r_i^{[N_\mathrm{A}-1]}\right)^4}{\left(r - r_i^{[N_\mathrm{A}]}\right)^4 + \left(r - r_i^{[N_\mathrm{A}-1]}\right)^4} & r_i^{[N_\mathrm{A}-1]} \le r < r_i^{[N_\mathrm{A}]} \\ 1 & r_i^{[N_\mathrm{A}]} \le r \end{cases}. \tag{6.3c}$$

In the present case of phenol, all diabatic calculations were carried out by fourfold-way diabatization using multi-configurational quasi-degenerate perturbation theory (MC-QDPT)[63] with the jul-cc-pVDZ basis set,[64] as described previously.[33] More specifically, we calculated the diabatic states U_1 ($^1\pi\pi$), U_2 ($^1\pi\pi^*$), and U_3 ($^1\pi\sigma^*$) along the chosen reaction coordinate *r* (O–H distance) and secondary coordinates θ (C1–O–H bond angle) and ϕ (C2–C1–O–H torsion) with other coordinates fixed, and we used these calculations to fit the primary and secondary potentials. The scans of *r* and ϕ were performed in the same way as the previous work;[33] in particular, rigid scans of the C1–O–H bend (θ, with

values of 90, 100, 107, 120, and 130°) were carried out at various r from 0.964 to 5.0 Å with other coordinates taken as the same as those obtained for the planar equilibrium geometry of ground state phenol by the complete-active-space self-consistent-field (CASSCF)[65] method with the aug-cc-pVTZ basis set[66].

Primary potentials. The primary potential of the diabatic $^1\pi\pi$ state was fit to the Varshni model potential,[67] given by

$$U_1^{[1]} = D_1\{1-(r_1/r)\exp[-\beta_1((r_1/r)^2-1)]\}^2 . \tag{6.4}$$

The diabatic $^1\pi\pi^*$ state has a minimum near the ground-state equilibrium distance r_e, and it crosses the diabatic first $^1\pi\sigma^*$ state at about 1.3 Å and a second $^1\pi\sigma^*$ state of higher energy at about 1.5 Å. For the photodissociation of phenol, the $^1\pi\pi^*$ state is only important in the small-r range, so it is acceptable to fit the $U_2^{[1]}(r)$ curve to a Morse potential[68] and we used

$$U_2^{[1]} = D_2\{1-\exp[-\alpha(r-r_2)]\}^2 + A_2 . \tag{6.5}$$

A three-term function was used to fit the repulsive potential of first diabatic $^1\pi\sigma^*$ state:

$$U_3^{[1]} = \sum_{i=1}^{3} a_i \exp[-\alpha_{3,i}(r-r_{3,i})] + A_3 . \tag{6.6}$$

Secondary potentials. The torsion potential $U_i^{[2]}(\phi\,|\,r)$ of diabatic state i is fitted with the following expression:

$$U_i^{[2,\phi]} = \sum_{j=1}^{n_j} W_{i,j}(r)(1-\cos 2\phi)^j , \tag{6.7}$$

where n_j is the number of terms to expand the torsion potential [n_j = 1 for diabatic states U_1 and U_2 ($^1\pi\pi$ and $^1\pi\pi^*$) and n_j = 2 for diabatic state U_3 ($^1\pi\sigma^*$)], and $W_{i,j}$ is the barrier

height of the *j*th term. The latter was expanded as a linear combination of Gaussian functions, given by

$$W_{i,j} = \sum_{k=1}^{n_k} A_{i,j,k} \exp[-\alpha_{i,j,k}(r - r_{i,j,k})^2]. \tag{6.8}$$

In fitting the C1–O–H bending potentials, we used $\cos\theta$ rather than θ in order to have the proper symmetry of bend potentials with respect to $\pi - \Delta\theta$ and $\pi + \Delta\theta$:

$$U_i^{[2,\theta]} = \sum_{j=2}^{n_j} k_{i,j}(r)(\cos\theta - \cos\theta_{i,0}(r))^j \tag{6.9}$$

The force constant $k_{i,j}$ was further expanded with linear combinations of Gaussians similar to eq. 6.8. A hyperbolic tangent function is used to fit the dependence of $\cos\theta_{i,0}$ on r:

$$\cos\theta_{i,0} = \cos\theta_{i,1} + \frac{1 + \tanh(a_{i,1}(r - r_{i,1}))}{2}(\cos\theta_{i,2} - \cos\theta_{i,1}) \tag{6.10}$$

where $\cos\theta_{i,1}$ and $\cos\theta_{i,2}$ are constant parameters.

Tertiary potentials. Now we turn to $U_i^{[3]}$, which depends on tertiary coordinates and depends parametrically on *r* through the use of anchor points. The dependence of the diabatic potentials on tertiary coordinates is needed only for small extensions from planar geometries. For planar geometries, the diabatic states U_1 ($^1\pi\pi$), U_2 ($^1\pi\pi^*$), and U_3 ($^1\pi\sigma^*$) belong to the A′, A′, and A″ irreducible representations, respectively, and as shown in Fig. 6.2, the two states with same symmetries are always well separated, while the intersecting diabatic states along the reaction coordinate *r* have different symmetries; thus the adiabatic states are good approximations to the diabatic states under the C_s symmetry constraint of the planar geometries. Hence we chose anchor points with planar structures

and obtained the diabatic states at each anchor point by adiabatic calculations of the correct symmetry as described next.

For diabatic states U_1 ($^1\pi\pi$) and U_3 ($^1\pi\sigma^*$), since they are the lowest states of their symmetry, we utilize ground-state Kohn-Sham calculations with the M06-2X exchange-correlation potential[69] and the jul-cc-pVDZ basis set to perform partial optimization (optimizing all secondary and tertiary coordinates for fixed r) and calculate the Hessians at each of the anchor points. For diabatic state U_2 ($^1\pi\pi^*$), since it is an excited state (S_1) in A′ symmetry, time-dependent density functional theory (TDDFT)[70,71] was used to perform the partial optimization and Hessian calculations, again with the M06-2X exchange-correlation potential and the jul-cc-pVDZ basis set.

For each diabatic state, four planar anchor points were chosen along the O–H dissociation coordinate; for U_1, they are at r = 0.964, 1.32, 2.00, and 5.00 Å, and for U_2 and U_3, they are at r = 0.964, 1.32, 2.26, and 5.00 Å. The first anchor point for each of the diabatic states has the ground-state equilibrium O–H bond length calculated by CASSCF/jul-cc-pVDZ; the second anchor point was chosen to have an O–H bond length close to the first conical intersection (CI1) in planar geometry; the third anchor points were chosen to have an O–H bond length close to the second conical intersection (CI2); and the final anchor points were chosen to yield the correct asymptotic limit of phenoxyl radical.

The ground state of phenoxyl is $\tilde{X}\ ^2B_1$ and it has a low-lying $\tilde{A}\ ^2B_2$ excited state; these states connect diabatically to surfaces U_3 ($^1\pi\sigma^*$) and U_1 ($^1\pi\pi$), respectively, and they were optimized with UM06-2X/jul-cc-pVDZ. The geometric parameters and Hessians of phenoxyl in these two states were used for the final anchor points with r =

5.00 Å. For anchor points with other O–H bond lengths, geometrical parameters and Hessians were obtained with partial optimizations. Since U_2 state is not very relevant after the first conical intersection (CI1), the geometrical parameters and Hessian elements at r = 1.32 Å were used for it at the next two anchor points r = 2.26 Å and 5.00 Å.

In our original APRP, the tertiary potential around anchor point a was expanded as

$$U_i^{[a]} = U_{\mathrm{rel},i}^{[a]} + \frac{1}{2}\mathbf{Q}_i^{[a]\mathsf{T}}\mathbf{F}_i^{[a]}\mathbf{Q}_i^{[a]}, \tag{6.11}$$

where $U_{\mathrm{rel},i}^{[a]}$ is the energy of state i at the partially optimized geometry of anchor point a, relative to the energy of a fixed reference geometry, $\mathbf{F}_i^{[a]}$ is the partial force constant matrix, and $\mathbf{Q}_i^{[a]}$ is a column vector of the internal displacements around anchor structure a with elements

$$Q_{ji}^{[a]} = Q_j - Q_{\mathrm{e},ji}^{[a]}, \tag{6.12}$$

where Q_j is an internal coordinate, and $Q_{\mathrm{e},ji}^{[a]}$ is the optimized value of Q_j for state i in the constrained optimized geometry of anchor point a. By partitioning internal displacements $\mathbf{Q}_i^{[a]}$ into stretches (S), bends (B), and torsions (T), eq 6.11 can be written as

$$U_i^{[a]} = U_{\mathrm{rel},i}^{[a]} + U_i^{\mathrm{SS},a} + U_i^{\mathrm{BB},a} + U_i^{\mathrm{TT},a} + U_i^{\mathrm{SB},a} + U_i^{\mathrm{ST},a} + U_i^{\mathrm{BT},a}, \tag{6.13}$$

where the SS, BB, and TT terms are the potentials from bond stretches, bond angle bends, and torsions, and the SB, ST, and BT terms are the potentials from stretch–bend couplings, stretch–torsion couplings, and bend–torsion couplings, respectively. The force

constant matrices in the terms of eq. 6.13 are respectively called $\mathbf{F}_i^{\mathrm{SS},a}$, $\mathbf{F}_i^{\mathrm{BB},a}$, $\mathbf{F}_i^{\mathrm{TT},a}$, $\mathbf{F}_i^{\mathrm{SB},a}$, $\mathbf{F}_i^{\mathrm{ST},a}$, and $\mathbf{F}_i^{\mathrm{BT},a}$.

In the current application of APRP to the construction of diabatic PESs of phenol, instead of using simple internal displacements $\mathbf{Q}_i^{[a]}$, we used variables with better global behaviors.

For bond stretches, instead of $r - r_e$, we use $R = (r - r_e)/r$. This coordinate was originally proposed by Simons, Parr, and Finlan (SPF)[72] for diatomic molecules. The use of SPF coordinates includes anharmonic effects and corrects the over-repulsion for large bond length ($r > r_e$) and under-repulsion for short bond length ($r < r_e$) of widely used force fields using $r - r_e$.

For bond angle bends, instead of $\theta - \theta_e$, we use $\cos\theta_e - \cos\theta$ to preserve the continuity when the bond angle crosses π.

For torsions, $\phi - \phi_e$ is replaced with $\sin\frac{n(\phi-\phi_e)}{2}$ or $\sin n(\phi-\phi_e)$ (depending on whether it is a diagonal or off-diagonal term) to maintain the correct periodicity behavior, where n is an integer number that indicates the local periodicity of the torsion. For phenol, the torsions in the phenoxyl ring all have $n = 1$.

With the new choice of variables, the terms in eq. 6.13 can be written explicitly as

$$U_i^{\mathrm{SS},a} = \frac{1}{2}\sum_{j=1}^{N_S} k_{jj,i}^{\mathrm{SS},a}\left(\frac{r_j - r_{e,ji}^{[a]}}{r_j}\right)^2 + \frac{1}{2}\sum_{j=1}^{N_S}\sum_{k\neq j}^{N_S} k_{jk,i}^{\mathrm{SS},a}\left(\frac{r_j - r_{e,ji}^{[a]}}{r_j}\right)\left(\frac{r_k - r_{e,ki}^{[a]}}{r_k}\right), \qquad (6.14a)$$

$$U_i^{\mathrm{BB},a} = \frac{1}{2}\sum_{j=1}^{N_\mathrm{B}} k_{jj,i}^{\mathrm{BB},a}(\cos\theta_j - \cos\theta_{\mathrm{e},ji}^{[a]})^2 + \frac{1}{2}\sum_{j=1}^{N_\mathrm{B}}\sum_{k\neq j}^{N_\mathrm{B}} k_{jk,i}^{\mathrm{BB},a}(\cos\theta_{\mathrm{e},ji}^{[a]} - \cos\theta_j)(\cos\theta_{\mathrm{e},ki}^{[a]} - \cos\theta_k) \quad , \tag{6.14b}$$

$$U_i^{\mathrm{TT},a} = \frac{1}{2}\sum_{j=1}^{N_\mathrm{T}} k_{jj,i}^{\mathrm{TT},a}\sin^2\frac{n_j\left(\phi_j - \phi_{\mathrm{e},ji}^{[a]}\right)}{2} + \frac{1}{2}\sum_{j=1}^{N_\mathrm{T}}\sum_{k\neq j}^{N_\mathrm{T}} k_{jk,i}^{\mathrm{TT},a}\sin n_j(\phi_j - \phi_{\mathrm{e},ji}^{[a]})\sin n_k(\phi_k - \phi_{\mathrm{e},ki}^{[a]}) \quad , \tag{6.14c}$$

$$U_i^{\mathrm{SB},a} = \sum_{j=1}^{N_\mathrm{S}}\sum_{k=1}^{N_\mathrm{B}} k_{jk,i}^{\mathrm{SB},a}\frac{r_j - r_{\mathrm{e},ji}^{[a]}}{r_j}(\cos\theta_{\mathrm{e},ki}^{[a]} - \cos\theta_k), \tag{6.14d}$$

$$U_i^{\mathrm{ST},a} = \sum_{j=1}^{N_\mathrm{S}}\sum_{k=1}^{N_\mathrm{T}} k_{jk,i}^{\mathrm{SB},a}\frac{r_j - r_{\mathrm{e},ji}^{[a]}}{r_j}\sin n_k(\phi_k - \phi_{\mathrm{e},ki}^{[a]}), \tag{6.14e}$$

$$U_i^{\mathrm{BT},a} = \sum_{j=1}^{N_\mathrm{B}}\sum_{k=1}^{N_\mathrm{T}} k_{jk,i}^{\mathrm{BT},a}(\cos\theta_{\mathrm{e},ji}^{[a]} - \cos\theta_j)\sin n_k(\phi_k - \phi_{\mathrm{e},ki}^{[a]}). \tag{6.14f}$$

Note that in eq. 6.14c, $\sin\frac{n(\phi-\phi_e)}{2}$ is used to build the local periodicity for the diagonal terms, while $\sin n(\phi-\phi_e)$ is used to replace $\phi-\phi_e$ in cross terms.

The force constants in eqs. 6.14a to 6.14f are related to the Hessian elements in eq. 6.13 by

$$k_{jk,i}^{\mathrm{SS},a} = F_{jk,i}^{\mathrm{SS},a} r_{e,ji}^{[a]} r_{\mathrm{e},ki}^{[a]},$$

$$k_{jk,i}^{\mathrm{BB},a} = \frac{F_{jk,i}^{\mathrm{BB},a}}{\sin\theta_{e,ji}^{[a]}\sin\theta_{\mathrm{e},ki}^{[a]}},$$

$$k_{jj,i}^{\mathrm{TT},a} = \frac{4F_{jj,i}^{\mathrm{TT},a}}{n_j^2},$$

$$k_{jk,i}^{\mathrm{TT},a} = \frac{F_{jk,i}^{\mathrm{TT},a}}{n_j n_k} \text{ for } j \neq k,$$

$$k_{jk,i}^{\mathrm{SB},a} = \frac{F_{jk,i}^{\mathrm{SB},a} r_{e,ji}^{[a]}}{\sin\theta_{\mathrm{e},ki}^{[a]}},$$

$$k_{jk,i}^{\mathrm{ST},a} = \frac{F_{jk,i}^{\mathrm{ST},a} r_{e,ji}^{[a]}}{n_k},$$

and

$$k_{jk,i}^{\mathrm{BT},a} = \frac{F_{jk,i}^{\mathrm{BT},a}}{\sin\theta_{\mathrm{e},ki}^{[a]} n_k}.$$

With our new choice of variables to describe bond stretches, bond angle bends, and torsions, eqs. 6.14 have much better behavior than the terms used previously for large distortions, although they require no more information. Thus, we recommend using them to construct force fields in the future.

In addition to the above terms, we added a repulsive Born-Mayer potential between all pairs (1-4, 2-5, and 3-6) of para carbon atoms to all three diabatic potentials (see Fig. 6.1 for atomic numbering); this prevents the nonbonded atoms from getting too close during trajectories. The Born-Mayer potential is given as

$$V_{\mathrm{BM}} = B \sum_{\mathrm{X-Y}=1-4,2-5,3-6} \exp(-\alpha r_{\mathrm{X-Y}}) \tag{6.15}$$

where the interaction parameters are taken from the literature:[73] B is 42000 kcal mol^{-1}, and α is 3.58 Å.

6.2.2 Diabatic couplings

The diabatic coupling U_{12} of diabatic state U_1 ($^1\pi\pi$) to diabatic state U_2 ($^1\pi\pi^*$) is not considered here (i.e., is set to zero) since the energy separation between those two states is quite large at all considered geometries. By symmetry, there is no contribution to diabatic couplings U_{13} and U_{23} from the in-plane vibrational coordinates of planar phenol. So we need only consider the contribution of out-of-plane modes to the diabatic couplings U_{13} and U_{23}. Phenol has ten out-of-plane coordinates, nine in the phenoxyl ring plus the C2–C1–O–H torsion ϕ. The nine out-of-plane phenoxyl coordinates we use (labeled S_1 to S_9) are similar to those used by Pongor *et al.*[74] These coordinates are given in Table 6.1.

In a similar spirit to that used in the APRP representations of the diabatic potentials, the diabatic couplings are expressed as

$$U_{ij} = U_{ij}^{[3,\mathbf{S}]}(\mathbf{S} \mid r) + U_{ij}^{[2,\phi]}(\phi \mid r), \tag{6.16}$$

where $U_{ij}^{[2,\phi]}$ is fitted to MC-QDPT data, and $U_{ij}^{[3,\mathbf{S}]}$is constructed by interpolating linear expansions around anchor structures with tent functions:

$$U_{ij}^{[3,\mathbf{S}]} = \sum_{a=1}^{N_A} \left(U_{ij,a}^{[0]} + \sum_{\alpha=1}^{9} A_{ija\alpha} S_\alpha \right) T_a(r), \tag{6.17}$$

where $U_{ij,a}^{[0]}$ is a constant parameter for anchor structure *a*, and $T_a(r)$ is the tent function with the same form as $T_i^{[a]}(r)$ used for tertiary potential. The parameter $A_{ija\alpha}$ in the representation of diabatic coupling U_{ij} equals the first partial derivative of U_{ij} with respect to S_α at anchor structure *a*. Four planar anchor points with other geometric

parameters fixed at CASSCF/aug-cc-pVTZ optimized ground state minimum were chosen along the O–H dissociation coordinate, and they are the same for both diabatic couplings: r = 0.964, 1.32, 2.26, and 5.00 Å. Since diabatic coupling U_{23} and U_{13} are important near the first conical intersection (near anchor point 2) and the second conical intersection (near anchor points 3), respectively, the gradients $A_{23a\alpha}$ (α = 1 to 9) and $A_{13a\alpha}$ (α = 1 to 9) were calculated numerically (with a step size of 10 degree) from MC-QDPT/jul-cc-pVDZ fourfold way calculations for anchor points 2 and 3, respectively. The gradients of diabatic couplings were set to zero for anchor points away from the relevant conical intersections.

To fit $U_{13}^{[2,\phi]}$ and $U_{23}^{[2,\phi]}$, flexible and general functional form needs to be used. As discussed previously, both of these couplings are zero at $\phi = 0°$ due to symmetry. At $\phi =$ 90°, the phenol molecule also has C_s symmetry and in this case, three diabatic states U_1 ($^1\pi\pi$), U_2 ($^1\pi\pi^*$), and U_3 ($^1\pi\sigma^*$) belong to A′, A″, and A′, respectively. Only $U_{23}^{[2,\phi]}$ would be zero at $\phi = 90°$ due to symmetry. We use the following functional forms to fit $U_{13}^{[2,\phi]}$ and $U_{23}^{[2,\phi]}$

$$U_{13}^{[2,\phi]} = \sum_{\eta=1}^{3} a_\eta(r)\sin^{2\eta-1}\phi, \tag{6.18a}$$

$$U_{23}^{[2,\phi]}(\phi \mid r) = \sum_{\eta=1}^{3} a_\eta(r)\sin 2\eta\phi, \tag{6.18b}$$

where $a_\eta(r)$ is fitted with a linear combination of N Gaussians:

$$a_\eta = \sum_{m=1}^{N} A_{\eta,m} \exp[-\alpha_{\eta,m}(r - r_{\eta,m})] \tag{6.19}$$

Three Gaussian functions were used to fit a_1 in eq. 6.18a, and two Gaussian functions were used to fit a_2 and a_3 in eq. 6.18a. All a_η (η = 1, 2, and 3) in eq. 6.18b were fitted with one Gaussian function.

6.2.3 Adiabatic potentials and nonadiabatic couplings

With diabatic potentials and couplings fitted in internal coordinates, the analytic Cartesian gradients of diabatic potentials and diabatic couplings $\nabla_n U_{ij}$ (n = 1, …, 3N) are evaluated straightforwardly by using Wilson B-matrices.[62] The adiabatic potential energies V_i are the eigenvalues of diabatic potential energy matrix **U** and can be obtained by diagonalizing the **U** matrix. The analytic Cartesian gradients of the adiabatic potentials $\nabla_n V_i$ and the nonadiabatic couplings $\mathbf{F}_{ij}$ are[34]

$$\nabla_n V_i = \sum_{j,k} c_{ij}^* c_{jk} \nabla_n U_{jk}\,, \tag{6.20}$$

and

$$\mathbf{F}_{ij} = \begin{cases} \dfrac{1}{V_j - V_i} \sum_{k,l} c_{ik}^* c_{jl} \nabla_n U_{kl} & (i \neq j) \\ 0 & (i = j) \end{cases}, \tag{6.21}$$

where n = 1, …, 3N and c_{ij} is the element of orthogonal matrix **C** that diagonalizes the diabatic potential matrix **U**.

6.2.4 Additional computational details

The reference orbitals and diabatic prototypes employed in the MC-QDPT fourfold-way diabatizations are specified in Ref. 33. These calculations were performed with *HONDOPLUS*.[75]

For fitting the tertiary potential, the adiabatic partial optimizations and Hessian calculations at anchor points were performed by Kohn-Sham density functional theory with the M06-2X exchange-correlation functional and the jul-cc-pVDZ basis set with ultrafine grids with *Gaussian09*.[76]

The geometry optimizations and frequency analyses of equilibrium and transition structures were performed by the *POLYRATE* program[77] with the APRP surfaces. The geometry of the minimum energy conical intersection (MECI) between adiabatic states V_i and V_j was obtained by minimizing the penalty function $F = \frac{1}{2}(V_i + V_j) + \alpha(V_i - V_j)^2$ with $\alpha = 10^5\ E_h^{-1}$ (where $E_h = 1$ hartree).

We ran thousands of sample dissociative coupled-surface trajectories to confirm that the final versions of the coupled potential energy surfaces conserve energy and angular momentum and do not visit regions of configuration space where the surfaces yield unphysical results. These calculations were carried out with the *ANT* program.[78]

6.3 RESULTS AND DISCUSSION

6.3.1 Equilibrium geometries

The bond lengths and bond angles of the $^1\pi\pi$ and $^1\pi\pi^*$ state of phenol and the $^2B_1$ and $^2B_2$ states of phenoxyl radical are given Tables 6.2, 6.3, and 6.4. For the $^1\pi\pi$ state of phenol, the experimental geometry is available by microwave spectroscopy[79] and

electron-diffraction.[80] The geometry of the $^1\pi\pi^*$ state of phenol is available from simultaneous fit to the vibronic intensities and effective rotational constants.[81] No experimental bond lengths and bond angles are available for phenoxyl radical, and theoretical results[82] obtained by CASPT2 calculations with 9 active electrons in 8 active orbitals with the aug-cc-pVTZ basis set are listed for comparison. Due to the use of Born-Mayer repulsion of para-situated C atoms to avoid unphysical behavior in test trajectory calculations, the C–C bond lengths optimized with our APRP surface are slightly larger than the M06-2X results, but the tables show that both are in very good agreement with the literature[79-82] results. The C1–O bond of ground-state phenol is a typical single bond, having the bond length of 1.365 Å. The C–C bond lengths increase from ~1.40 Å in the ground state phenol to ~1.43 Å in the S_1 state of phenol, suggesting the benzene ring is expanded upon excited to the S_1 state.

The excited $^2B_2$ state of phenoxyl radical resembles the ground-state geometry of phenol (to which it connects diabatically) in that it has all C–C bond distances around 1.40 Å and a C1–O bond length of 1.33 Å. However, the equilibrium geometry of the ground state ($^2B_1$) of phenoxyl radical differs significantly from the geometries of both the $^1\pi\pi$ state of phenol and the $^2B_2$ state of phenoxyl radical. The ground state of phenoxyl radical has a geometry similar to that of a quinone, with much shorter C1–O bond length of 1.246 Å, and the C–C bond lengths are less symmetrical, with 1.461 Å for C1–C2 and C1–C6, 1.379 Å for C2-C3 and C5–C6, and 1.416 Å for C3–C4 and C4–C5, comparable to the C–O bond length (1.222 Å) and two C–C bond lengths (1.334, and 1.477 Å) in 1,4-benzoquinone.[83] The vibrational frequencies of the ground-state adiabatic surface were calculated at the minimum-energy geometries of the APRP surface,

and they are compared in Fig. 6.3 to M06-2X frequencies and available experimental fundamental frequencies of phenol[84] and phenoxyl radical.[85] The frequencies calculated with our adiabatic PES reproduce the M06-2X results, both overestimating the experimental frequencies slightly. The overestimate by M06-2X is consistent with known trends,[86] but nevertheless we did not scale the density functional frequencies or Hessians in the present work.

6.3.2 Energetics and thermal rate constants

The adiabatic vertical excitation energies of phenol and phenoxyl radical calculated with the APRP PESs are shown and compared with previous theoretical and available experimental results in Table 6.5. Experimentally, the spectrum for the optically allowed excitation of phenol from its ground state to the $^1\pi\pi^*$ state has a maximum at 4.58 eV.[87] The excitation to the $^1\pi\sigma^*$ state is electric dipole forbidden, and no reliable experimental result is available. Previous high-level ab initio studies suggested that the vertical excitation energy of the $^1\pi\sigma^*$ state should in the range 5.6-5.9 eV. [33,44,50] Our APRP surface predicts vertical excitation energies to be 4.58 and 5.88 eV for excitations to the $^1\pi\pi^*$ state and the $^1\pi\sigma^*$ state, respectively, in good agreement with these reference values. In comparison to these results, the MC-QDPT/jul-cc-pVDZ results that were used in the construction of primary and secondary potential yield vertical excitation energies of 4.70 and 5.86 eV for the two states of phenol.[33] The slight difference between the APRP and MC-QDPT values is a result of the different equilibrium geometry of phenol used in the calculations. The CASSCF/aug-cc-pVTZ optimized geometry was used in the calculation with MC-QDPT while the equilibrium geometries of the APRP surface were used for the APRP result. The fact that the APRP agrees slightly better with the reference values is just a fortuitous result of this technical shift in geometric parameters.

The excitation energy of ground state phenoxyl radical to the $^2B_2$ state was first determined to be 1.06 eV in a gas-phase ultraviolet photoelectron spectroscopy experiments.[88] It was later observed to be 1.10 eV by UV-VIS and IR polarization spectroscopy of phenoxyl radical in cryogenic argon matrices.[89] The excitation energy of phenoxyl radial from the $^2B_1$state to the $^2B_2$ state calculated by our APRP surface is 1.07 eV, agreeing quite well with experimental results.

The equilibrium dissociation energy of the O–H bond calculated from the APRP PES is 3.93 eV, which is smaller than the experimentally derived D_e,[33,90,91] as shown in Table 6.5.

The classical adiabatic excitation energy, i.e., the energy of the S_1 state minimum minus that of the S_0 state minimum on the APRP surfaces was calculated to be 4.42 eV. We can calculate the quantal adiabatic excitation energy, i.e., the 0_0^0 energy, which is the energy of the S_1 zero point level minus that of the S_0 zero point level on the APRP surfaces, by adding the S_1 zero point energy (2.66 eV) and subtracting the S_0 zero point energy (2.85 eV); that yields 4.22 eV. This may be compared to the experimental value[50] of 4.51 eV.

Although there has been considerable emphasis on the location of the conical intersection, we should keep in mind that there is generally a saddle point on the lower adiabatic surface on the side of a conical intersection,[92] and for some purposes the characteristics of this saddle point are equally important or more important than the characteristics of the conical intersection. The transition state (i.e., saddle point) for H dissociation on the first excited adiabatic state surface was located, with a classical barrier height of 0.72 eV with respect to the S_1 minimum (or 5.14 eV with respect to the

S_0 minimum). At the saddle point geometry, the energies of the S_0 and S_2 states of phenol are 1.66 and 5.95 eV, respectively. The large energy gap (0.81 eV) between the S_1 and S_2 states at the saddle point suggests that an adiabatic model of dissociation on the S_1 surface might be a good zero-order model for the early dynamics of H-dissociation. The transition state has two nonplanar structures, which are mirror images, with C2–C1–O–H torsion angles of -20.5 and 20.5°. As shown in Fig. 6.1, the C–C and C–O bond lengths in the transition state structures are very close to those in the ground state phenoxyl radical. The O–H bond length of the transition state structures is 1.33 Å, close to 1.32 Å at which value the S_1 and S_2 states of phenol intersect for planar geometry at the MC-QDPT level.[33] The imaginary frequency at the saddle point is $4254i$ cm^{-1}, which is rather high because the reduced mass for hydrogenic dissociation is low and because the saddle point is so close to a conical intersection. (A barrier due to a CI may be thin because the CI is pointy at the top, as compared to flat for a saddle point.) The minimum energy path in mass-scaled (i.e., isoinertial) coordinates[93,94] (MEP) was calculated using the Page-McIver algorithm,[95] and the calculated potential energy V_{MEP} along the MEP is shown in Fig. 6.4a. The abscissa of this figure is the reaction coordinate *s*, defined as the distance along the curved MEP through the isoinertial coordinates scaled to a reduced mass of 1 amu. We already noted the high imaginary frequency, which shows that the barrier is thin at the top, but Fig. 6.4a shows it is thin farther down as well. In fact, the V_{MEP} barrier of photodissociation of phenol on the S_1 excited state surface is much thinner than V_{MEP} curves of typical chemical reactions, consistent with the large imaginary frequency.

The zero point vibrational energy of the saddle point is 2.58 eV, as compared to the zero point vibrational energy of 2.66 eV for the equilibrium structure on S_1. The ground-state vibrationally adiabatic potential (V_a^G) curve is defined as the sum of V_{MEP} and the zero point energy of modes transverse to the reaction path; this potential is important because it serves as an effective potential energy for vibrationally adiabatic tunneling.[93-100] The ground-state vibrationally adiabatic barrier V_a^G along the S_1 surface of phenol is shown in Fig. 6.4b. The sum of the potential energy and the zero point energy at the saddle point is 3.30 eV, and the maximum value of this sum (i.e., of the ground-state vibrationally adiabatic potential) is also 3.30 eV, and this occurs very close to the saddle, at s = –0.004 Å, where r_{OH} = 1.32 Å. Only two states (n = 0 and n = 1) of the O–H stretching mode have energies below the barrier as shown in Fig. 6.4b.

Figure 6.4b can be used to illustrate the thinness of the effective barrier for tunneling by comparing it to that for the H + H_2 hydrogen-exchange reaction. The ground-state vibrationally adiabatic potential (V_a^G) curve for the H + H_2 reaction is shown in Fig. 3 of a previous paper.[101] In that figure, as in the present article, the reaction coordinate is scaled to 1 amu, so it is meaningful to compare the widths of the barriers. Examination of V_a^G for the H + H_2 reaction at an energy 0.10 eV below the barrier top shows a width of 0.7 Å, whereas the width of V_a^G in Fig. 6.4b at an energy 0.10 eV below the barrier top is only 0.12 Å, a factor of six thinner. This is certainly a dramatic difference. This may uncover a previously unappreciated general phenomenon, namely that barriers close to conical intersections may sometimes be very thin, allowing considerable tunneling on the lower surface at energies below the barrier.

Figure 6.4c shows the minimum energy reaction path is roughly divided into two stages, first the torsion angle changes with approximately constant O-H distance, then the O-H bond breaks at roughly constant torsion angle. If we consider the MEP in the downward direction, this means that the MEP approaches the minimum along the lowest-frequency normal mode, which is the expected result.[102,103] When the reaction path changes from the O–H stretch to the torsion, the potential energy barrier becomes more gradual (the rise from the equilibrium geometry is less steep along a low-frequency mode than along a high-frequency one). Although this change in character of the MEP and the associated V_{MEP} is interesting mechanistically, it has little effect on the tunneling because, as shown in Fig. 6.4, the change of character of the reaction path to be the torsion occurs for $s < -0.3$ Å, whereas the tunneling occurs in the region with $s > -0.3$ Å. If the change in character of the MEP were to occur at higher energy, the barrier would not retain its thin shape all the way down to the lowest tunneling energy.

It is interesting to calculate the rate constants for the electronically adiabatic thermal dissociation of H on the S_1 surface; such rate constants cannot be compared directly to experiment not only because the actually dissociation is not completely electronically adiabatic but also, and perhaps more significantly, because phenol need not become thermalized on the S_1 surface prior to dissociation. Nevertheless, the calculation – being the first calculation of the tunneling process to include all degrees of freedom – provides valuable insight. The thermal rate constants of the unimolecular H-dissociation of phenol on the V_2 surface were calculated with canonical variational theory (CVT),[104,105] with vibrations transverse to the reaction coordinate quantized. Tunneling was included in the calculations by four different methods: the zero-curvature tunneling (ZCT) approximation,[93,106] the small-curvature tunneling (SCT) approximation,[100] the

large curvature tunneling (LCT) approximation,[107,108] and the microcanonically optimized tunneling (μOMT) approximation.[108,109] The ZCT calculation may be considered to be an approximation to the SCT one (as explained further below). The SCT calculations are vibrationally adiabatic and the LCT calculation is vibrationally nonadiabatic, and they also have different tunneling paths appropriate to the limits of small curvature of the reaction path and large curvature of the reaction path; the μOMT approximation chooses between them on the basis that, for each tunneling energy, the tunneling approximation that yields the most tunneling (largest rate constant) is expected to be most accurate.[110,111] Since only two vibrational states of the O-H stretching mode have energy levels below the barrier, we performed the calculations using quantized-reactant-state tunneling calculations.[112,113] We found that the SCT and μOMT approximations give nearly the same result, both larger than the result given by LCT approximation. Therefore the SCT result is our most accurate, but we show both the ZCT and SCT results in Table 6.6 because the comparison is physically interesting. The ZCT result shows the effect of tunneling along the MEP as if it were a straight path in isoinertial coordinates, whereas the SCT result includes corner cutting across the concave side of the curved path to shorten the tunneling path and increase the tunneling probability. The unimolecular thermal rate constants increase by many orders of magnitude when one includes tunneling, and the effect of corner cutting is very significant.

The SCT tunneling probability in the $n = 0$ state of the O–H stretch (at an energy 2.66 eV above the equilibrium minimum of the S_1 potential) is 7.8×10^{-6}, and the SCT tunneling probability in the $n = 1$ state of the O–H stretch (at an energy of 3.07 eV) is 0.051.

Without considering the tunneling effect, the lifetime of the S_1 state, which is the reciprocal of the tabulated unimolecular rate constant, is calculated to be 3.4×10^7 ns at 300 K. Including tunneling by the SCT approximation, the lifetime is found to be between 0.5 and 6 ns for the temperatures shown in Table 6.6. Although we cautioned that the electronically adiabatic thermal lifetime cannot be compared directly to the photochemical lifetime, it is still interesting that the experimental lifetime of the S_1 state of phenol was reported to be $\tau \approx 2$ ns,[48] which shows that the calculation is not entirely unreasonable even if the remarkably good agreement of such an approximate calculation is partly fortuitous. Independent of this quantitative comparison though, the calculations show that without a doubt the dissociation reaction proceeds many orders of magnitude faster due to tunneling.

6.3.3 Selected scans and 3D plots of conical intersections

Figure 6.2 show the diabatic potential energy curves of three states, namely, the ground $^1\pi\pi$ state, the $^1\pi\pi^*$ state, and the repulsive $^1\pi\sigma^*$ state along the O–H stretch with the other geometric parameters fixed at the equilibrium geometry of ground-state phenol. As the O–H bond length increases, the APRP $^1\pi\sigma^*$ state intersects the $^1\pi\pi^*$ state at 1.32 Å (CI1); then it further intersects the $^1\pi\pi$ state at 2.23 Å (CI2), and it finally dissociates to the ground state of phenoxyl radical ($^2B_1$ state) and H atom. The $^1\pi\pi$ state, which is the ground state of phenol at short O–H bond length, intersects the $^1\pi\sigma^*$ state at 2.23 Å, and it dissociates to the excited state of phenoxyl radical ($^2B_2$ state) and H atom. MC-QDPT diabatic potential curves are also shown in Fig. 6.2 for comparison. The MC-QDPT curves cross at $r_{OH} \approx 1.32$ and 2.26 Å for $^1\pi\pi^*/^1\pi\sigma^*$ and $^1\pi\pi/^1\pi\sigma^*$.[33] Figure 6.2

shows clearly that – despite the small difference in the location of CI2 – the APRP PES reproduces the MC-QDPT diabatic potential curves very well.

For planar geometry, the diabatic couplings are zero by symmetry, so the adiabatic states also intersect at r = 1.316 (CI1), where $V_2 = V_3$ = 5.613 eV and r = 2.232 Å (CI2) where $V_1 = V_2$ = 4.434 eV. Those points belong to the seams of conical intersections along which two adiabatic state are degenerate.

In Fig. 6.5, the diabatic potential (U_1, U_2, and U_3) and diabatic couplings (U_{13} and U_{23}) are shown along the O–H bond stretch coordinate at various torsion angles (ϕ = 30, 50, 70, and 90°). The diabatic potential curves calculated by fourfold way diabatization with MC-QDPT wave functions are also presented in Fig. 6.5 to show how well our PES reproduce both the calculated diabatic potentials and diabatic couplings. For a nonzero value of the C2–C1–O–H torsion angle, the diabatic potential U_3 still crosses U_2 and U_1 along the O–H bond stretch, but the C2–C1–O–H torsion breaks the planar symmetry and results in nonzero diabatic couplings, thus lifting the degeneracy all along the adiabatic curves and converting the intersections to avoided crossings. (Note that the term "avoided crossing" should not be understood as implying that surfaces do not cross;[32] rather it means that they do not cross along the path under discussion.) The only exception is at ϕ = 90°, where the phenol molecule again has C_s symmetry, but now with the symmetry plane perpendicular to the benzene ring; diabatic states U_2 ($^1\pi\pi^*$) and U_3 ($^1\pi\sigma^*$) now have A′ and A″ symmetry, respectively, and the diabatic coupling U_{23} is zero by symmetry. Our PES yields zero diabatic coupling of U_{23} at ϕ = 90° by construction, shown in Fig. 6.5d.

Three-dimensional plots of diabatic surfaces U_2 and U_3 and adiabatic surfaces V_2 and V_3 are shown in Fig. 6.6 as functions of the O–H bond stretch and the C2–C1–O–H torsion coordinate with the other geometric parameters fixed with their values corresponding to the equilibrium structure of ground-state phenol. The diabatic states cross at both planar and non-planar geometries, forming a seam with $U_2 = U_3$ in the r and ϕ space. The diabatic coupling U_{23} is not zero for most nonplanar geometries, but it is zero along the $\phi = 0$ that intersects the diabatic intersection scheme at $r = 1.316$ Å to yield a conical intersection there, this is simply another view of the CI1 intersection geometry shown in Fig. 6.2. We should keep in mind that at $\phi = 90°$, U_{23} is zero along the O–H bond stretching coordinate by symmetry, and there is another conical intersection with $V_2 = V_3$.

In Fig. 6.7, we also provide plots similar to Fig. 6.6 but now for U_1, U_3, V_1, and V_2. This provides another view of the intersection at $r = 2.232$ Å and $\phi = 0°$, labeled CI2 in Fig. 6.2. The ability to reproduce the conical intersection with our diabatic PES reflects one advantage of developing PESs in a diabatic representation – namely we do not have to fit the cusps in the adiabatic representation near conical intersections or to line up avoid crossings in the nearly degenerate adiabatic surfaces; these features emerge naturally from the diagonalization.

Although the conical intersections look like points in Figs. 6.6 and 6.7, we should keep in mind that these are just points on 31-dimensional intersection seams. The point with the lowest energy along a seam of conical intersections is called the minimum energy conical intersection (MECI), and its energy is an important characteristic of the coupled surfaces. With our analytic PESs, we located the MECI between V_2 and V_3

(MECI1) and the MECI between V_1 and V_2 (MECI2). Both MECIs have planar structures. MECI1 has r_{OH} = 1.273 Å with $V_2 = V_3$ = 5.351 eV and MECI2 has r_{OH} = 1.971 Å with $V_1 = V_2$ = 4.172 eV. The C–C, C–O, and O–H bond lengths and C–O–H bond angles of MECI1 and MECI2 are shown in Fig. 6.8, along with those of ground state phenol and phenoxyl radical. Both MECIs have C–C bond lengths similar to those in the equilibrium ground state phenoxyl radical equilibrium which corresponds to the diabatic state U_3 ($^1\pi\sigma^*$); these ring distortions lower the energy of the $^1\pi\sigma^*$ state with respect to what is shown in Fig. 6.2, and consequently the conical intersections have lower energies and shorter O–H bond lengths than the CIs in Fig. 6.2 (1.273 v. s. 1.316 Å for the first CI and 1.971 v. s. 2.231 Å for the second CI).

The energy of MECI1, 5.35 eV, is 0.18 eV higher than the saddle point discussed in the previous subsection. This small difference is consistent with the statement made there that the saddle point is close to a conical intersection and yet the gap between V_2 and V_3 increases from 0 to 0.81 eV as one moves from MECI1 to the V_2 saddle point, so the dynamics is much more adiabatic near the saddle point than near the CI. The displacement of the minimum energy path from the conical intersection does make the gap nonzero, but the gap is still much smaller than in the H + H_2 reaction where the gap at the saddle pot is more than 6 eV.[114]

6.3.4 Scans for out-of-plane geometries

When out-of-plane modes are involved, the C_s symmetry of the phenol molecule is broken. The diabatic potential U_3 still crosses U_2 and U_1 along the O–H stretching coordinate, but the adiabatic potentials V_1, V_2, and V_3 need not intersect each other because of the non-zero diabatic couplings. Figure 6.9 shows one-dimensional cuts

through the potential surfaces for nonplanar geometries with the C2–C1–O–H torsion angle equal to $\phi = 145°$. The phenoxyl ring is fixed at the ground state equilibrium geometry of phenol with $\theta_{COH} = 107°$ and 130° in Figs. 6.9a and 6.9b; the phenoxyl ring is fixed at the transition state geometry of the S_1 excited state with $\theta_{COH} = 112°$ in Fig. 6.9c; and the phenoxyl ring is fixed at the ground-state equilibrium geometry of phenoxyl radical with $\theta_{COH} = 115°$ in Fig. 6.9d. In all cases, the adiabatic potential curves show avoided intersections along the O–H stretching coordinate, as expected.

Near conical intersections, diabatic potential energy curves may cross along the C2–C1–O–H torsion coordinate. But adiabatic potential energy curves avoid crossing since the nonzero diabatic couplings lift the degeneracy of diabatic states. This is shown clearly in Fig. 6.10. In Fig. 6.10a, for $r_{OH} = 1.29$ Å with all other geometric parameters except ϕ fixed at the ground equilibrium geometry of phenol, the diabatic potential U_3 crosses U_2 at $\phi = 25°$, but the adiabatic potential curves V_2 and V_3 avoid crossing. In fig. 6.10b, for $r_{OH} = 2.10$ Å, the diabatic potential U_3 crosses U_1 at $\phi = 24°$, but again the adiabatic potential curves V_1 and V_2 avoid crossing.

So far we have shown cuts through the APRP PESs for a fixed geometry of the phenoxyl moiety of phenol. The good performance of our APRP PES for those geometries is expected since we used general functional forms to fit the dependence of MC-QDPT diabatic potentials and couplings on the primary and secondary coordinates. Next we examine the PESs for some nonplanar geometries with distorted phenoxyl groups. In the language of the APRP, we are looking here at how the PESs and couplings vary for geometries with distortions in tertiary coordinates. In particular, we examine the dependence on the ν_{16a} (an out-of-plane ring puckering/twisting vibration of a´´

symmetry) and ν_{16b} modes that have been singled out for attention in experimental studies.[45,50] (We use Wilson's labeling scheme[115] for the phenol and phenoxyl vibrational modes.)

The diabatic potentials and relevant diabatic couplings along Cartesian normal-mode displacements of the ν_{16a} and ν_{16b} modes were calculated with our APRP PESs and compared with MC-QDPT results at the two conical intersections in Figs. 6.11 and 6.12. The normalized Cartesian normal-mode displacements of ν_{16a} and ν_{16b} modes calculated by the M06-L functional[116] with the aug-cc-pVTZ basis set were used in order to be consistent with previous MC-QDPT calculations.[33] The APRP diabatic potentials and couplings agree qualitatively with the MC-QDPT results. The diabatic coupling U_{23} increases linearly along the Cartesian normal-mode displacements of both ν_{16a} and ν_{16b} modes at CI1. At CI2, the diabatic coupling U_{13} also increases linearly along the Cartesian normal-mode displacement of the ν_{16a} mode. However, it remains very small along the Cartesian normal-mode displacement of the ν16b mode. These calculations of the diabatic couplings for out-of-plane distortion of the ring in phenol can be used in the future for full-dimensional studies of the effects of vibrational mode coupling on the dynamics of photodissociation of phenol. However, we can also gain insight into the photodissociation dynamics by studying the couplings even without carrying out full dynamics studies, and we consider that next.

First we recall the Ehrenfest effective PES, which we will call $\bar{V}$, for multi-electronic-state molecular dynamics is a weighted average over the adiabatic PESs, V_j, where the weights are the diagonal elements, ρ_{jj}, of the electronic density matrix.[34,117-120] Then we consider a photoexcited system with $\rho_{22} >> \rho_{11}$ and $\rho_{22} >> \rho_{33}$

approaching CI1. If the system is not adiabatic, we expect to see ρ_{33} increase, and that puts a higher weight on V_3 and raises $\bar{V}$, which makes it less likely that the system dissociates. Now let the system undergo a vibration in an out-of-plane mode while it approaches CI1; this has two consequences: (1) the vibration causes U_2 and V_2 to go up, which raises $\bar{V}$, decreasing the probability of dissociation; and (2) the vibration causes $|U_{23}|$ to go up, which makes the system more adiabatic, which keeps ρ_{33} low, which tends to keep $\bar{V}$ low, which increases the probability of dissociation. For some modes, call them "inactive" modes, effect (1) may dominate. For other modes, call then "active" modes, effect (2) may dominate. We conclude that reaction will preferentially occur through those molecules that happen to have active modes excited as they get to CI1.

When one experimentally observes the products (as Ashfold and coworkers[45,50] do), one will then see an excess of molecules with active modes excited since those are the ones that preferentially reacted. Under the conditions of the experiments, most of the vibrational modes are initially in their ground vibrational state. Let q_m be an out-of-plane vibrational mode, and let Z_m be the zero point energy in that mode. Near a planar geometry,

$$U_2 = U_2(q=0) + \frac{1}{2} k_m q_m^2, \tag{6.22}$$

and

$$U_{23} = C_m q_m, \tag{6.23}$$

where k_m is a force constant, and C_m depends on the fit to the diabatic couplings. (Both k_m and C_m depend on geometry in the APRP.) Let $D_m = |C_m|$, and let Q_m be the harmonic turning point of q_m:

$$Q_m = \sqrt{2Z_m / k_m}, \tag{6.24}$$

Since an active mode has $|U_{23}|$ large and $U_2(Q_m) - U_2(0)$ small, we define

$$X(Q_{\mathrm{m}}) \equiv \frac{|U_{23}(Q_{\mathrm{m}})|}{U_2(Q_{\mathrm{m}}) - U_2(0)}. \tag{6.25}$$

Substituting eqs. 6.22, 6.23, and 6.24 into eq. 6.25, we have

$$X(Q_m) = D_m \sqrt{2 / k_m Z_m}. \tag{6.26}$$

This is the simplest unitless quantity that goes up when $|U_{23}|$ goes up and is larger when the rise in U_2 is smaller.

We calculated $X(Q_{\mathrm{m}})$ for all out-of-plane modes at a planar geometry of the S_1 state of phenol that has the same OH distance as the transition state but the rest of the coordinates the same as in the equilibrium geometry of the S_1 state. We found that $X(Q_{\mathrm{m}})$ is 0.12 for mode ν_{16a} (103 cm^{-1}), 0.064 for mode 11 (197 cm^{-1}), and 0.050 for mode 10a (389 cm^{-1}), but it ranges between 0.013 and 2×10^{-4} for the other seven out-of-plane modes of phenol (with frequencies in the range 81–865 cm^{-1}). This provides a simple explanation for why ν_{16a} mode is the most prominent excited mode observed[45,50] in the products of the photodissociation reaction; and we note that mode 10a is also observed[50] to be excited in the products. We note that vibrational modes can also be excited during the energy release phase as the system progresses from the region of the

saddle point and CI1 down to products, but the analysis just given is consistent with the interpretation[50] of at least some of the observed vibrational mode selectivity as arising from the ability of various vibrational modes to promote state coupling. Unfortunately this is called promotion of "nonadiabatic transitions" in Ref. 50, but actually—as the above discussion should make clear—the relevant consideration is promotion of diabatic coupling, which leads to adiabatic passage, not nonadiabatic transitions.

6.3.5 Nonplanar conical intersections

The conical intersections occur in a $(3N - 8)$-dimensional manifold, where N is the number of atoms. Thus, in phenol molecule, the conical intersection should have a dimension of 31. Both U_{13} and U_{23} vanish for planar geometries, which form a 23-dimensional manifold, because $2N - 3 = 23$. With the further constraint of $U_{22} = U_{33}$ or $U_{11} = U_{33}$, the $^1\pi\pi^*/^1\pi\sigma^*$ and $^1\pi\pi/^1\pi\sigma^*$conical intersections occur in a 22-dimensional manifold in planar geometry. This is a relatively low-dimensional subset of the full 31-dimensional seam, and therefore most of the conical intersection seam has nonplanar geometry.

Locating conical intersections that are not determined by symmetry can be carried out by special algorithms in the adiabatic representation.[121,122] However, with the analytic diabatic PES matrices of phenol on hand, we can locate such conical intersections more easily.[123,124] Contour plots of U_2 - U_3 and U_{23} with respect to the C2–C1–O–H torsion angle ϕ and one of the H out-of-plane bend angles, in particular $\theta_{8-2-1-3}$, which denotes the deviation of atom 8 from the 2-1-3 plane, are shown in Fig. 6.13 at $r = 1.29$ Å. At the planar geometries, both ϕ and $\theta_{8-2-1-3}$ are zero, and adiabatic state V_3 is 0.21 eV higher in energy than adiabatic state V_2. The seam with $U_{22} = U_{33} = 0$

and the seam with $U_{23} = 0$ cross at $\phi = 40.1°$ and $\theta_{8-2-1-3} = 25.0°$. If these two diabatic states formed a closed space, that point (solid circle in Fig. 6.13) will be a nonplanar conical intersection of V_2 and V_3, but due to the perturbation by diabatic state U_1, the location of the true conical intersection is displaced from this point. Nevertheless this is a good starting point for a search, and by making a contour plot of $V_2 - V_3$ in this vicinity (which is inexpensive because we have an analytic representation), we find that $V_2 = V_3 = 6.00$ eV at $\phi = 50.9°$ and $\theta_{8-2-1-3} = 15.4°$ (solid square in Fig. 6.13).

In Fig. 6.14, we present the contour plots of U_1 - U_3 and U_{13} with respect to the C–C–O–H torsion angle ϕ and one of the H out-of-plane bend angles $\theta_{9-3-2-4}$ at $r = 2.20$ Å. The seam with U_1 - $U_3 = 0$ eV and the seam with $U_{13} = 0$ eV cross at $\phi_{2-1-7-13} = 12.4°$ and $\theta_{9-3-2-4} = -16.2°$ which is also a nonplanar conical intersection with $V_1 = V_2 = 4.54$ eV as a result of the smallness of the perturbation by diabatic state U_2 at this geometry.

6.4 Summary and concluding

We have improved the APRP method to use internal coordinates with better global behavior. For the three-state photodissociation of phenol, we have used the improved APRP method to develop analytic full-dimensional diabatic potential energy surfaces with analytic gradients, analytic diabatic coupling surfaces and their gradients, adiabatic energy surfaces and their gradients, and adiabatic nonadiabatic couplings. Selected scans show that our APRP diabatic potential PESs and diabatic couplings surfaces reproduce well the results calculated previously by the fourfold way with the MC-QDPT method. We illustrate the magnitudes of the diabatic couplings and adiabatic gaps for various nonplanar geometries and show how they may be used to provide a simple estimate of

which vibrational modes promote the dissociation process. By diagonalizing the diabatic potential matrices, conical intersections can be correctly reproduced, and we show how to use the APRP potential to locate points on conical intersection seams at nonsymmetrical geometries.

We used the APRP potentials to locate the transition state, minimum-energy path, and vibrationally adiabatic potential energy curve for photodissociation of phenol on the S_1 surface and to study of thermal rate constants for adiabatic dissociation, which confirmed the importance of tunneling for S_1 state photodissociation of phenol.

The APRP potential for phenol can be used for the study of dynamics of photodissociation of phenol to elucidate the effect of ring motion, including out-of-plane vibrational modes. The success of the APRP method in producing coupled surfaces and couplings suitable for full-scale dynamics calculations is very encouraging, and improved APRP method can be used to map out coupled potential energy surfaces and their couplings for other complex systems, thereby allowing much more complete molecular dynamics simulations than have been practical in the past.

6.5 References

[1] M. Born and R. Oppenheimer, Ann. Phys. **84**, 457 (1927).
[2] B. K. Kendrick, C. A. Mead and D. G. Truhlar, Chem. Phys. **277**, 31 (2002).
[3] A. W. Jasper, C. Zhu, S. Nangia and D. G. Truhlar, Faraday Discuss. **127**, 1 (2004).
[4] C. A. Mead and D. G. Truhlar, J. Chem. Phys. **77**, 6090 (1982).
[5] W. Lichten, Phys. Rev. **131**, 229 (1963).
[6] T. F. O'Malley, J. Chem. Phys. **51**, 322 (1969).
[7] B. C. Garrett and D. G. Truhlar, in *Theoretical Chemistry: Advances and Perspectives*, Vol. 6A, edited by D. Henderson (Academic Press, New York, 1981), p. 215.
[8] H.-J. Werner and W. Meyer, J. Chem. Phys. **74**, 5802 (1981).
[9] J. B. Delos, Rev. Mod. Phys. **53**, 287 (1981).
[10] D. Stahel, M. Leoni and K. Dressler, J. Chem. Phys. **79**, 2541 (1983).
[11] M. H. Alexander, Chem Phys. **92**, 337 (1985).
[12] T. C. Thompson, D. G. Truhlar and C. A. Mead, J. Chem. Phys. **82**, 2392 (1985).
[13] T. Pacher, L. S. Cederbaum and H. Köppel, J. Chem. Phys. **89**, 7367 (1988).
[14] A. Boutalib and F. X. Gadéa, J. Chem. Phys. **97**, 1144 (1992).
[15] M. Marchi, J. N. Gehlen, D. Chandler and M. Newton, J. Am. Chem. Soc. **115**, 4178 (1993).
[16] Y. Mo and J. Gao, J. Comput. Chem. **21**, 1458 (2000).
[17] H. Nakamura and D. G. Truhlar, J. Chem. Phys. **115**, 10353 (2001); H. Nakamura and D. G. Truhlar, ibid, **117**, 5576 (2002); H. Nakamura and D. G. Truhlar, ibid, **118**, 6816 (2003).
[18] P. H.-L. Sit, M. Cococcioni and N. Marzari, Phys. Rev. Lett. **97**, 28303 (2006).
[19] O. Godsi, C. R. Evenhuis and M. A. Collins, J. Chem. Phys. **125**, 104105 (2006).
[20] G. A. Arteca and O. Tapia, Int. J. Quantum Chem. **107**, 382 (2007).
[21] F. D. X. George and S. Kumar, J. Chem. Phys. **119**, 409 (2007).
[22] B. N. Papas, M. S. Schuuman and D. R. Yarkony, J. Chem. Phys. **129**, 124104 (2008).
[23] J. E. Subotnik, S. Yeganeh, R. J. Cave and M. A. Ratner, J. Chem. Phys. **129**, 244101 (2008).
[24] T. Ichino, J. Gauss and J. F. Stanton, J. Chem. Phys. **130**, 174105 (2009).
[25] T. van Voorhis, T. Kowalczak, B. Kaduk, L.-P. Wang, C.-L. Cheng and Q. Wu, Annu. Rev. Phys. Chem. **61**, 149 (2010).
[26] A. Sirjoosingh and S. Hammes-Schiffer, J. Phys. Chem. A **115**, 2367 (2011).
[27] E. Alguire and J. E. Subotnik, J. Chem. Phys. **135**, 44114 (2011).
[28] M. Pavanello and J. Neugebauer, J. Chem. Phys. **135**, 134113 (2011).

[29] Y. C. Park, H. An, H. Choi, Y. S. Lee and K. K. Baeck, Theor. Chem. Acc. **131**, 1212 (2012).
[30] X. Zhu and D. R. Yarkony, J. Chem. Phys. **137**, 22A511 (2012).
[31] K. R. Yang, X. Xu and D. G. Truhlar, Chem. Phys. Lett. **573**, 84 (2013).
[32] D. G. Truhlar and C. A. Mead, Phys. Rev. A **68**, 32501 (2003).
[33] X. Xu, K. R. Yang and D. G. Truhlar, J. Chem. Theory Comput. **9**, 3612 (2013).
[34] A. W. Jasper and D. G. Truhlar, in *Conical Intersections: Theory, Computation, and Experiment*, edited by W. Domcke, D. Yarkony and H. Köppel (World Scientific, Singapore, 2011), pp. 375-414.
[35] A. L. Sobolewski and W. Domcke, J. Phys. Chem. A **105**, 9275 (2001).
[36] A. L. Sobolewski, W. Domcke, C. Dedonder-Lardeux and C. Jouvet, Phys. Chem. Chem. Phys. **4**, 1093 (2002).
[37] Z. Lan, W. Domcke, V. Vallet, A. L. Sobolewski and S. Mahapatra, J. Chem. Phys. **122**, 224315 (2005).
[38] M. N. R. Ashfold, B. Cronin, A. L. Devine, R. N. Dixon and M. G. D. Nix, Science **312**, 1637 (2006).
[39] C.-M. Tseng, Y. T. Lee, M.-F. Lin, C.-K. Ni, S.-Y. Liu, Y.-P. Lee, Z. F. Xu and M. C. Lin, J. Phys. Chem. A **111**, 9463 (2007).
[40] A. L. Devine, M. G. D. Nix, B. Cronin and M. N. R. Ashfold, Phys. Chem. Chem. Phys. **9**, 3749 (2007).
[41] G. A. King, A. L. Devine, M. G. D. Nix, D. E. Kelly and M. N. R. Ashfold, Phys. Chem. Chem. Phys. **10**, 6417 (2008).
[42] M. N. R. Ashfold, A. L. Devine, R. N. Dixon, G. A. King, M. G. D. Nix and T. A. A. Oliver, Proc. Natl. Acad. Sci. U. S. A. **105**, 12701 (2008).
[43] M. G. D. Nix, A. L. Devine, R. N. Dixon and M. N. R. Ashfold, Chem. Phys. Lett. **463**, 305 (2008).
[44] O. P. J. Vieuxmaire, Z. Lan, A. L. Sobolewski and W. Domcke, J. Chem. Phys. **129**, 224307 (2008).
[45] G. A. King, T. A. A. Oliver, M. G. D. Nix and M. N. R. Ashfold, J. Phys. Chem. A **113**, 7984 (2009).
[46] A. Iqbal, M. S. Y. Cheung, M. G. D. Nix and V. G. Stavros, J. Phys. Chem. A **113**, 8157 (2009).
[47] M. N. R. Ashfold, G. A. King, D. Murdock, M. G. D. Nix, T. A. A. Oliver and A. G. Sage, Phys. Chem. Chem. Phys. **12**, 1218 (2010).
[48] A. Pino, A. N. Oldani, E. Marceca, M. Fujii, S.-I. Ishiuchi, M. Miyazaki, M. Broquier, C. Dedonder and C. Jouvet, J. Chem. Phys. **133**, 124313 (2010).
[49] H. An and K. K. Baeck, J. Phys. Chem. A **115**, 13309 (2011).

[50] R. N. Dixon, T. A. A. Oliver and M. N. R. Ashfold, J. Chem. Phys. **134**, 194303 (2011).
[51] Y. Zhang, T. A. A. Oliver, M. N. R. Ashfold and S. E. Bradforth, Faraday Discuss. **157**, 141 (2012).
[52] S. G. Ramesh and W. Domcke, Faraday Discuss. **163**, 73 (2013).
[53] X. Zhu and D. R. Yarkony, J. Chem. Phys. **140**, 024112 (2014).
[54] M. C. Capello, M. Broquier, S.-I. Ishiuchi, W. Y. Sohn, M. Fujii, C. Dedonder-Lardeux, C. Jouvet and G. A. Pino, J. Phys. Chem. A **118**, 2056 (2014).
[55] T. N. V. Karsili, A. M. Wenge, B. Marchetti and M. N. R. Ashfold, Phys. Chem. Chem. Phys. **16**, 588 (2014).
[56] B. J. Braams and J. M. Bowman, Int. Rev. Phys. Chem. 28, 577 (2009).
[57] J. M. Bowman, B. J. Braams, S. Carter, C. Chen, G. Czakó, B. Fu, X. Huang, E. Kamarchik, A. R. Sharma, B. C. Shepler, Y. Wang and Z. Xie, J. Phys. Chem. Lett. 1, 1866 (2010).
[58] Y. Paukku, K. R. Yang, Z. Varga and D. G. Truhlar, J. Chem. Phys. 139, 044309 (2013).
[59] R. Dawes, D. L. Thompson, Y. Guo, A. F. Wagner and M. Minkoff, J. Chem. Phys. 126, 184108 (2007).
[60] Y. Guo, I. Tokmakov, D. L. Thompson, A. F. Wagner and M. Minkoff, J. Chem. Phys. 127, 214106 (2007).
[61] J. D. Bender, S. Doraiswamy, D. G. Truhlar and G. Candler, J. Chem. Phys. 140, 054302 (2014).
[62] K. R. Yang, X. Xu and D. G. Truhlar, J. Chem. Theory Comput. **10**, 924 (2014).
[63] H. Nakano, J. Chem. Phys. **99**, 7983 (1993); H. Nakano, Chem. Phys. Lett. **207**, 372 (1993).
[64] E. Papajak and D. G. Truhlar, J. Chem. Theory Comput. 7, 10 (2011).
[65] P. Siegbahn, A. Heiberg, B. O. Roos and B. A. Levy, Phys. Scr. **21**, 323 (1980); B. O. Roos, P. R. Taylor and P. E. M. Siegbahn, Chem. Phys. **48**, 157 (1980); K. Ruedenberg, M. W. Schmidt, G. M. Gillbert and S. T. Elbert, Chem. Phys. **71**, 41 (1982).
[66] T. H. Dunning, Jr., J. Chem. Phys. **90**, 1007 (1989); R. A. Kendall and T. H. Dunning, Jr., J. Chem. Phys. **96**, 6796 (1992).
[67] Y. P. Varshni, Rev. Mod. Phys. **29**, 664 (1957); erratum: **31**, 839 (1959).
[68] P. M. Morse, Phys. Rev. **34**, 1957 (1929).
[69] Y. Zhao and D. G. Truhlar, Theor. Chem. Acc. **120**, 215 (2008).
[70] M. E. Casida, C. Jamorski, K. C. Casida and D. R. Salahub, J. Chem. Phys. **108**, 4439 (1998).
[71] R. E. Stratmann, G. E. Scuseria and M. J. Frisch, J. Chem. Phys. **109**, 8218 (1998).

[72] G. Simons, R. G. Parr and J. M. Finlan, J. Chem. Phys. **84**, 891 (1973).
[73] S. Gupta, K. Dharamvir and V. K. Jindal, Int. J. Mod. Phys. B **18**, 1021 (2004).
[74] G. Pongor, G. Fogarasi, J. E. Boggs and P. Pulay, J. Mol. Spectrosc. **114**, 445 (1985).
[75] H. Nakamura, J. D. Xidos, A. C. Chamberlin, C. P. Kelly, R. Valero, K. R. Yang, J. D. Thompson, J. Li, G. D. Hawkins, T. Zhu, B. J. Lynch, Y. Volobuev, D. Rinaldi, D. A. Liotard, C. J. Cramer and D. G. Truhlar, *HONDOPLUS-v*5.2, University of Minnesota, Minneapolis, MN, 2013.
[76] M. J. Frisch, G. W. Trucks, H. B. Schlegel, G. E. Scuseria, M. A. Robb, J. R. Cheeseman, G. Scalmani, V. Barone, B. Mennucci, G. A. Petersson, H. Nakatsuji, M. Caricato, X. Li, H. P. Hratchian, A. F. Izmaylov, J. Bloino, G. Zheng, J. L. Sonnenberg, M. Hada, M. Ehara, K. Toyota, R. Fukuda, J. Hasegawa, M. Ishida, T. Nakajima, Y. Honda, O. Kitao, H. Nakai, T. Vreven, J. A. Montgomery, Jr. J. E. Peralta, F. Ogliaro, M. Bearpark, J. J. Heyd, E. Brothers, K. N. Kudin, V. N. Staroverov, R. Kobayashi, J. Normand, K. Raghavachari, A. Rendell, J. C. Burant, S. S. Iyengar, J. Tomasi, M. Cossi, N. Rega, J. M. Millam, M. Klene, J. E. Knox, J. B. Cross, V. Bakken, C. Adamo, J. Jaramillo, R. Gomperts, R. E. Stratmann, O. Yazyev, A. J. Austin, R. Cammi, C. Pomelli, J. W. Ochterski, R. L. Martin, K. Morokuma, V. G. Zakrzewski, G. A. Voth, P. Salvador, J. J. Dannenberg, S. Dapprich, A. D. Daniels, Ö. Farkas, J. B. Foresman, J. V. Ortiz, J. Cioslowski and D. J. Fox, Gaussian 09, Revision D.01, Gaussian, Inc. Wallingford CT, 2009.
[77] J. Zheng, S. Zhang, B. J. Lynch, J. C. Corchado, Y.-Y. Chuang, P. L. Fast, W.-P. Hu, Y.-P. Liu, G. C. Lynch, K. A. Nguyen, C. F. Jackels, A. Fernandez Ramos, B. A. Ellingson, V. S. Melissas, J. Villà, I. Rossi, E. L. Coitiño, J. Pu, T. V. Albu, R. Steckler, B. C. Garrett, A. D. Isaacson and D. G. Truhlar, POLYRATE–version 2010, University of Minnesota, Minneapolis, 2010.
[78] J. Zheng, Z. H. Li, A. W. Jasper, D. A. Bonhommeau, R. Valero, R. Meana-Pañeda and D. G. Truhlar, ANT–version 2014, University of Minnesota, Minneapolis, MN, 2014. http://comp.chem.umn.edu/ant (accessed May 26, 2014)
[79] N. W. Larsen, J. Mol. Struct. **51**, 175 (1979).
[80] G. Portalone, G. Schultz, A. Domenicano and I. Hargittai, Chem. Phys. Lett. **197**, 482 (1992).
[81] D. Spangenberg, P. Imhof and K. Kleinermanns, Phys. Chem. Chem. Phys. **5**, 2505 (2003).
[82] C.-W. Cheng, Y.-P. Lee and H. A. Witek, J. Phys. Chem. A **112**, 2648 (2008).
[83] F. van Bolhuis and C. T. Kiers, Acta Cryst. **B34**, 1015 (1978).
[84] G. Keresztury, F. Billes, M. Kubinyi and T. Sundius, J. Phys. Chem. A **102**, 1371 (1998).

[85] J. Spanget-Larsen, M. Gil, A. Gorski, D. M. Blake, J. Waluk and J. G. Radziszewski, J. Am. Chem. Soc. **123**, 11253 (2003).
[86] I. M. Alecu, J. Zheng, Y. Zhao and D. G. Truhlar, J. Chem. Theory Comput. **6**, 2872 (2010).
[87] R. C. Fuh, Oregon Medical Laser Center, Portland, OR, 1995; http://omlc.ogi.edu/spectra/PhotochemCAD/html/072.html . (accessed May 17, 2014).
[88] R. F. Gunion, M. K. Gilles, M. L. Polak and W. C. Lineberger, Int. J. Mass Spectrom. Ion Proc. **117**, 602 (1992).
[89] J. G. Radziszewski, M. Gil, A. Gorski, J. Spanger-Larsen, J. Waluk and B. J. Mróz, J. Chem. Phys. **115**, 9733 (2001).
[90] Y.-R. Luo, *Handbook of Bond Dissociation Energies in Organic Compounds* (University of Science and Technology of China: Hefei, 2006), p. 182.
[91] H. D Bist, J. C. D. Brand and D. R. Williams, J. Mol. Spectrosc. **21**, 76 (1966); H. D Bist, J. C. D. Brand and D. R. Williams, J. Mol. Spectrosc. **24**, 402 (1967); H. D Bist, J. C. D. Brand and D. R. Williams, J. Mol. Spectrosc. **24**, 413 (1967).
[92] O. Tishchenko, D. G. Truhlar, A. Ceulemans and M. T. Nguyen, J. Am. Chem. Soc. **130**, 7000 (2008).
[93] D. G. Truhlar and A. Kuppermann, J. Am. Chem. Soc. **93**, 1840 (1971).
[94] A. D. Isaacson and D. G. Truhlar, J. Chem. Phys. **75**, 4090 (1981).
[95] M. Page and J. W. McIver Jr., J. Chem. Phys. **88**, 922 (1988).
[96] J. O. Hirschfelder and E. Wigner, J. Chem. Phys. 1939, **7**, 616 (1939).
[97] M. A. Eliason and J. O. Hirschfelder, J. Chem. Phys. **30**, 1426 (1959).
[98] R. A. Marcus, J. Chem. Phys. **46**, 959 (1967).
[99] R. T. Skodje, D. G. Truhlar and B. C. Garrett, J. Chem. Phys. **77**, 5955 (1982).
[100] Y.-P. Liu, G. C. Lynch, T. N. Truong, D.-H. Lu, D. G. Truhlar and B. C. Garrett, J. Am. Chem. Soc. **115**, 2408 (1993).
[101] D. C. Chatfield, R. S. Friedman, D. G. Truhlar, B. C. Garrett and D. W. Schwenke, J. Am. Chem. Soc. **113**, 486 (1991).
[102] A. Tachibana and K. Fukui, Theor. Chen. Acta. **51**,189 (1979).
[103] G. C. Hancock, P. Rejto, R. Steckler, F. B. Brown, D. W. Schwenke and D. G. Truhlar, J. Chem. Phys. **85**, 4997 (1986).
[104] D. G. Truhlar, A. D. Isaacson, R. T. Skodje and B. C. Garrett, J. Phys. Chem. **86**, 2252 (1982).
[105] D. G. Truhlar, A. D. Isaacson and B. C. Garrett, in *The Theory of Chemical Reaction Dynamic*s, Vol. 4, edited by M. Baer (CRC Press, Boca Raton, FL, 1985), p. 65-137.
[106] A. Fernandez-Ramos, B. A. Ellingson, B. C. Garrett and D. G. Truhlar, Rev. Comput. Chem. **23**, 125 (2007).

[107] B. C. Garrett, D. G. Truhlar, A. F. Wagner and T. H. Dunning Jr., J. Chem. Phys. **78**, 4400 (1983).
[108] A. Fernandez-Ramos and D. G. Truhlar, J. Chem. Phys. **114**, 1491 (2001).
[109] Y.-P. Liu, D.-H. Lu, A. Gonzàlez-Lafont, D. G. Truhlar and B. C. Garrett, J. Am. Chem. Soc. **115**, 7806 (1993).
[110] B. C. Garrett and D. G. Truhlar, J. Chem. Phys. **79**, 4931 (1983).
[111] R. Meana-Pañeda, D. G. Truhlar and A. Fernández-Ramos, J. Chem. Theory Comput. **6**, 6 (2010).
[112] J. G. Lauderdale and D. G. Truhlar, Surf. Sci. **164**, 558 (1985).
[113] S. E. Wonchoba, W.-P. Hu and D. G. Truhlar, in *Theoretical and Computational Approaches to Interface Phenomena*, edited by H. L. Sellers and J. T. Golab (Plenum, New York, 1994), p. 7.
[114] A. J. C. Varandas, F. B. Brown, C. A. Mead, D. G. Truhlar and N. C. Blais, J. Chem. Phys. **86**, 6258 (1987).
[115] E. B. Wilson, Phys. Rev., **45**, 706 (1934).
[116] Y. Zhao and D. G. Truhlar, J. Chem. Phys. **125**, 194101 (2006).
[117] H.-D. Meyer and W. H. Miller, J. Chem. Phys. **70**, 1334 (1979).
[118] A. D. Micha, J. Chem. Phys. **78**, 7138 (1983).
[119] M. Amarouche, F. X. Gadea and J. Durup, Chem. Phys. **130**, 145 (1989).
[120] M. D. Hack and D. G. Truhlar, J. Chem. Phys., **114**, 9305 (2011).
[121] M. J. Bearpark, M. A. Robb and H. B. Schlegel, Chem. Phys. Lett. **223**, 269 (1994).
[122] M. Dallos, H. Lischka, R. Shepard, D. R. Yarkony and P. G. Szalay, J. Chem. Phys **120**, 7330 (2004).
[123] S. Nangia and D. G. Truhlar, J. Chem. Phys. **124**, 124309 (2006).
[124] Z. H. Li, R. Valero and D. G. Truhlar, Theor. Chem. Acc. **118**, 9 (2007).

Table 6.1. Out-of-plane coordinates of phenoxyl

Coordinate	Definition
δ_1	C2–C1–C6–C5 torsion
δ_2	C1–C6–C5–C4 torsion
δ_3	C6–C5–C4–C3 torsion
δ_4	C5–C4–C3–C2 torsion
δ_5	C4–C3–C2–C1 torsion
δ_6	C3–C2–C1–C6 torsion
S_1	$6^{-1/2}(\delta_1 - \delta_2 + \delta_3 - \delta_4 + \delta_5 - \delta_6)$
S_2	$12^{-1/2}(-\delta_1 + 2\delta_2 - \delta_3 - \delta_4 + 2\delta_5 - \delta_6)$
S_3	$4^{-1/2}(-\delta_1 + \delta_3 - \delta_4 + \delta_6)$
S_4	O7 out-of-plane bend
S_5	H12 out-of-plane bend
S_6	H11 out-of-plane bend
S_7	H10 out-of-plane bend
S_8	H9 out-of-plane bend
S_9	H8 out-of-plane bend

Table 6.2. Calculated and experimental geometric parameters of the ground $^1\pi\pi$ state of phenol[a]

	APRP	M06-2X[b]	microwave[c]	electron-diffraction[d]
			bond lengths (Å)	
C1–C2	1.402	1.396	1.391	1.399
C2–C3	1.400	1.395	1.394	1.399
C3–C4	1.399	1.394	1.395	1.399
C4–C5	1.402	1.397	1.395	1.399
C5–C6	1.397	1.392	1.392	1.399
C6–C1	1.402	1.396	1.391	1.399
C2–H8	1.092	1.092	1.086	1.083
C3–H9	1.090	1.090	1.084	1.083
C4–H10	1.089	1.089	1.080	1.083
C5–H11	1.090	1.090	1.084	1.083
C6–H12	1.089	1.089	1.081	1.083
C1–O7	1.365	1.365	1.375	1.381
O7–H13	1.022	0.964	0.957	0.958
			bond angles (deg)	
C6–C1–C2	120.4	120.4	120.9	121.6
C1–C2–C3	119.5	119.6	119.4	118.8
C2–C3–C4	120.6	120.6	120.5	120.6
C3–C4–C5	119.3	119.3	119.2	119.7
C4–C5–C6	120.8	120.8	120.8	120.6
C5–C6–C1	119.4	119.4	119.2	118.8
C1–C2–H8	120.0	120.0	120.0	
C2–C3–H9	119.3	119.3	119.5	
C3–C4–H10	120.3	120.3	120.3	
C4–C5–H11	119.9	119.9	119.8	
C5–C6–H12	121.7	121.7	121.6	
C6–C1–O7	117.1	117.1	117.0	117.2
C1–O7–H13	107.2	109.5	108.8	106.4

[a] See Fig. 6.1 for numbering of atoms.
[b] jul-cc-pVDZ
[c] Ref. 79
[d] Ref. 80

Table 6.3. Calculated and experimental geometric parameters of the $^1\pi\pi^*$ state of phenol[a]

	APRP	M06-2X [b]	Expt. [c]
	bond lengths (Å)		
C1–C2	1.434	1.429	1.421
C2–C3	1.424	1.419	1.420
C3–C4	1.427	1.421	1.431
C4–C5	1.425	1.419	1.425
C5–C6	1.426	1.421	1.426
C6–C1	1.425	1.420	1.413
C2–H8	1.090	1.090	1.083
C3–H9	1.087	1.087	1.080
C4–H10	1.090	1.091	1.079
C5–H11	1.087	1.087	1.080
C6–H12	1.087	1.087	1.079
C1–O7	1.338	1.338	1.356
O7–H13	1.034	0.967	0.992
	bond angles (degree)		
C6–C1–C2	123.6	124.0	123.4
C1–C2–C3	117.5	117.3	118.5
C2–C3–C4	119.4	119.3	118.5
C3–C4–C5	122.4	122.7	123.1
C4–C5–C6	119.1	118.9	118.6
C5–C6–C1	118.0	117.8	118.4
C1–C2–H8	120.0	120.1	120.2
C2–C3–H9	120.7	120.8	
C3–C4–H10	118.7	118.5	
C4–C5–H11	120.2	120.2	
C5–C6–H12	123.3	123.4	122.3
C6–C1–O7	116.2	116.0	115.9
C1–O7–H13	106.5	109.5	108.8

[a] See Fig. 6.1 for numbering of atoms.
[b] TD-DFT with the M06-2X functional and the jul-cc-pVDZ basis set
[c] Ref. 81

Table 6.4. Calculated geometric parameters of the $\tilde{X}\ ^2B_1$ and $\tilde{A}\ ^2B_2$ states of phenoxyl radical[a]

	APRP	M06-2X[b]	CASPT2[c]
		$\tilde{X}\ ^2B_1$ state	
		bond lengths (Å)	
C1–C2	1.461	1.453	1.448
C2–C3	1.379	1.375	1.379
C3–C4	1.416	1.410	1.408
C1–O7	1.246	1.249	1.255
C2–H8	1.090	1.090	1.081
C3–H9	1.090	1.090	1.081
C4–H10	1.090	1.090	1.081
		bond angles (deg)	
C6–C1–C2	121.0	121.0	120.9
C1–C2–C3	118.7	118.7	118.9
C2–C3–C4	121.3	121.2	121.1
C1–C2–H8	119.6	119.6	119.7
C4–C3–H9	118.7	118.7	118.8
		$\tilde{A}\ ^2B_2$ state	
		bond lengths (Å)	
C1–C2	1.409	1.403	1.402
C2–C3	1.397	1.392	1.393
C3–C4	1.400	1.394	1.394
C1–O7	1.331	1.333	1.330
C2–H8	1.088	1.088	1.079
C3–H9	1.090	1.090	1.081
C4–H10	1.088	1.088	1.079
		bond angles (deg)	
C6–C1–C2	121.0	121.0	120.9
C1–C2–C3	118.7	118.7	118.9
C2–C3–C4	121.3	121.2	121.1
C1–C2–H8	119.6	119.6	119.7
C4–C3–H9	118.7	118.7	118.8

[a] See Fig. 1 for numbering of atoms.
[b] jul-cc-pVDZ
[c] Ref. 82

Table 6.5. Vertical excitation energies of phenol and phenoxyl and the equilibrium dissociation energy of phenol (in eV)

	phenol			phenoxyl
	$^1\pi\pi^* - {}^1\pi\pi$	$^1\pi\sigma^* - {}^1\pi\pi$	D_e	$^2B_2 - {}^2B_1$
APRP[a]	4.58	5.88	3.93	1.07
SA(3)-CAS(12,11)/jul-cc-pVDZ[b]	5.04	5.56	2.54	1.79
SA(3)-MC-QDPT(12,11)/jul-cc-pVDZ[b]	4.70	5.86	4.37	0.94
CC2/aug-cc-pVDZ[c]	4.86	5.36		
MRCI/aug-cc-pVDZ[d]	4.75	5.76		
CASPT2(10/10)/aug(O)-cc-pVTZ[e]	4.52	5.64	4.05	0.65
EOM-CCSD/aug(O)-cc-pVTZ[e]	4.97	5.67		
Experimental	4.58[f]		4.18[g] /4.08[g]	1. 06[h]/1. 10[i]

[a] The equilibrium geometries of phenol and phenoxyl radical were optimized with the fitted PES and were used to calculate the vertical excitation energies and the equilibrium dissociation energy for breaking the O–H bond.
[b] Ref. 33
[c] Ref. 48
[d] Ref. 44
[e] Ref. 50
[f] Highest peak value obtained from Ref. 87
[g] Derived in Ref. 33 from Ref. 90 (first value) and Ref. 91 (second value)
[h] Ref. 88
[i] Ref. 89

Table 6.6. Thermal unimolecular rate constants and lifetimes for hydrogen dissociation of phenol on the V_2 surface at various temperatures

T(K)	CVT	CVT/ZCT	CVT/SCT
	Rate constant (s^{-1})		
150	8.1×10^{-10}	4.8×10^{6}	5.2×10^{8}
300	2.9×10^{1}	1.8×10^{6}	1.8×10^{8}
600	4.3×10^{6}	1.1×10^{8}	2.1×10^{8}
1000	5.0×10^{8}	1.6×10^{9}	2.1×10^{9}
	Lifetime (ns)		
150	1.2×10^{18}	210	1.9
300	3.4×10^{7}	556	5.5
600	235	9.3	4.8
1000	2.0	0.6	0.5

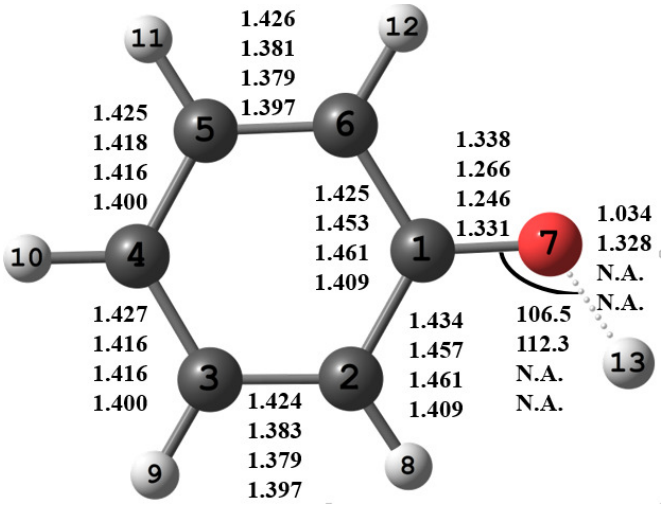

Figure 6.1. The figure shows the structure of the transition state on adiabatic surface S_1, and it also shows four sets of bond distances for key eight C–C, C–O, and O–H bond lengths (in Å) and the C–O–H bond angle (in degrees). From top to bottom are values for the equilibrium geometry of the S_1 state of phenol, the saddle point of the S_1 state (the structure shown), the $\tilde{X}\ ^2B_1$ state of phenoxyl radical, and the $\tilde{A}\ ^2B_2$ state phenoxyl radical. "N.A." denotes not applicable.

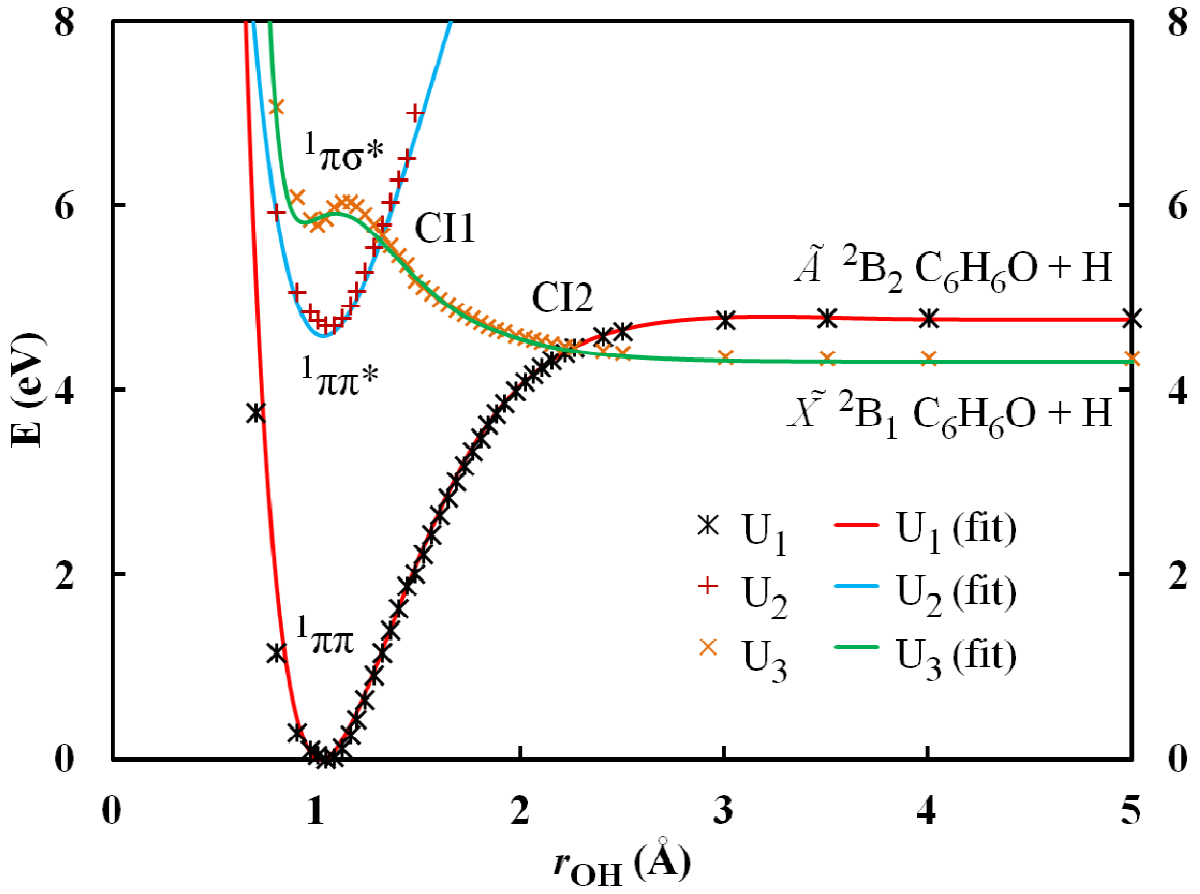

Figure 6.2. Calculated and fitted diabatic potential energy curves of phenol along the O–H dissociation coordinate. The other geometric parameters are fixed at their values at the equilibrium geometry of ground state phenol. The locations of the conical intersections on the APRP surfaces for these cuts are r = 1.316 Å and r = 2.232 Å, respectively.

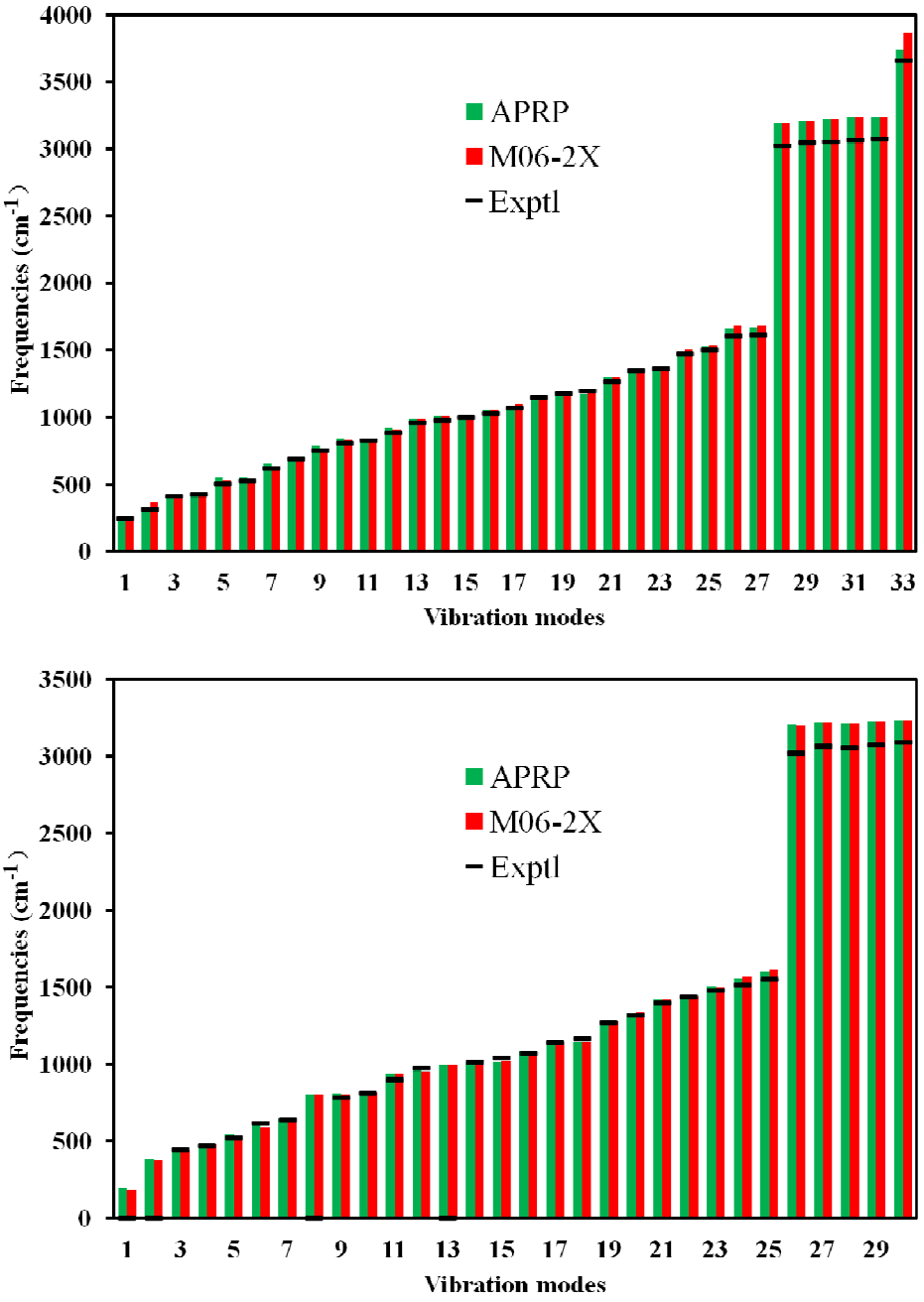

Figure 6.3. Comparison of vibrational frequencies calculated from the ground-state APRP surface, from M06-2X and DFT calculations with available experimental results. Top: the $^1\pi\pi$ state of phenol; bottom: the $\tilde{X}\ ^2B_1$ state of phenoxyl radical.

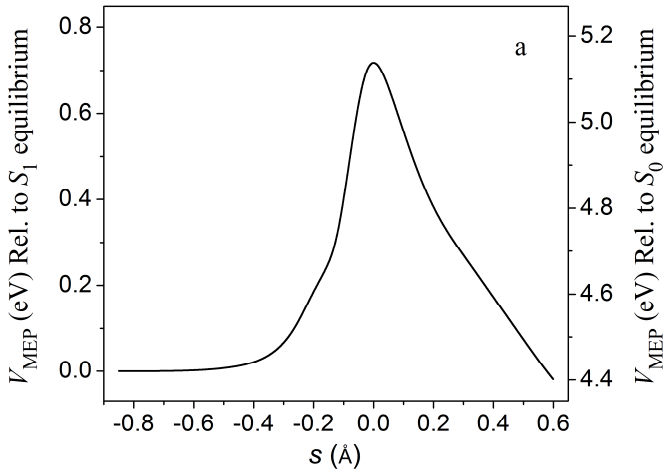
a
V_{MEP} (eV) Rel. to S_1 equilibrium
V_{MEP} (eV) Rel. to S_0 equilibrium
s (Å)

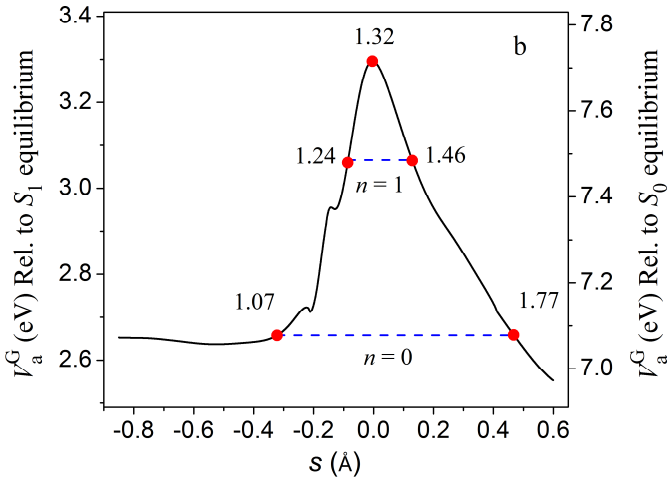
b
1.32
1.24
1.46
$n = 1$
1.07
1.77
$n = 0$
V_a^G (eV) Rel. to S_1 equilibrium
V_a^G (eV) Rel. to S_0 equilibrium
s (Å)

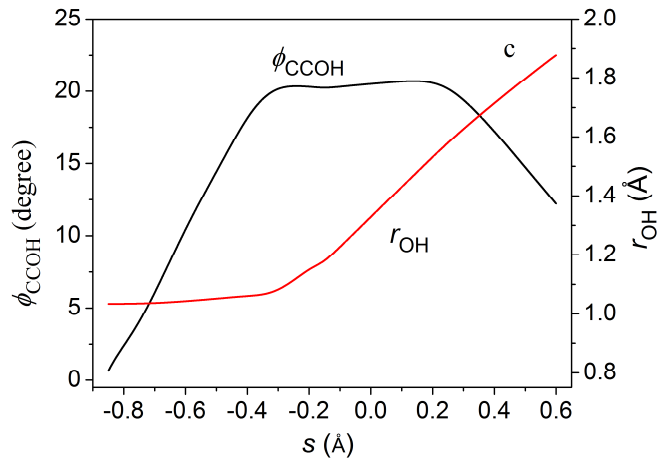
c
ϕ_{CCOH}
r_{OH}
ϕ_{CCOH} (degree)
r_{OH} (Å)
s (Å)

Figure 6.4. (a) Calculated V_{MEP} vs the reaction coordinate s (scaled to a reduced mass of one amu) for the photodissociation of phenol on the S_1 state surface. (b) Calculated ground-state vibrationally adiabatic potential ($V_{\mathrm{a}}^{\mathrm{G}}$) vs the reaction coordinate s. n = 0 and n = 1denote the energy levels with vibrational quantum number of 0 and 1 for the O–H stretch and 0 for other vibrational modes. The numbers denotes the values of O–H bond length at corresponding reaction coordinates. (c) Calculated O–H bond length and C2–C1–O–H torsion angle vs the reaction coordinate s.

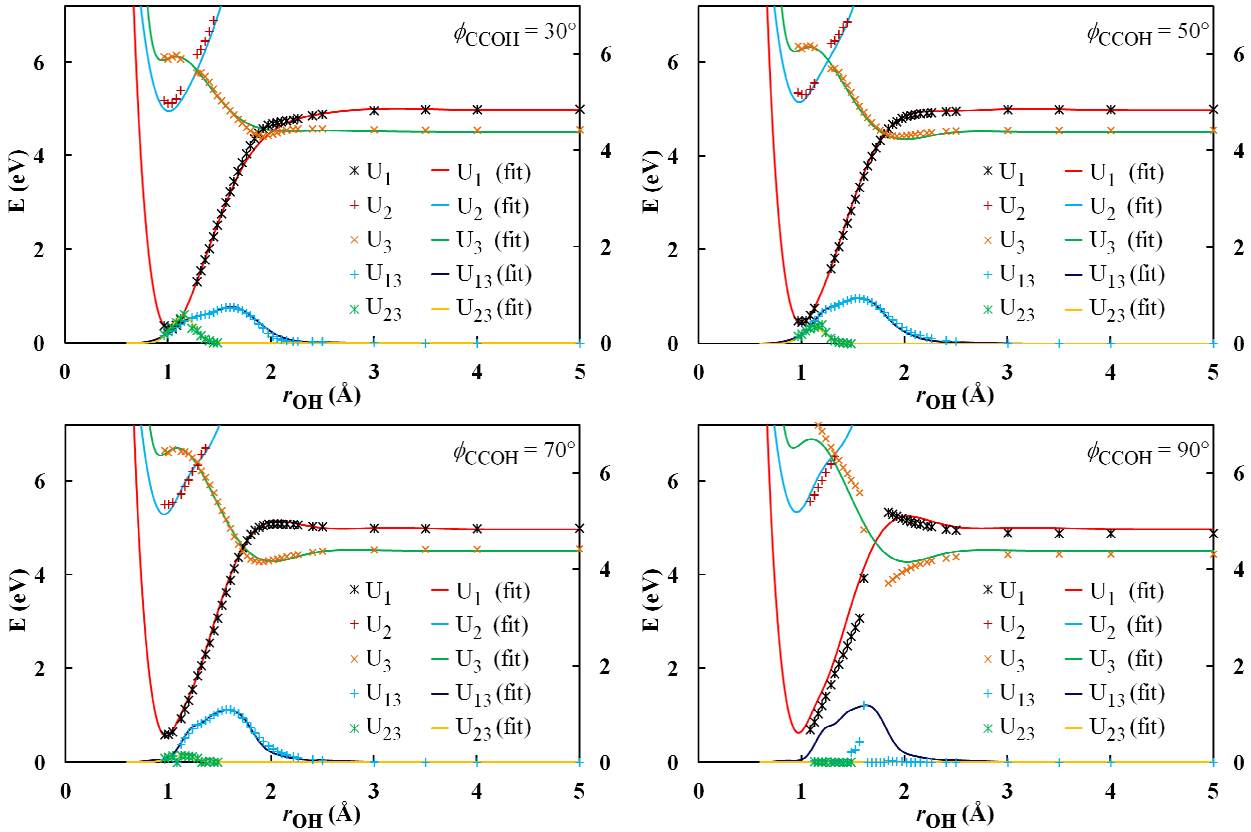

Figure 6.5. Calculated and fitted diabatic potentials (U_1, U_2, and U_3) and diabatic couplings (U_{13} and U_{23}) of phenol along the O–H dissociation coordinate r at various C2–C1–O–H torsion angles ϕ. The other geometric parameters are fixed at their values at the equilibrium geometry of ground state phenol.

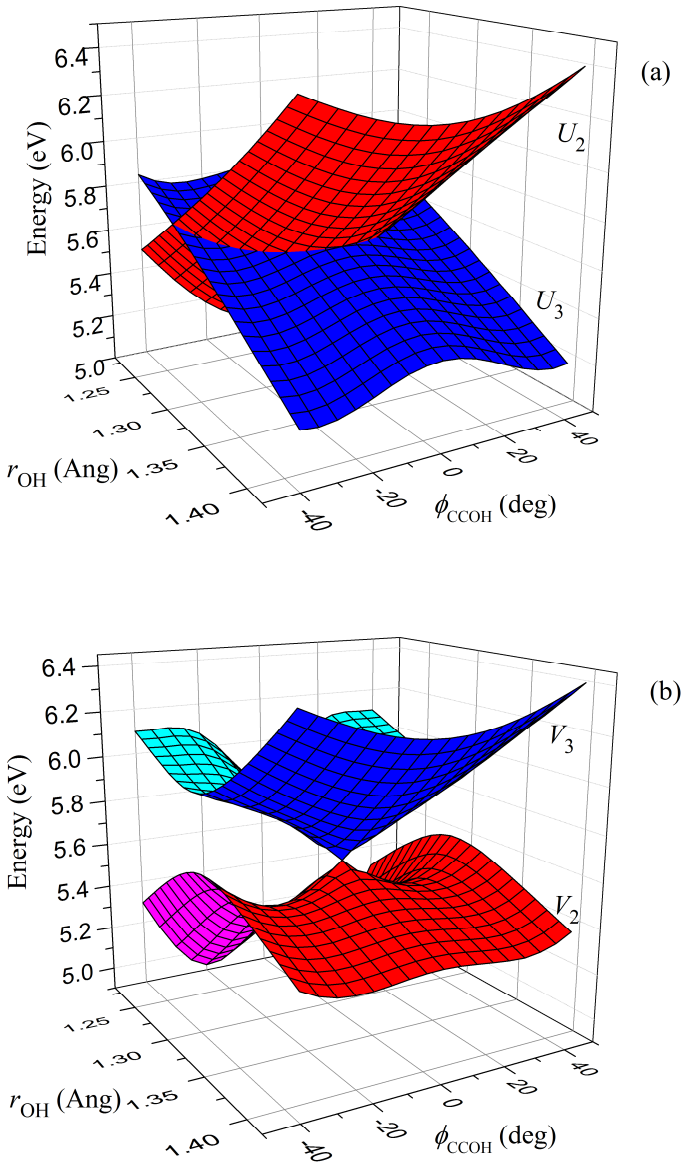

Figure 6.6. Three-dimensional plots of (a) the U_{22} and U_{33} diabatic potential-energy surfaces showing the diabatic crossing of the $^1\pi\pi^*$ and $^1\pi\sigma^*$ states and (b) the V_2 and V_3 adiabatic potential-energy surfaces of phenol as functions of r and ϕ. The conical intersection (CI1) is seen at $r = 1.32$ Å and $\phi = 0°$ with all other geometric parameters fixed at the ground state equilibrium geometry of phenol.

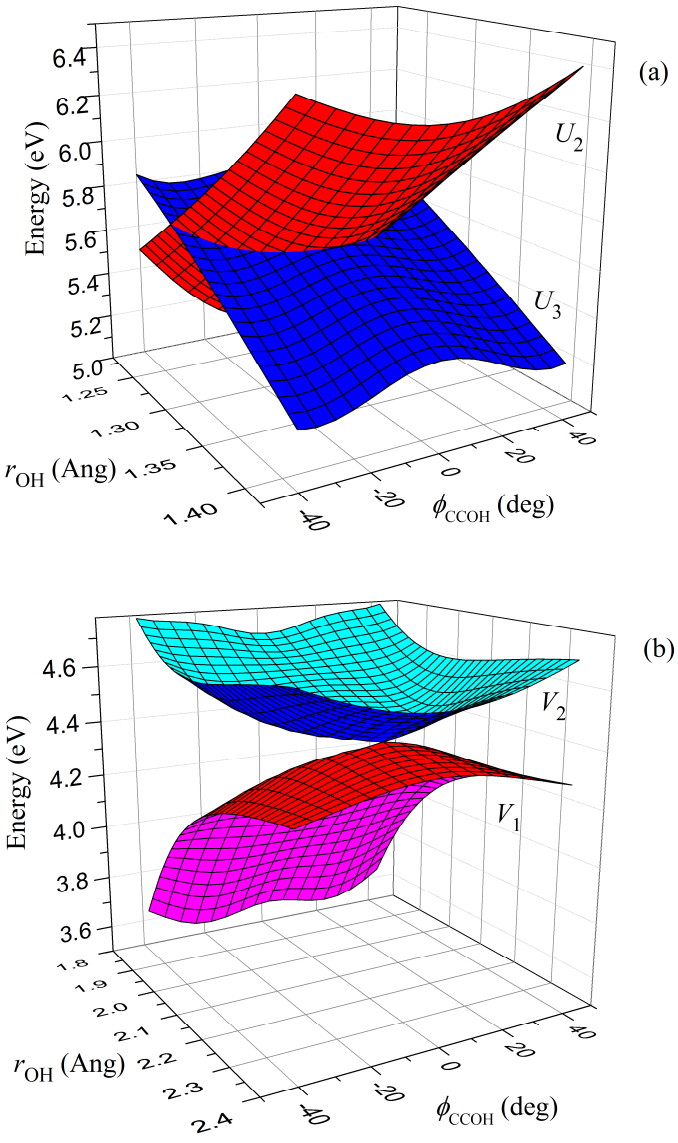

Figure 6.7. Three-dimensional plots of (a) the U_1 and U_3 diabatic potential-energy surfaces showing the diabatic crossing of the $^1\pi\pi$ and $^1\pi\sigma^*$ states and (b) the V_1 and V_2 adiabatic potential-energy surfaces of phenol as functions of r and ϕ. The conical intersection (CI2) is seen at $r = 2.23$ Å and $\phi = 0°$ with all other geometric parameters fixes at the ground state equilibrium geometry of phenol.

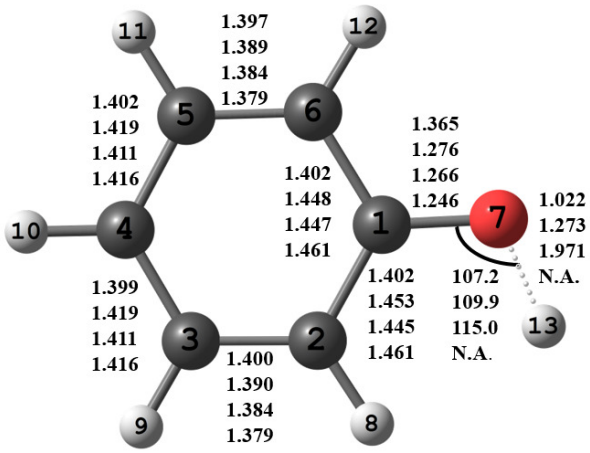

Figure 6.8. The figure shows the structure of MECI1 and four sets of bond distances for key eight C–C, C–O, and O–H bond lengths (in Å) and the C–O–H bond angle (in degrees). From top to bottom are values for the equilibrium geometry of the S_0 state of phenol, MECI1, MECI2, and the $\tilde{X}\ ^2B_1$ state phenoxyl radical. "N.A." denotes not applicable.

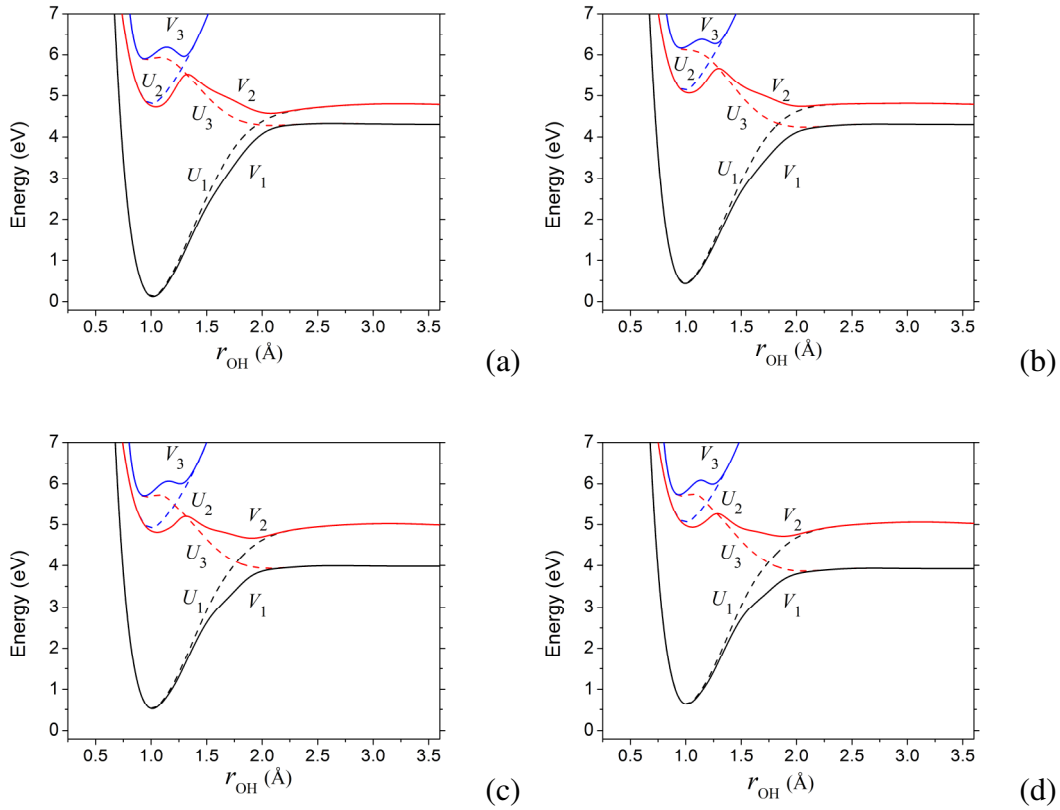

Figure 6.9. Diabatic potentials (U_1, U_2, and U_3) and adiabatic potentials (V_1, V_2, and V_3) versus r_{OH} with C2–C1–O–H torsion ϕ_{CCOH} = 145°, (a) all other geometric parameters fixed at the ground equilibrium geometry of phenol, (b) θ_{COH} = 130° and all other geometric parameters fixed at the ground equilibrium geometry of phenol, (c) all other geometric parameters fixed at the excited state (S_1) transition state geometry of phenol, (d) θ_{COH} = 115° and all other geometric parameters fixed at the ground equilibrium geometry of phenoxyl radical.

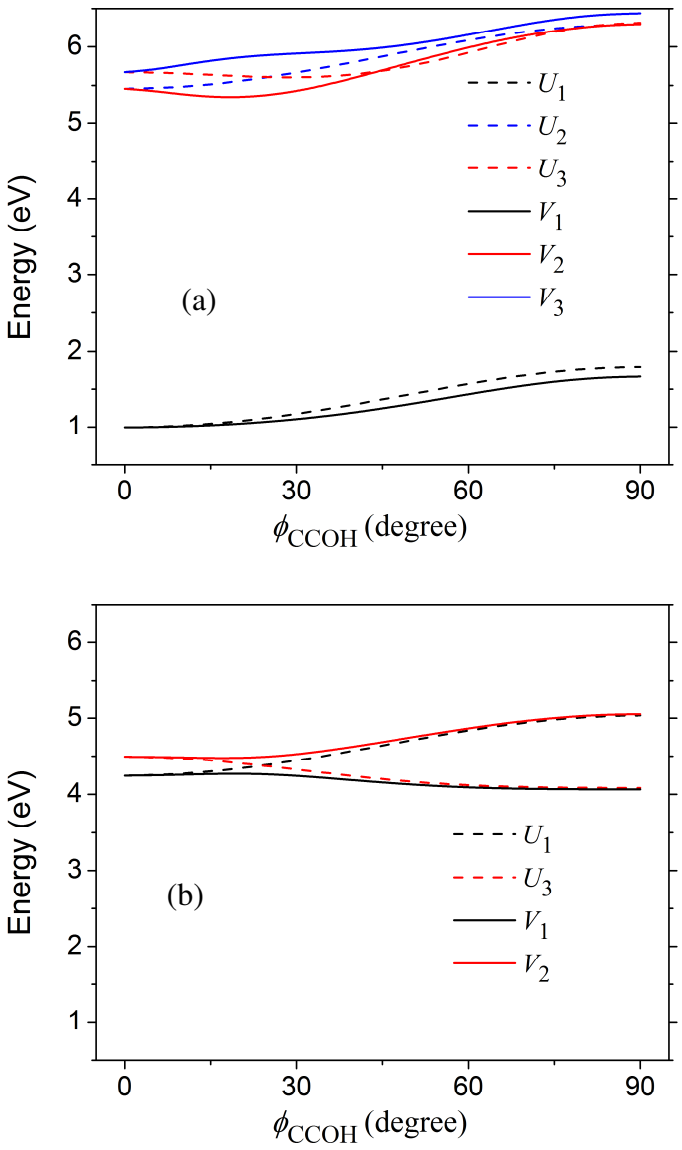

Figure 6.10. Diabatic potentials (U_1, U_2, and U_3) and adiabatic potentials (V_1, V_2, and V_3) versus C2–C1–O–H torsion ϕ_{CCOH} (a) with r_{OH} = 1.29 Å and all other geometric parameters fixed at the ground equilibrium geometry of phenol, (b) with r_{OH} = 2.10 Å and all other geometric parameters fixed at the ground equilibrium geometry of phenol.

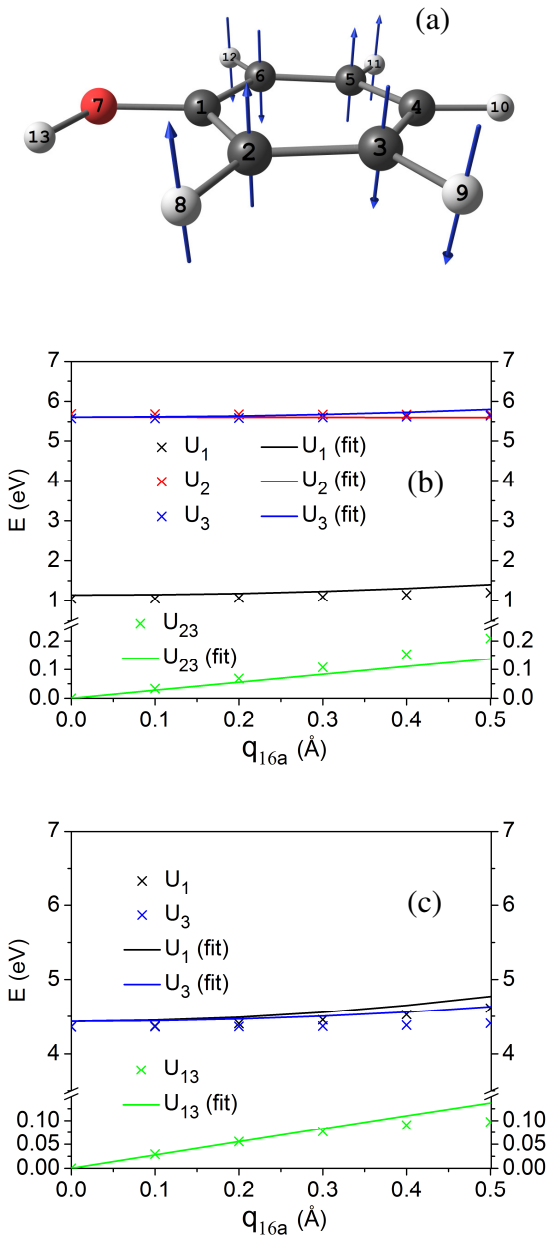

Figure 6.11. The atomic displacements of vibrational mode ν_{16a} (a), and calculated and fitted diabatic potentials and the most relevant diabatic couplings at conical intersections of the $^1\pi\pi^*$ and $^1\pi\sigma^*$ states (b) and the $^1\pi\pi$ and $^1\pi\sigma^*$ states (c) the states along scaled Cartesian normal-mode displacements.

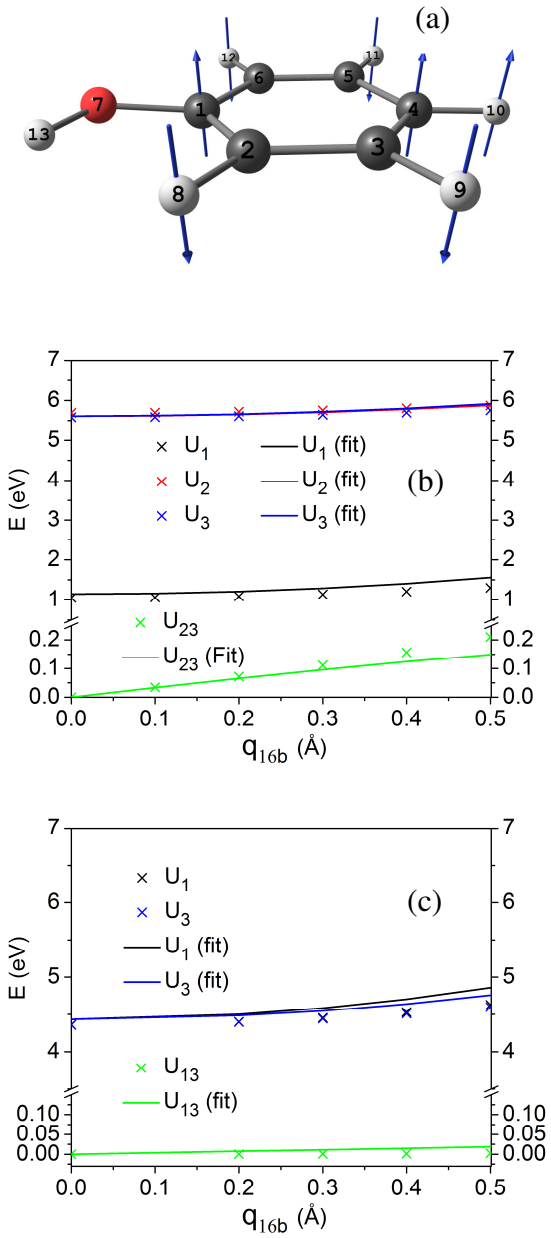

Figure 6.12. The atomic displacements of vibrational mode v16b (a), and calculated and fitted diabatic potentials and the most relevant diabatic couplings at conical intersections of the $^1\pi\pi^*$ and $^1\pi\sigma^*$ states (b) and the $^1\pi\pi$ and $^1\pi\sigma^*$ states (c) the states along scaled Cartesian normal-mode displacements.

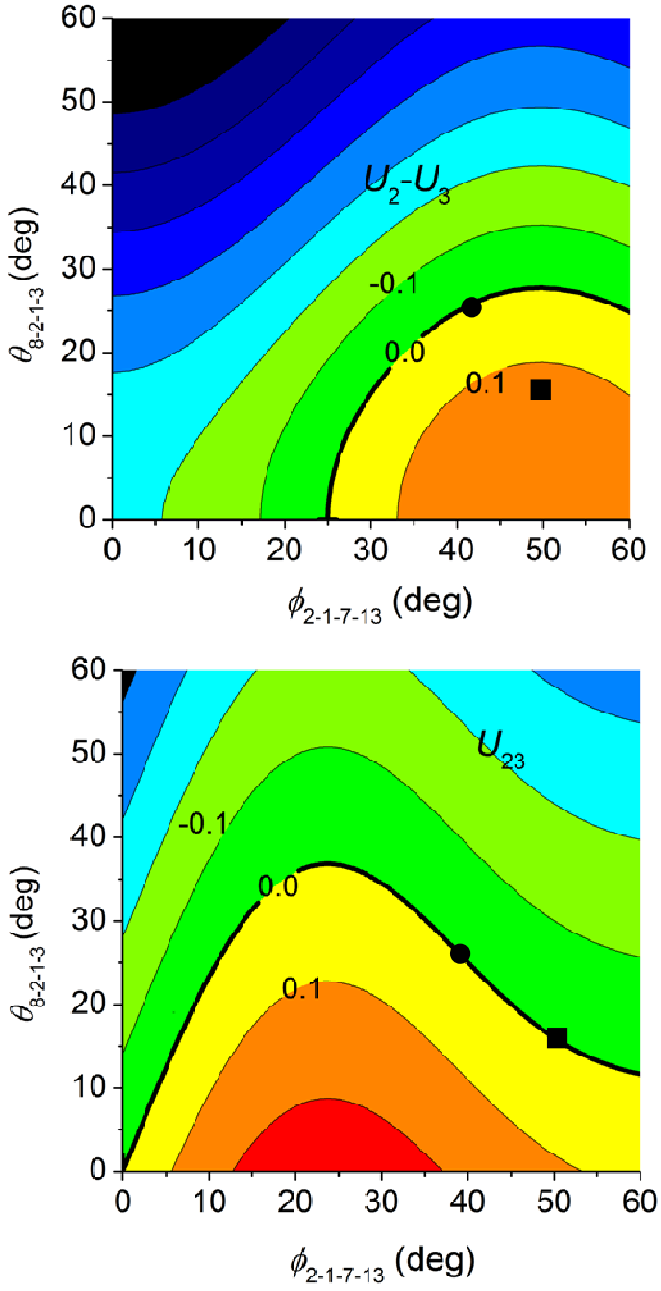

Figure 6.13. Contour plots of $U_2 - U_3$ and U_{23} (in eV) to locate the non-planar conical intersection of the $^1\pi\pi^*$ and $^1\pi\sigma^*$ states at r_{OH} = 1.29 Å. The solid square and circle are explained in Section 6.3.5.

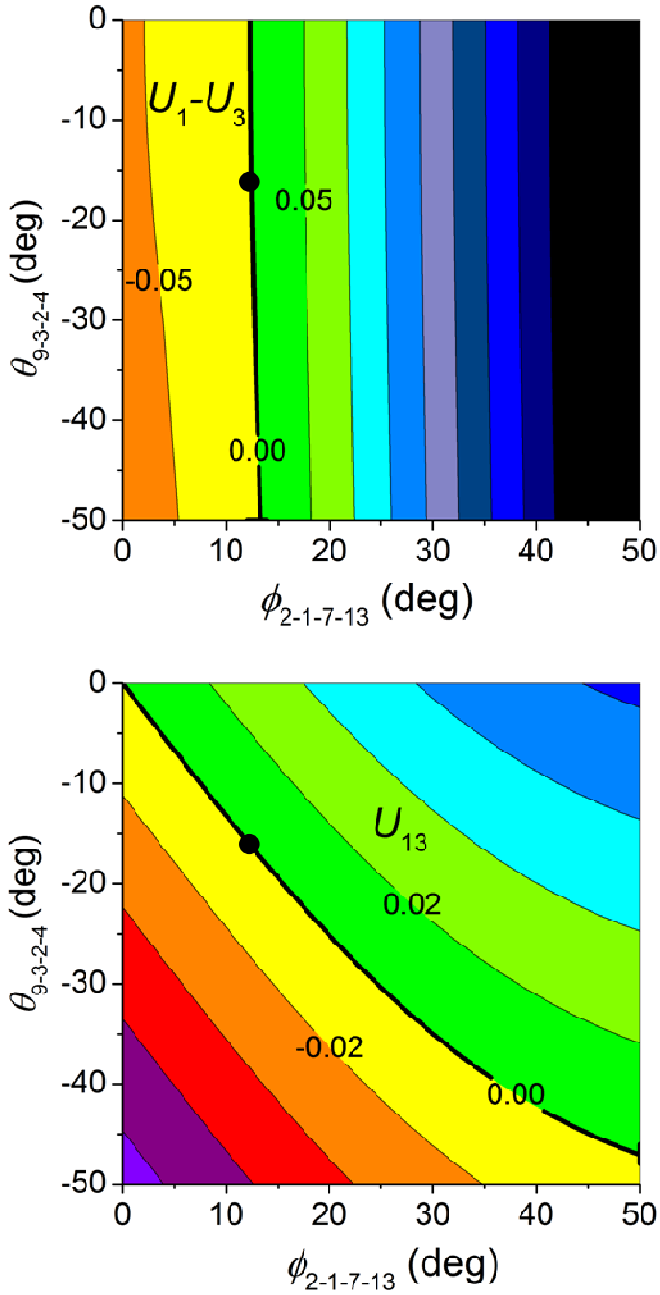

Figure 6.14. Contour plots of $U_1 - U_3$ and U_{13} (in eV) to locate the non-planar conical intersection of the $^1\pi\pi$ and $^1\pi\sigma^*$ states at $r = 2.20$ Å.

Bibliography

A. Aguado, P. Barragán, R. Prosmiti, G. Delgado-Barrio, P. Villarreal, and O. Roncero, J. Chem. Phys. **133**, 024306 (2010).

A. Aguado and M. Paniagua, J. Chem. Phys. **96**, 1265 (1992).

A. Aguado, C. Suárez, and M. Paniagua, J. Chem. Phys. **101**, 4004 (1994).

T. V. Albu, J. Espinosa-García, and D. G. Truhlar, Chem. Rev. **107**, 5101 (2007).

I. M. Alecu, J. Zheng, Y. Zhao and D. G. Truhlar, J. Chem. Theory Comput. **6**, 2872 (2010).

M. H. Alexander, Chem Phys. **92**, 337 (1985).

E. Alguire and J. E. Subotnik, J. Chem. Phys. **135**, 44114 (2011).

N. L. Allinger, Y. H. Yuh, J.-H. Lii, J. Am. Chem. Soc. **111**, 8551 (1989).

M. Amarouche, F. X. Gadea and J. Durup, Chem. Phys. **130**, 145 (1989).

H. An and K. K. Baeck, J. Phys. Chem. A **115**, 13309 (2011).

K. Andersson, Theor. Chim. Acta **91**, 31 (1995).

K. Andersson, P.-Å. Malmqvist, B. O. Roos, A. J. Sadlej, and K. Wolinski, J. Phys. Chem. **94**, 5488 (1990).

K. Andersson, P.-Å. Malmqvist, and B. O. Roos, J. Chem. Phys. **96**, 1218 (1992).

V. Aquilanti, M. Bartolomei, D. Cappelletti, E. Carmona-Novillo, and F. Pirani, J. Chem. Phys. **117**, 615 (2002).

G. A. Arteca and O. Tapia, Int. J. Quantum Chem. **107**, 382 (2007).

M. N. R. Ashfold, B. Cronin, A. L. Devine, R. N. Dixon and M. G. D. Nix, Science **312**, 1637 (2006).

M. N. R. Ashfold, A. L. Devine, R. N. Dixon, G. A. King, M. G. D. Nix and T. A. A. Oliver, Proc. Natl. Acad. Sci. U. S. A. **105**, 12701 (2008).

M. N. R. Ashfold, G. A. King, D. Murdock, M. G. D. Nix, T. A. A. Oliver and A. G. Sage, Phys. Chem. Chem. Phys. **12**, 1218 (2010).

G. J. Atchity and K. Ruedenberg, J. Chem. Phys. **99**, 3790 (1993).

G. J. Atchity and K. Ruedenberg, Theor. Chem. Acc. **97**, 47 (1997).

D. Babikov, P. Zhang, and K. Morokuma, J. Chem. Phys. **121**, 6743 (2004).

M. Baer, Chem. Phys. Lett. **35**, 112 (1975).

M. Baer, Mol. Phys. **40**, 1011 (1980).

V. Barone, I. Cacelli, N. De Mitri, D. Licari, S. Monti, and G. Prampolini, Phys. Chem. Chem. Phys. **15**, 3736 (2013).

M. J. Bearpark, M. A. Robb and H. B. Schlegel, Chem. Phys. Lett. **223**, 269 (1994).

J. D. Bender, S. Doraiswamy, D. G. Truhlar and G. Candler, J. Chem. Phys. 140, 054302 (2014).

I. B. Bersuker, Chem. Rev. **101**, 1067 (2001).

H. D Bist, J. C. D. Brand and D. R. Williams, J. Mol. Spectrosc. **21**, 76 (1966).

H. D Bist, J. C. D. Brand and D. R. Williams, J. Mol. Spectrosc. **24**, 402 (1967).

H. D Bist, J. C. D. Brand and D. R. Williams, J. Mol. Spectrosc. **24**, 413 (1967).

H.-J. Böhm and R. Ahlrichs, Mol. Phys. **55**, 1159 (1985).
D. Bonhommeau and D. G. Truhlar, J. Chem. Phys. **129**, 14302 (2008).
D. Bonhommeau, R. Valero, D. G. Truhlar, A. Jasper, J. Chem. Phys. **130**, 234303 (2009).
M. Born and R. Oppenheimer, Ann. Phys. **84**, 457 (1927).
A. Boutalib and F. X. Gadéa, J. Chem. Phys. **97**, 1144 (1992).
J. M. Bowman, B. J. Braams, S. Carter, C. Chen, G. Czakó, B. Fu, X. Huang, E. Kamarchik, A. R. Sharma, B. C. Shepler, Y. Wang and Z. Xie, J. Phys. Chem. Lett. 1, 1866 (2010).
B. J. Braams and J. M. Bowman, Int. Rev. Phys. Chem. 28, 577 (2009).
C. R. Brazier, P. F. Bernath, J. B. Burkholder, and C. J. Howard, J. Chem. Phys. **89**, 1762 (1988).
D. W. Brenner, O. A. Shenderova, J. A. Harrison, S. J. Stuart, B. Ni, and S. B. Sinnott, J. Phys. Condens. Matter **14**, 783 (2002).
D. W. Brenner, O. A. Shenderova, J. D. Schall, D. A. Areshkin, S. Adiga, J. A. Harrsion, and S. J. Stuart, in *Handbook of Nanoscience, Engineering, and Technology*, edited by W. A. Goddard III, D. W. Brenner, S. E. Lyshevski, and G. J. Iafrate (CRC Press, Boca Raton, 2003) chapter 24.
B. R. Brooks, R. E. Bruccoleri, B. D. Olafson, D. J. States, S. Swaminathan, and M. Karplus, J. Comput. Chem. **4**, 187 (1983).
F. B. Brown and D. G. Truhlar, Chem. Phys. Lett. **113**, 441 (1985).
I. Cacelli and G. Prampolini, J. Chem. Theory. Comput. **3**, 1803 (2007).
M. C. Capello, M. Broquier, S.-I. Ishiuchi, W. Y. Sohn, M. Fujii, C. Dedonder-Lardeux, C. Jouvet and G. A. Pino, J. Phys. Chem. A **118**, 2056 (2014).
D. Cappelletti, F. Pirani, B. Bussery-Honvault, L. Gomez, and M. Bartolomei, Phys. Chem. Chem. Phys. **10**, 4281 (2008).
D. Cappelletti, F. Vecchiocattivi, F. Pirani, E. L. Heck, and A. S. Dickinson, Mol. Phys. **93**, 485 (1998).
M. E. Casida, C. Jamorski, K. C. Casida and D. R. Salahub, J. Chem. Phys. **108**, 4439 (1998).
R. J. Cave and M. D. Newton, J. Chem. Phys. **106**, 9213 (1997).
L. S. Cederbaum, H. Köppel and W. Domcke, Int. J. Quantum Chem. Symp. **15**, 251 (1981).
L. S. Cederbaum, J. Schirmer, and H. D. Meyer, J. Phys. A **22**, 2427 (1989).
A. Chakraborty, Y. Zhao, H. Lin, and D. G. Truhlar, J. Chem. Phys. **124**, 044315 (2006).
D. C. Chatfield, R. S. Friedman, D. G. Truhlar, B. C. Garrett and D. W. Schwenke, J. Am. Chem. Soc. **113**, 486 (1991).
M. S. Child, in *Atom-Molecule Collision Theory*, edited by R. B. Bernstein (Plenum, New York, 1979), p. 427-465.
B. Chen and J. I. Siepmann, J. Phys. Chem. B **103**, 5370 (1999).
C.-W. Cheng, Y.-P. Lee and H. A. Witek, J. Phys. Chem. A **112**, 2648 (2008).
R. Cimiraglia, J. P. Malrieu, M. Persico, and F. Spiegelmann, J. Phys. B **18**, 3073 (1985).

T. Clark, J. Chandrasekhar, G. W. Spitznagel, and P. v. R. Schleyer, J. Comput. Chem. **4**, 294 (1983).
R. E. Continetti, D. R. Cyr, D. L. Osborn, D. J. Leahy, and D. M. Neumark, J. Chem. Phys. **99**, 2616 (1993).
W. D. Cornell, P. Cieplak, C. I. Bayly, I. R. Gould, K. M. Merz Jr., D. M. Ferguson, D. C. Spellmeyer, T. Fox, J. W. Caldwell, and P. A. Kollman, J. Am. Chem. Soc. **117**, 5179 (1995).
O. Couronne and Y. Ellinger, Chem. Phys. Lett. **306**, 71 (1999).
C. J. Cramer, Essentials of Computational Chemistry: Theories and Models, 2nd ed., (Wiley & Sons, Chichester, 2004) p. 17-68
M. Dallos, H. Lischka, R. Shepard, D. R. Yarkony and P. G. Szalay, J. Chem. Phys **120**, 7330 (2004).
W. Damm, A. Frontera, J. Tirado-Rives, and W. L. Jorgensen, J. Comput. Chem. **18**, 1955 (1997).
S. Dasgupta, K. A. Brameld, C.-F. Fan, and W. A. Goddard III, Spectrochim. Acta. **53**, 1347 (1997).
R. Dawes, D. L. Thompson, Y. Guo, A. F. Wagner and M. Minkoff, J. Chem. Phys. 126, 184108 (2007).
R. Dawes, D. L. Thompson, A. F. Wagner, and M. Minkoff, J. Chem. Phys. **128**, 084107 (2008).
P. H. Dederichs, S. Blügel, R. Zeller R, and H. Akai, Phys. Rev. Lett. **53**, 2512 (1984).
J. B. Delos, Rev. Mod. Phys. **53**, 287 (1981).
J. R. Delos and W. R. Thorson, J. Chem. Phys. **70**, 1774 (1979).
A. L. Devine, M. G. D. Nix, B. Cronin and M. N. R. Ashfold, Phys. Chem. Chem. Phys. **9**, 3749 (2007).
R. N. Dixon, T. A. A. Oliver and M. N. R. Ashfold, J. Chem. Phys. **134**, 194303 (2011).
T. H. Dunning Jr., J. Chem. Phys. **90**, 1007 (1989).
W. Domcke and C. Woywood, Chem. Phys. Lett. **216**, 362 (1993).
W. Domcke, C. Woywood, and M. Stengle, Chem. Phys. Lett. **226**, 257 (1994).
M. A. Eliason and J. O. Hirschfelder, J. Chem. Phys. **30**, 1426 (1959).
A. Fernández-Ramos, B. A. Ellingson, B. C. Garrett and D. G. Truhlar, Rev. Comput. Chem. **23**, 125 (2007).
A. Fernández-Ramos, J. A. Miller, S. J. Klippenstein, and D. G. Truhlar, Chem. Rev. **106**, 4518 (2006).
A. Fernández-Ramos and D. G. Truhlar, J. Chem. Phys. **114**, 1491 (2001).
J. Finley, P.-Å. Malmqvist, B. O. Roos, and L. Serrano-Andrés, Chem. Phys. Lett. **288**, 299 (1998).
M. M. Francl and J. P. Chesick, J. Phys. Chem. **94**, 526 (1990).
R. A. Friesner and V. Guallar, Annu. Rev. Phys. Chem. **56**, 389 (2005).
M. J. Frisch, J. A. Pople, and J. S. Binkley, J. Chem. Phys. **80**, 3265 (1983).
B. Fu, E. Kamarchik, and J. M. Bowman, J. Chem. Phys. **133**, 164306 (2010).

B. R. L. Galvão and A. J. C. Varandas, J. Phys. Chem. A **113**, 14424 (2009).
B. R. L. Galvão and A. J. C. Varandas, J. Phys. Chem. A **115**, 12390 (2011).
E. Garcià and A. Laganà, J. Phys. Chem. A **101**, 4734 (1997).
V. M. García, M. Reguero, R. Caballol, and J. P. Malrieu, Chem. Phys. Lett. **281**, 161 (1997).
E. Garcià, A. Saracibar, S. Gómez-Carrasco, and A. Laganà, Phys. Chem. Chem. Phys. **10**, 2552 (2008).
J. Gao, Rev. Comp. Chem. **7**, 119 (1996).
J. Gao and D. G. Truhlar, Annu. Rev. Phys. Chem. **53**, 467 (2002).
B. C. Garrett and D. G. Truhlar, in *Theoretical Chemistry: Advances and Perspectives*, Vol. 6A, edited by D. Henderson (Academic Press, New York, 1981), p. 215.
B. C. Garrett and D. G. Truhlar, in *Theoretical Chemistry – Theory of Scattering: Papers in Honor of Henry Eyring*, edited by D. Henderson (Academic Press, New York, 1981), p. 216-289.
B. C. Garrett and D. G. Truhlar, J. Chem. Phys. **79**, 4931 (1983).
B. C. Garrett, D. G. Truhlar, and C. F. Melius, in *Energy Storage and Redistribution in Molecules*, edited by J. Hinze, (Plenum: New York, 1983), p. 375–395.
B. C. Garrett, D. G. Truhlar, A. F. Wagner and T. H. Dunning Jr., J. Chem. Phys. **78**, 4400 (1983).
F. D. X. George and S. Kumar, J. Chem. Phys. **119**, 409 (2007).
N. I. Gidopoulos and E. K. U. Gross, arXiv:cond-mat/0502433.
F. R. Gilmore, J. Quant. Spectrosc. Radiat. Transfer **5**, 369 (1965).
O. Godsi, C. R. Evenhuis and M. A. Collins, J. Chem. Phys. **125**, 104105 (2006).
L. Gomez, B. Bussery-Honvault, T. Cauchy, M. Bartolomei, D. Cappelletti, and F. Pirani, Chem. Phys. Lett. **445**, 99 (2007).
M. S. Gordon and M. W. Schmidt, in *Theory and Applications of Computational Chemistry: The First Forty Years*, edited by C. E. Dykstra, G. Frenking, K. S. Kim, and G. E. Scuseria (Elsevier, Amsterdam, 2005) p. 1167−1189.
A. Granovsky, J. Chem. Phys. **134**, 214113 (2011).
R. Grice and D. R. Herschbach, Mol. Phys. **27**, 159 (1974).
R. F. Gunion, M. K. Gilles, M. L. Polak and W. C. Lineberger, Int. J. Mass Spectrom. Ion Proc. **117**, 602 (1992).
Y. Guo, I. Tokmakov, D. L. Thompson, A. F. Wagner and M. Minkoff, J. Chem. Phys. 127, 214106 (2007).
S. Gupta, K. Dharamvir and V. K. Jindal, Int. J. Mod. Phys. B **18**, 1021 (2004).
M. D. Hack and D. G. Truhlar, J. Chem. Phys., **114**, 9305 (2011).
T. A. Halgren, J. Comput. Chem. **17**, 490 (1996).
T. A. Halgren, J. Comput. Chem. **17**, 520 (1996).
T. A. Halgren, J. Comput. Chem. **17**, 553 (1996).
T. A. Halgren and R. B. Nachbar, J. Comput. Chem. **17**, 587 (1996).
T. A. Halgren and W. N. Lipscomb, Chem. Phys. Lett. **49**, 225 (1977).

G. C. Hancock, P. Rejto, R. Steckler, F. B. Brown, D. W. Schwenke and D. G. Truhlar, J. Chem. Phys. **85**, 4997 (1986).
P. C. Hariharan and J. A. Pople, Theoretica. Chimica. Acta. **3**, 213 (1973).
W. J. Hehre, R. Ditchfield, and J. A. Pople, J. Chem. Phys. **56**, 2257 (1972).
R. Hellmann, Mol. Phys. **111**, 387 (2012).
J. Hendekovic, Chem. Phys. Lett. **90**, 193 (1982).
J. Hendekovic, Croat. Chem. Acta **56**, 375 (1983).
K. Hirao, Chem. Phys. Lett. **190**, 374 (1992).
G. Hirsch, R. J. Buenker, and C. Petrongolo, Mol. Phys. **70**, 825 (1990).
G. Hirsch, R. J. Buenker, and C. Petrongolo, Mol. Phys. **70**, 835 (1990).
J. O. Hirschfelder and E. Wigner, J. Chem. Phys. 1939, **7**, 616 (1939).
T. Hollebeek, T.-S. Ho, and H. Rabitz, Annu. Rev. Phys. Chem. **1990**, *50*, 537-570.
V. Hornak, R. Abel, A. Okur, B. Strockbine, A. Roitberg, and C. Simmerling, Protein **65**, 712 (2006).
H. Hu and W. Yang, Annu. Rev. Phys. Chem. **59**, 573 (2008).
K. P. Huber and G. Herzberg, *Molecular Spectra and Molecular Structure. IV. Constants of Diatomic Molecules* (Van Nostrand Reinhold Co., 1979) p. 412.
N. S. Hush, Progr. Inorg. Chem. **8**, 391 (1967).
T. Ichino, J. Gauss and J. F. Stanton, J. Chem. Phys. **130**, 174105 (2009).
A. Iqbal, M. S. Y. Cheung, M. G. D. Nix and V. G. Stavros, J. Phys. Chem. A **113**, 8157 (2009).
A. D. Isaacson and D. G. Truhlar, J. Chem. Phys. **75**, 4090 (1981).
A. W. Jasper, M. D. Hack, D. G. Truhlar, and P. Piecuch, J. Chem. Phys. **116**, 8353 (2002).
A. W. Jasper, B. K. Kendrick, C. A. Mead, D. G. Truhlar, in *Modern Trends in Chemical Reaction Dynamics*, edited by X. Yang, K. Liu (World Scientific, Singapore, 2003), p. 329-391.
A. W. Jasper, N. E. Schultz, and D. G. Truhlar, J. Phys. Chem. B **109**, 3915 (2005).
A. W. Jasper and D. G. Truhlar, in *Conical Intersections: Theory, Computation, and Experiment*, edited by W. Domcke, D. Yarkony and H. Köppel (World Scientific, Singapore, 2011), pp. 375-414.
A. W. Jasper, C. Zhu, S. Nangia and D. G. Truhlar, Faraday Discuss. **127**, 1 (2004).
H. S. Johnston, Adv. Chem. Phys. **3**, 131 (1961).
J. D. Johnson, M. S. Shaw, and B. L. Holian, J. Chem. Phys. **80**, 1279 (1983).
W. L. Jorgensen and J. Tirado-Rives, J. Comput. Chem. **26**, 1689 (2005).
L. R. Kahn, P. J. Hay, and I. Shavitt, J. Chem. Phys. **61**, 3530 (1974).
G. Kaminski, E. M. Duffy, T. Matsui, and W. L. Jorgensen, J. Phys. Chem. **98**, 13077 (1994).
M. H. Karimi-Jafari and M. Ashouri, Phys. Chem. Chem. Phys. **13**, 9887 (2011).
M. H. Karimi-Jafari, A. Maghari, and S. Shahbazian, Chem. Phys. **314**, 249 (2005).
T. N. V. Karsili, A. M. Wenge, B. Marchetti and M. N. R. Ashfold, Phys. Chem. Chem. Phys. **16**, 588 (2014).

R. A. Kendall and T. H. Dunning, Jr., J. Chem. Phys. **96**, 6796 (1992).
B. K. Kendrick, C. A. Mead and D. G. Truhlar, Chem. Phys. **277**, 31 (2002).
G. Keresztury, F. Billes, M. Kubinyi and T. Sundius, J. Phys. Chem. A **102**, 1371 (1998).
I. S. K. Kerkines, Z. Wang, P. Zhang, and K. Morokuma, Mol. Phys. **107**, 1017 (2009).
H. J. Kim, and J. T. Hynes, J. Am. Chem. Soc. **114**,10508 (1992).
G. A. King, A. L. Devine, M. G. D. Nix, D. E. Kelly and M. N. R. Ashfold, Phys. Chem. Chem. Phys. **10**, 6417 (2008).
G. A. King, T. A. A. Oliver, M. G. D. Nix and M. N. R. Ashfold, J. Phys. Chem. A **113**, 7984 (2009).
P. J. Knowles and H.-J. Werner, Chem. Phys. Lett. **115,** 259 (1985).
H. Köppel, in Conical Intersections: Electronic Structures, Dynamics and Spectroscopy, edited by W. Domcke, D. R. Yarkony, and H. Köppel (World Scientific, Singapore,2004), p. 175-204.
P. M. Kozlowski and E. R. Davidson, Chem. Phys. Lett. **222**, 615 (1994).
R. Krishnan, J. S. Binkley, R. Seeger, and J. A. Pople, J. Chem. Phys. **72**, 650 (1980).
E. S. Kryachenko and D. R. Yarkony, Int. J. Quantum Chem. **76**, 235 (2000).
J. Kucar, M. Pavlovic, and J. Hendekovic, Int. J. Quantum Chem. **32**, 699 (1987).
A. Kulkarni, D. G. Truhlar, S. G. Srinivasan, A. C. T. van Duin, P. Norman, and T. E. Schwartzentruber, J. Phys. Chem. C **117**, 258 (2013).
A. Laganà, G. O. D. Aspuru, E. Garcia, J. Chem. Phys. **108**, 3886 (1998).
A. Laganà, E. Garcià, and L. Ciccarelli, J. Phys. Chem. **91**, 312 (1987).
Z. Lan, W. Domcke, V. Vallet, A. L. Sobolewski and S. Mahapatra, J. Chem. Phys. **122**, 224315 (2005).
N. W. Larsen, J. Mol. Struct. **51**, 175 (1979).
J. G. Lauderdale and D. G. Truhlar, Surf. Sci. **164**, 558 (1985).
T. J. Lee and J. E. Rice, J. Chem. Phys. **94**, 1215 (1991).
M. L. Leininger, T. J. Van Huis, and H. F. Schaefer III, J. Phys. Chem. A **101**, 4460 (1997).
G. Lendvay, J. Mol. Strucrt. THEOCHEM **501-502**, 389 (2000).
K. Leonhard and U. K. Deiters, Mol. Phys. **100**, 2571 (2002).
Z. H. Li, R. Valero and D. G. Truhlar, Theor. Chem. Acc. **118**, 9 (2007).
W. Lichten, Phys. Rev. **131**, 229 (1963).
J.-H. Lii and N. L. Allinger, J. Am. Chem. Soc. **111**, 8566 (1989).
J.-H. Lii and N. L. Allinger, J. Am. Chem. Soc. **111**, 8576 (1989).
H. Lin, and D. G. Truhlar, Theor. Chem. Acc. **117**, 185 (2007).
K. Lindorff-Larsen, S. Piana, K. Palmo, P. Maragakis, J. L. Klepeis, R. O. Dror, and D. E. Shaw, Proteins **78**, 1950 (2010).
R. J. Lipert and S. D. Colson, J. Phys. Chem. 93, 135 (1989).
H. Lischka, M. Dallos, P. G. Szalay, D. R. Yarkony, and R. Shepard, J. Chem. Phys. **120**, 7322 (2004).
Y.-P. Liu, D.-H. Lu, A. Gonzàlez-Lafont, D. G. Truhlar and B. C. Garrett, J. Am. Chem. Soc. **115**, 7806 (1993).

Y.-P. Liu, G. C. Lynch, T. N. Truong, D.-H. Lu, D. G. Truhlar and B. C. Garrett, J. Am. Chem. Soc. **115**, 2408 (1993).
Y.-R. Luo, *Handbook of Bond Dissociation Energies in Organic Compounds* (University of Science and Technology of China: Hefei, 2006), p. 182.
A. D. MacKerell Jr., D.; Bashford, M. Bellott, R. L. Dunbrack Jr., J. D. Evanseck, M. J. Field, S. Fischer, J. Gao, H. Guo, S. Ha, D. Joseph-McCarthy, L. Kuchnir, K. Kuczera, F. T. K. Lau, C. Mattos, S. Michnick, T. Ngo, D. T. Nguyen, B. Prodhom, W. E. Reiher III, B. Roux, M. Schlenkrich, J. C. Smith, R. Stote, J. Straub, M. Watanabe, J. Wiorkiewicz-Kuczera, D. Yin, and M. Karplus, J. Phys. Chem. B **102**, 3586 (1998).
A. D. MacKerell Jr., M. Feig, and C. L. Brooks, J. Comput. Chem. **25**, 1400 (2004).
J. P. Malrieu and F. Spiegelmann, in *Photophysics and Photochemistry Above 6 eV*, edited by F. Lahmani (Elsevier, Amsterdam, 1985), p. 305-317.
M. Marchi, J. N. Gehlen, D. Chandler and M. Newton, J. Am. Chem. Soc. **115**, 4178 (1993).
R. A. Marcus, J. Chem. Phys. **46**, 959 (1967).
J. M. L. Martin, J. P. François, and R. Gijbels, J. Chem. Phys. **93**, 4485 (1990).
J. W. McGowan and H. H. Michels, Adv. Chem. Phys. **45**, 224 (1981).
D. F. McIntosh and K. H. Michaelian, Can. J. Spectrosc. **24**, 65 (1979).
C. A. Mead, Rev. Mod. Phys. **64**, 51 (1992).
C. A. Mead, J. Chem. Phys. **125**, 204109 (2006).
C. A. Mead and D. G. Truhlar, J. Chem. Phys. **77**, 6090 (1982).
R. Meana-Pañeda, D. G. Truhlar and A. Fernández-Ramos, J. Chem. Theory Comput. **6**, 6 (2010).
H.-D. Meyer and W. H. Miller, J. Chem. Phys. **70**, 1334 (1979).
A. D. Micha, J. Chem. Phys. **78**, 7138 (1983).
Y. Mo and J. Gao, J. Comput. Chem. **21**, 1458 (2000).
G. Monard and K. M. Merz Jr., Acc. Chem. Res. **32**, 904 (1999).
P. M. Morse, Phys. Rev. **34**, 1957 (1929).
R. S. Mulliken, J. Am. Chem. Soc. **64**, 811 (1952).
J. N. Murrell, O. Novaro, and S. Castillo, Chem. Phys. Lett. **90**, 421 (1982).
H. Nakamura and D. G. Truhlar, J. Chem. Phys. **115**, 10353 (2001).
H. Nakamura and D. G. Truhlar, J. Chem. Phys. **117**, 5576 (2002).
H. Nakamura and D. G. Truhlar, J. Chem. Phys. **118**, 6816 (2003).
H. Nakano, Chem. Phys. Lett. **207**, 372 (1993).
H. Nakano, J. Chem. Phys. **99**, 7983 (1993).
S. Nangia and D. G. Truhlar, J. Chem. Phys. **124**, 124309 (2006).
M. G. D. Nix, A. L. Devine, B. C. Cronin, R. N. Dixon, and M. N. R. Ashfold, J. Chem. Phys. **125**, 133318 (2006).
M. G. D. Nix, A. L. Devine, R. N. Dixon and M. N. R. Ashfold, Chem. Phys. Lett. **463**, 305 (2008).
I. Nompelis, G. V. Candler, and M. S. Holden, AIAA J. **41**, 2162 (2003).
R. W. Numrich and D. G. Truhlar, J. Phys. Chem. **79**, 2745 (1975).

S. Olsen and R. H. McKenzie, J. Chem. Phys. **131**, 234306 (2009).
E. H. M. Olsson, G.-Y. Hong, and A. Warshel, J. Am. Chem. Soc. **125**, 5025 (2003).
T. F. O'Malley, J. Chem. Phys. **51**, 322 (1969).
T. Pacher, L. S. Cederbaum and H. Köppel, J. Chem. Phys. **89**, 7367 (1988).
T. Pacher, L. S. Cederbaum, and H. Köppel, Adv. Chem. Phys. **84**, 293 (1993).
T. Pacher, H. Köppel, and L. S. Cederbaum, J. Chem. Phys. **95**, 6668 (1991).
M. Page and J. W. McIver Jr., J. Chem. Phys. **88**, 922 (1988).
B. N. Papas, M. S. Schuuman and D. R. Yarkony, J. Chem. Phys. **129**, 124104 (2008).
E. Papajak, H. R. Leverentz, J. Zheng, and D. G. Truhlar, J. Chem. Theory Comput. **5**, 1197 (2009); erratum: **5**, 3330 (2009).
E. Papajak and D. G. Truhlar, J. Chem. Theory Comput. 7, 10 (2011).
Y. C. Park, H. An, H. Choi, Y. S. Lee and K. K. Baeck, Theor. Chem. Acc. **131**, 1212 (2012).
Y. Paukku, K. R. Yang, Z. Varga and D. G. Truhlar, J. Chem. Phys. 139, 044309 (2013).
L. Pauling, *The Nature of the Chemical Bond*, 3rd. ed.; Cornell University Press: Ithaca, NY, 1960.
M. Pavanello and J. Neugebauer, J. Chem. Phys. **135**, 134113 (2011).
A. Pérez, I. Marchán, D. Svozil, J. Sponer, T. E. Cheatham, C. A. Laughton, and M. Orozco, Biophys. J. **92**, 3817 (2007).
M. Peric, R. J. Buencker, and S. D. Peyerimhoff, Mol. Phys. **71**, 673 (1990).
C. Petrongolo, J. Mol. Struct. **175,** 215 (1988).
A. Pino, A. N. Oldani, E. Marceca, M. Fujii, S.-I. Ishiuchi, M. Miyazaki, M. Broquier, C. Dedonder and C. Jouvet, J. Chem. Phys. **133**, 124313 (2010).
G. Pongor, G. Fogarezi, J. E. Boggs, and P. Pulay, J. Mol. Spectrosc. **114**, 445 (1985).
G. Portalone, G. Schultz, A. Domenicano and I. Hargittai, Chem. Phys. Lett. **197**, 482 (1992).
P. Pulay, G. Fogarasi, F. Pang, and J. E. Boggs, J. Am. Chem. Soc. **101**, 2550 (1979).
J. G. Radziszewski, M. Gil, A. Gorski, J. Spanger-Larsen, J. Waluk and B. J. Mróz, J. Chem. Phys. **115**, 9733 (2001).
S. G. Ramesh and W. Domcke, Faraday Discuss. **163**, 73 (2013).
N. Rai and J. I. Siepmann, J. Phys. Chem. B **117**, 273 (2013).
A. K. Rappe, C. J. Casewit, K. S. Colwell, W. A. Goddard III, and W. M. Skiff, J. Am. Chem. Soc. **114**, 10024 (1992).
B. O. Roos and K. Andersson, Chem. Phys. Lett. **245**, 215 (1995).
B. O. Roos, P. R. Taylor and P. E. M. Siegbahn, Chem. Phys. **48**, 157 (1980).
K. Ruedenberg and G. J. Atchity, J. Chem. Phys. **99**, 3799 (1993).
K. Ruedenberg, M. W. Schmidt, G. M. Gillbert and S. T. Elbert, Chem. Phys. **71**, 41 (1982).
F. Sasaki and M. Yoshimine, Phys. Rev. A **9**, 26 (1974).
G. C. Schatz, Rev. Mod. Phys. **61**, 669 (1989).

W. R. P. Scott, P. H. Hunenberger, I. G. Tironi, A. E. Mark, S. R. Billeter, J. Fennen, A. E. Torda, T. Huber, P. Kruger, and W. F. van Gunsteren, J. Phys. Chem. A **103**, 3596 (1999).
H. M. Senn and W. Thiel, Angew. Chem. Int. Ed. **48**, 1198 (2009).
T. Shiozaki, W. Győrffy, P. Celani, and H.-J. Werner, J. Chem. Phys. **135**, 81106 (2011).
P. Siegbahn, A. Heiberg, B. O. Roos and B. A. Levy, Phys. Scr. **21**, 323 (1980).
D. Simah, B. Hartke, and H.-J. Werner, J. Chem. Phys. **111**, 4523 (1999).
G. Simons, R. G. Parr and J. M. Finlan, J. Chem. Phys. **84**, 891 (1973).
A. Sirjoosingh and S. Hammes-Schiffer, J. Phys. Chem. A **115**, 2367 (2011).
P. H.-L. Sit, M. Cococcioni and N. Marzari, Phys. Rev. Lett. **97**, 28303 (2006).
R. T. Skodje, D. G. Truhlar and B. C. Garrett, J. Chem. Phys. **77**, 5955 (1982).
F. T. Smith, Phys. Rev. **179**, 111 (1969).
A. L. Sobolewski and W. Domcke, J. Phys. Chem. A **105**, 9275 (2001).
A. L. Sobolewski, W. Domcke, C. Dedonder-Lardeux and C. Jouvet, Phys. Chem. Chem. Phys. **4**, 1093 (2002).
L. Song and J. Gao, J. Phys. Chem. A **112**, 12925 (2008).
K. S. Sorbie and J. N. Murrell, Mol. Phys. **29**, 1387 (1975).
A. Soudackov and S. Hammes-Schiffer, J. Chem. Phys. **113**, 2385 (2000).
D. Spangenberg, P. Imhof and K. Kleinermanns, Phys. Chem. Chem. Phys. **5**, 2505 (2003).
J. Spanget-Larsen, M. Gil, A. Gorski, D. M. Blake, J. Waluk and J. G. Radziszewski, J. Am. Chem. Soc. **123**, 11253 (2003).
F. Spiegelmann and J. P. Malrieu, J. Phys. B: At. Mol. Phys. **17**, 1259 (1984).
D. Stahel, M. Leoni and K. Dressler, J. Chem. Phys. **79**, 2541 (1983).
J. R. Stallcop and H. Partridge, Chem. Phys. Lett. **281**, 212 (1997).
D. Steele, E. R. Lippincott, and J. T. Vanderslice, Rev. Mod. Phys. **34**, 239 (1962).
P. Strąk and S. Krukowski, J. Chem. Phys. **126**, 194501 (2007).
R. E. Stratmann, G. E. Scuseria and M. J. Frisch, J. Chem. Phys. **109**, 8218 (1998).
J. E. Subotnik, S. Yeganeh, R. J. Cave and M. A. Ratner, J. Chem. Phys. **129**, 244101 (2008).
A. Sur and P. M. Johnson, J. Chem. Phys. **84**, 1206 (1986).
C. Tablero, A. Aguado, and M. Paniagua, J. Chem. Phys. **110**, 7796 (1999).
A. Tachibana and K. Fukui, Theor. Chen. Acta. **51**,189 (1979).
K. C. Thompson, M. J. T. Jordan, and M. A. Collins, J. Chem. Phys. **108**, 8302 (1998).
T. C. Thompson, D. G. Truhlar and C. A. Mead, J. Chem. Phys. **82**, 2392 (1985).
O. Tishchenko and D. G. Truhlar, J. Chem. Phys. **132**, 084109 (2010).
O. Tishchenko, D. G. Truhlar, A. Ceulemans and M. T. Nguyen, J. Am. Chem. Soc. **130**, 7000 (2008).
M. S. Topaler, D. G.Truhlar, X. Y. Chang, P. Piecuch, and J. C. Polanyi, J. Chem. Phys. **108**, 5349 (1998).
D. G. Truhlar, J. Comput. Chem. **28**, 73 (2007).

D. G. Truhlar, A. D. Isaacson, and B. C. Garrett, in *The Theory of Chemical Reaction Dynamic*s, Vol. 4, edited by M. Baer (CRC Press, Boca Raton, FL, 1985), p. 65-137.
D. G. Truhlar, A. D. Isaacson, R. T. Skodje and B. C. Garrett, J. Phys. Chem. **86**, 2252 (1982).
D. G. Truhlar and A. Kuppermann, J. Am. Chem. Soc. **93**, 1840 (1971).
D. G. Truhlar and C. A. Mead, Phys. Rev. A **68**, 32501 (2003).
C.-M. Tseng, Y. T. Lee, M.-F. Lin, C.-K. Ni, S.-Y. Liu, Y.-P. Lee, Z. F. Xu and M. C. Lin, J. Phys. Chem. A **111**, 9463 (2007).
R. Valero and D. G. Truhlar, J. Chem. Phys. **125**, 194305 (2006).
R. Valero and D. G. Truhlar, J. Chem. Phys. **137**, 22A539 (2012).
R. Valero, D. G. Truhlar, and A. W. Jasper, J. Phys. Chem. A **112**, 5756 (2008).
F. van Bolhuis and C. T. Kiers, Acta Cryst. **B34**, 1015 (1978).
A. van der Avoird, P. E. S. Wormer, and A. P. J. Jansen, J. Chem. Phys. **84**, 1629 (1985).
A. C. T. van Duin, S. Dasgupta, F. Lorant, and W. A. Goddard III, J. Phys. Chem. A **105**, 9396 (2001).
K. Vanommeslaeghe, E. Hatcher, C. Acharya, S. Kundu, S. Zhong, J. Shim, E. Darian, O. Gubench, P. Lopes, I. Vorobyov, and A. D. Mackerell Jr., J. Comput. Chem. **31**, 671 (2010).
T. van Voorhis, T. Kowalczak, B. Kaduk, L.-P. Wang, C.-L. Cheng and Q. Wu, Annu. Rev. Phys. Chem. **61**, 149 (2010).
A. J. C. Varandas, F. B. Brown, C. A. Mead, D. G. Truhlar and N. C. Blais, J. Chem. Phys. **86**, 6258 (1987).
A. J. C. Varandas and J. N. Murrell, Farad. Discuss. **62**, 92 (1977).
Y. P. Varshni, Rev. Mod. Phys. **29**, 664 (1957); erratum: **31**, 839 (1959).
O. P. J. Vieuxmaire, Z. Lan, A. L. Sobolewski and W. Domcke, J. Chem. Phys. **129**, 224307 (2008).
A. Wada, H. Kanamori, and S. Iwata, J. Chem. Phys. **109**, 9434 (1998).
Z. Wang, I. S. K. Kerkines, K. Morokuma, and P. Zhang, J. Chem. Phys. **130**, 044313 (2009).
D. Wang, J. R. Stallcop, W. M. Huo, C. E. Dateo, D. W. Schwenke, and H. Partridge, J. Chem. Phys. **118**, 2186 (2003).
J. Wang, R. M. Wolf, J. W. Caldwell, P. A. Kollman, and D. A. Case, J. Comput. Chem. **25**, 1157 (2004).
B. Ward, Spectrochim. Acta Part A **24**, 813 (1968).
S. J. Weiner, P. A. Kollman, D.T. Nguyen, and D. A. Case, J. Comput. Chem. **7**, 230 (1986).
H.-J. Werner, Mol. Phys. **89**, 645 (1996).
H.-J. Werner and W. Meyer, J. Chem. Phys. **74**, 5802 (1981).
H.-J. Werner, P. J. Knowles, G. Knizia, F. R. Manby, and M. Schütz, WIREs Comput. Mol. Sci. **2**, 242 (2012).
H.-J. Werner and W. Meyer, J. Chem. Phys. **74**, 5802 (1981).
T. A. Wesolowski and A. Warshel, J. Phys. Chem. **97**, 8050 (1993)

I. H. Williams, J. Mol. Spectrosc. **66**, 288 (1977).
E. B. Wilson, Phys. Rev., **45**, 706 (1934).
E. B. Wilson Jr., J. C. Decius, and P. C. Cross, *Molecular vibrations: The theory of infrared and raman vibrational spectra*. McGraw-Hill: London, 1955, p. 54-63.
H. A. Witek, Y.-K. Choe, J. P. Finley, and K. Hirao, J. Comput. Chem. **23**, 957 (2002).
S. E. Wonchoba, W.-P. Hu and D. G. Truhlar, in *Theoretical and Computational Approaches to Interface Phenomena*, edited by H. L. Sellers and J. T. Golab (Plenum, New York, 1994), p. 7.
C. Woywod, W. Domcke, A. L. Sobolewski, and H.-J. Werner, J. Chem. Phys. **100**, 1400 (1994).
Q. Wu and T. van Voorhis, Phys. Rev. A **72**, 024502 (2005).
Q. Wu and T. van Voorhis, J. Phys. Chem. A **110**, 9212 (2006).
Q. Wu and T. van Voorhis, J. Chem. Phys. **125**, 164105 (2006).
Q. Wu and T. van Voorhis, J. Chem. Theory Comput. **2**, 765 (2006).
Z. Xie and J. M. Bowman, J. Chem. Theory Comput. **6**, 26 (2010).
X. Xu, K. R. Yang, and D. G. Truhlar, J. Chem. Theory Comput. **9**, 3612 (2013).
K. R. Yang, X. Xu and D. G. Truhlar, Chem. Phys. Lett. **573**, 84 (2013).
K. R. Yang, X. Xu and D. G. Truhlar, J. Chem. Theory Comput. **10**, 924 (2014).
D. R. Yarkony, J. Phys. Chem. **100**, 18612 (1996).
D. R. Yarkony, J. Phys. Chem. A **102**, 8073 (1998).
P. Zhang, K. Morokuma, and A. M. Wodtke, J. Chem. Phys. **122**, 014106 (2005).
Y. Zhang, T. A. A. Oliver, M. N. R. Ashfold and S. E. Bradforth, Faraday Discuss. **157**, 141 (2012).
M. Zhao, M. A. Iron, P. Staszewski, N. E. Schultz, R. Valero, and D. G. Truhlar, J. Chem. Theory Comput. **5**, 594 (2009).
Y. Zhao and D. G. Truhlar, J. Chem. Phys. **125**, 194101 (2006).
Y. Zhao and D. G. Truhlar, Theor. Chem. Acc. **120**, 215 (2008).
X. Zhu and D. R. Yarkony, J. Chem. Phys. **137**, 22A511 (2012).
X. Zhu and D. R. Yarkony, J. Chem. Phys. **140**, 024112 (2014).